Volumetric Quantitative Brain Magnetic Resonance Imaging – Application to Cancer

by

Jean-David Jutras

A thesis submitted in partial fulfillment of the requirements for the degree of

Doctor of Philosophy

in

Medical Physics

Department of Oncology

University of Alberta

Abstract

Quantitative Magnetic Resonance Imaging (qMRI) is occupying an increasingly prominent role in the study of the brain, by virtue of its sensitivity to physiological and anatomical changes. However, because qMRI techniques tend to suffer from long scan durations and/or post-processing times, as well as a propensity for various systematic errors and image artifacts, they still remain somewhat separated from the standard clinical practice. This doctoral dissertation proposes new solutions for overcoming some of these challenges, especially within the context of radiation treatment planning and post-treatment monitoring of brain cancer. This application requires: 1) geometrical fidelity, 2) high resolution and contrast-to-noise ratios, and 3) accurate dose simulation directly on MRI voxels. To meet these requirements, time-efficient image acquisition strategies and post-processing pipelines are newly designed and optimized for generating quantitative proton-density, T_1, T_2, T_2^*, magnetization transfer and synthetic Computed Tomography maps.

In chapter 3, bipolar multi-echo gradient echo sequences are optimized for structural brain imaging and multi-parameter mapping, yielding SNR gains of 1.3- to 1.6-fold while reducing geometrical distortions by 3-fold over their conventional single-echo counterparts. In chapter 4, closed-form analytical solutions are derived to enable fast T_2 mapping from bSSFP sequences while minimizing errors arising from off-resonance and magnetization-transfer effects. In chapter 5, we propose a new correction technique for transmit and receive RF inhomogeneity in proton-density and T_1 maps using a bias-field correction algorithm, outperforming conventional B_1 mapping. Finally, chapter 6 presents an improved automatic tissue classification method using an ultra-short TE MRI sequence, generating continuous-valued synthetic CT images for the

purpose of automatic dose simulation in radiation treatment planning. The synthetic CT images yield equivalent dose distributions (~1% difference in dose volume histograms) in brain cancer patients.

The imaging methodologies developed throughout this thesis are also tested both on healthy volunteers and cancer patients with primary brain tumors. Although the focus of this thesis is primarily on cancer care, the qMRI techniques developed and discussed throughout are applicable to brain imaging for numerous other diseases.

Preface

Chapters 3 and 4 of this thesis have been adapted from two journal articles published in Magnetic Resonance in Medicine, respectively:

Jutras, J.-D., K. Wachowicz, G. Gilbert, N. De Zanche. (2016) SNR Efficiency of combined bipolar gradient echoes: Comparison of three-dimensional FLASH, MPRAGE and multiparameter mapping with VFA-FLASH and MP2RAGE. Magnetic Resonance in Medicine (Early View). DOI: 10.1002/mrm.26306

Jutras, J.-D., K. Wachowicz, N. De Zanche. (2016) Analytical corrections of banding artifacts in driven equilibrium single pulse observation of T2 (DESPOT2). Magnetic Resonance in Medicine 76:1790-1804. DOI: 10.1002/mrm.26074

In both of these articles, I, Jean-David, contributed the majority of the ideas, experiments and analysis of the research involved and wrote each manuscript. Dr. De Zanche, the principal investigator, significantly contributed to both the writing and reviewing process. Dr. Wachowicz also partook in the reviewing process and Dr. Gilbert coded the patch required to run the MP2RAGE pulse sequence on the Philips 3T Achieva scanner, as well as a few additional modifications for increasing the number of echoes and slices beyond their default settings.

The finite-element simulations in chapter 5 were all performed by Mrs. Atefeh Kordzadeh, under the supervision and help of Dr. De Zanche, while I, Jean-David, conducted all the experiments and data analysis.

This thesis contains in vivo brain volunteer and patient MR images, acquired following both informed consent and approval by the Health Research Ethics Board of Alberta (HREBA).

Acknowledgements

First and foremost, I acknowledge the triune God for giving me the intelligence, interest, and perseverance to pursue and complete this doctoral research project. Without the Creator, the creature can do nothing. Secondly, I especially thank my supervisor Dr. Nicola De Zanche for guiding this project from the start and making an effort to provide feedback continuously throughout. I also wish to thank every other member of the supervisory committee, including Dr. B. Gino Fallone, Dr. Satyapal Rathee, Dr. Keith Wachowicz, and Dr. Richard Thompson for providing helpful comments and expert advice at every supervisory committee. An additional thank you also to Dr. Rathee for his assistance with the operation of the CT scanner when scanning phantoms. I am also very grateful to Dr. Albert Murtha for his willingness to serve as principal investigator in a clinical trial on brain cancer patients, as well as Dr. John Amanie and Dr. Samir Patel for helping recruit the patients, and Mr. David Boryski for his assistance in scanning the patients. Thank you also to all the MRI volunteers and patients who took part in this research.

I also wish to thank the University of Alberta and the Alberta Cancer Foundation for providing the funding via various scholarships and grants, as well as two companies, including GyroTools via correspondence with Dr. Martin Buhrer, and Philips Healthcare via correspondence with Dr. Guillaume Gilbert for their technical help and support. I also thank the machine shop workers, including Mr. Ken Hennig, Mr. Curtis Osinchuck and Mr. Lance Spiridon for their help and ideas in building plastic phantoms.

I also thank my fellow graduate student colleagues for the fun time and conversations we had in the lab over the past 8 years, especially Andrei Ghila for faithfully pumping iron with me at the gym three to four times weekly. I believe it was quite therapeutical in helping to overcome the normal frustrations and stress associated with graduate student life. Finally, I am also grateful to my family members, especially my father Dominique, and mother Francine, for their prayers and support during all these years of graduate school.

Table of Contents

List of Tables

List of Figures

Chapter 1: Overview of the Thesis

"All the mathematical sciences are founded on relations between physical laws and laws of numbers, so that the aim of exact science is to reduce the problems of nature to the determination of quantities by operations with numbers."

— James Clerk Maxwell, from *Faraday's Lines of Force* (1865)

1.1 Background and Motivation

Radiation therapy is a common method for treating many types of cancer, with over 60% of cancer patients in the USA receiving some form of it over the course of their treatment [1]. The Royal College of Radiologists in the UK reported that radiation therapy was the second most effective modality for cancer treatment after surgery, and is prescribed to 40% of all patients who are cured [2]. With advances in medical imaging technology over the past 30 years, image guidance has become essential to radiation therapy. The same is also true for surgery (called image-guided surgery or IGS). About a decade following its invention in 1971, computed tomography (CT) was integrated to the Radiation Treatment Planning (RTP) process for tumor delineation and dose simulation. Since then, CT has been the predominant imaging modality in RTP, by virtue of its speed and robustness. With the invention of Magnetic Resonance Imaging (MRI) in 1977, and the availability of the first commercial MRI scanners in the early 1980s, it was soon recognized that MRI provides significantly better soft-tissue contrast than CT. Consequently, MRI was integrated to the RTP pipeline in the early 1990s for the purpose of tumor delineation, while CT was still used to provide the electronic density information required for dose simulation. In the early 2000s, it was proposed that RTP planning be based on MRI alone for the sake of simplicity and reducing the challenges associated with the MR-CT image registration process [3]. However, two problems must be addressed to make this possible:

- The lack of electron or tissue density information in MRI images, which implies that unlike CT, dose inhomogeneity correction (simulation) cannot be performed directly on MRI data.
- The possibility that geometrical distortions in MRI might degrade the accuracy of the targeting and dosimetry, leading to sub-optimal treatments (over-dosing healthy tissue and/or under-dosing the tumor).

Over the past decade, many studies have aimed to correct [4], [5], monitor [6], or avoid [7], [8] geometrical distortions in MRI-based RTP. It is generally agreed that maximal geometrical distortions should be constrained to <2 mm in conventional RTP [3], and <1 mm in stereotactic radiosurgery treatment planning [7].

Unlike CT, where the image intensity is directly proportional to the linear attenuation coefficient (μ) of tissues, MRI has been largely a qualitative imaging modality, with images being

"weighted" by a number of different physical parameters and arbitrarily scaled (usually on a 12-bit gray scale). This mixed signal weighting is actually intrinsic to the physics of MRI, which is modelled by the Bloch equations, and depends on both tissue type (intrinsic parameters, e.g., the T_1/T_2 relaxation times defined in section 2.1) and machine settings (extrinsic parameters, e.g., echo time and repetition time). Consequently, MR images are said to be T_1-/T_2-, proton-density- or diffusion-weighted (DWI), etc. Much current MRI research is pushing for faster and more robust acquisition and post-processing techniques to obtain quantitative images instead (i.e. parametric maps, such as T_1, T_2, proton-density and diffusion tensor imaging (DTI)). The primary motivations for replacing conventional weighted images by parametric maps include: first, the ability to achieve better contrast-to-noise ratio (CNR) and tumor visibility [9], secondly, the search for more sensitive biomarkers of disease progression/regression (i.e., tissue characterization), and thirdly the advantage conferred by quantitative images that are reproducible and comparable across different scanner manufacturers and imaging centers [10], [11]. As an example, Figure 1.1 shows a CT image, a T_1-weighted image, a T_1 map and a T_2 map of a primary brain tumor patient. In the CT image, gray matter has a mean CT number of ~31 HU, while white matter is ~24 HU, yielding a contrast of merely ~7 HU, hardly above the noise floor. The T_1-weighted image clearly has significantly better gray-white matter contrast-to-noise ratio (CNR) and better reveals the extent of the tumor (white arrow), but not quite as clearly as the T_1 map. Finally, the T_2 map has lower gray-white matter contrast, but better reveals the cerebral edema, which extends significantly further from the bulk tumor volume.

In practice, a minimum of two images are required to solve for a given parameter, and sometimes as many as one thousand are used (e.g., MR fingerprinting, MRF [12]). The question arises as to why parametric mapping is only starting to gain popularity, after already three decades of MRI research. It should be noted that T_1/T_2 relaxometry was explored even before the demonstration of MR imaging [13], as a potential tool for grading/classifying tumors. However, pure relaxometry alone was found to be unsuccessful in differentiating between different types of brain tumors, (even benign versus malignant lesions)[14]. This early failure may have caused a loss of interest in quantitative MRI, although three more reasons are probably just as noteworthy. First, for many years the main research driver was the development of better MRI hardware, and more sophisticated pulse sequences leading to higher-quality images. Secondly, long scan times prevented the application of quantitative MRI in the clinic and the need for speed was more

important than the need for quantification. Thirdly, motion-correction and artifact-correction techniques were higher on the list of research priorities, and still remain so in abdominal and cardiac MRI today. Only after these three basic requirements have been met can quantitative MRI become advantageous and generally accepted. Finally, it could also be argued that for typical clinical applications like diagnosis and tumor delineation, conventional weighted images are sufficient.

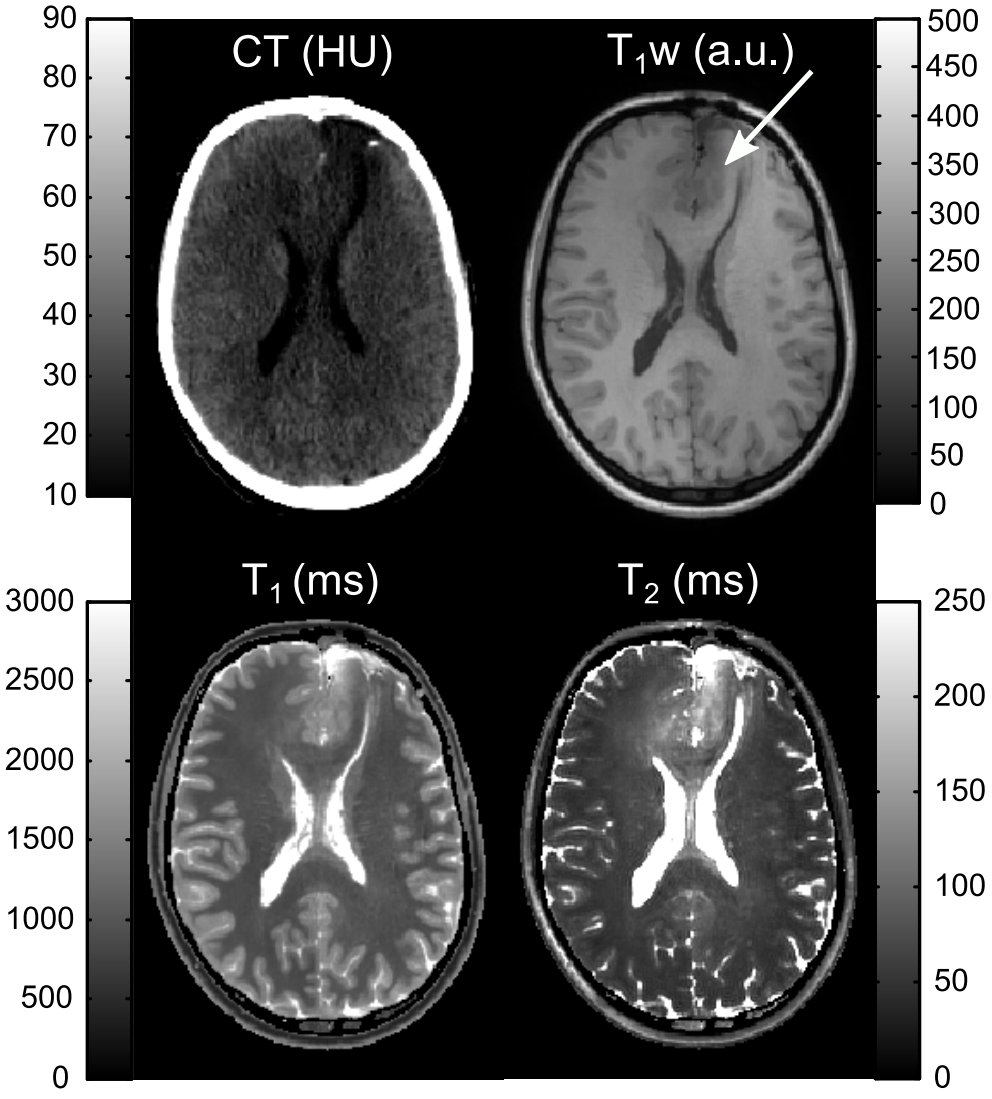

Figure 1.1: Comparison of a CT image (120 kVp, 284 mA·s), a conventional T_1-weighted image, a T_1 map and a T_2 map at 3T. Both CT and MRI were acquired following tumor resection and before the start of the radiation therapy cycle.

The field of RTP would greatly benefit from the latest advances in quantitative MRI, provided that the problems of geometrical distortions and the lack of electron density information are addressed simultaneously. Besides providing better tumor visualization at the planning stage, quantitative parametric maps could be useful for more accurately assessing and monitoring the cancer treatment outcome at different time points. At present, this is usually performed by comparing multiple follow-up MRI datasets with the pre-treatment baseline dataset (usually a contrast-enhanced T_1-weighted acquisition). In certain brain tumors, a phenomenon called Pseudo-Progression (psPD) tends to occur. In psPD, the tumor following treatment will appear larger and/or brighter from greater contrast uptake on a post-treatment MRI as compared to the pre-treatment baseline MRI. This may mislead the oncologist into concluding that the tumor is undergoing true progression, when in fact, these changes are transient and the tumor will stabilize and even shrink over time. The ability to distinguish true progression from psPD is a major challenge in brain cancer care, and a failure to correctly distinguish between the two can lead to unnecessary treatment and/or a detrimental outcome for the patient. A recent study by Sanghera et al [15] showed that within a cohort of 110 patients, 26% were identified with early progression (ePD), and within this group 32% had psPD. The median survival rate was considerably higher for those with psPD (~2.4y) than those with true progression (~0.7y). Early progression was defined using the RECIST criterion (Response Evaluation Criteria in Solid Tumors). The use of quantitative multi-parametric MRI, combined potentially with texture-analysis and/or machine-learning could provide a more powerful tool to correctly distinguish psPD from true progression.

The following points summarize the underlying ideas behind this Ph.D. dissertation:

- Convert conventional T_1-/T_2-weighted MRI into quantitative parametric maps of the same resolution (~1 mm isotropic) to achieve:
  - Negligible geometrical distortions
  - Higher CNR (defined[1] as $CNR_{A,B} = \frac{|S_A - S_B|}{\sqrt{(\sigma_A^2 + \sigma_B^2)/2}}$, for tissue A and B)

[1] In conventional MRI, an SNR (defined as $SNR_{A,B} = S_{A,B}/\sigma_{A,B}$) increase does not necessarily imply a CNR increase because the signal (and contrast) may change with the scan parameters. However, in parametric mapping the final image signal (the parameter, e.g. T_1) is independent of the scan parameters (e.g. flip angle, TR, etc…), therefore an SNR increase is equivalent to a CNR increase and both terms are interchangeable.

    - Low pixel-wise coefficients of variation (CoV) in the parametric maps (i.e. better reproducibility)
- Assign electron-density information for RTP via direct automatic tissue classification on MRI.
- Acquire and compare quantitative parametric maps at different time points for post-treatment monitoring (follow-up) of cancer patients.

While the quantitative MRI (parametric mapping/relaxometry) techniques developed throughout this thesis are applied to the radiation treatment planning and post-treatment monitoring of cancer, they are equally applicable to the study of many brain diseases, including Multiple Sclerosis, Parkinson's disease, Alzheimer's, etc., as well as other types of cancer treatment options like surgery and chemotherapy.

1.2 Organization of the Thesis

This thesis is organized into 5 main chapters, excluding the introduction (this chapter) and the conclusion and future work chapter.

Chapter 2 covers the underlying theory of MRI physics and image-processing tools that are employed throughout the rest of this thesis. Note that the reader is assumed to have some familiarity with basic Nuclear Magnetic Resonance and MRI physics, such as the rotating reference frame, phase and frequency-encoding, gradient and RF pulses, and the signal equation. These basic concepts of MRI were covered as part of my M.Sc. thesis [16] available online (https://era.library.ualberta.ca/files/dj52w5188#.V6Y2dJgrKUk) and will not be substantially repeated here.

Chapter 3 is adapted from a journal article published in Magnetic Resonance in Medicine [17], entitled: "SNR efficiency of combined bipolar gradient echoes: comparison of three-dimensional FLASH, MPRAGE, and multi-parameter mapping with VFA-FLASH and MP2RAGE." It outlines the theoretical motivation and experimental validation for replacing conventional single-echo low-bandwidth MRI sequences by multi-echo (bipolar) high-bandwidth sequences, which include improved CNR, geometrical fidelity and the enabling of multi-parameter mapping.

Chapter 4 is based on a second publication also in Magnetic Resonance in Medicine, entitled: "Analytical corrections of banding artifacts in Driven Equilibrium Single Pulse Observation of

T_2." It presents a collection of closed-form analytical solutions derived to address the problem of banding artifacts in T_2 mapping using balanced Steady State Free Precession (bSSFP) imaging.

Chapter 5 presents a fast retrospective RF inhomogeneity correction using the N4ITK bias-field correction algorithm, focusing on how the algorithm was optimized to correct for RF inhomogeneity (both transmit and receive B_1^+/B_1^-) in multi-parameter mapping (especially T_1, M_0, T_2 and MT_{sat}), via the variable flip angle (VFA) technique. It also tests the method on 5 cancer patients with primary brain tumors.

Chapter 6 employs a triple-echo Dixon ultra-short TE (UTE) radial pulse sequence followed by an image-processing pipeline to automatically classify tissues, including soft-tissue, air, fat and bone. It builds upon the previous method of Berker et al [18] in generating a synthetic CT, but generalizes the discrete tissue classification (with discreet CT numbers of attenuation coefficients μ) into a more accurate continuous-valued classification, thus taking variable bone density and partial volume effects into account. The mean absolute error is used as a metric to compare the synthetic CT with the actual planning CT of 12 patients. We also perform dose simulation on the synthetic CT datasets of two patients and compare the results with the traditional CT-based plans to assess the clinical viability of the UTE-based RTP.

Chapter 7 presents a clinical application of Multi-Parameter Mapping as was developed throughout chapters 3, 4 and 5. We show some preliminary results from a clinical trial on brain cancer patients, which started in the spring of 2016, and will probably require two years to complete.

Chapter 2: Theory of Magnetic Resonance Imaging and Image-Processing Tools

"Accordingly, we find Euler and D'Alembert devoting their talent and their patience to the establishment of the laws of rotation of the solid bodies. Lagrange has incorporated his own analysis of the problem with his general treatment of mechanics, and since his time M. Poinsôt has brought the subject under the power of a more searching analysis than that of the calculus, in which ideas take the place of symbols, and intelligent propositions supersede equations."

— James Clerk Maxwell

J. C. Maxwell on Louis Poinsôt (1777-1859) in "On a Dynamical Top" (1857). In W. D. Niven (ed.), *The Scientific Papers of James Clerk Maxwell* (1890), Vol. 1, 248.

2.1 The Bloch Equations

The nuclear magnetic resonance phenomenon is accurately modelled on the macroscopic scale by a set of first-order differential equations derived by Felix Bloch, named the *Bloch equations*. Given $\mathbf{M}(t)=(M_x(t), M_y(t), M_z(t))$ as the nuclear magnetization and $\mathbf{B}(t)=(B_x(t), B_y(t), B_0+\Delta B_z(t))$ as the magnetic field

$$\begin{aligned}\frac{dM_x(t)}{dt} &= \gamma\big(\mathbf{M}(t)\times\mathbf{B}(t)\big)_x - \frac{M_x(t)}{T_2},\\ \frac{dM_y(t)}{dt} &= \gamma\big(\mathbf{M}(t)\times\mathbf{B}(t)\big)_y - \frac{M_y(t)}{T_2},\\ \frac{dM_z(t)}{dt} &= \gamma\big(\mathbf{M}(t)\times\mathbf{B}(t)\big)_z - \frac{M_z(t)-M_0}{T_1},\end{aligned} \qquad (2.1\text{ a, b, c})$$

where γ is the gyromagnetic ratio, T_2 is the spin-spin or transverse relaxation constant and T_1 is the spin-lattice (a.k.a. longitudinal) relaxation constant. The Bloch equations can also be re-cast into a matrix equation, after expanding the cross product term: $\mathbf{M}(t)\times\mathbf{B}(t) = \hat{\mathbf{x}}\,(M_yB_z - M_zB_y) - \hat{\mathbf{y}}\,(M_xB_z - M_zB_x) + \hat{\mathbf{z}}\,(M_xB_y - M_yB_x)$, yielding

$$\frac{d}{dt}\begin{pmatrix}M_x\\M_y\\M_z\end{pmatrix} = \begin{pmatrix}-\frac{1}{T_2} & \gamma B_z & -\gamma B_y\\ -\gamma B_z & -\frac{1}{T_2} & \gamma B_x\\ \gamma B_y & -\gamma B_x & -\frac{1}{T_1}\end{pmatrix}\begin{pmatrix}M_x\\M_y\\M_z\end{pmatrix} + \begin{pmatrix}0\\0\\\frac{M_0}{T_1}\end{pmatrix}. \qquad (2.2)$$

Equation (2.1) can be expressed using complex notation, by re-writing $M_+ = M_x + i\,M_y$, $B_+ = B_x + i\,B_y$, $B_- = B_+^*$, $M_- = M_+^*$, yielding

$$\begin{aligned}\frac{dM_+(t)}{dt} &= -i\gamma\big(M_+(t)B_z(t) - M_z(t)B_+(t)\big) - \frac{M_+(t)}{T_2}\\ \frac{dM_z(t)}{dt} &= \frac{i\gamma}{2}\big(M_+(t)B_-(t) - M_-(t)B_+(t)\big) - \frac{M_z(t)-M_0}{T_1}\end{aligned} \qquad (2.3\text{ a, b})$$

The Bloch equations can also be simplified by expressing them within a rotating frame of reference. Assume that (x, y, z) is the Cartesian coordinate system of the laboratory frame. Let $(x', y', z') = (x', y', z)$ be a Cartesian coordinate system that is rotating around the z-axis with an angular frequency of ω_{rf}. The new magnetization can then be expressed in terms of Eq. (2.3) as $M_z'(t) = M_z(t)$ and $M_x'(t) = e^{+i\,\omega_{rf}t}M_+(t)$. To find the new equations of motion within the rotating frame of reference, we first take the derivative on both sides:

$$\frac{dM'_+(t)}{dt} = e^{i\omega t}\frac{dM_+(t)}{dt} + i\omega\, e^{i\omega t}M_+(t) = e^{i\omega t}\frac{dM_+(t)}{dt} + i\,\omega\, M'_+(t) \tag{2.4}$$

Substituting Eq. (2.3b) into the above expression, we get

$$\frac{dM'_+(t)}{dt} = e^{i\omega t}\left(-i\,\gamma\big(M_+(t)B_z(t) - M_z(t)B_+(t)\big) - \frac{M_+(t)}{T_2}\right) + i\omega M'_+ \tag{2.5}$$

Since $B_z(t) = B_0 + \Delta B_z(t)$, as previously noted, we can further simplify this into

$$\frac{dM'_+(t)}{dt} = i(\omega - \omega_0)M'_+(t) - i\gamma\,\Delta B_z(t)M'_+(t) + i\gamma\, B'_+(t)M_z(t) - \frac{M'_+(t)}{T_2} \tag{2.6}$$

Therefore, if a purely transverse time-varying magnetic field is applied (i.e. $\Delta B_z = 0$), the above equation simplifies to

$$\frac{dM'_+(t)}{dt} = i(\omega - \omega_0)M'_+(t) + i\gamma\, B'_+(t)M_z(t) - \frac{M'_+(t)}{T_2} \tag{2.7}$$

If the transverse time-varying magnetic field is also circularly polarized (i.e. $B_x(t) + i\,B_y(t) = B_1 \cos(\omega t) - i\,B_1 \sin(\omega t)$), Eqs. (2.7) and (2.3b) can be used to obtain

$$\frac{d}{dt}\begin{pmatrix} M'_x \\ M'_y \\ M'_z \end{pmatrix} = \begin{pmatrix} -1/T_2 & -\Delta\omega & \gamma B_1 \sin(\omega t) \\ -\gamma B_z & -1/T_2 & \gamma B_1 \cos(\omega t) \\ -\gamma B_1 \sin(\omega t) & -\gamma B_1 \cos(\omega t) & -1/T_1 \end{pmatrix}\begin{pmatrix} M'_x \\ M'_y \\ M'_z \end{pmatrix} + \begin{pmatrix} 0 \\ 0 \\ M_0/T_1 \end{pmatrix} \tag{2.8}$$

which is the equivalent of Eq. (2.2) in the rotating frame of reference. The rotating frame of reference becomes especially useful when studying the effect of RF pulses on the magnetization.

2.2 BPP (Bloembergen, Purcell and Pound) Theory of Relaxation

The question arises as to what physical phenomena cause T_1 and T_2 relaxation, and whether these constants can be predicted (or derived) from fundamental physics (i.e. basic quantum mechanics). A simple answer is that T_1 and T_2 are driven by fluctuations in the local magnetic fields as a result of proton motion and their physical interactions. As the precessional frequency of a proton is governed by the magnitude of the magnetic field (B_0), variations in the field strength will alter the precessional frequency of the proton. In a pool of proton spins with their magnetic moments initially aligned (in phase), each proton will experience slightly different

field oscillations as they interact with one another, causing a reduction in the net magnetic moment. This is the phenomenon of T_2 relaxation. On the other hand, T_1 (or spin-lattice) relaxation is governed by the fact that spins also undergo transitions between their parallel and anti-parallel states, with respect to B_0. In general, T_2 depends on T_1 and $T_2 \leq T_1$. Moreover, T_1 also tends to increase with temperature and B_0, while T_2 tends to be less dependent on B_0 but still somewhat dependent on temperature. Thus, in practice T_1 and T_2 are not fundamental constants easily derived from basic physics. Nevertheless, Bloembergen, Purcell and Pound [19] have derived a theoretical relationship between, T_1, T_2, and magnetic proton spin interactions within idealized homogeneous media (called BPP theory), yielding

$$\frac{1}{T_1} = K\left(\frac{\tau_c}{1+\omega_0^2\tau_c^2} + \frac{4\tau_c}{1+4\omega_0^2\tau_c^2}\right),$$
$$\frac{1}{T_2} = K\left(\frac{3}{2}\tau_c + \frac{5\tau_c/2}{1+\omega_0^2\tau_c^2} + \frac{\tau_c}{1+4\omega_0^2\tau_c^2}\right), \qquad K = \frac{3\mu_0^2}{160\,\pi^2}\frac{\hbar^2\gamma^4}{r^6} \tag{2.9}$$

Here, τ_c is the correlation time of the molecular tumbling motion, $\omega_0=\gamma B_0$ (the larmor frequency), μ_0 is the magnetic permeability of free space, r is the average distance between two nuclei carrying magnetic dipole moment, $\hbar$ is the reduced Plank constant, and γ is the gyromagnetic ratio. While BPP theory cannot accurately predict experimental T_1 and T_2 values measured in biological tissues, it still provides a useful qualitative assessment of the relaxation times with respect to viscosity (proportional to τ_c) and field strength. In general, liquid protons, such as in cerebrospinal fluid (CSF), have long relaxation times (T_1/T_2~4300/2500 ms) while white matter (WM)/gray matter (GM) have intermediate T_1~1000–2000 ms and short T_2~50–100 ms, and solid protons (such as in proteins) have long T_1 ~1000 ms but ultra-short T_2~10 μs. Moreover, except in liquids (e.g., cerebrospinal fluid), T_1 values generally increase with increasing field strength, while T_2 tends to remain the same or slightly decrease.

The fact that solids have extremely short T_2 also leads to further ramifications concerning the visible proton density M_0 in MRI. Conventional MRI cannot detect signal from solid protons, which relax too quickly; therefore, the proton density that appears in MRI is not the absolute proton density of tissues, but rather the "visible" proton density which comes primarily from the water inside the cells. Consequently, although WM and GM both have an absolute proton density

within ~1% of each other, because their proportion of solid protons is quite different, the visible proton-density of WM is ~71% while that of GM is ~81% of pure water.

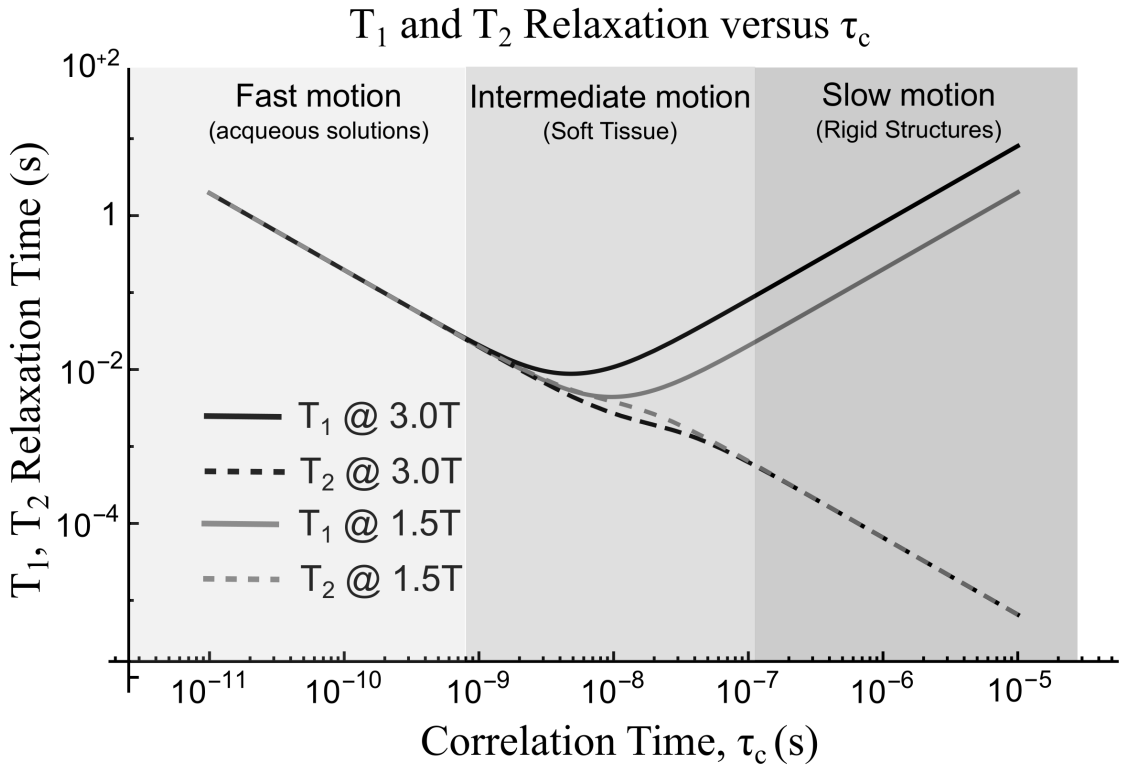

Figure 2.1: Plot of T_1 and T_2 versus τ_c on a log-log scale. BPP theory predicts that the T_1 of soft tissues generally increases with field strength, while the T_2 slightly decreases or remains unchanged.

2.3 Radio-Frequency Pulse Excitation

When a sample of protons is placed within a parallel static magnetic field B_0, the net magnetization will precess at the Larmor frequency $\omega_0 = \gamma B_0$. By convention, the static magnetic field always points along the z-axis. If a transverse time-varying magnetic field B_1 is now applied, the Bloch equations predict that a resonance condition will take place, reaching a maximum at a transmit frequency of $\omega_{rf} = \omega_0$, (which is said to be on-resonance). Using Eq. (2.8) with initial conditions $\left[M'_x(0), M'_y(0), M'_z(0)\right]^T = [0, 0, M_0]^T$ and assuming that T_1 and T_2 decay are negligible during the excitation (i.e.: T_1, $T_2 \sim \infty$) we get

$$\frac{d}{dt}\begin{pmatrix} M'_x(t) \\ M'_y(t) \\ M'_z(t) \end{pmatrix} = \begin{pmatrix} 0 & 0 & 0 \\ 0 & 0 & \gamma B_1 \\ 0 & -\gamma B_1 & 0 \end{pmatrix}\begin{pmatrix} M'_x(t) \\ M'_y(t) \\ M'_z(t) \end{pmatrix} \tag{2.10}$$

The closed-form solution to this initial-value problem can be found by making the substitution $\widetilde{M} = M_z + iM_y$, and using the identity: $e^{i\theta}$=cos(θ)+i sin(θ), to yield

$$\begin{aligned} M'_x(t) &= 0 \\ M'_y(t) &= M_0 \sin\left(\int_0^\tau B_1(t)dt\right) \\ M'_z(t) &= M_0 \cos\left(\int_0^\tau B_1(t)dt\right) \end{aligned} \tag{2.11}$$

These equations indicate that the effect of the on-resonance excitation B_1 field is a precession of the net magnetization about the x'-axis. The angle

$$\alpha = \gamma \int_0^\tau B_1(t)dt \tag{2.12}$$

is commonly called the *flip* or *tip* angle. In general, the B_1 field can have any orientation with respect to the rotating frame, including an azimuthal angle θ, between the B_1 vector and the z'-axis, and a polar angle ϕ, between the B_1 vector and the x'-axis. In this case, three rotation operators $\mathbf{R_x}$, $\mathbf{R_y}$ and $\mathbf{R_z}$ can be used to model the effect of an RF pulse on the magnetization

$$\mathbf{R}_\mathrm{x} = \begin{pmatrix} 1 & 0 & 0 \\ 0 & \cos\alpha & \sin\alpha \\ 0 & -sin\ \alpha & \cos\alpha \end{pmatrix},\ \mathbf{R}_\mathrm{y} = \begin{pmatrix} \cos\alpha & 0 & -\sin\alpha \\ 0 & 1 & 0 \\ \sin\alpha & 0 & \cos\alpha \end{pmatrix},$$
$$\mathbf{R}_\mathrm{z} = \begin{pmatrix} \cos\alpha & \sin\alpha & 0 \\ -\sin\alpha & \cos\alpha & 0 \\ 0 & 0 & 1 \end{pmatrix} \tag{2.13}$$

The effect of an α_ϕ pulse can be represented by three cascaded spin rotations:

$$\mathbf{M}_\mathrm{n}^+ = \mathbf{R}_\mathrm{z}(\phi)\mathbf{R}_\mathrm{x}(\alpha)\mathbf{R}_\mathrm{z}(-\phi)\mathbf{M}_\mathrm{n}^- \tag{2.14}$$

where $\mathbf{M_n}^-$/$\mathbf{M_n}^+$ is the magnetization before/after the n^{th} RF pulse. The phase ϕ of the RF pulse has important implications in pulse sequences. In gradient-echo sequences, it is usually incremented from one RF pulse to the next according to a phase-cycling scheme, in order to manipulate the final signal and contrast of the image.

2.4 Spatial Encoding and Image Reconstruction

The first MR image was acquired in 1977 by Raymond Damadian using a whole-body scanner that relied on a very rudimentary method of spatial encoding [20]. The method, termed *field-focusing*, consisted of acquiring a single voxel at a time by shimming the static magnetic field at a single point and performing an NMR experiment. The object had to be moved point-by-point to cover the entire field-of-view, resulting in a total scan time of about five hours for a single slice of the human thorax containing 106 voxels. The major break-through in spatial encoding came with Paul Lauterbur and Peter Mansfield's idea of using spatially-varying linear magnetic field gradients [21], [22]. The linear magnetic field gradients cause the Larmor frequency to vary linearly with space. The Fourier transform can then be employed to convert the signal acquisition matrix from the frequency space into the image space.

2.4.1 Linear Magnetic Field Gradients

In a modern MRI scanner, linear magnetic field gradient coils are designed to generate a gradient field:

$$\mathbf{G} = \frac{\partial B_z}{\partial x}\hat{\mathbf{x}} + \frac{\partial B_z}{\partial y}\hat{\mathbf{y}} + \frac{\partial B_z}{\partial z}\hat{\mathbf{z}} \equiv G_x\,\hat{\mathbf{x}} + G_y\,\hat{\mathbf{y}} + G_z\,\hat{\mathbf{z}} \tag{2.15}$$

such that the magnetic field is $\mathbf{B} = (G_x\,x + G_y\,y + G_z\,z + B_0)\hat{\mathbf{z}}$, and its angular frequency is $\omega = \gamma(B_0 + \mathbf{G}\cdot\mathbf{r})$ In practice however, the x and y-components of the magnetic field will still be non-zero ($B_x \neq 0, B_y \neq 0$), called *concomitant* magnetic fields, which is a consequence of Gauss's law for magnetism ($\nabla\cdot\mathbf{B} = 0$). Minimizing the effect of the concomitant fields can be important in certain MRI pulse sequences and techniques to avoid image artifacts. The x, y and z magnetic field gradients are used to create pulses of certain time durations to refocus the magnetization and/or read the NMR signal. The net phase accumulation will be

$$\phi(t) = \omega(x,y,z)t = \gamma\,B_0 t + \gamma\left[\int_0^t \mathbf{G}(\tau)\,d\tau\right]\cdot\mathbf{r} = \omega_0 t + \mathbf{k}(t)\cdot\mathbf{r} \tag{2.16}$$

where the variable $\mathbf{k}(t) = \gamma\ \int_0^t \mathbf{G}(\tau)\,d\tau$, is the position in *k-space* or *frequency space*. In MRI, gradients are used for 5 main purposes, including, frequency encoding or "readout gradient" ($\mathbf{G_r}$), phase encoding ($\mathbf{G_p}$), slice selection ($\mathbf{G_s}$), spoiling (i.e. resetting the transverse magnetization to zero), and crushing (i.e. avoiding free-induction decays).

2.4.2 Slice Selection

In conventional MRI, RF pulses will be either selective, or non-selective. Unlike non-selective pulses, selective pulses are usually played concurrently with a slice-selection gradient. Non-selective pulses are commonly used in 3D pulse sequences, which have two phase-encoding directions, while selective pulses are used in 2D sequences. Using Eq. (2.7), it can be demonstrated that at low flip angles, the pulse profile is approximately equal to the Fourier transform of the pulse envelope. Ignoring T_2 relaxation during the excitation, (and dropping the prime convention, since the rotating reference frame is now the assumed default frame) we have

$$\frac{dM_+(t)}{dt} = i\,\Delta\omega\, M_+(t) + i\gamma\, B_1(t) M_z(t) \tag{2.17}$$

With the initial condition $M_+(0) = 0$, the above first-order differential equation has the solution

$$M_+(t) = i\gamma\, e^{-i\,\Delta\omega\, t} \int_0^t M_z(\tau) B_1(\tau) e^{i\,\Delta\omega\,\tau}\, d\tau \approx i\gamma\, e^{-i\,\Delta\omega\, t} M_0 \int_0^t B_1(\tau) e^{i\,\Delta\omega\,\tau} d\tau \tag{2.18}$$

Note that we have made the approximation $M_z(t)=M_0\cos(\alpha) \approx M_0$, which is only valid for a small flip angle. Taking the magnitude, we get

$$\begin{aligned} |M_+(t)| &\approx \gamma M_0 \left| \int_0^t B_1(\tau) e^{i\,\Delta\omega\,\tau} d\tau \right|, \\ \sin(\alpha) = \pm\frac{|M_+(t)|}{M_0} &\approx \gamma \left| \int_0^t B_1(\tau) e^{i\,\Delta\omega\,\tau} d\tau \right|, \\ &\approx \alpha(\Delta\omega) \approx \pm\gamma \left| \int_0^t B_1(\tau) e^{i\,\Delta\omega\,\tau} d\tau \right| \end{aligned} \tag{2.19}$$

since $M_y(t)=M_0\sin(\alpha)$, and $\sin(\alpha) \approx \alpha$ for small flip angles. Because the Fourier transform of a sinc is a square box, sinc-shaped pulses are frequently used in selective RF excitation. On the other hand, non-selective pulses (a. k. a. "hard" pulses) are designed to excite a wide range of frequencies (the entire object), and thus require a large bandwidth, or equivalently, a short time duration τ_p. Consequently, block-shaped RF pulses are usually used in non-selective excitation. An example of a selective and a non-selective RF pulse, with corresponding slice-selection gradient and magnetization profiles are shown in Figure 2.2 for comparison. The pulse profiles were simulated using MRiLab v1.2, which is a freely available MRI simulator toolbox for

MATLAB (https://sourceforge.net/projects/mrilab/). In selective excitation, the frequency bandwidth $\Delta\omega$ is induced by a linear magnetic field gradient $\mathbf{G}_s$, such that

$$\Delta\omega = \gamma\, \mathbf{G}_s \cdot (\mathbf{s} - \mathbf{s}_0), \qquad \mathbf{s}_0 = \frac{\omega_{rf} - \omega_0}{\mathbf{G}_s} \tag{2.20}$$

where $\mathbf{s}$ is the position from the center of the slice and $\mathbf{s_0}$ is the slice location. Therefore, assuming that a slice is selected in the z direction at position z_0, the required transmit frequency of the RF pulse is

$$\omega_{rf} = \omega_0 + \gamma\, G_z z_0 \tag{2.21}$$

and the slice thickness is given by

$$\Delta z = \frac{\Delta\omega}{\gamma G_z} \tag{2.22}$$

where $\Delta\omega$ is the bandwidth of the RF pulse. If the RF pulse is symmetric about $t=\tau_p/2$, Eq. (2.18) becomes

$$M_+(z,t) = i\,\gamma M_0\, e^{-i\gamma G_z (z-z_0)\tau_p/2} \int_{-\tau_p/2}^{\tau_p/2} B_1\left(t + \frac{\tau_p}{2}\right) e^{i\gamma G_z (z-z_0)t}\, dt \tag{2.23}$$

The term $e^{-i\gamma G_z (z-z_0)\tau_p/2}$ corresponds to a linear phase shift introduced across the slice thickness. Unless corrected for, it will lead to an undesirable signal loss. Therefore, following a slice-selection gradient, a rephrasing (negative) gradient lobe (see Figure 2.2) with half the area of the selective gradient is usually incorporated to re-phase the spin isochromats within the slice. For further details and a mathematical proof of this concept, see [23], pp.149-150.

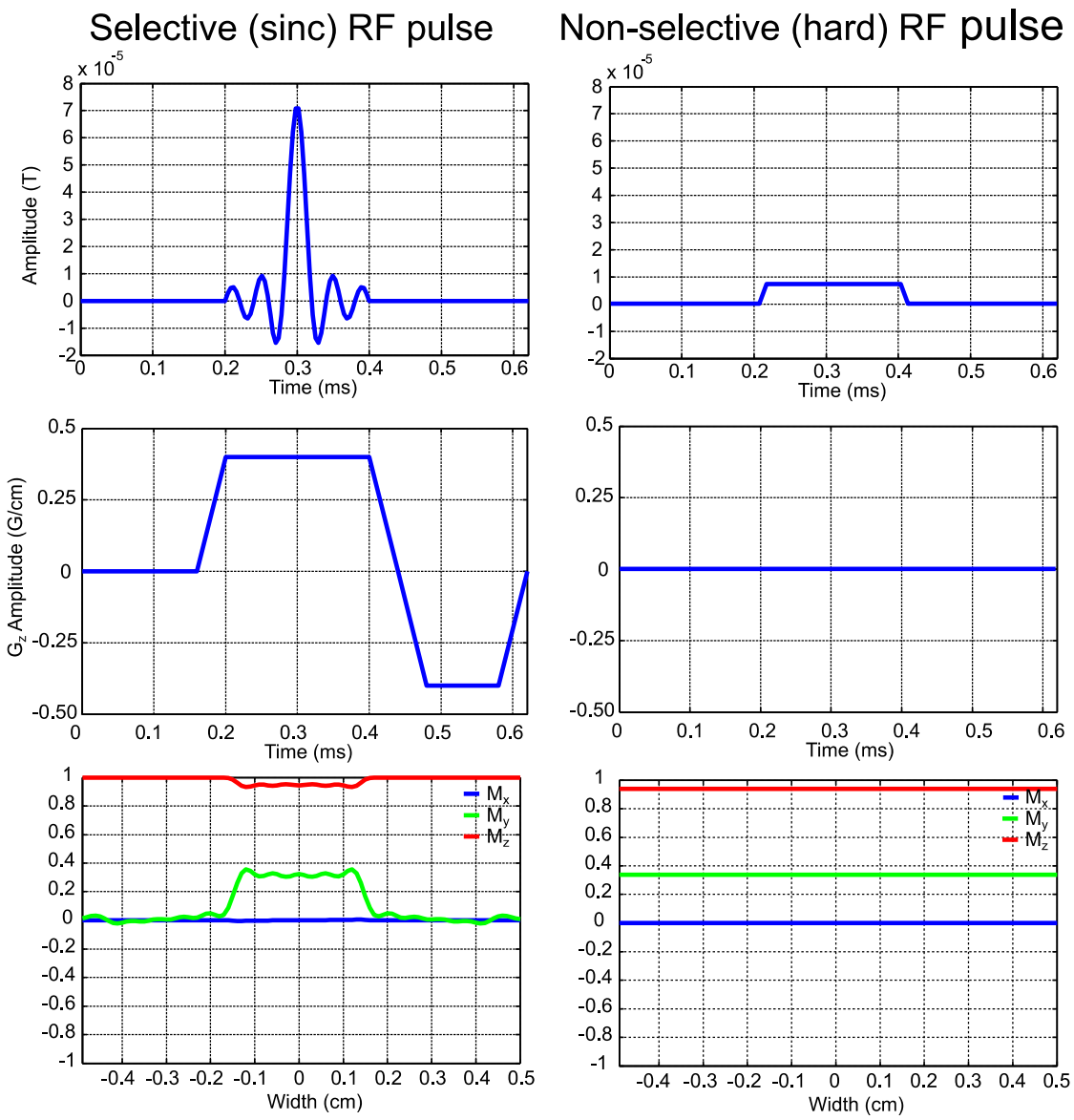

Figure 2.2: Comparison of a selective (sinc) and a non-selective (hard) RF pulse with a flip angle of 20º, simulated using MRiLab 1.2.

2.4.3 Signal Detection

Once the net magnetization in a sample of proton spins has been flipped into the xy-plane following RF excitation, Faraday's Law predicts that if a coil is placed near the sample, a magnetic flux will be induced in the coil, according to

$$\Phi(t) = \oint_V \mathbf{B_1^-}(\mathbf{r}) \cdot \mathbf{M}(\mathbf{r}, t)\, d\mathbf{r} \tag{2.24}$$

where $\mathbf{B_1}^-$ is the receive magnetic field sensitivity profile and **M** is the magnetization. The signal picked up by the coil is essentially proportional to the voltage (electromagnetic force) generated, and given by

$$V(t) = -\frac{\partial \Phi(t)}{\partial t} = -\frac{\partial}{\partial t}\oint \mathbf{B_1^-}(\mathbf{r}) \cdot \mathbf{M}(\mathbf{r},t)d\mathbf{r} = -\int \left[B_{1,x}^-(\mathbf{r})\frac{\partial M_x(\mathbf{r},t)}{\partial t} + B_{1,y}^-(\mathbf{r})\frac{\partial M_y(\mathbf{r},t)}{\partial t}\right] d\mathbf{r} \qquad (2.25)$$

where the z component of the magnetization has been ignored because it varies very slowly compared to the x and y components (i.e. $\partial M_z/\partial t \approx 0$). Using complex notation, we can express the dot product in Eq. (2.25) as

$$V(t) = -\int \mathrm{Re}\left[B_{1,+}^-(\mathbf{r})\frac{\partial M_-(\mathbf{r},t)}{\partial t}\right] d\mathbf{r} \qquad (2.26)$$

In general, M_- and $B_{1,+}^-$, can be expressed[2] as

$$M_-(\mathbf{r},t) \equiv |M_+(\mathbf{r},0)|e^{-i[\omega(\mathbf{r})t-\phi_e(\mathbf{r})]}e^{-t/T_2(\mathbf{r})}, \text{ and } B_{1,+}^-(\mathbf{r}) \equiv \left|B_{1,+}^-(\mathbf{r})\right|e^{i\phi_r(\mathbf{r})} \qquad (2.27)$$

where $\phi_r(\mathbf{r})$ is the reception phase angle, and $\phi_e(\mathbf{r})$ is the initial phase shift introduced by the RF excitation. (The term $i\gamma B_+(t)M_z(t)$ in Eq. (2.7) becomes $\phi_e(\mathbf{r})$ after integration). Taking the derivative, we have

$$\begin{aligned}\frac{\partial M_-(\mathbf{r},t)}{\partial t} = {} & |M_+(\mathbf{r},0)|e^{-i[\omega(\mathbf{r})t-\phi_e(\mathbf{r})]}e^{-t/T_2(\mathbf{r})}\frac{-1}{T_2(\mathbf{r})} \\ & - i\omega(\mathbf{r})|M_+(\mathbf{r},0)|e^{-i[\omega(\mathbf{r})t-\phi_e(\mathbf{r})]}e^{-t/T_2(\mathbf{r})}\end{aligned} \qquad (2.28)$$

Since in general $\omega(\mathbf{r}) >> 1/T_2(\mathbf{r})$, we can ignore the first term of Eq. (2.28). Putting it all together, we get

$$\begin{aligned}V(t) &= -\int \mathrm{Re}\left[i\omega(\mathbf{r})\left|B_{1,+}^-(\mathbf{r})\right||M_+(\mathbf{r},0)|e^{-t/T_2(\mathbf{r})}\, e^{-i[\omega(\mathbf{r})t-\phi_e(\mathbf{r})+\phi_r(\mathbf{r})]}\right]d\mathbf{r} \\ &= \int \omega(\mathbf{r})\left|B_{1,+}^-(\mathbf{r})\right|\,|M_+(\mathbf{r},0)|\,e^{-t/T_2(\mathbf{r})}\sin\left(\omega(\mathbf{r})t-\phi_e(\mathbf{r})+\phi_r(\mathbf{r})\right)d\mathbf{r}\end{aligned} \qquad (2.29)$$

In general, two issues arise when attempting to detect *V(t)*. First, *V(t)* is a high-frequency signal because the transverse magnetization precesses at the Larmor frequency (i.e. $\omega(\mathbf{r})=\omega_0+\Delta\omega(\mathbf{r})$), and secondly, given the phase shifts, there is no way to distinguish clockwise from

[2] N.B.: $B_{1,+} = B_{1,x} + iB_{1,y}$, $M_+(\mathbf{r},t) = M_x(\mathbf{r},t) + iM_y(\mathbf{r},t)$, $M_+^* = M_-$, and $B_{1,+}^* = B_{1,-}$.

counterclockwise rotation (i.e. $\Delta\omega > 0$ or $\Delta\omega < 0$). In order to overcome these issues, *signal demodulation* and *quadrature detection* are used. Signal demodulation consists of removing the high-frequency component ω_0 from the signal, and quadrature detection means that the signal is split into two branches. One branch is multiplied by a reference signal[3] of $2\cos(\omega_0 t)$ and the second branch is multiplied by $2\sin(\omega_0 t)$, which has a 90º phase shift with respect to the first branch. The signal is then mixed, low-pass filtered, and output as a complex signal $S(t)=S_R(t) + i\,S_I(t)$. Following this quadrature detection system, the final signal $S(t)$ becomes

$$\begin{aligned} S(t) &= \omega_0 \int \left|B_{1,+}^{-}(\mathbf{r})\right| |M_{+}(\mathbf{r},0)| e^{-t/T_2(\mathbf{r})} e^{-i[\Delta\omega(\mathbf{r})t - \phi_e(\mathbf{r}) + \phi_r(\mathbf{r}) - \frac{\pi}{2}]} d\mathbf{r} \\ &= \omega_0\, e^{i\pi/2} \int B_{1,+}^{-}(\mathbf{r})^{*} M_{-}(\mathbf{r},0) e^{-t/T_2(\mathbf{r})} e^{-i\Delta\omega(\mathbf{r})t} d\mathbf{r} \end{aligned} \tag{2.30}$$

For further details, and more intermediate steps in the mathematical derivations, see [23], pp. 94-100.

2.4.4 Image Reconstruction

In general, because the frequency variation $\Delta\omega(\mathbf{r})$ is generated by the linear magnetic field gradients (G_x, G_y, G_z), using Eq. (2.16) we may write

$$S(t) \propto \int B_{1,+}^{-}(\mathbf{r})^{*} M_{-}(\mathbf{r},0)\, e^{-t/T_2(\mathbf{r})}\, e^{-i\,\mathbf{k}(t)\cdot\mathbf{r}} d\mathbf{r} \tag{2.31}$$

Equation (2.31) is essentially a Fourier transform. Therefore, the final MR image can be obtained by taking the inverse Fourier transform of the signal after it has been sampled on a Cartesian grid, leading to

$$I(\mathbf{r}) = \int e^{i\,\mathbf{k}\cdot\mathbf{r}} \int B_{1,+}^{-}(\mathbf{r})^{*}\, M_{-}(\mathbf{r},0)\, e^{-t/T_2(\mathbf{r})} e^{-i\,\mathbf{k}(t)\cdot\mathbf{r}} d\mathbf{r}\, d\mathbf{k} \tag{2.32}$$

From the properties of Fourier transforms, the signal at the center of k-space (i.e. $\mathbf{k}=\mathbf{0}$) is responsible for governing the image intensity and contrast. The 3D Fourier transform of f and its inverse can be defined as

$$F(k_x,k_y,k_z) = \iiint_{-\infty}^{\infty} f(x,y,z) e^{i2\pi(k_x x + k_y y + k_z z)}\, dxdydz, \tag{2.33 a, b}$$

[3] N.B.: The factor of 2 is just used to later simplify the math.

$$f(x,y,z) = \iiint_{-\infty}^{\infty} F(k_x,k_y,k_z)e^{-i2\pi(k_x x+k_y y+k_z z)}dk_x dk_y dk_z$$

which explains why the signal at the center of k-space is equal to the volume integral of the entire image, since

$$F(0,0,0) = \iiint_{-\infty}^{\infty} f(x,y,z)\,dxdydz. \tag{2.34}$$

Therefore, for best signal-to-noise ratio, the center of k-space should be sampled when the signal is maximum. The time required to read the center of a line in k-space, following the RF excitation, is known as the echo time (*TE*), and the time elapsed between two successive RF excitations is known as the repetition time (*TR*). The maximum signal in a voxel occurs when all the spin isochromats are in-phase. Following RF excitation, the spins isochromats will start to de-phase over time, due to the presence of static field inhomogeneities $\Delta B_0(x, y, z)$, and transverse (T_2) relaxation will occur. The isochromats can be re-phased during the readout using either a refocusing RF pulse, or else a gradient pulse, inducing an *echo*. Alternatively, the signal can be read without refocusing, which in this case is called a free-induction decay (FID). Using a series of RF and gradient pulses, a large variety of *pulse sequences* can be designed, leading to drastically different image types (with varying contrasts and weightings).

2.5 Pulse Sequences

In MRI, two families of pulse sequences exist: the RF spin echo and the gradient echo family. As their names imply, the main difference between the two lies in how the echoes are generated in each case. RF spin echoes also differ significantly from gradient echoes in that they affect both the transverse and the longitudinal magnetization (M_+ and M_z), while gradient echoes only affect the transverse magnetization (M_+). Because gradient echoes leave the longitudinal magnetization undisturbed, the image signal in gradient-echo pulse sequences (either 2D or 3D) can be more easily expressed as a closed-form analytical solution of the Bloch equations and the scan parameters (e.g. *TE*, *TR* and flip angle α). This is generally less true of spin-echo pulse sequences, especially when a long train of low-angle refocusing pulses is used (to be discussed in section 2.5.1.1). Some analytical signal equations do exist for simple 2D spin echo sequences[4],

[4] By 2D, I am referring to sequences that have only one phase-encode direction and are commonly implemented on commercial MRI scanners.

but not for 3D fast spin echo sequences[5]. Consequently, gradient echo sequences have become the work-horse of 3D quantitative MRI, as their simple analytical solutions can be linearized to perform fast voxel-wise curve-fitting.

A second advantage of gradient echo sequences is that their longitudinal magnetization M_z usually reaches a steady-state (or sometimes a pseudo steady-state) following a sufficient number of RF excitation pulses. This implies that the available transverse magnetization M_+ is the same throughout each acquisition window (in the case of true steady-state) or acquisition module (in the case of pseudo steady-state, where a module consists of N phase-encoding lines in k-space (see Figure 2.13)). Sequences that are in steady-state usually create images with narrower point-spread-function (PSF) (i.e. sharper) than those that are not in steady-state. Moreover, in true steady-state sequences, the image contrast remains unaffected by the choice of k-space sampling trajectory. In this section we shall cover some basic spin echo and gradient echo sequences, but the primary focus will be on gradient echo sequences.

2.5.1 RF Spin Echo Sequences

An example of the simplest two-dimensional RF spin echo sequence is shown in Figure 2.3. In order to create a full echo, the pre-phaser gradient lobe must have half the area of the readout gradient, and the center of the readout window must be located at twice the time duration elapsed between the excitation pulse and the refocusing pulse. The area of the crusher and spoiler gradients is quite arbitrary, but will have some effect on moving spins (e.g. blood flow). Solving the Bloch equations for this pulse sequence yields the following signal equation (assuming $TR>>TE$)

$$\begin{aligned} S &= M_0\left(1-2e^{-(TR-TE/2)/T_1}+e^{-TR/T_1}\right)e^{-TE/T_2} \\ &\approx M_0\left(1-e^{-TR/T_1}\right)e^{-TE/T_2} \end{aligned} \tag{2.35}$$

From this equation, it is straightforward to find the parameters required to achieve a desired image contrast weighting. For T_1 weighting we must minimize the dependence on T_2, therefore, a short TE and a $TR\sim T_1$ is required.

[5] This is true for 3D sequences that are commonly used in a clinical setting; one could always implement a 3D sequence that can be easily modeled analytically, but the scan time would be too long to be of clinical value.

Contrast Weighting	TE (ms)	TR (ms)
T_1	≤30	500-800
T_2	100-200	≥2000
Proton-Density	≤30	≥2000

Table 2.1: Typical scan parameters required to achieve various contrast weightings using an RF spin echo sequence.

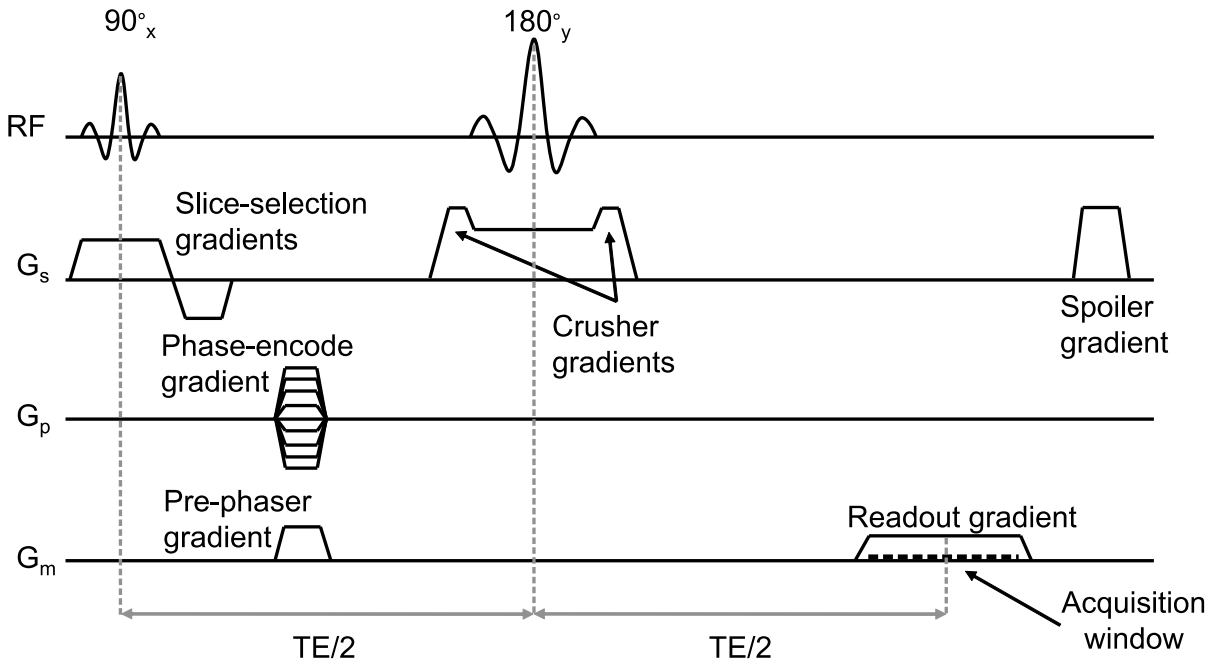

Figure 2.3: A typical 2D RF spin echo sequence with the different gradient lobes labelled.

2.5.1.1 Turbo Spin Echo

Spin echo pulse sequences tend to be time-consuming because of their long repetition times, especially when trying to achieve good T_2-weighting. While multiple slices can be acquired consecutively, thus reducing the amount of dead-time naturally found within the sequence, the scan duration can be reduced further by acquiring multiple lines of k-space following a single RF excitation pulse. This technique is commonly called *Turbo Spin Echo* (TSE) or *Fast Spin Echo* (FSE). An example of a 2D TSE pulse sequence (realistically programmed on a Philips scanner) is shown in Figure 2.4. Observe that the pulse shapes are a two-lobe sinc for excitation and a single-lobe sinc for refocusing; moreover, the refocusing pulse angles are 120°, rather than 180°. Using five-lobe sinc pulses with a refocusing angle of 180° (as in Figure 2.3) would be too time-

consuming and also lead to high energy deposition (*specific absorption rate*, SAR). Besides, the transverse magnetization can be refocused with any choice of angle, and the refocusing pulse width can be made equal or greater than the slice selection. The main drawback is that narrow refocusing pulse widths and especially with angles of <180°, will tend to introduce more T_1 weighting, as well as *stimulated echoes*, resulting in a poorer T_2 weighting. Stimulated echoes occur when left-over magnetization accumulates longitudinally (along the z-axis) and gets flipped back unto the xy-plane by a later refocusing pulse. The number of refocusing pulses (also equal to the number of k-space lines acquired following a single RF excitation and *TR*) is commonly called the *echo train length* (ETL[6]), or the *turbo spin echo factor* (TSE factor) and the time elapsed between consecutive echoes is called the *echo spacing* (ESP). A third important concept in MRI is the *profile order* (a.k.a. *view-order*), which is the order in which k-space lines are acquired. The two most common profile order schemes are *centric* and *linear*. In the centric scheme, the central lines of k-space are acquired first following the excitation, and the phase-encode steps move center-out of k-space (i.e. k=0, +1, -1, +2, -2, +3, -3, …, +128, -128). In the linear scheme, k-space is read from k_{min} to k_{max} (i.e. k=-128, -127, -126, …, 126, 127, 128). An effective echo time TE_{eff} can be defined as the average time at which the centre of k-space is sampled, following the RF excitation. If the profile order is linear, this will correspond to about half the echo train length. To achieve a desired contrast weighting the TE_{eff} should have a value similar to *TE* in Table 2.1. Moreover, the signal equation in a TSE sequence can be approximated as

$$S = M_0\left(1 - e^{-\frac{TR-ETL\cdot ESP}{T_1}}\right)e^{-TE_{eff}/T_2} \tag{2.36}$$

2.5.1.2 Carr-Purcell-Meiboom-Gill (CPMG)

CPMG is a type of TSE pulse sequence which obeys the CPMG condition, defined by the following two requirements: 1) The refocusing pulses must be 90 degree out of phase with the excitation pulses and be evenly positioned with equal spacing between any two consecutive refocusing pulses (i.e.: $TE_2=2\times TE_1$, $TE_3=3\times TE_1$, etc). 2) The phase accumulated by a spin isochromat between any two consecutive RF pulses must be equal. This implies that the crusher gradient pairs surrounding the refocusing pulses must have the same area, and that each phase-

[6] Sometimes, ETL is defined as the combined time duration of all the echoes (per TR), as in Ref. [189].

encoding gradient must be accompanied by a phase-rewinding gradient after the readout window. Note that the TSE sequence in Figure 2.4 also obeys the CPMG condition. Two-dimensional CPMG sequences are frequently used in T_2 mapping, both single-component and multi-component; in that case, the same line in k-space will be sampled N times, leading to N images at different TE_n. The pulse sequence diagram will look almost identical to that of Figure 2.4, except that the phase-encoding gradient will not be incremented throughout the shot (the positive and negative lobes of $\mathbf{G_p}$ will be identical). A CPMG-based T_2 mapping technique will be used later in chapter 4 to verify the accuracy of a gradient-echo based T_2 mapping technique.

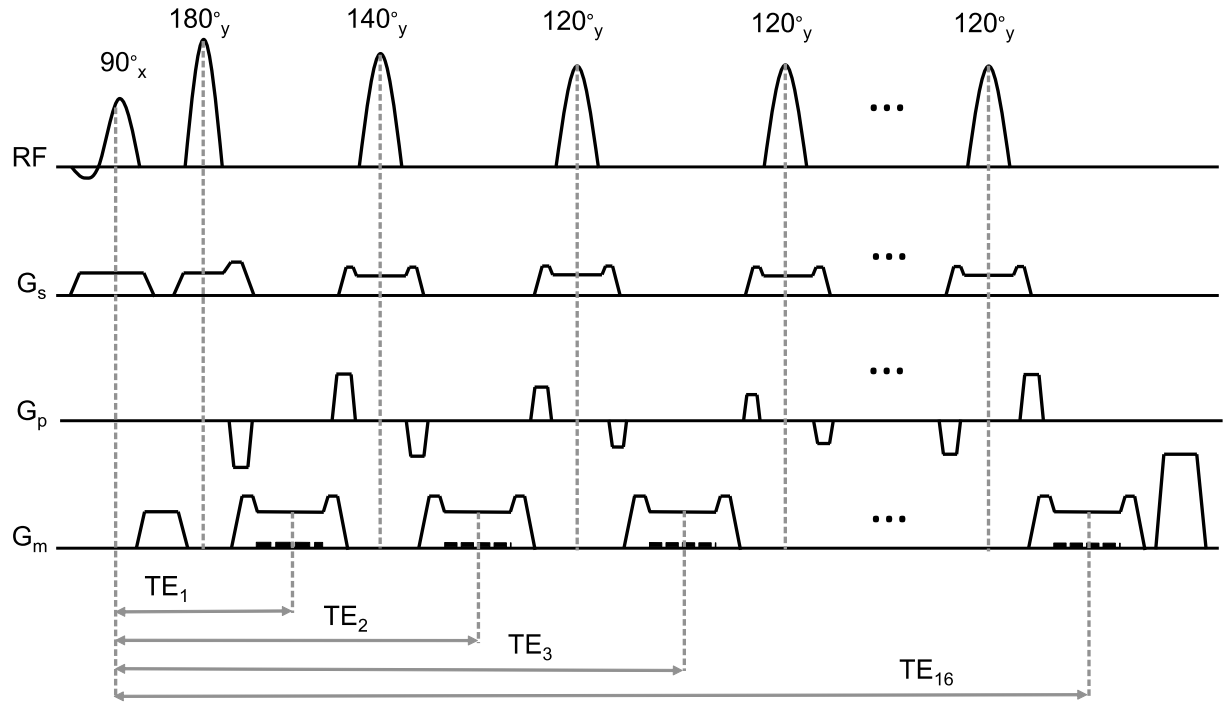

Figure 2.4: A 2D turbo spin echo pulse sequence with an echo-train length (*ETL*) of 16. Observe that crusher gradients are used both along the slice and the frequency encode direction, and the profile-order is linear, therefore $TE_{eff} = TE_8$.

2.5.1.3 Three-Dimensional TSE Sequences

A main disadvantage of 2D spin echo sequences is that slice cross-talk may occur, leading to signal saturation effects, and a consequent loss of contrast-to-noise ratio (CNR). If a slice gap is acceptable, then this is usually not an issue. Diagnostic MRI examinations often consist of multi-slice 2D sequences containing slice gaps, since a small gap between consecutive slices (i.e. 1–2

mm) is unlikely going to lead to a misdiagnosis of the patient. In RTP, however, where the tumor must be contoured as precisely as possible, a dataset containing slice gaps would be unacceptable. An additional disadvantage of 2D sequences is that they may suffer from geometrical distortions and water-fat shifts[7] both along the frequency and the through-slice direction. As previously mentioned in the introduction, minimizing geometrical distortions is important in MRI-based RTP to ensure accurate dose simulation and/or accurate co-registration with the CT dataset. Finally, reformatting (or resampling) a 2D multi-slice dataset following co-registration with CT may result in aliasing [24]. Therefore, 3D sequences are usually preferred in both RTP and image-guided surgery over multi-slice 2D sequences.

Three dimensional TSE sequences are commonly used to achieve T_2-weighting [25], while 3D gradient echo sequences (N.B. to be discussed in the next section) are more commonly used for T_1-weighting [26]. An example of a 3D T_2w TSE and a 3D T_1w TSE sequence available on a Philips 3T Achieva scanner is shown in Figure 2.5. Observe that a slice-selective excitation pulse is used, along with a train of non-selective refocusing pulses with low angles [27]. The train of refocusing pulses also has optimized variable flip angles (including dummy pulses) designed to drive the transverse magnetization to a pseudo-steady state before sampling begins. The dummy pulses in (b) are particularly crucial to ensure a good image point-spread function, since a centric profile-order is more prone to blurring by a signal modulation along the phase-encode direction [28]. The 3D T_1w TSE also has a flip-back pulse that mirrors the excitation pulse in order to return the magnetization along the *z*-axis. In general, the image signal in 3D TSE sequences cannot be expressed as a simple closed-form analytical solution of the Bloch equations given the scan parameters; instead, it must be modelled via numerical simulations. This requirement may explain why 3D TSE sequences are not as commonly used for quantitative MRI applications.

2.5.2 Gradient Echo Sequences

Gradient echo (GRE) sequences use gradient pulses to refocus the transverse magnetization. Unlike RF pulses, gradient pulses have no effect on the longitudinal component (z-axis) of the magnetization, but only affect the transverse component. Therefore, spin dephasing arising from static magnetic field inhomogeneities $\Delta B_0(x,y,z)$ will not be refocused following a gradient pulse,

[7] Through-slice water-fat shifts result from of an additional frequency offset Δf =440 Hz (at 3T) in Eq. (2.18). The water-fat shift and geometrical distortion effect in the frequency-encode direction are explained later in section 2.5.4.

leading to an apparent T_2 relaxation that is shorter than the true T_2, denoted as T_2^*. The relationship between T_2^* and $\Delta B_0(x,y,z)$ is most often derived by integrating the signal of a free-induction decay, assuming a Lorentzian spectral density function of spins:

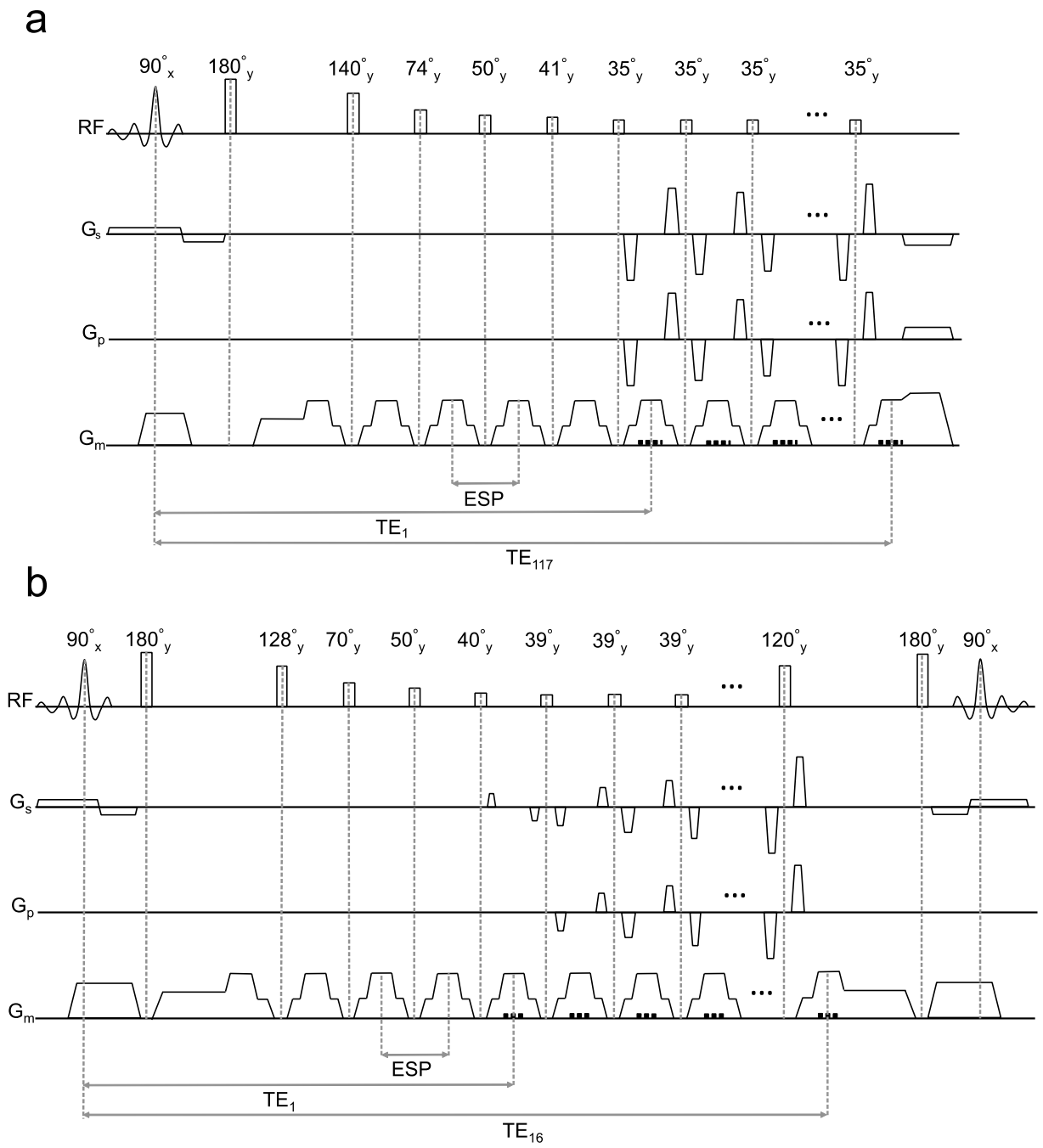

Figure 2.5: (a) A 3D T_2w TSE sequence with a linear profile order; other scan parameters for this sequence include $TR/TE_{eff}/ESP/ETL$= 2500/250/3.7 ms/117. (b) A 3D T_1w TSE sequence with a centric profile order; other scan parameters for this sequence include $TR/TE_{eff}/ESP/ETL$= 500/27/3.8 ms/16. Note

that the full *TR* duration in either (a) and (b) is not shown, since it consists primarily of dead-time and is much longer than the *ETL*.

$$S(t) = \sin\alpha \int_{-\infty}^{\infty} M_0 \frac{(\gamma\Delta B_0)^2}{(\gamma\Delta B_0)^2 + (\omega - \omega_0)^2}\, e^{-i\omega t} e^{-t/T_2} d\omega, \\ = \pi M_0 \gamma \Delta B_0 \sin\alpha\, e^{-\gamma\Delta B_0 t} e^{-t/T_2} e^{-i\omega_0 t} \tag{2.37}$$

leading to $1/T_2^* = 1/T_2 + \gamma\Delta B_0$. In 3D gradient echo imaging of the brain with a high (~1 mm) isotropic resolution, the T_2^* will usually be about 90% of the T_2 in typical WM/GM tissues, except in locations where the iron content is high (e.g. globus pallidus).

The three most common gradient echo pulse sequences are the *gradient-spoiled*, the *RF-spoiled* and the *balanced gradient echo* (usually called *balanced steady-state free precession,* or *bSSFP)*. We shall focus only on the RF-spoiled and the balanced gradient echo, since they are the most clinically useful and will be employed throughout the next chapters of this thesis.

2.5.2.1 Spoiled Gradient Echo

The spoiled gradient echo, (a.k.a. Fast Low Angle Shot (FLASH), Spoiled Gradient Recalled (SPGR), or T_1 Fast Field Echo (T_1FFE)) uses RF spoiling to generate images with a mixture of proton-density and T_1 weighting. RF spoiling implies that the phase of the RF pulse (i.e. direction of the B_1^+ field) is continuously incremented according to a specified schedule in order to reset the transverse magnetization (M_+) to zero following the readout gradient. A typical single-echo gradient echo sequence is shown in Figure 2.6 (a) for the 2D case (with slice-selective excitation) and in (b) for the 3D case with non-selective excitation. In most SPGR implementations, a short *TR* (≤ 30 ms), a short *TE* (≤5 ms) and a low flip angle (3–40°) is used.

Multi-echo SPGR sequences are also commonly used, especially when T_2^* weighting or quantitative mapping is desirable. In that case, the gradient polarity of the read gradient can have alternating polarity for odd/even echoes (a *bipolar* sequence), or the same polarity for all the echoes (i.e. the gradients are rewinded before sampling the next echo, hence a *unipolar* sequence). An example of a 3D bipolar 6-echo SPGR sequence is shown in Figure 2.7(a), and a 3D unipolar sequence in (b). Multi-echo bipolar SPGR sequences will be encountered frequently throughout this thesis. Unlike CPMG TSE sequences, multi-echo SPGR sequences do not cause stimulated echoes, since the magnetization along the z-axis remains unaffected by the multiple

gradient echoes. Therefore, the echoes can be treated separately, and the contrast simply becomes more strongly T_2^*-weighted at latter echoes. As will be discussed in Chapter 3:, the echoes (i.e., each echo yields a separate image) can be combined in root-sum-of-squares to increase the SNR. Bipolar gradient echoes are also frequently used to enhance or quantify flow effects [29] (pp. 281–291) as in MR angiography [30], (pp. 177–189) and venography [31] (although the bipolar sequences employed thoughout this thesis only incidentally provide qualitative flow information).

The GRE signal can be derived via a recursive application of the Bloch equations using the following operators:

$$\mathbf{M}_{\mathrm{n}}^{+} = \mathbf{R}_{\mathbf{z}}(\phi_n)\mathbf{R}_{\mathrm{x}}(\alpha)\mathbf{R}_{\mathrm{z}}(-\phi_n)\mathbf{M}_{\mathrm{n}}^{-},$$
$$\mathbf{M}_{\mathrm{n+1}}^{-} = \mathbf{R}_{\mathrm{z}}(\theta_n)\mathbf{E}(TR, T_1, T_2)\mathbf{M}_{\mathrm{n}}^{+} + (1 - E_1)\mathbf{M}_0, \qquad \mathbf{E} = \begin{pmatrix} E_2 & 0 & 0 \\ 0 & E_2 & 0 \\ 0 & 0 & E_1 \end{pmatrix} \tag{2.38}$$

where $\mathbf{R_z}$ and $\mathbf{R_x}$ are the rotation operators previously defined in Eq. (2.13); ϕ_n , and α_n are the phase and flip angle of the nth RF pulse, θ_n is the gradient-induced phase rotation during the period between the nth and (n+1)th RF pulses. Note that $E_2=exp(-TR/T_2)$, $E_1=exp(-TR/T_1)$, $\mathbf{M}_0 = (0,\ 0,\ M_0)^{\mathrm{T}}$, and $\mathbf{M} = (M_x, M_y, M_z)^{\mathrm{T}}$, the magnetization vector of a spin isochromat. The negative/ positive superscripts indicate the state of the magnetization before/after an RF pulse. The gradient-induced phase rotation can be further expressed as

$$\begin{aligned} \theta_n &= \theta_0 + (n-1)\Delta\theta, \\ \theta_0 &= \gamma(x\ G_x\tau_x + y\ G_y^0\tau_y + z\ G_z\tau_z + \Delta B_0(x,y,z)TR, \\ \Delta\theta &= \gamma\left(y\ \Delta G_y^0\tau_y\right) \end{aligned} \tag{2.39}$$

where G_y^0 is the initial value of the phase-encoding gradient, ΔG_y is its increment, and τ_x, τ_y, τ_z, are the net integrated time durations of the x, y, and z, gradients (i.e. 1/3rd of each total gradient duration or ½ of each positive gradient lobe duration). Note that we are assuming no phase-rewinding gradient and no spoiler gradients (i.e. the phase increment acts simultaneously a phase-encode and variable spoiler). Finally, to obtain the final GRE signal, we must integrate the magnetization of a sufficient number of spin isochromats over their phase accumulation [32]:

$$\widetilde{\mathbf{M}}_{\mathrm{n}}^{-} = \int_{-\pi}^{\pi} \mathbf{M}_{\mathrm{n}}^{-}(\theta_{n-1}) d\theta_{n-1}, \quad \widetilde{\mathbf{M}}_{\mathrm{n}}^{+} = \int_{-\pi}^{\pi} \mathbf{M}_{\mathrm{n}}^{+}(\theta_{n-1}) d\theta_{n-1} \tag{2.40}$$

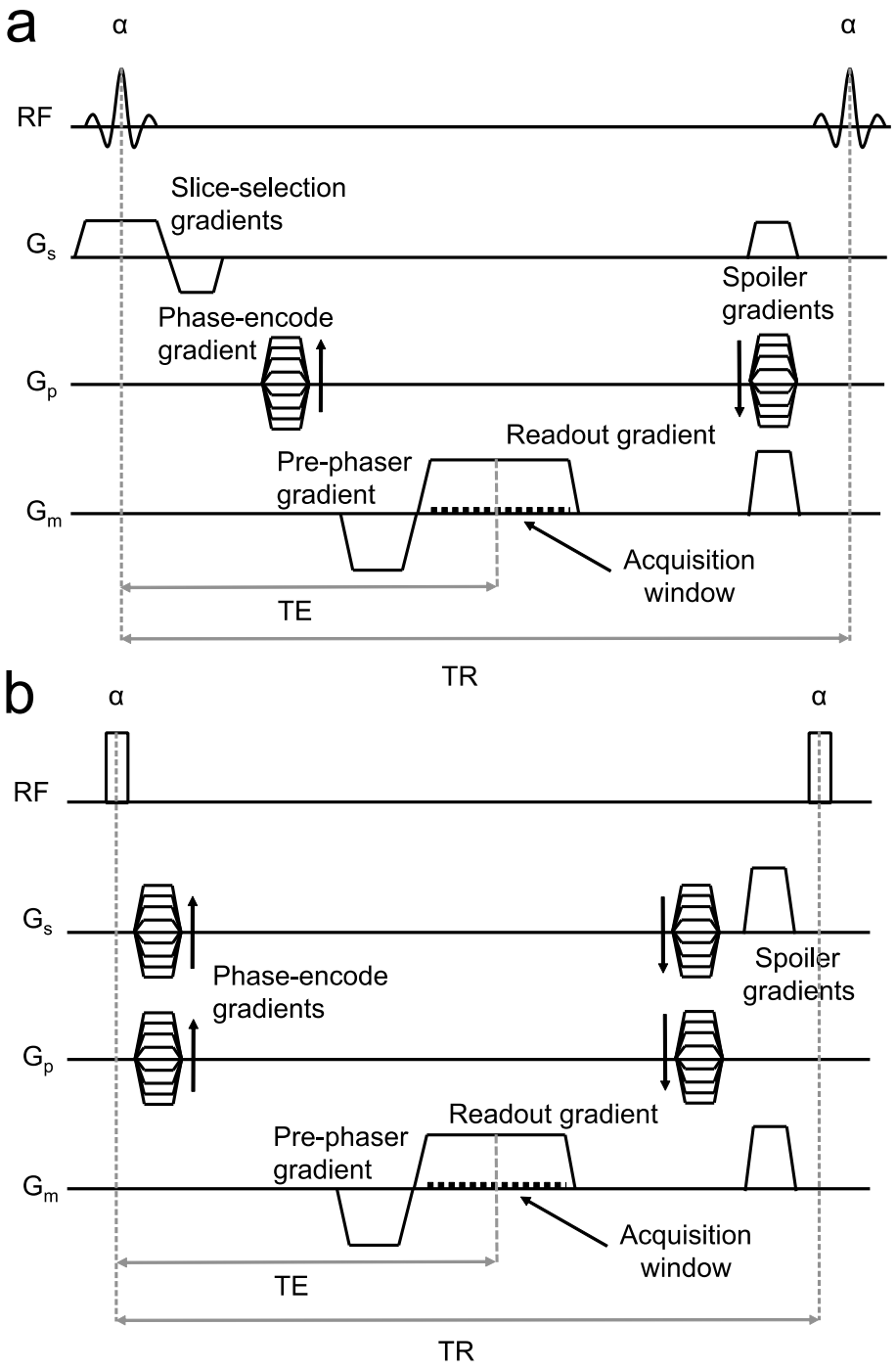

Figure 2.6: (a) A typical 2D spoiled gradient echo sequence. (b) A 3D spoiled gradient echo with non-selective RF excitation. Note that the phase-encode gradients is usually rewound to avoid phase errors.

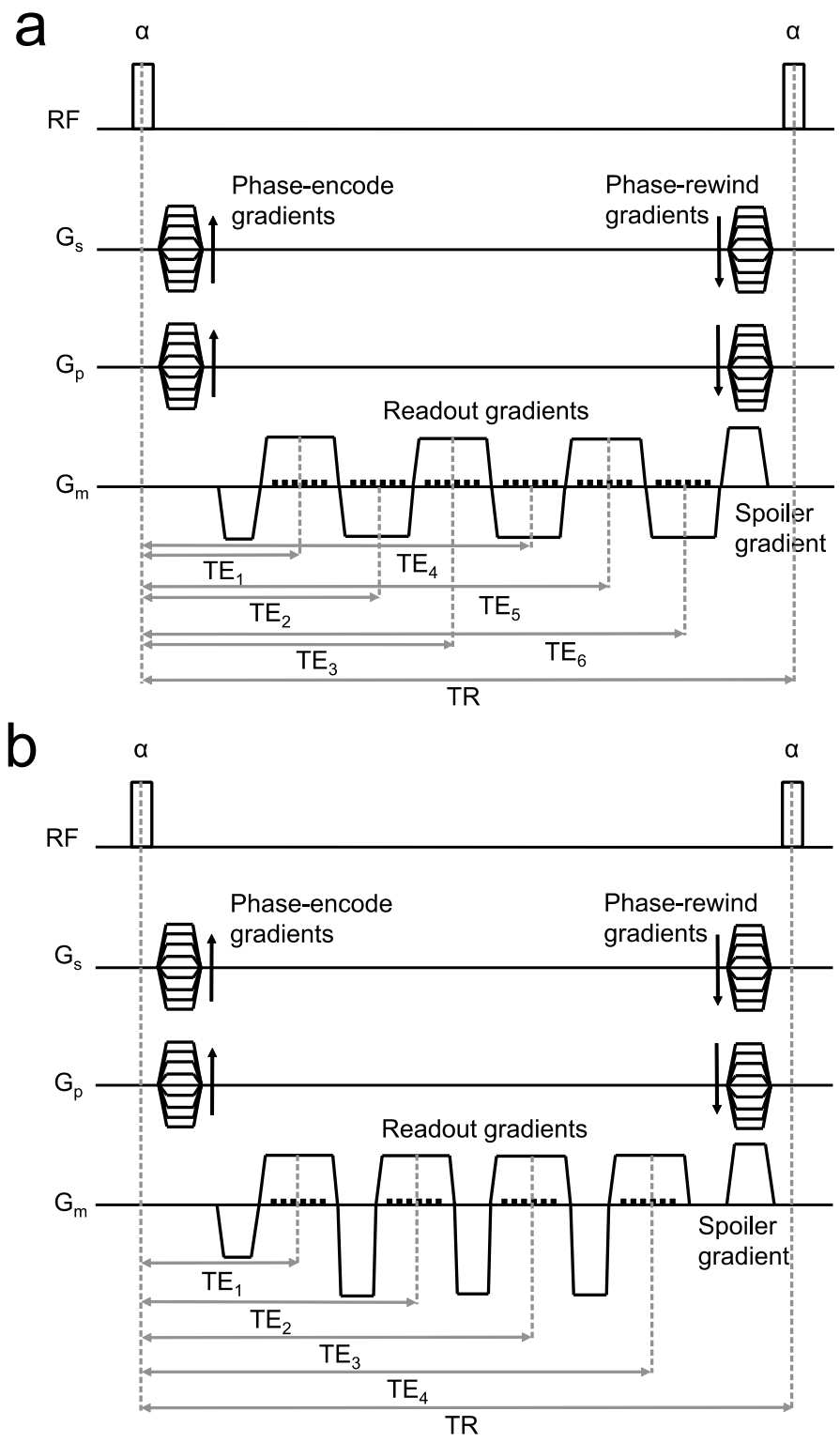

Figure 2.7: (a) A typical 3D bipolar multi-echo SPGR, and a (b) 3D unipolar multi-echo SPGR. The bipolar sequence has the best sampling efficiency (lowest amount of dead-time), but the geometrical distortions will point in opposite directions for even versus odd echoes.

It can be easily shown (see Figure 2.8) that after a sufficient number of RF pulses, all net components of $\mathbf{M_n}^+$ and $\mathbf{M_n}^-$ will reach a steady-state. Moreover, depending on the choice of $\Delta\theta$, and ϕ_n the left-over transverse magnetization preceding the RF pulse $|M_+^-|$ can be made nearly equal to zero. When this component is zero, the steady-state GRE signal is said to be *ideally spoiled*, and a simple analytical solution can be derived by assuming $M_x^- = M_y^- = 0$. In this case, the Bloch equations simply become:

$$\begin{aligned} \widetilde{M}_x^+ &= \widetilde{M}_x^- = 0, \\ \widetilde{M}_z^- &= M_0(1 - E_1) + \widetilde{M}_z^- E_1 \cos\alpha, \\ \widetilde{M}_y^+ &= \widetilde{M}_z^- \sin\alpha \end{aligned} \tag{2.41}$$

with the simple solution

$$S = \left|\widetilde{M}_y^+\right| = \frac{M_0(1 - E_1)\sin\alpha}{1 - E_1\cos\alpha} \tag{2.42}$$

To take T_2^* decay during the readout into account, we can simply multiply Eq. (2.42) by $exp(-TE/T_2^*)$. On modern MRI scanners, spoiling is usually achieved by cycling the RF phase ϕ_n according to a quadratic scheme of the form

$$\phi_n = \phi_{n-1} + n\phi_0 = \frac{1}{2}\phi_0\,(n^2 + n + 2) \tag{2.43}$$

since it is more practical than setting $\Delta\theta \neq 0$. In fact, choosing ϕ_0=φ and $\Delta\theta$=0 is mathematically equivalent to setting $\Delta\theta$=φ, and ϕ_0=0. The MRI scientist should be aware that there is no universal agreement on the best choice of phase cycle increment ϕ_0, and different MRI scanner manufacturers use different default values, such as 150° on Philips scanners, and 115.4° on General Electric scanners [33]. Other previously proposed values include 117°[34], and 50°, which is expected to be more stable [35]. As an example, we have plotted $|M_+^+|, |M_+^-|, M_z^+$, and M_z^- in Figure 2.8, for a choice of ϕ_0=0 in (a) (no spoiling) and ϕ_0=150° in (b) (default spoiling on a Philips scanner). Note that we have dropped the tilde notation for the sake of brevity. In Figure 2.9, the percent difference between the true SPGR signal and the ideal signal is plotted as a function of the phase cycle increment ϕ_0 for three different typical brain tissues (WM, GM and CSF) and using α/TR = 35°/30 ms. In general, RF spoiling is quite close to ideal spoiling in tissues that have small T_2/T_1 ratios such as WM and GM, with deviations of -1.4/-2.1 % but not

in tissues with long T_2, such as CSF, where the error is -23% at ϕ_0=150°. As explained by Yarnykh, diffusion effects induced by the spoiler gradients can dampen the effect of incomplete spoiling, thus making the signal more ideally spoiled [33]. As will be discussed in the later chapters of this thesis, the assumption of ideal spoiling and the choice of ϕ_0 can lead do biases when mapping the flip angle (B_1), proton-density and T_1 via the SPGR sequence.

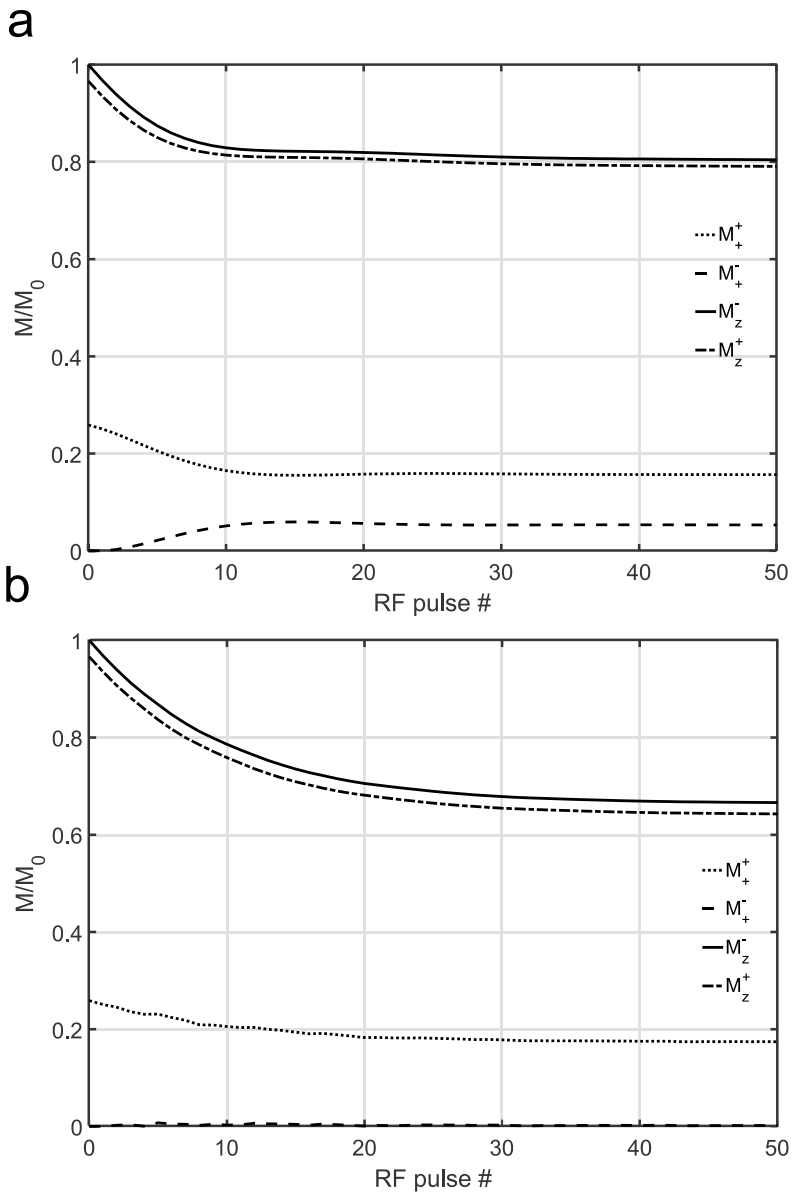

Figure 2.8: (a) GRE signal magnitude components plotted using Eqs. (2.38)–(2.40) with $T_1/T_2/TR/\alpha$ = 300/100/20 ms/15° and ϕ_0=0°. (b) GRE signal magnitude components plotted with ϕ_0=150°.

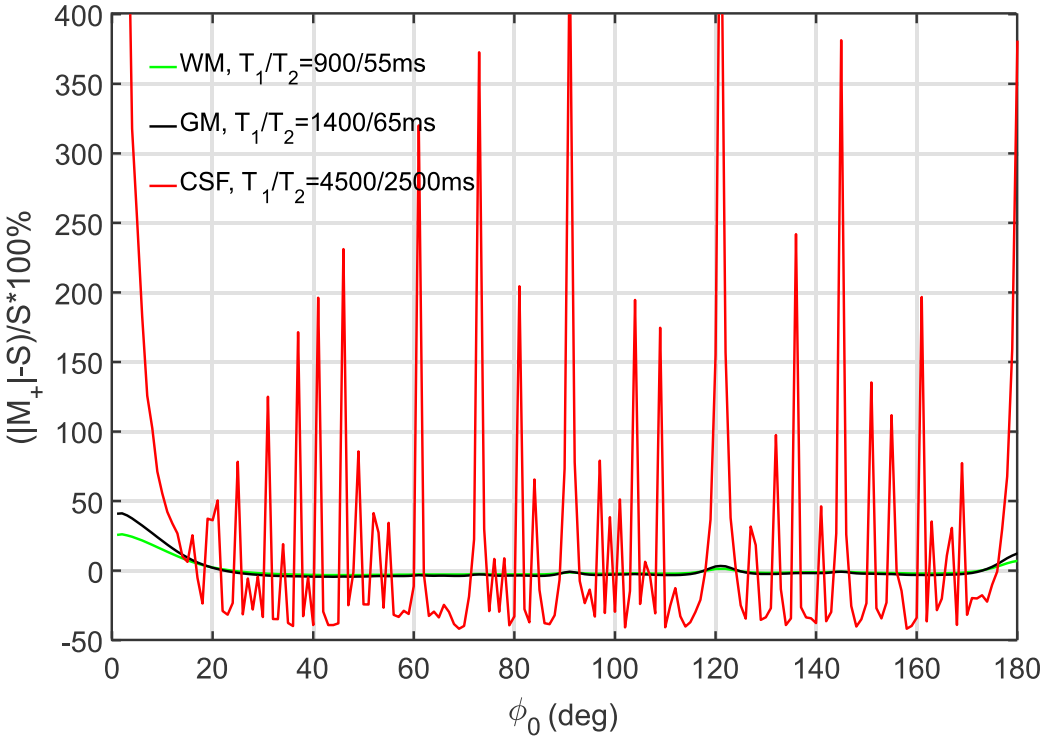

Figure 2.9: Plot of the percent difference between the actual SPRG signal and the ideal signal (with α/TR=35°/30 ms) in three different types of brain tissues at 3T.

2.5.2.2 Balanced Steady-State Free Precession

In the balanced steady-state free precession (bSSFP) sequence, all gradient lobes (along s, p, and m) are rewinded before the end of each repetition time such that their net integrated area is zero. An example of 2D and 3D bSSFP sequence is shown in Figure 2.10. Therefore in that case,

$$\theta_n = \theta_0 = \gamma\, \Delta B_0(x,y,z)\, TR \tag{2.44}$$

Moreover, the phase of the RF pulse is usually cycled according to $\phi_n = \phi_{n-1} + \phi_0$. In this case, assuming ϕ_0=0 for simplicity, Eq. (2.38) becomes

$$\begin{aligned} \mathbf{M}_{n+1}^{-} &= \mathbf{R}_z(\theta_0)\mathbf{E}(TR,T_1,T_2)\mathbf{R}_x(\alpha)\mathbf{M}_n^{-} + (1-E_1)\mathbf{M}_0, \\ \mathbf{M}_{n+1}^{+} &= \mathbf{R}_x(\alpha)\mathbf{R}_z(\theta_0)\mathbf{E}(TR,T_1,T_2)\mathbf{M}_n^{+} + (1-E_1)\mathbf{M}_0 \end{aligned} \tag{2.45a, b}$$

When the variation of θ_0 within a voxel can be neglected, we may assume that the magnetization of a voxel is equal to the magnetization of a spin isochromat contained in that voxel, and Eq. (2.40)

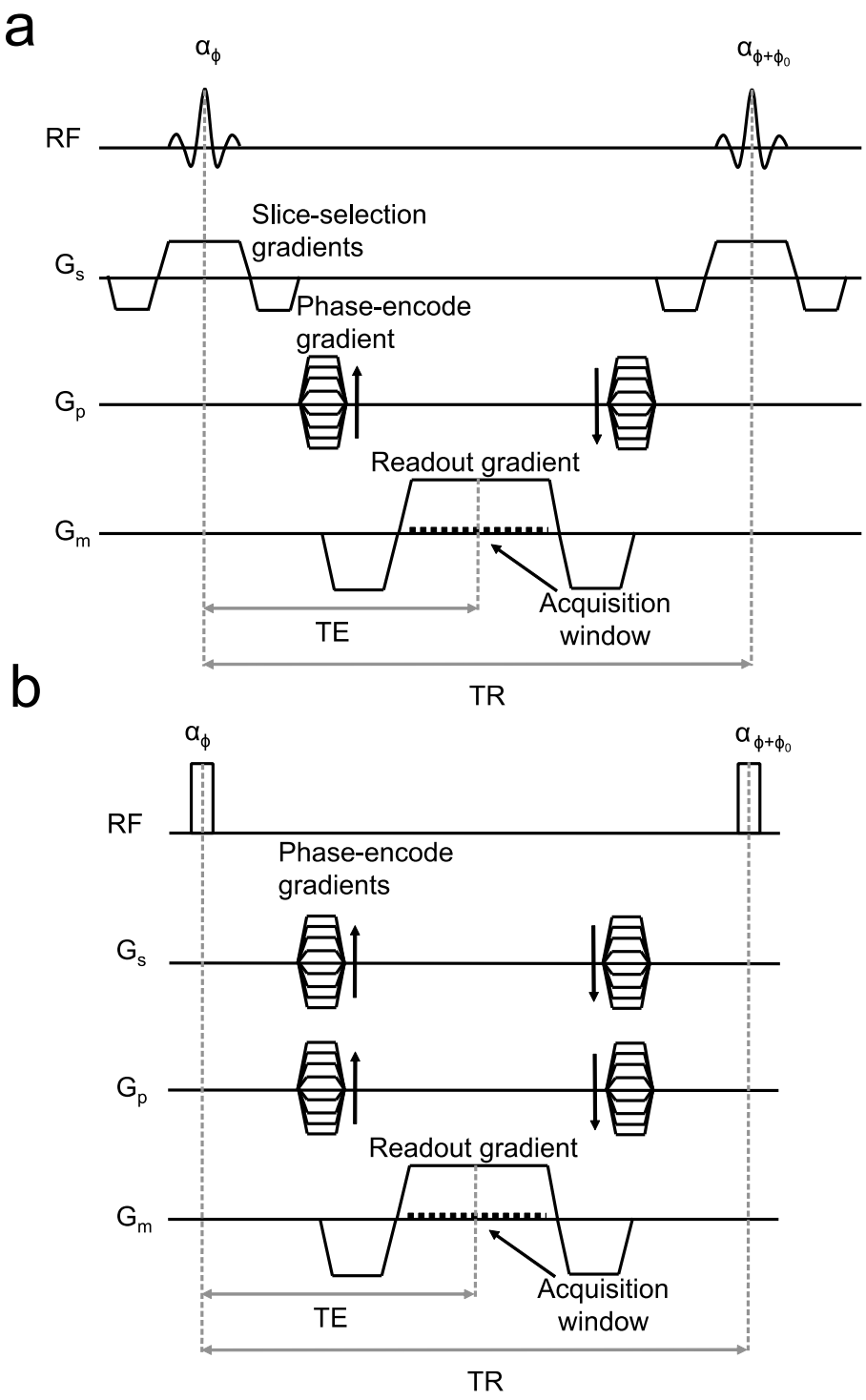

Figure 2.10: (a) A 2D bSSFP pulse sequence. Observe that both the slice-encode and readout gradients are rewound before the next RF pulse. (b) A 3D (non-selective) bSSFP pulse sequence.

simply becomes $\widetilde{\mathbf{M}}_{\mathrm{n}}^{+} = \mathbf{M}_{\mathrm{n}}^{+}$ and $\widetilde{\mathbf{M}}_{\mathrm{n}}^{-} = \mathbf{M}_{\mathrm{n}}^{-}$. It can be shown that Eq. (2.45) will also reach a steady state, such that

$$\begin{aligned} \mathbf{M}_{\mathrm{n+1}}^{-} &= \mathbf{M}_{\mathrm{n}}^{-} = \mathbf{M}_{\mathrm{steady}}^{-} \\ \mathbf{M}_{\mathrm{n+1}}^{+} &= \mathbf{M}_{\mathrm{n}}^{+} = \mathbf{M}_{\mathrm{steady}}^{+} \end{aligned} \tag{2.46}$$

The solution of the steady state can be found by solving

$$\begin{aligned} \mathbf{M}_{\mathrm{steady}}^{-} &= \left(\mathbf{I} - \mathbf{R}_{\mathrm{z}}(\theta_0)\mathbf{E}(TR, T_1, T_2)\mathbf{R}_{\mathrm{x}}(\alpha)\right)^{-1}\mathbf{M}_0(1 - E_1) \\ \mathbf{M}_{\mathrm{steady}}^{+} &= \left(\mathbf{I} - \mathbf{R}_{\mathrm{x}}(\alpha)\mathbf{R}_{\mathrm{z}}(\theta_0)\mathbf{E}(TR, T_1, T_2)\right)^{-1}\mathbf{M}_0(1 - E_1) \end{aligned} \tag{2.47a, b}$$

In terms of the individual x, y, and z components, the solution is

$$\begin{aligned} M_x^{-} &= M_0(1 - E_1)E_2 \sin\alpha \sin\theta_0 / D, \\ M_y^{-} &= M_0(1 - E_1)(\cos\theta_0 - E_2)E_2 \sin\alpha / D, \\ M_z^{-} &= M_0(1 - E_1)[1 - E_2\cos\theta_0 - E_2\cos\alpha\ (\cos\theta_0 - E_2)]/D, \\ M_x^{+} &= M_x^{-}, \\ M_y^{+} &= M_0(1 - E_1)(1 - E_2\cos\theta_0)\sin\alpha\ /D, \\ M_z^{+} &= M_0(1 - E_1)[E_2(E_2 - \cos\theta_0) + (1 - E_2\cos\theta_0)\cos\alpha]/D, \\ \text{where } D &= (1 - E_1\cos\alpha)(1 - E_2\cos\theta_0) - E_2(E_1 - \cos\alpha)(E_2 - \cos\theta_0) \end{aligned} \tag{2.48}$$

Recalling the complex notation $M_{+}^{+} = M_x^{+} + iM_y^{+}$, the positive solution of Eq. (2.48) is sometimes rearranged into the following form

$$\begin{aligned} M_{+} &= \frac{a\, e^{-i\theta_0} + b}{c\cos\theta_0 + d}, \\ a = -M_0(1 - E_1)\sin\alpha\, E_2,\ \ b &= M_0(1 - E_1)\sin\alpha, \\ c = E_2(E_1 - 1)(1 + \cos\alpha),\ \ d &= (1 - E_1\cos\alpha) - (E_1 - \cos\alpha)E_2^2 \end{aligned} \tag{2.49}$$

If the readout window is placed at the center of the repetition time, (i.e. *TE*=*TR*/2), the signal simply becomes $M_{+}e^{-TE/T_2}$. It can be shown that bSSFP yields T_2/T_1-weighting at high flip angles and a mixture of proton-density and T_2/T_1-weighting at lower flip angle. Moreover, the

SPGR and bSSFP signal each have a maximum value at a particular flip angle called the *Ernst angle* (α_E). The Ernst angle is easily found by setting the derivative with respect to α equal to zero in Eq. (2.42) and Eq. (2.49), yielding

$$\alpha_E^{SPGR} = \cos^{-1}(E_1),$$
$$\alpha_E^{bSSFP} = \cos^{-1}\left(\frac{E_1 + E_2(\cos\theta_0 - E_2)/(1 - E_2\cos\theta_0)}{1 + E_1E_2(\cos\theta_0 - E_2)/(1 - E_2\cos\theta_0)}\right) \quad (2.50\text{ a, b})$$

The bSSFP signal of Eq. (2.49) holds quite accurately in simple solutions and agar phantoms, but may deviate considerably from the true signal in vivo. In practice, complex tissue microstructure (especially tissues with high protein and macromolecular content such as muscle, WM and GM) leads to higher-order effects, including magnetization transfer and multi-pool proton exchanges. The matrices in Eq. (2.45) become 6×6 for a two-pool system, and 9×9 for two-pools plus magnetization transfer (equivalent to three pools)[36]. Moreover, Eqs. (2.45)–(2.49) were derived assuming infinitesimal RF pulse durations. In practice, finite RF pulse effects can become significant at short *TR*, and accurate pulse sequence modelling requires taking into account T_1 and T_2 relaxation during the RF pulse [37].

The main limitation of bSSFP imaging lies in the problem of *banding artifacts* which occur in voxels where $\theta_0 \rightarrow \pi$, resulting in a dark band of missing signal. Band artifacts tend to corrupt anatomical information and decrease the diagnostic quality of an image. The location of the bands can always be shifted by changing the transmit frequency or the phase of the RF pulse. In the past, phase-cycled bSSFP imaging was the common approach used to reduce the deleterious effect of banding artifacts. In phase-cycled bSSFP, N different images are acquired with different phase offsets equally distributed over a 2π period (e.g. θ=0, $\pi/2$, π, $3\pi/2$). A final image is then obtain by taking the sum of all N images along the real and imaginary component (i.e. M_x and M_y), and then taking the magnitude. This is often called the *complex sum* (CS). However, in 2014 a closed-form solution to the problem of banding artifacts was discovered by Xiang and Hoff for the case of N=4, called the *geometric solution* (GS) [38]. Therefore, it is likely that GS will replace CS and most other approximate methods of removing band artifacts in future clinical applications. In Chapter 4 of this thesis, we shall present a novel technique of mapping T_2 using SPGR and bSSFP, while simultaneously correcting for band artifacts.

2.5.3 Additional Modules

Modern MRI pulse sequences often consist of the basic turbo spin echo or spoiled gradient echo sequences previously described with additional "building blocks" inserted to further manipulate the final image contrast. These building blocks, typically known as *modules*, contain additional RF and/or gradient pulses that are played at regular time intervals. A module may be inserted before/after every repetition time, or it may return only after N repetition times. A turbo factor *TFE* may be defined as the number of excitation pulses that are played for every module. Therefore, if *TFE*=1, the module is played before/after very RF pulse excitation, while *TFE*=128 implies that the module returns after every 128 excitations (or phase-encode steps in the case of a GRE). Two common additional modules that will be encountered in this thesis, include inversion recovery (IR), and magnetization transfer (MT).

2.5.3.1 Inversion/Saturation Recovery

Inversion recovery typically consists of using either a 180° selective or non-selective RF pulse to invert all the magnetization from the z to the -z direction (i.e. $M_z^- = M_0$, and $M_z^+ = -M_0$). A saturation-recovery pulse is similar, except that a 90° flip angle is used such that the magnetization is nulled along the z-axis by flipping it into the xy-plane, (i.e. $M_z^- = M_0$, and $M_z^+ = 0$). A delay time called the *inversion time TI* (typically in the order of 400–2000 ms) is also inserted between the inversion pulse and the first excitation pulse in order to allow T_1 relaxation. By changing the inversion time, the amount of T_1-weighting can thus be manipulated. One or more excitation pulses (depending on the *TFE* or *TSE* factor) with lower flip angles $\alpha \leq 90°$, are used to sample k-space before the inversion/saturation recovery module returns again. A typical inversion recovery module is shown in Figure 2.11(a). A spoiler gradient is also optionally inserted along the slice direction after the pulse to spoil residual magnetization that might have fallen unto the *xy*-plane.

Inversion-recovery pulses often belong to a special class of RF pulses called *adiabatic* pulses, which are able to uniformly excite, refocus or invert magnetization even in the presence of a non-uniform B_1 field. The concept of adiabaticity can be understood by alluding to the effective magnetic field defined as

$$\mathbf{B_{eff}}(t) = B_x(t)\hat{\mathbf{x}} + B_z(t)\hat{\mathbf{z}}\,, \quad |\mathbf{B_{eff}}| = \sqrt{B_x^2(t) + B_z^2(t)}\,,$$
$$\psi(t) = \tan^{-1}\left(\frac{B_x(t)}{B_z(t)}\right) \tag{2.51}$$

where $\psi(t)$ is the angle between the *x* and *z* component of the effective magnetic field, and the *y*-component of the B_1 pulse is assumed to be zero for simplicity (see Figure 2.12). If the adiabatic condition is satisfied, a magnetization vector that is initially collinear with B_{eff} will remain collinear and one that is initially perpendicular to B_{eff} will precess about B_{eff} in a plane normal to B_{eff} during the course of the pulse. This implies that B_{eff} can effectively capture the magnetization vector and bring it into the *xy*-plane or along -*z*, provided that the adiabatic condition is fulfilled, which occurs when

$$\left|\frac{d\psi}{dt}\right| \ll \gamma|\mathbf{B_{eff}}(t)| \tag{2.52}$$

Typical adiabatic pulses include sine/cosine and sech/tanh function pairs for the amplitude/ frequency modulation, since according to Eq. (2.52), the adiabatic condition inherently requires that the derivative of the amplitude modulation be proportional to the frequency modulation waveform. Therefore, typical examples of amplitude and frequency modulation waveforms include

$$B_1(t) = [A_0\,\mathrm{sech}(\beta t)]^{1+i\mu},\ \omega_{rf}(t) = \omega_0 - \mu\beta\tanh(\beta t), \tag{2.53}$$

for a sech/tanh pulse and

$$B_1(t) = A(t)e^{-i\omega_{rf}(t)t},\ A(t) = B_{x,0}\sin(\xi t),\ \omega_{rf}(t) = \omega_0 - \gamma B_{z,0}\cos(\xi t) \tag{2.54}$$

for a sine/cosine pulse. The A_0, μ, β, $B_{x,0}$, $B_{z,0}$ and ξ parameters are then optimized to meet the adiabatic condition.

In the case of an IR module inserted within a 2D TSE sequence (i.e. IR-TSE), the signal equation becomes

$$S = M_0\left(1 - 2e^{-TI/T_1} + e^{-(TR-ETL\cdot ESP/T_1)}\right)e^{-TE_{eff}/T_2} \tag{2.55}$$

where it is assumed again that $TR >> TE_{eff}$. The *TI* can be selected to null the signal of a specific tissue type. If the *TI* is adjusted to null the CSF signal, the sequence is commonly called a *FLuid*

Attenuated Inversion Recovery (FLAIR), while if it is adjusted to null fat, it is commonly called a *Short TI Inversion Recovery* (STIR). Typical choices of *TI* for FLAIR/STIR are ~2200/160 ms, respectively.

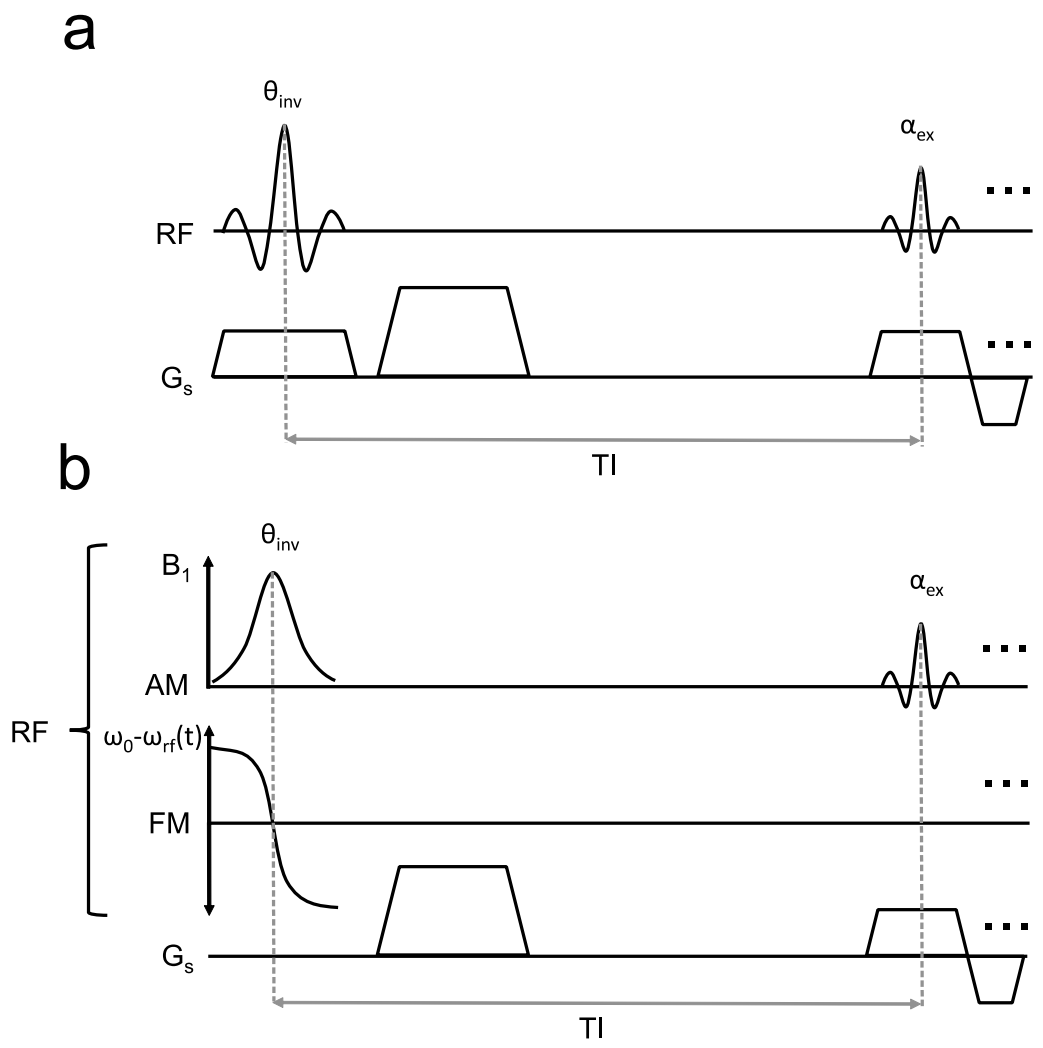

Figure 2.11: (a) An example of a slice-selective inversion-recovery module, and (b) a non-selective adiabatic inversion recovery module with a sech pulse.

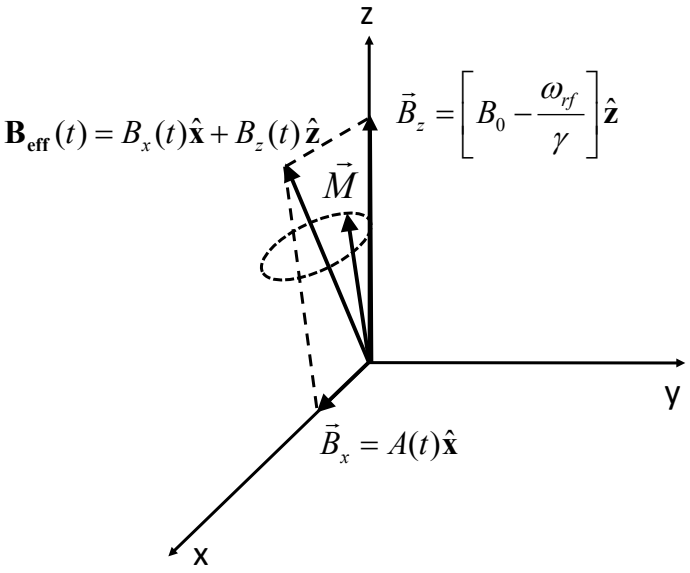

Figure 2.12: Vector diagram showing the effect of an adiabatic RF pulse on the magnetization.

2.5.3.2 Magnetization-Prepared RApid Gradient Echo (MP-RAGE)

The MPRAGE pulse sequence typically consists of an inversion-recovery module inserted into a SPGR sequence. Having first been proposed by Mugler and Brookeman in 1990 [39], it has become by far the most popular sequence used to achieve T_1-weighting in high-resolution structural imaging of the brain. There are many variants of MPRAGE, and different manufacturers have slightly different implementations under various commercial names, such as T_1TFE (Philips), and IR-SPGR (GE). Most of the variants differ in terms of their profile order, such as whether a linear, centric, elliptical-centric (MP-EFGRE)[40] or a spiral (MP-SAGE)[41] profile order is used. When a centric profile order is chosen, variable flip angles are usually optimized to speed up the descent to steady-state as done similarly in a 3D T_1w TSE sequence [42]. A typical pulse sequence diagram of MPRAGE is shown in Figure 2.13(a). In general, *TI* is defined as the time elapsed between the inversion pulse and the point at which the center of k-space is sampled, *TD* is the delay time following the acquisition block and the next inversion pulse, TR_{MP} is the shot duration and *TFE* is the *turbo field echo* factor (number of phase-encode/excitations per acquisition block). The choice of profile order usually affects the PSF and SNR, but does not have a significant impact on the final image signal and contrast, which can be

accurately approximated by a closed-form analytical solution derived by Deichmann et al. [43], [9] (provided that the timings are kept consistent):

$$S = M_0 \sin\alpha \; \frac{E_D(1 - 2E_A + E_A E_B) + \frac{T_1^*}{T_1}(1 + E_A E_B E_C - E_A E_B E_D - E_D)}{1 + E_A E_B E_C} e^{-TE/T_2^*}$$

$$E_A = e^{-(TI - TFE \cdot \frac{TR}{2})/T_1},\; E_B = e^{-TD/T_1},\; E_C = e^{-TFE \cdot TR/T_1^*},\; E_D = e^{-(TFE \cdot \frac{TR}{2T_1^*})}, \qquad (2.56)$$

$$T_1^* = \left[\frac{1}{T_1} - \frac{1}{TR} \cdot \log(\cos\alpha)\right]^{-1}$$

Recently, a new variant of MPRAGE named *MP2RAGE* was proposed by Marques et al. [44]. As shown in Figure 2.13(b), it consists of adding a second acquisition block before the next inversion pulse, thus resulting in two effective inversion times TI_1 and TI_2, and three delay times (before, between and after the two blocks), denoted as *TA*, *TB* and *TC*, respectively. If desired, the two acquisition blocks can have a different flip angles α_1/α_2.This sequence thus yields two images, the first being T_1-weighted and the second being proton-density-weighted. Using an analytical combination of the complex signal, a real normalized image can be obtained which is purely T_1-weighted and also bias-field corrected (to first order). The MP2RAGE image can also be converted to a T_1 map using a lookup table, since a closed-form analytical solution of the image signal as a function of scan parameters also exists [44]. In the future, MP2RAGE is likely going to overshadow MPRAGE in popularity, since it was recently shown to achieve better image quality and CNR efficiency [45]. In chapter 3, a multi-echo MP2RAGE sequence is tested and compared to a novel technique for simultaneously mapping proton-density (M_0), T_1 and T_2^*.

A comparison of two sagittal images obtained using the 3D T_1w TSE, and the T_2w TSE pulse sequences previously described in Figure 2.5(a) and (b) is given in Figure 2.14(a) and (b). Moreover, a comparison of a single-echo MPRAGE with a lower bandwidth of 217 Hz/pixel and a 7-echo MPRAGE with a high bandwidth of 989 Hz/pix is shown in (c) and (d), respectively. In all four cases, the voxel resolution is 1 mm (isotropic) with a field-of-view of 25×25×18 cm^3. The scan parameters are $\alpha/TFE/TE/TR/TR_{MP}$ = 7°/240/4.6/8.3/3000 ms in (c) and $\alpha/TFE/TE_1/\Delta TE\ /TR/TR_{MP}$ = 9.5°/128/2.0/1.7/15.5/3000 ms in (d), (adjusted to yield equivalent contrast). Notice how MPRAGE provides better T_1-weithing and CNR than the T_1w TSE (see the cerebellum), which explains why it is more commonly used. The larger water-fat-shift in

MPRAGE can be avoided using the multi-echo MPRAGE with a root-sum-of-squares (RSS) echo combination. Flow effects are also different for MPRAGE vs TSE, with blood vessels appearing much darker in (a) and (b), than in (c) and (d).

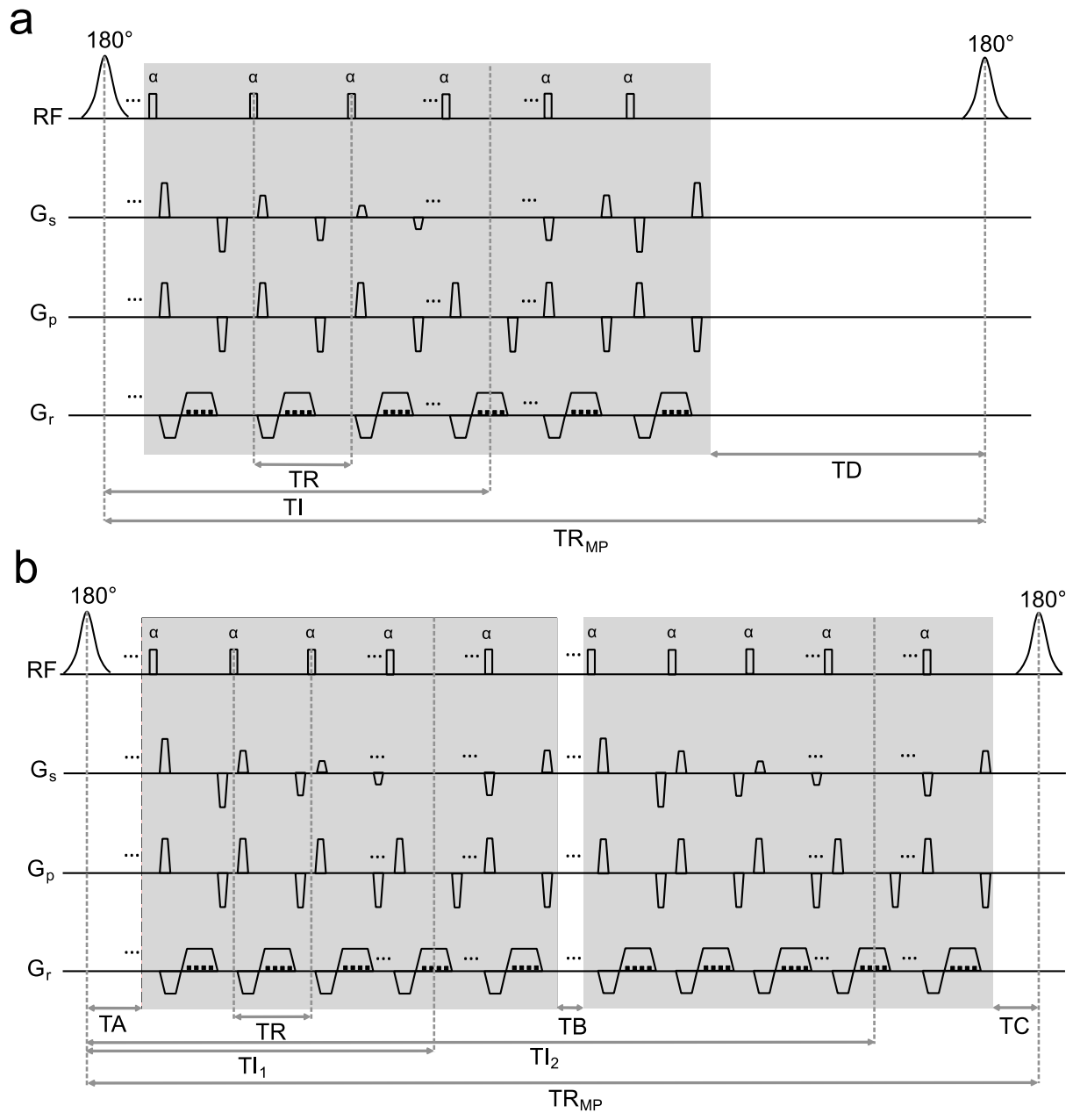

Figure 2.13: (a) A typical 3D MPRAGE pulse sequence with a linear profile order. (b) An MP2RAGE pulse sequence, also with a linear profile order. The gray boxes correspond to the acquisition block (or acquisition module).

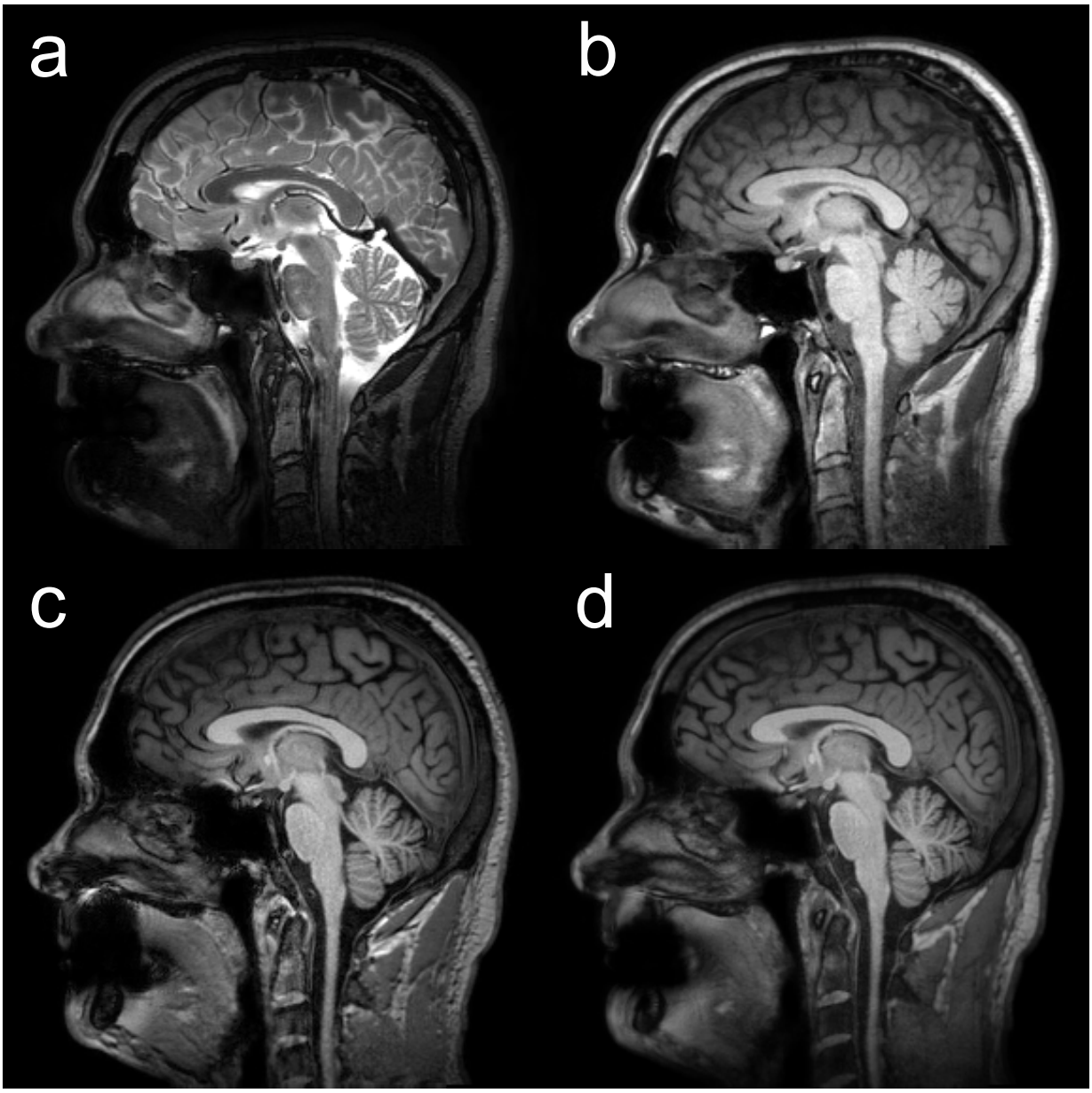

Figure 2.14: A sagittal image obtained using (a) the 3D T_2w TSE, (b) the 3D T_1w TSE sequence previously described in Figure 2.5, (c) a 3D single-echo MPRAGE with low bandwidth of 217 Hz/pix and (d) a 3D 7-echo MPRAGE with a high bandwidth of 990 Hz/pix (same as for the TSE).

2.5.3.3 Magnetization Transfer (MT)

Recall from section 2.2 (on BPP theory) that viscous protons (those with a longer correlation time) have an ultra-short T_2 relaxation, but a moderately long T_1 (see Figure 2.1). Such protons are commonly found in biological tissues as part of macromolecules (such as molecules containing hydroxyl groups). On the other hand, liquid protons are part of the free water

molecules found both within and outside the cells. Although the macromolecular protons are invisible to conventional MRI, their presence can still be detected indirectly through the phenomenon of magnetization transfer (MT). In magnetization transfer, the solid protons (within the solid or "restricted" pool) can transfer their magnetization to the liquid protons (within the liquid or "free" pool), leading to a loss of signal in the visible pool, and thus the image signal. As shown in Figure 2.15(a), the transfer occurs because a rapid exchange rate R exists between the two pools. Magnetization transfer contrast is possible, because different tissue types have different proportions of solid and liquid protons (denoted by $M_{0,f}$ and $M_{0,r}$). In practice, magnetization transfer occurs to some degree in all pulse sequences, whether voluntarily or involuntarily. To voluntarily create MT contrast, a MT module can be inserted into a typical SPGR sequence. The MT module typically consists of a non-selective Gaussian or Fermi RF pulse with a very high flip angle α_{MT} (>200°) and a frequency offset of $\Delta\omega$ (from the Larmor frequency ω_0). The frequency offset is usually in the order of 1-10 kHz, and the module often contains a spoiler gradient along the slice-encode direction following the MT pulse, but before the excitation pulse. Usually the module is played within every repetition time of a SPGR sequence (TFE=1), although to limit the SAR, it may be played less frequently. An example of an MT-FLASH sequence (with multiple echoes) is shown in Figure 2.15(c). The MT phenomenon can be modelled by a set of coupled differential equations [46]

$$\begin{aligned}
\frac{dM_{x,f}}{dt} &= -\frac{M_{x,f}}{T_{2,f}} - \Delta\omega M_{y,f} - \mathrm{Im}(\omega_1)M_{z,f}, \\
\frac{dM_{y,f}}{dt} &= -\frac{M_{y,f}}{T_{2,f}} - \Delta\omega M_{x,f} + \mathrm{Re}(\omega_1)M_{z,f}, \\
\frac{dM_{z,f}}{dt} &= \frac{M_{0,f} - M_{z,f}}{T_{1,f}} - k_f M_{z,f} + k_r M_{z,r} + \mathrm{Im}(\omega_1)M_{x,f} - \mathrm{Re}(\omega_1)M_{y,f}\,, \\
\frac{dM_{z,r}}{dt} &= \frac{M_{0,r} - M_{z,r}}{T_{1,r}} - k_r M_{z,r} + k_f M_{z,f} - W M_{z,r}\,,
\end{aligned} \tag{2.57}$$

Here, the subscripts f/r stands for the free/restricted proton pools, respectively, while x, y, z are the components of the magnetization vector, and the RF pulse shape is $\omega_1(t)=\gamma B_1(t)$. The fractional size of the restricted pool is defined as $F=M_{0,r}/M_{0,f}$, the exchange rates are $k_r=k_f/F$, and W is the mean saturation rate (a.k.a. transition rate), given by

$$W = \frac{\pi}{\tau_{rf}} \int_0^{\tau_{rf}} \omega_1^2(t) dt \; G(\Delta\omega) \tag{2.58}$$

where $G(\Delta\omega)$ is the absorption lineshape function for the restricted pool (usually a Gaussian for solids and gels, or super-Lorentzian for tissues). The exchange rates k_r and k_f are related to a global rate R, according to $k_f = R \cdot M_{0,r}$, and $k_r = R \cdot M_{0,f}$ (see Figure 2.15a). As depicted in Figure 2.15(b), the width of a proton pool's lineshape function is inversely proportional to its T_2 (i.e. $FWHM \propto 1/T_2$); therefore, the solid pool will have a very broad absorption spectrum while the liquid pool will have a very narrow spectrum, making the solid pool orders of magnitude more sensitive to off-resonance irradiation than the liquid pool. Notice from Eq. (2.57) that some MT effect will still occur in the case of on-resonance irradiation (i.e. $\Delta\omega \rightarrow 0$). This is especially the case in high-SAR pulse sequences, such as bSSFP with short TR and high flip angles. The bSSFP signal equation can also be solved using Eqs. (2.57) with $\Delta\omega \rightarrow 0$ and a derivation similar to Eqs. (2.45)–(2.47), which takes MT effects into account [47].

The concept of MTR (MT ratio) is often used to quantify the amount of MT contrast, which is defined as

$$MTR = \frac{S_0 - S_{sat}}{S_0}, \tag{2.59}$$
$$S_{sat} = S_{dir} + S_{MT}$$

where S_{sat} is the signal of the sequence with the MT module and S_0 is the signal of the sequence without the module, while keeping other scan parameters identical. S_{sat} may also be further decomposed as the sum of a direct component S_{dir} (direct attenuation of the liquid pool) and the true MT component S_{MT}. In practice, the MTR is not a truly quantitative metric since it also depends on the T_1 relaxation of the tissue, as well as other scan parameters, including TR and α. Recently, Helms et al. [48] have proposed using a different parameter to better quantify a two-point MT experiment, called MT saturation (MT_{sat}). MT_{sat} corresponds to the fractional reduction of longitudinal magnetization by a single MT pulse, and describes the effect of the MT pulse with only minor residual influence on T_1, α and RF inhomogeneity. If the SPGR signal of Eq. (2.42) is approximated by using the second degree Taylor polynomial of E_1, $cos(\alpha)$ and $sin(\alpha)$, (valid for a small α<25°) we obtain

$$S_0 = M_0 e^{-TE/T_2^*} \frac{\alpha TR/T_1}{TR/T_1 + \alpha^2/2} \tag{2.60}$$

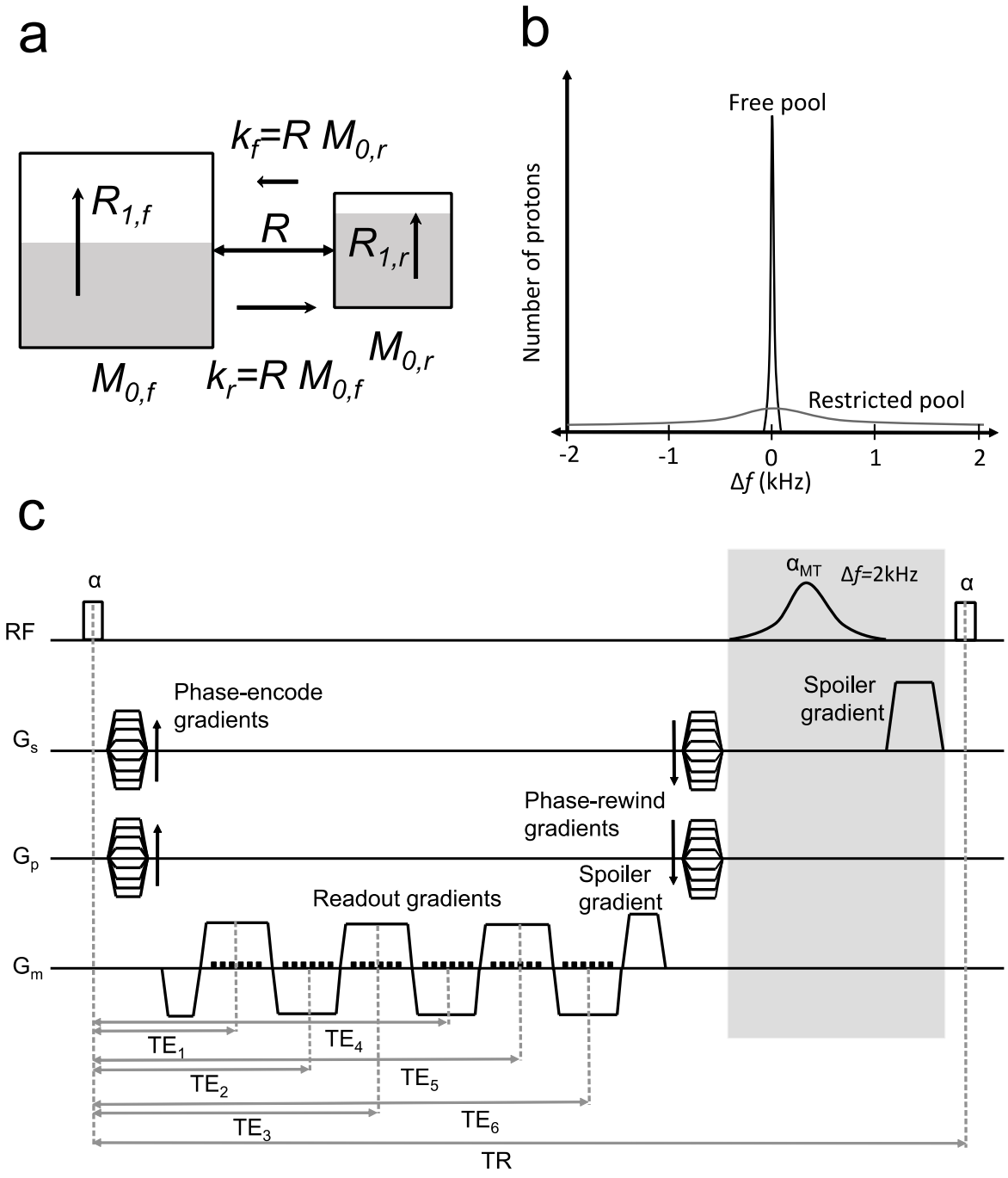

Figure 2.15: (a) Graphical representation of the binary spin bath model for MT. (b) Absorption spectrum of free-pool and restricted proton pools as a function of frequency offset. (c) A typical MT-FLASH sequence (with multiple bipolar echoes). The MT module corresponds to the gray box.

If an MT module is placed within the same SPGR sequence (while keeping other scan parameters the same), Helms et al. [48], [49] have shown that the signal is approximately related to MT_{sat} and other scan parameters according to

$$S_{sat} = M_0 e^{-TE/T_2^*} \frac{\alpha TR/T_1}{MT_{sat} + TR/T_1 + \alpha^2/2}, \qquad MT_{sat} = D\frac{\alpha_{MT}^2}{\tau_{MT}} \tag{2.61}$$

where D is a proportionality factor that depends on the frequency offset and shape of the MT pulse (via the absorption spectrum), α_{MT} is the flip angle of the MT pulse, and τ_{MT} is the MT pulse duration. The *MTR* is related to the MT_{sat}, according to

$$\frac{1}{MTR} = \frac{\alpha^2/2 + MT_{sat}}{MT_{sat}} + \frac{TR/T_1}{MT_{sat}} \tag{2.62}$$

Since MT_{sat} mapping requires T_1 information, it is usually done in conjunction with T_1 mapping. Equation (2.62) will be used later in chapter 5 to map MT_{sat} in brain cancer patients using 3 SPGR datasets.

2.5.4 K-Space Sampling Trajectories

So far we have described pulse sequences where the k-space is sampled rectilinearly, via frequency-encoding and phase-encoding. These pulse sequences may be also classified as *Cartesian MRI* or *Cartesian sampling* as opposed to *non-Cartesian MRI*. Cartesian MRI can vary in terms of profile order, especially in the case of 3D pulse sequences where the second phase-encode (i.e. slice-encode) direction can have a nearly infinite variety of profile orders, including *spiral*, *radial* and *elliptical-centric* (as previously discussed regarding MP-RAGE). Moreover, in 3D Cartesian MRI, it is possible to skip phase-encode lines in the corners of k-space (known as an *elliptical shutter*) to decrease the scan time without causing a loss of resolution or SNR. In that case, the corners are simply zero-filled prior to applying the 3D Fourier transform.

Another subtype or Cartesian sampling is known as *Echo-Planar Imaging* (EPI). EPI differs from other Cartesian sampling trajectories in that multiple lines of k-space are sampled within the same *TR*, and the frequency-encode direction is continually alternated from one line to the next, in order to minimize the amount of dead-time. Therefore, this sequence is similar to the multi-echo bipolar SPGR shown in Figure 2.7(a), except that a phase-encode gradient blip is inserted between each readout gradient lobe, such that multiple k-space lines are sampled (rather

than the same line at different *TEs*). An EPI sequence can be single-shot, in which case the entire k-space is sampled following a single RF excitation, or multi-shot, in which case the k-space is sampled over several excitations and *TR*. The EPI factor is the number of k-space lines sampled per *TR*. Since EPI is the gradient-echo analogue of TSE, it can also be combined with TSE to form a hybrid sequence called *GRAdient Spin Echo* (GRASE). Similarly to TSE, EPI and GRASE are frequently used in conjunction with other modules for the purpose of rapid imaging, such as IR-EPI. Later in chapter 3 and 4, IR-EPI will be employed as a gold standard to map T_1 relaxation.

A major drawback of EPI is a propensity for heavy geometrical distortions and water-fat shifts along the phase-encode direction. The distortions and water-fat shifts will be proportional to the EPI factor. Moreover, eddy-currents caused by fast gradient-switching can result in image ghosts, especially at high EPI factors. The geometrical distortions and water-fat shifts both arise as a result of a difference between the assumed and the actual Larmor frequency at a pixel location, denoted as a frequency offset $\Delta f=\gamma\Delta B_0/2\pi$. Along the frequency-encode direction, an off-resonance Δf will then cause a pixel-shift Δr, given by

$$\Delta r = \frac{2\pi\Delta f}{\gamma G_r} = \frac{\Delta f\ FOV_r}{BW\ N_r} \tag{2.63}$$

where G_r is the read gradient strength, *FOV* is the field-of-view (in m), *BW* is the readout bandwidth, ($BW=1/T_{acq}$, where T_{acq} is the acquisition time of a full k-space line), N_r is the number of voxels (grid size) along the frequency direction. Given a typical off-resonance of ~440 Hz for fat tissue at 3T, a FOV of 25 cm, a grid-size of 256 pixels, and a readout bandwidth of 200 Hz (per pixel), Eq. (2.63) predicts a water-fat shift of 2.15 mm or ~2.1 pixels. The right-hand side of Eq. (2.63) can also be modified to predict the geometrical distortions along the phase-encode direction within an EPI sequence, by replacing the readout bandwidth by the inverse of the shot duration. Since the shot duration is often in the order of tens of milliseconds, the distortions in an EPI sequence can be particularly severe (5 mm or more). Minimizing geometrical distortions while maintaining high SNR is of particular interest in RTP where geometrical fidelity is paramount to accurate dose calculation and treatment delivery.

The two most common non-Cartesian sampling trajectories include *spiral* and *radial* sampling, as illustrated in Figure 2.16(b) and (c). As for EPI, spiral sampling can be either single-shot or

multi-shot. In spiral MRI, off-resonance results in blurring as opposed to geometrical distortions, since the point-spread function is isotropic. In non-Cartesian MRI, the k-space samples must be gridded unto a Cartesian grid prior to taking the Fourier transform, or alternatively, a non-uniform fast Fourier transform (NUFFT) algorithm must be employed. Since spiral MRI acquisition and image processing was extensively covered as part of my M.Sc. thesis, the reader is referred thereunto [16].

Unlike spiral sampling, radial sampling is always multi-shot, with typically one spoke (sampled from $-k_{max}$ to $+k_{max}$) per *TR*. Multi-echo radial MRI is also possible, by sampling the same spoke repeatedly at different echo times. Spiral and especially radial trajectories have the advantage of being able to achieve very short echo times, via a center-out k-space trajectory. There also exists a special subclass of radial trajectories called Ultra-short TE (UTE) MRI, which will be employed later in chapter 6 of this thesis. A 3D UTE radial sequence typically consists of a first half echo (from k=0 to k=k_{max}, followed by a second full echo from (k=k_{max} to k=$-k_{max}$), as illustrated in Figure 2.16(d). Unlike other radial trajectories, in UTE the sampling begins while the read gradient is still ramping up in order to minimize the first TE. In a 3D UTE sequence, the spokes are usually positioned isotropically within a 3D sphere of k-space, forming a trajectory commonly called *kooshball* trajectory. The kooshball trajectory has the advantage of being particularly robust to motion, breathing and undersampling artifacts [50]. In fact, the kooshball trajectory can be massively undersampled and combined with a partial k-space reconstruction technique to greatly accelerate the image acquisition (see chapter 6) [51].

2.6 Parallel Imaging

Magnetic Resonance Imaging has the disadvantage of being a relatively slow imaging modality compared to CT or ultrasound. The speed of MRI acquisition is somewhat limited by the relaxation constants (T_1, T_2, etc.) that are intrinsic to biological tissues. Therefore, certain contrast mechanisms cannot be achieved apart from long repetition times (e.g. FLAIR). As we have already discussed, one method of speeding up the MRI acquisition consists of acquiring multiple k-space lines following a common excitation (or *TR*), as in EPI or TSE. Another approach known as *parallel imaging* uses the redundant sensitivity information gleaned from multi-channel receiver arrays in order to speed up the acquisition.

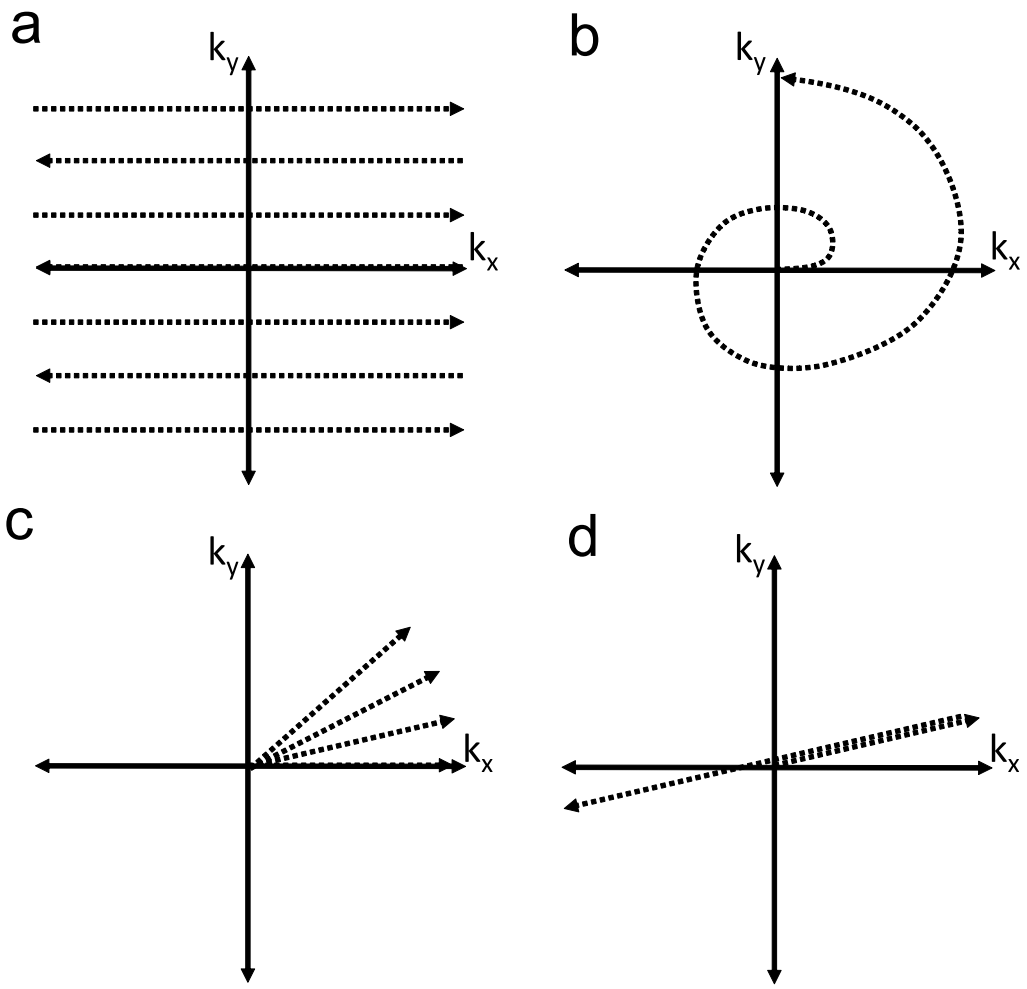

Figure 2.16: Example of (a) an EPI trajectory in with EPI factor of 7, (b) a spiral trajectory, (c) a center-out radial trajectory and (d) a double-echo UTE radial trajectory in. Note that the second spoke was purposefully shifted slightly to enable better visualization, but would in practice perfectly overlap with the first.

This is usually achieved by skipping lines in k-space (undersampling), and recovering the missing information after the fact as part of the image reconstruction workflow. The two most common techniques of parallel imaging are known as SENSitivity Encoding (SENSE) [52] and GeneRalized Autocalibrating Partially Parallel Acquisitions (GRAPPA) [53]. The main difference between the two techniques lies primarily in how the missing information is recovered. In SENSE, the missing information is recovered in the image domain, after applying the Fourier transform, while in GRAPPA, the missing information is recovered in k-space prior to taking the Fourier transform. In both cases, a reference scan is required to obtain the missing

information. Different MRI manufacturers have either one or both of these methods implemented on commercial MRI scanners. In this section, we shall only discuss SENSE, since it is the parallel imaging technique implemented on Philips scanners and is employed throughout this thesis. In the absence of motion and geometrical distortions (as in EPI), SENSE generally yields better image quality than GRAPPA, having also the advantage of being compatible with an optimal-SNR coil combination [53].

2.6.1 Sensitivity Encoding (SENSE)

In parallel imaging, the reduction factor (a.k.a. acceleration factor) R is given by

$$R = \frac{n_k^{full}}{n_k^{red}} \tag{2.64}$$

where n_k^{full}/n_k^{red} is the number of k-space (phase-encode) lines in the case of full/reduced sampling, respectively. Reduced sampling has the effect of reducing the FOV by the factor R, thus resulting in an image folded along the phase encode direction (after taking the Fourier transform). If n_c different surface coils are used to detect the object signal, then n_c different folded images result. Letting n_p denote the number of superimposed pixels at location $\boldsymbol{r}_\rho$, the complex coil sensitivities at the n_p superimposed positions form an $n_c \times n_p$ matrix S:

$$S_{\gamma,\rho} = s_\gamma(\mathbf{r}_\rho) \tag{2.65}$$

where γ, ρ count the coils and the super-imposed pixels, respectively, $\mathbf{r}_\rho$ denotes the position of the pixel ρ, and s_γ is the spatial sensitivity of the coil γ. If we assemble into an *aliased* signal vector $\mathbf{a}$, the complex image values that the chosen pixel has in the n_c intermediate images, the n_p separated pixels (assembled in vector $\mathbf{v}$) can be solved by a matrix operation:

$$\mathbf{v} = U\mathbf{a} \tag{2.66}$$

where U is the $n_p \times n_c$ *unfolding matrix*, given by

$$U = (S^H \Psi^{-1} S)^{-1} S^H \Psi^{-1} \tag{2.67}$$

Here, Ψ is the *receiver noise correlation matrix* with $n_c \times n_c$ entries, which accounts for the levels and correlation of noise in the receiver channels. Prior to performing a SENSE acquisition, a reference scan and a noise scan are both required to calculate the coil sensitivities s_γ, and the

noise matrix Ψ. The reference scan usually consists of an image with a coarser voxel resolution (~5 mm isotropic) received separately with the body coil, and the receiver array (usually a SPGR with α/TR~4–7°/2–4 ms). Similarly, the noise scan usually consists of a fast acquisition with coarse resolution but without any RF pulses (α=0°). The n_c coil sensitivities are then simply measured by dividing each receiver coil image $I_{c,\gamma}$ by the body coil image I_B (i.e. $s_\gamma = I_{c,\gamma} / I_B$). The noise matrix Ψ is easily calculated by calculating the covariance of the n_c noise images. In practice, the coil sensitivity maps will be noisy. In the classical SENSE image reconstruction, the sensitivity maps are smoothened via a 2D or 3D polynomial fit to avoid propagating this noise into the final unfolded image; however, the contemporary SENSE image reconstruction implemented on modern MRI scanners usually employ a regularization scheme in place of polynomial smoothing to avoid propagating the noise.

It can be proven that the final SNR_ρ^{red} in the unfolded image under a SENSE acceleration factor R is related to the SNR_ρ^{full} in the fully sampled image by

$$SNR_\rho^{red} = \frac{SNR_\rho^{full}}{g_\rho \sqrt{R}} \ , \quad g_\rho = \sqrt{[(S^H \Psi^{-1} S)^{-1}]_{\rho,\rho} (S^H \Psi^{-1} S)_{\rho,\rho}} \geq 1 \tag{2.68}$$

Here, g_ρ is the local coil geometry factor. It should be noted that in the regularized SENSE implementation, it is common for the local geometry factor to be less than unity in certain locations.

2.6.2 Regularized SENSE

In a regularized SENSE reconstruction, Eq. (2.66) becomes a minimization problem [54]

$$\mathbf{v}^\lambda = \min_a \left\{ \left\| \tilde{S}\mathbf{v} - \tilde{\mathbf{a}} \right\|_2 + \lambda^2 \| L(\mathbf{v} - \mathbf{v}^0) \|_2 \right\} \tag{2.69}$$

where $\tilde{S} = \Lambda^{-1/2} V^H S$ and $\tilde{\mathbf{a}} = \Lambda^{-1/2} V^H \mathbf{a}$, are the sensitivity matrix and aliased vectors transformed by an eigenvector decomposition of the noise correlation matrix (i.e. $\Psi = V \Lambda V^H$, or $\Psi^{-1} = V \Lambda^{-1} V^H$), λ is the regularization parameter, L is a positive semi-definite linear transformation, $\mathbf{v}^0$ denotes the prior information about the solution $\mathbf{v}$ and $\|\bullet\|_2$ represents the L-2 norm. In the case where λ^2=0, Eq. (2.69) reverts to the classical SENSE reconstruction of Eq. (2.67), while at the other extreme (when λ^2 is too large), the solution will be a copy of the prior information $\mathbf{v}^0$. In general, regularized SENSE has the advantage of enabling higher acceleration

factors with smaller g factors. Parallel imaging is particularly important in 3D MRI protocol optimization, in order to constrain the total scan duration. Since 3D MRI comprises two phase-encode directions, 2D SENSE can be employed, providing even greater net acceleration factors with lower SNR loss and artifacts than standard 2D MRI [55].

An example of a 1D classical SENSE and GRAPPA image reconstruction is given in Figure 2.17, under varying acceleration factors (R=1–5) for an in vivo brain image using a circular-symmetric arrangement of eight receiver coils. Interestingly, as may be assessed from the artifact power (listed at the bottom-right corner of each image), SENSE outperforms GRAPPA at lower acceleration factors ($R\leq3$), while GRAPPA outperforms SENSE at higher acceleration factors ($R>3$). This simulation was performed using the freely available PULSAR MATLAB toolbox [56].

2.7 Image Registration and Resampling

In quantitative MRI, parametric maps are often calculated from images acquired at different time-points during an examination. Even when patients or volunteers attempt to remain motionless during the course of the examination, it is not uncommon for some subject motion or drift to occur over time (usually in the order of 0–2 mm). Moreover, a pixel-wise comparison of two image datasets acquired several weeks or months apart may be necessary to obtain complementary diagnostic information, such as when preparing a Radiation Treatment Plan. In all these instances, *image registration* becomes a crucial step of the image-processing pipeline. By definition, image registration (or co-registration) involves transforming one image (called the *moving image*) such that it matches a second image (called the *fixed image*) in such a way that all anatomical features are aligned (correspond) as closely as possible.

Image registration may be within-modality (e.g. MR-MR) or across-modality (e.g. MR-CT). Image registration techniques can also be classified in terms of the number of degrees of freedoms (DOF) allowed by the transformation. The three most common types of image registration transforms include the *rigid* (6 DOF), the *affine* (12 DOF) and the *non-rigid* (a.k.a. *deformable* registration, with more than 12 DOF). Deformable registration can be particularly useful in situations where anatomical tissue deformations are present in the moving image, with respect to the fixed image.

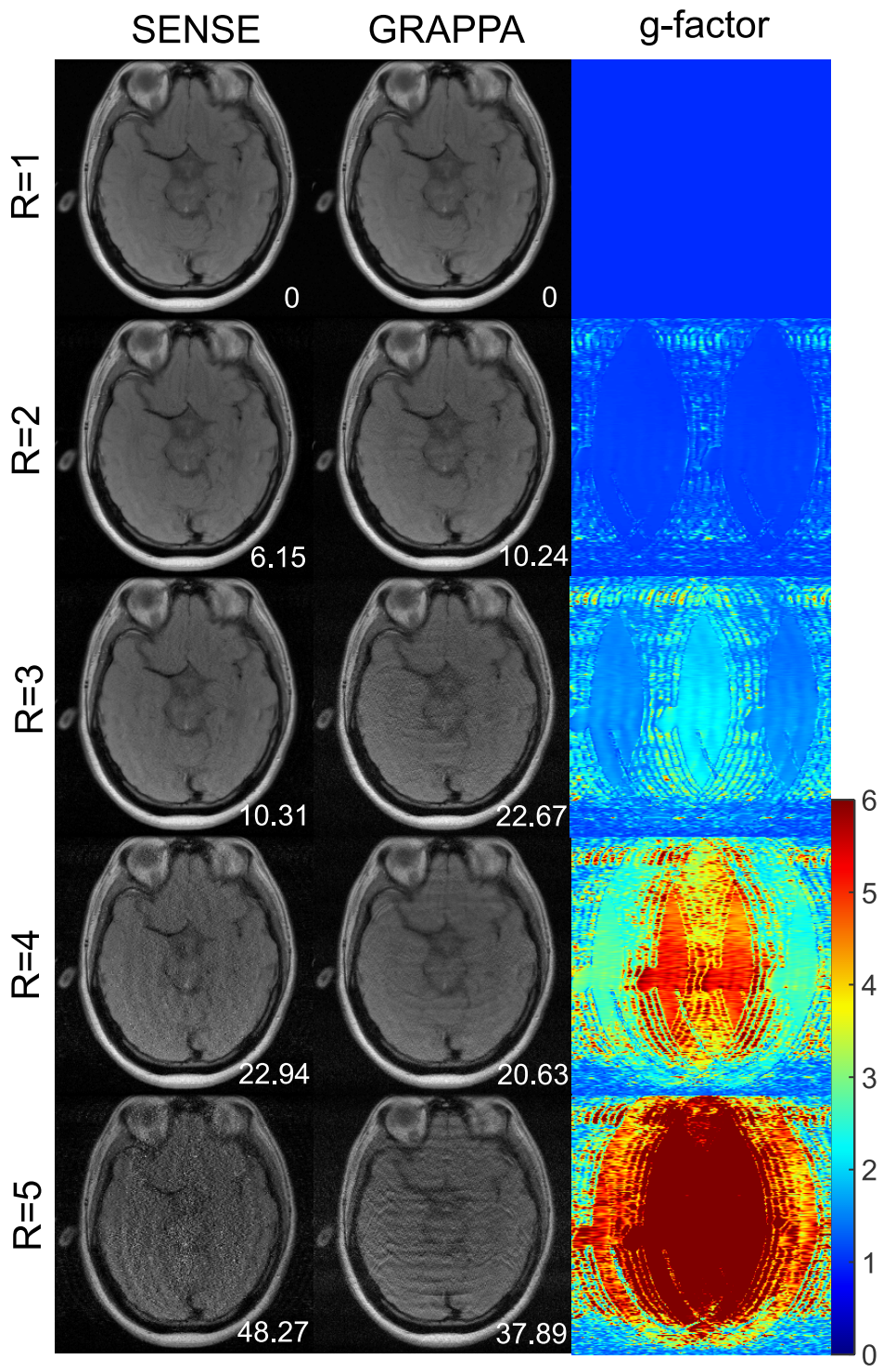

Figure 2.17: Comparison of classical SENSE and GRAPPA image reconstructions under varying acceleration factors using a circular-symmetric arrangement of 8 coils around the head. The SENSE g-factor maps are also shown on the right. The artifact power (sum-of-squares error) is shown at the bottom right corner of each image.

Deformations may be due to the imager's hardware imperfections (such as gradient nonlinearities or static field inhomogeneities in MRI), or caused by a different positioning of the subject's anatomy (such as patient's abdomen on a flat versus a curved bed). Deformable registration is also commonly employed when creating anatomical atlases from many different patients or subjects. Image registration algorithms typically consist of two components, including 1) a cost function, and 2) an optimization process. The optimization scheme will attempt to find the transformation that minimizes the cost function. In order for the registration algorithm to converge to a global minimum, the moving image must be lie within the *capture range* of the fixed image. A manual rigid registration is often a first necessary step needed to bring the moving image within the capture range of the automatic registration algorithm.

2.7.1 The transform matrix formulation

Both affine and rigid transformations can be represented by an augmented 4×4 matrix, containing 12 elements that are allowed to vary, (since the bottom row of the matrix always remains [0 0 0 1]). The rigid-body transformation $\mathbf{T_{rigid}}$ is often represented by a 3×3 rotation matrix $\mathbf{R}=\mathbf{R_z}\times\mathbf{R_y}\times\mathbf{R_x}$ and a translation vector $\mathbf{t} = [t_x, t_y, t_z]^T$, combined into the 4×4 matrix such that

$$\mathbf{r}' = \mathbf{T_{rigid}}\mathbf{r}$$

$$\begin{pmatrix} x' \\ y' \\ z' \\ 1 \end{pmatrix} = \begin{pmatrix} \cos\beta\cos\gamma & \cos\alpha\sin\gamma + \sin\alpha\sin\beta\cos\gamma & \sin\alpha\sin\gamma - \cos\alpha\sin\beta\cos\gamma & t_x \\ -\cos\beta\sin\gamma & \cos\alpha\cos\gamma - \sin\alpha\sin\beta\sin\gamma & \sin\alpha\cos\gamma + \cos\alpha\sin\beta\sin\gamma & t_y \\ \sin\beta & -\sin\alpha\cos\beta & \cos\alpha\cos\beta & t_z \\ 0 & 0 & 0 & 1 \end{pmatrix} \begin{pmatrix} x \\ y \\ z \\ 1 \end{pmatrix} \quad (2.70)$$

$$= \begin{pmatrix} 1 & 0 & 0 & t_x \\ 0 & 1 & 0 & t_y \\ 0 & 0 & 1 & t_z \\ 0 & 0 & 0 & 1 \end{pmatrix} \begin{pmatrix} \cos\gamma & \sin\gamma & 0 & 0 \\ -\sin\gamma & \cos\gamma & 0 & 0 \\ 0 & 0 & 1 & 0 \\ 0 & 0 & 0 & 1 \end{pmatrix} \begin{pmatrix} \cos\beta & 0 & -\sin\beta & 0 \\ 0 & 1 & 0 & 0 \\ \sin\beta & 0 & \cos\beta & 0 \\ 0 & 0 & 0 & 1 \end{pmatrix} \begin{pmatrix} 1 & 0 & 0 & 0 \\ 0 & \cos\alpha & \sin\alpha & 0 \\ 0 & -\sin\alpha & \cos\alpha & 0 \\ 0 & 0 & 0 & 1 \end{pmatrix} \begin{pmatrix} x \\ y \\ z \\ 1 \end{pmatrix}$$

Here, the angles α, β and γ are called *pitch*, *roll* and *yaw*, corresponding to rotations about the x, y and z axis, respectively. (A positive yaw of +90° implies that the rotation will map $+y$ unto the $+x$ axis. Similarly a positive roll of +90°, will map the $+x$ unto the $+z$ axis, and a positive pitch of +90°, will map the $+z$ unto the $+y$ axis). While the transform itself is unique, the order in which the rotations and translations are applied does matter, with 3!×2!=12 possible combinations. Depending on this order, the values of the three angles and three translations will change to yield the same final transformation. Moreover, for the practical purpose of doing a manual rigid

transformation, and since the transform depends on the location of the origin, it is easiest to place the origin of the coordinate system at approximately the center of the 3D image. The origin and coordinate system of the image are usually defined within the header of the image file (whether a dicom, mha, or nifti image file). The 9-DOF affine transformation allows for anisotropic scaling (magnification) of the image by incorporating the scaling matrix into Eq. (2.70) to yield

$$\mathbf{T_{9DOF}} = \begin{pmatrix} 1 & 0 & 0 & t_x \\ 0 & 1 & 0 & t_y \\ 0 & 0 & 1 & t_z \\ 0 & 0 & 0 & 1 \end{pmatrix} \begin{pmatrix} \cos\gamma & \sin\gamma & 0 & 0 \\ -\sin\gamma & \cos\gamma & 0 & 0 \\ 0 & 0 & 1 & 0 \\ 0 & 0 & 0 & 1 \end{pmatrix} \begin{pmatrix} \cos\beta & 0 & -\sin\beta & 0 \\ 0 & 1 & 0 & 0 \\ \sin\beta & 0 & \cos\beta & 0 \\ 0 & 0 & 0 & 1 \end{pmatrix}$$

$$\begin{pmatrix} 1 & 0 & 0 & 0 \\ 0 & \cos\alpha & \sin\alpha & 0 \\ 0 & -\sin\alpha & \cos\alpha & 0 \\ 0 & 0 & 0 & 1 \end{pmatrix} \begin{pmatrix} m_x & 0 & 0 & 0 \\ 0 & m_y & 0 & 0 \\ 0 & 0 & m_z & 0 \\ 0 & 0 & 0 & 1 \end{pmatrix} \tag{2.71}$$

$$= \begin{pmatrix} m_x \cos\beta\cos\gamma & m_x(\cos\alpha\sin\gamma + \sin\alpha\sin\beta\cos\gamma) & m_x(\sin\alpha\sin\gamma - \cos\alpha\sin\beta\cos\gamma) & t_x \\ -m_y\cos\beta\sin\gamma & m_y(\cos\alpha\cos\gamma - \sin\alpha\sin\beta\sin\gamma) & m_y(\sin\alpha\cos\gamma + \cos\alpha\sin\beta\sin\gamma) & t_y \\ m_z\sin\beta & -m_z\sin\alpha\cos\beta & m_z\cos\alpha\cos\beta & t_z \\ 0 & 0 & 0 & 1 \end{pmatrix}$$

Unlike the previous models, the general affine model (with 12 DOF) does not require the computation of sines and cosines. Instead, each of the 12 entries within the transform matrix is allowed to vary independently, additionally enabling image skews and shears. An important property of the affine transformation is that lines that are parallel before the transformation, remain parallel after the transformation.

2.7.2 Cost Functions

The three most commonly used cost functions are the *sum-of-squares difference* (SSD) or sometimes called *mean squared error* (MSE), the normalized correlation (NC), also known as correlation coefficient (CC) and the *mutual information* (MI). For N overlapping voxels i in images A and B, the *SSD* is defined as

$$SSD = \frac{1}{N}\sum_i |A(i) - B(i)|^2 \tag{2.72}$$

Similarly, the correlation coefficient is defined as

$$CC = \frac{1}{N}\frac{\sum_i (A(i) - \bar{A})(B(i) - \bar{B})}{(\sum_i (A(i) - \bar{A})^2 \cdot \sum_i (B(i) - \bar{B})^2)^{1/2}} \tag{2.73}$$

where $\overline{A}$ and $\overline{B}$ are the mean intensity values in images *A* and *B*, respectively. In the case where the intensity of two images only differ by Gaussian noise, the *SSD* has been found to be the most optimal cost function, being able to achieve sub-voxel accuracy even for high-resolution MRI [57]. The CC was one of the first cost functions used for within-modality image registration. When two images of the same intensity are perfectly registered, CC=1. The CC is the optimal cost function in the case where a linear relationship exists between the intensity values in the two images.

Mutual information is probably the most popular cost function used in both within-modality and across-modality image registration. It is based on the concept of information entropy, defined as

$$H = -\sum_i p_i \log p_i \tag{2.74}$$

H can be understood as the average information supplied by a set of *i* symbols whose probabilities are given by $p_1, p_2, p_3, \ldots, p_i$. The entropy will have a maximum value if all symbols have equal probability of occurring, and will have a minimum value of zero if one symbol as 100% probability of occurring and the other symbols have zero probability. Based on this definition, the joint entropy of two images *A* and *B* is defined as

$$H(A,B) = -\sum_a \sum_b p_{AB}(a,b) \log(p_{AB}(a,b)) \tag{2.75}$$

where $p_{AB}\ (a,b)$ is the joint probability distribution function (normalized joint histogram) of images *A* and *B*, while *a* and *b* are the selected intensity bins. Similarly, the entropy of each image is defined as $H(A) = -\sum_a p_A \log(p_A)$ and $H(B) = -\sum_b p_B \log(p_B)$, where p_A and p_B are the normalized histograms of images *A* and *B*, respectively. The mutual information *I(A,B)* is then defined as

$$I(A,B) = H(A) + H(B) - H(A,B)$$
$$= \sum_a \sum_b p_{AB}(a,b) \log\left(\frac{p_{AB}(a,b)}{p_A(a) \cdot p_B(b)}\right) \tag{2.76}$$

Mutual information can be qualitatively understood as how well one image explains the other. In general, mutual information works best when the images are free of bias-field (image intensity non-uniformity) and contain high anatomical contrast. For example, mutual information works well when registering a T_1w to a T_2w MR image, since different tissue classes have very distinct signal intensities with CSF appearing dark in the T_1w image, as opposed to bright in the T_2w image. However, for MR-CT registration where the CT image contains poor soft-tissue contrast, mutual information does not always work as well as another technique called *chamfor matching* [57], which uses a cost function based on the distance transform. As in most image registration techniques, the robustness of mutual information will vary with the amount of overlap between two images. A normalized mutual information cost function: $\tilde{I}(A,B) = (H(A) + H(B))/H(A,B)$, has been shown to provide increased robustness when the two fields-of-view (FOVs) differ significantly. However, in most image registration algorithms or softwares, such as the BRAINSFit module in 3D Slicer, the problem of overlap is best addressed by defining a mask that excludes regions of non-overlap between the two images.

2.7.3 Resampling and Interpolation

Image resampling is an important step as part of any registration algorithm. A poor choice of resampling technique can result in serious degradation or artifacts in the final registered image. Resampling by interpolation generally consists of the following four steps [57]: 1) Take a set of discrete data f_k. 2) Build by interpolation a continuous function f. 3) Perform a geometric transformation T that yields $f\big(T(\mathbf{x})\big) = \sum c_{k_1} \varphi(T(\mathbf{x}) - \boldsymbol{k_1})$. 4) Summarize the continuous function $f(T(\mathbf{x}))$ by a set of discrete data samples $f(T(\boldsymbol{k_2}))$. Here, φ is the choice of interpolant, which significantly affects both the quality of the interpolation and the execution time. The ideal interpolant is the sinc function, but since it is not band-limited, it is in practice too computationally impractical. The fastest but lowest quality of interpolant is the *nearest-neighbor*, defined in 1D as

$$\varphi^0(x) = \begin{cases} 0, & x < -1/2 \\ 1, & -1/2 \leq x < 1/2 \\ 0, & 1/2 \leq x \end{cases} \tag{2.77}$$

A more common choice is *linear* interpolation, given in 1D by

$$\varphi^1(x) = \begin{cases} 1 - |x|, & |x| < 1 \\ 0, & 1 \leq x \end{cases} \tag{2.78}$$

Linear interpolation often provides an acceptable image quality in many cases. However, for high-resolution 3D MRI datasets, linear interpolation will tend to blur the final image, especially in anatomical regions of high spatial frequencies, such as the cerebellum, as shown in Figure 2.18. In this case, a higher-quality interpolant (that resembles more a sinc function) should be employed. Common choices include the windowed-sinc and the B-spline interpolation [57]. An important point is that the final interpolation scheme selected to resample the final registered dataset (using the optimal registration parameters), does not have to be the same scheme employed when resampling the moving image at each iteration of the optimization process.

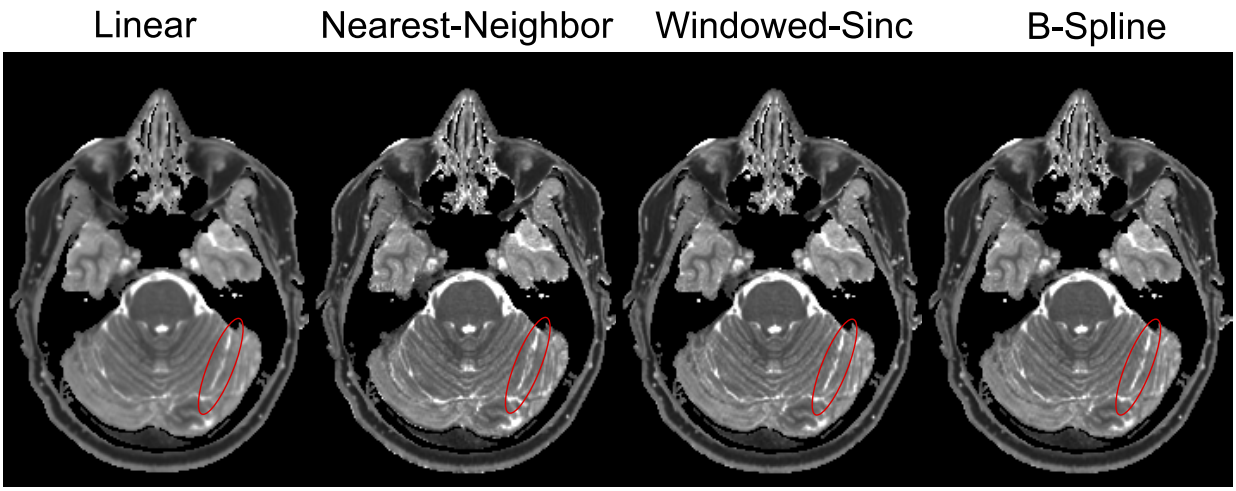

Figure 2.18: Comparison of 4 T_1 maps (obtained via the variable flip angle technique presented in chapter 3) after shifting and resampling the original T_1w and PDw SPGR datasets. Observe how the linear interpolation blurs the T_1 map, while the nearest-neighbor causes some double-edge effects in the CSF track circled in red. Best results are obtained using either the windowed-sinc or B-spline interpolation.

2.8 Image Intensity Non-Uniformity Correction

It is common for imaging modalities to suffer from signal non-uniformity over their field-of-view. This signal non-uniformity is commonly called *bias field*. In CT, the effect of X-ray beam-

hardening naturally results in *cupping artifact* over the object, which is usually minimized via a combination of calibration and/or an iterative post-processing correction [58]. In MRI, electrodynamic interactions between the RF field and the electromagnetic properties of tissues also lead to a bias field. Since this bias field is more complex and depends on the hardware (RF coils), the object's geometry, size and tissue composition, it is normally left uncorrected on MRI scanners. The bias field is caused by a combination of transmit B_1^+ (flip-angle) and receive B_1^- (sensitivity profile) non-uniformity. When performing a SENSE reconstruction (or an optimal SNR coil combination with uniform sensitivity), the receive sensitivity profile of the multi-channel array becomes interchanged for the profile of the body-coil, which helps reduce the receiver (B_1^-) inhomogeneity in the final image to some extent. However, non-uniformity in the flip angle over the image will still be present, with the center/edges of the image usually having a higher/lower flip angle than the nominal value (defined in Eq. (2.12)), respectively. Three common ways of correcting the bias field include performing finite-element simulations, using a B_1-mapping pulse sequence, and using a bias-field correction algorithm.

2.8.1 Finite Element Simulations

Assuming a complex harmonic time-dependence of the electric and auxiliary magnetic fields (i.e.: $\mathbf{E}(\mathbf{r},t) = \mathbf{E}(\mathbf{r})e^{-i\omega t}$ and $\mathbf{H}(\mathbf{r},t) = \mathbf{H}(\mathbf{r})e^{-i\omega t}$), where ω is the transmit or Larmor frequency (≈127.8 MHz at 3T), the wave equation for both **H** and **E** reduces to the Helmholtz equation [59], [60]

$$\begin{aligned} &\nabla^2\mathbf{H} - \kappa^2\mathbf{H} = \mathbf{0}, \\ &\nabla^2\mathbf{E} - \kappa^2\mathbf{E} = \mathbf{0}, \qquad \kappa^2 = \omega\mu(\omega\epsilon_r - i\sigma) \end{aligned} \tag{2.79}$$

Here, ε_r is the real part of the electric permittivity (≈$76\varepsilon_0$ for water at 3T), σ is the conductivity (which typically ranges from 0–1.0 S/m for biological tissues), and μ is the magnetic permeability (≈μ_0 for biological tissues). In practice, only one of the two above partial differential equations needs be solved by finite element methods under the correct boundary conditions, and the other can be solved via the Maxwell equations (i.e.: $\nabla \times \mathbf{E} = -\frac{\partial \mathbf{B}}{\partial t} = -i\omega\mu\mathbf{H}$). The magnitude B_1^+/B_1^- fields over the object is then given by [61]

$$B_1^+ = \mu\frac{\left|H_x + iH_y\right|}{2},\ B_1^- = \mu\frac{\left|\left(H_x - iH_y\right)^*\right|}{2} \tag{2.80}$$

In general, the bias field worsens with increasing B_0 field strength (ω) and increasing ε_r. Fat and oil have a relatively low $\varepsilon_r \approx 6–12\varepsilon_0$, which explains why a mineral oil phantom will have a significantly more uniform signal profile than a water phantom of the same size. Unfortunately, a finite-element simulation is often the most computationally intensive (and thus time-consuming) method for modelling the bias field, and as will be shown in chapter 6, it is not necessarily the most accurate. It is nonetheless commonly used when designing new transmit RF coils (and sometimes transmit/receive coils) to verify that the theoretical B_1^+ field and SAR (based on the coil hardware design and electronic components) agree with measurements.

2.8.2 B_1^+ (flip angle) mapping

Another method commonly used to correct the bias field, especially when mapping the T_1 relaxation or proton density, is to measure it directly via a B_1-mapping pulse sequence. Many pulse sequences have been designed to map the flip angle. The Double-Angle Method (DAM) is probably the simplest approach, which consists of acquiring two GRE images at nominal flip angles $\alpha/2\alpha$~60°/120° with very long TR (>3×T_1). Taking the ratio of the two images yields

$$\frac{I_2}{I_1} = \frac{\sin(2\alpha)}{\sin\alpha} = 2\cos\alpha\,,\quad \alpha = \cos^{-1}\left|\frac{I_2}{2I_1}\right| \tag{2.81}$$

The B_1^- field cancels out (since the same receiver coil is employed for both images) and the flip angle α (or the normalized B_1^+ field $c_{RF}^+ = \alpha_{meas}/\alpha_{nom}$) can be mapped voxel-wise. The main disadvantage of a 3D DAM acquisition is the long scan duration caused by the long TR; therefore, it is usually limited to single-slice or multi-slice 2D MRI, especially when comparing with other B_1-mapping techniques. An improved version of DAM consists of adding saturation pulses to reset the spins into the same state (regardless of α) after each acquisition window, such that $I_1 \propto \sin(\alpha)\, f_1(T_1, TR)$, and $I_2 \propto \sin(2\alpha)\, f_2(T_1, TR)$ with $f_1 = f_2 \neq 1$. Using such as sequence (called Saturated Double Angle Method or (SDAM) [62], Eq. (2.81) remains valid at much shorter TR (<200 ms), and is also compatible with an EPI or a spiral sampling trajectory, thus enabling fast volumetric 3D flip-angle mapping within a few minutes. A limitation common to both DAM and SDAM is is that noise and artifacts tend to increase significantly with decreasing B_1. Another popular B_1-mapping technique called Actual Flip angle Imaging (AFI), is based on a

dual-TR SPGR acquisition (also used in this thesis). This sequence consists of two consecutive sampling windows with the same TE and flip angle α but using a shorter TR_1 and longer TR_2~5×TR_1. Yarnykh shows that taking the ratio of the two signals (images) yields [63]

$$r = \frac{S_2}{S_1} = \frac{1 - E_{1,1} + (1 - E_{1,2})E_{1,1}\cos\alpha}{1 - E_{1,2} + (1 - E_{1,1})E_{1,2}\cos\alpha} \approx \frac{1 + n\cos\alpha}{n + \cos\alpha} \tag{2.82}$$

where $E_{1,1} = e^{-TR_1/T_1}$, $E_{1,2} = e^{-TR_2/T_1}$ and n=TR_2/TR_1. The flip angle is then simply given by

$$\alpha \approx \cos^{-1}\left(\frac{nr - 1}{n - r}\right) \tag{2.83}$$

The accuracy of AFI is limited by the assumption that T_1>>TR_1, TR_2 and also by a bias due to non-ideal RF spoiling (just as SPGR itself), although the latter can be effectively mitigated by inserting strong spoiler gradients [33]. The main disadvantage of B_1-mapping techniques is that there is no universally-accepted gold standard for measuring the B_1 field in vivo (except perhaps for the prohibitive DAM), and different MRI manufacturers have different B_1-mapping sequences implemented, leading to some hardware-dependent biases or errors. Moreover, B_1-mapping techniques usually require a coarse voxel resolution of 5−10 mm (isotropic), leading to partial-volume effects and the need for additional filtering and extrapolation (to avoid errors at the object's edges). Moreover, in many pulse sequences, the bias field cannot be simply corrected using a B_1 map, since the receiver B_1^- profile is still present (with $B_1^- \neq B_1^+$) and the B_1^+ cannot be expressed as a closed-form solution of the intrinsic (T_1/T_2, etc.) or extrinsic (TE/TR, etc.) scan parameters, even if they are known.

2.8.3 Bias Field Correction Algorithms

Probably the most popular and time-efficient approach for correcting image non-uniformity is to employ a bias-field correction algorithm. Such an algorithm usually fits the low spatial frequency components of the image to estimate the bias field and then removes it via a normalization step. Many bias field correction algorithms have been designed and are implemented in various image-processing software packages such as FSL (FMRIB Software Library, http://fsl.fmrib.ox.ac.uk/fsl/fslwiki/, SPM (Statistical Parametric Mapping, http://www.fil.ion.ucl.ac.uk/spm/), FreeSurfer, http://freesurfer.net/fswiki, and ITK (Insight Tool Kit, https://itk.org/). Some bias field correction algorithms are designed to work exclusively on specific anatomies, such as the

brain (e.g. New Segment Toolbox in SPM8), since they rely on atlas-based registration and segmentation, while others are more versatile. Probably one of the most versatile and robust algorithm is N4ITK (a.k.a. N4), which is the newer and improved algorithm based on the older *nonparametric nonuniform intensity normalization* (N3, a.k.a. N3NMI) cousin developed at the Montreal Neurological Institute [64]. N4 is also freely available as part of the Insight Tool Kit (ITK) C++ library for image processing, or within 3D Slicer, a user-friendly GUI containing numerous ITK tools.

Many studies have been published on how to correctly optimize N3 and SPM8 for best bias-field estimation [65], [66]. A poor optimization of such algorithms will result in under-fitting or over-fitting of the image. Under-fitting implies that the fitting distance is too long, and much signal inhomogeneity remains while over-fitting implies that the fitting distance is too short, leading to an alteration of the image contrast. Both N3 and N4 assume the following image formation model

$$v(\mathbf{x}) = u(\mathbf{x})f(\mathbf{x}) + n(\mathbf{x}) \tag{2.84}$$

where u is the uncorrupted image, f is the bias field, n is the noise (assumed to be Gaussian), and v is the actual image. The algorithm works on the logarithm of the image (with $\hat{u} = \log u$) which makes it less sensitive to the contrast. If ignoring noise:

$$\hat{v}(\mathbf{x}) = \hat{u}(\mathbf{x}) + \hat{f}(\mathbf{x}) \tag{2.85}$$

The N3 algorithm applies the following iterative solution

$$\hat{u}^n = \hat{v} - \hat{f}_e^n = \hat{v} - S\{\hat{v} - E[\hat{u}|\hat{u}^{n-1}]\} \tag{2.86}$$

where $\hat{f}_e^0$ is the initial bias field estimate (usually set to zero), S is the smoothing operator (a B-spline approximator), and $E[\hat{u}|\hat{u}^{n-1}]$ is the expected value of the true image given the current estimate of the corrected image. The N4 algorithm makes the following improvement

$$\hat{u}^n = \hat{u}^{n-1} - \hat{f}_r^n = \hat{u}^{n-1} - S^*\{\hat{u}^{n-1} - E[\hat{u}|\hat{u}^{n-1}]\} \tag{2.87}$$

where S^* is a different (more robust) B-spline approximator, and $\hat{f}_r^n$ is the estimated *residual* bias field at the nth iteration [64]. The advantage of N4 over N3 is better and faster convergence, as

well as more robustness to noise. In chapter 6, N4ITK is used to estimate and correct both the relative B_1^+ and B_1^- inhomogeneity in multi-parameter mapping of the brain.

2.9 Filtering

Filtering is a common step as part of many image processing pipelines. In fact, MR images are usually filtered in k-space prior to applying the Fourier transform in order to reduce Gibbs-ringing, via an apodization function such as a hamming window. A general hamming window can defined (in 1D) as

$$w(n) = 1 - \frac{s}{2} - \frac{s}{2}\cos\left(\frac{2\pi n}{N}\right),\ 0 \le n \le N,\ 0 \le s \le 1, \tag{2.88}$$

where n is the k-space voxel index and $N = FOV_k - 1$ (the FOV in k-space) and s is the filter strength, which attenuates the edges of k-space by s ×100%. The signal in k-space is multiplied by the window to reduce the signal clipped at the edges of k-space, thus reducing Gibbs ringing. A typical value for s in the MR images shown in this thesis is ~0.25–0.35. The SNR of the image will increase while ringing will decrease with the filter strength, but at the cost of reduced spatial resolution; therefore, a compromise must be made for best image quality.

Filtering is also commonly done in the image-space domain, by convolving the image *f(m,n)* with a kernel *w(k,l)* of $2K+1 \times 2L+1$ pixels. The filtered image *g(m,n)* can be expressed mathematically as [57]

$$g(m,n) = w(k,l) * f(m,n) = \sum_{k=-K}^{K} \sum_{l=-L}^{L} w(k,l) \cdot f(m-k, n-l) \tag{2.89}$$

The kernel is centered on an image pixel *(m,n)*, the point-by-point products of the kernel coefficients and corresponding image pixels are obtained, and the sum of these products is used as the value of the output pixel *g(m,n)*. The same operation is performed on all pixels of the image to obtain the final filtered image.

The process of filtering while preserving edges and relevant image details (avoiding blurring) is commonly called *denoising*. Denoising is frequently applied prior to image segmentation or classification, in order to better delineate the object's edges and minimize locally-disconnected voxels in the final binary mask. Two popular types of denoising techniques include *median*

filtering, and the advanced *gradient anisotropic diffusion* algorithm. In median filtering, a kernel is also defined as in Eq. (2.89), but no convolution is performed; instead, the kernel frame is centered on each pixel *(m,n)* of the original image, and the median value of the pixels within the frame is computed and assigned to the central *(m,n)* pixel.

Gradient anisotropic diffusion (GAD) is based on the diffusion (a.k.a. heat) equation [67]

$$\frac{\partial}{\partial t} I(\mathbf{r}, t) = \nabla \cdot (c(\mathbf{r}, t) \nabla I(\mathbf{r}, t)) \tag{2.90}$$

where $I(\mathbf{r},t)$ is the image at location $\mathbf{r}$, t is the iteration step, and $c(\mathbf{r},t)$ is the diffusion function, a monotonically decreasing function of the image gradient magnitude, such as

$$c(\mathbf{r}, t) = \exp\left(-\left(\frac{|\nabla I(\mathbf{r}, t)|}{\sqrt{2}K} \right)^2 \right) \tag{2.91}$$

Here, K is the diffusion or flow constant. The discrete diffusion updates each pixel by an amount equal to the flow contributed by its nearest four or eight neighbors (by scaling the diagonal neighbors accordingly). The default parameters for GAD filtering in 3D Slicer are: dt=0.0625, K=1.00, and 5 iterations. An example of an axial T_2^* map from an in vivo brain volunteer filtered using median filtering and GAD is shown in Figure 2.19. Observe how GAD in (c) preserves the edges better than median filtering in (b). The T_2^* histograms are shown in (d) for the unfiltered and filtered datasets.

2.10 Segmentation and Classification

The process of segmentation in computer vision may be described as the need to identify an object of interest in an image from its background [30]. Image segmentation consists of dividing an image into smaller groups (or regions) of pixels that share something in common. On the other hand, classification means to assign to each point (or region) of an image a tissue class, where the classes are already determined (or defined) in advance. Therefore, in general, different organs may need to be *segmented* while different tissue types may need to be *classified*. There are many instances where classification and/or segmentation are required as part an imaging study or when planning a radiation treatment. For instance, as part of the RTP process, the tumor must be contoured and different organs at risk must be segmented prior to computing and

optimizing the dose distribution. Dose-volume histograms can then be calculated for the different organs and used to assess the quality of the treatment plan.

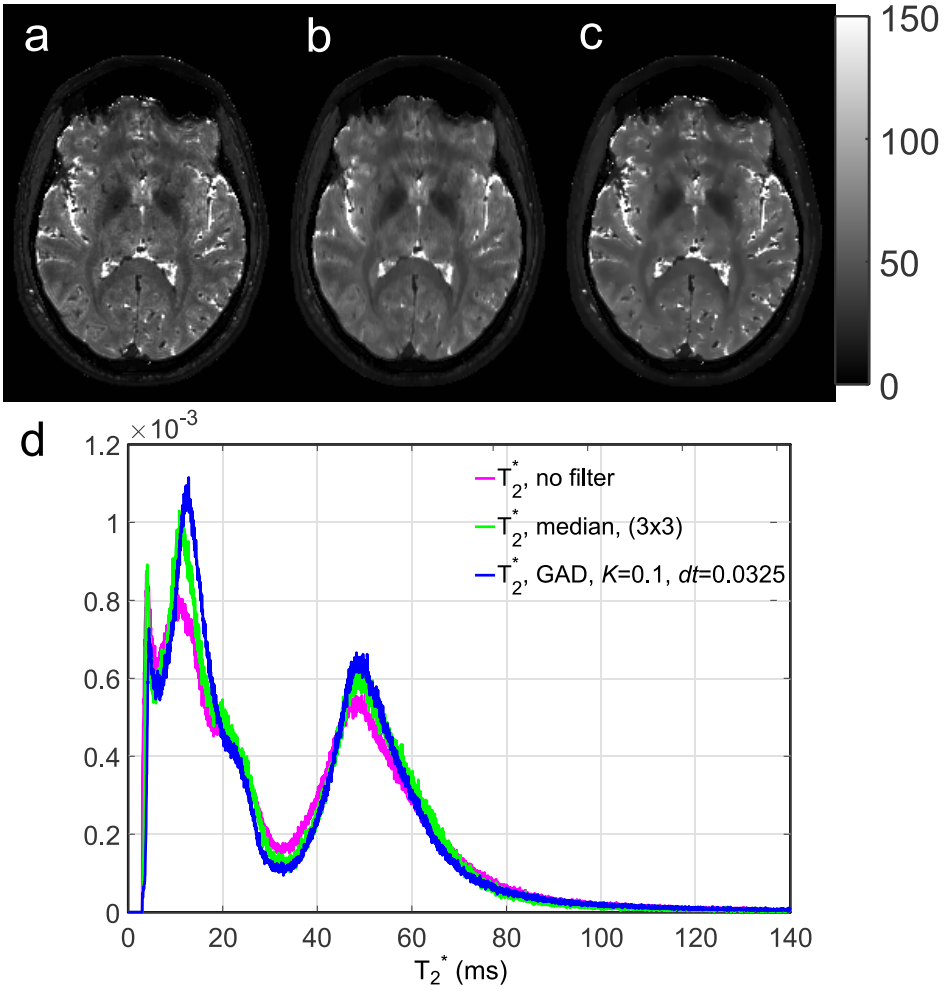

Figure 2.19: Example of a T_2^* map (a) unfiltered, (b) filtered using a median filter with a kernel of 3×3 pixels, (c) filtered using gradient anisotropic diffusion with K=0.1, a time step of 0.0325 and 24 iterations. Histograms of the T_2^* maps (full 3D datasets) are plotted in (d).

The field of image segmentation and classification is too big to be summarized here concisely. Techniques of image segmentation can be classified into three groups, including *data-driven* (bottom-up), *model-driven* (top-down) and *hybrid* techniques. The three most common types of data-driven techniques include *pixel-based clustering*, *adaptive thresholding* and *region-growing*, while the most common type of model-driven technique is *atlas-based* segmentation. Popular hybrid techniques include *active contours* and *level sets*, which are based on partial

different equations with boundary conditions. Two basic techniques of segmentation are used in this thesis, including basic histogram-based thresholding and Fuzzy C-means (FCM) clustering.

2.10.1 Histogram thresholding

An image histogram is defined as a vector that contains the count of the number of pixels in the image at each gray level (e.g. ranging from 0 to *P*-1). A 1D histogram is defined mathematically as [57], (p.4)

$$h(i) = \sum_{m=0}^{M-1} \sum_{n=0}^{N-1} \delta(f(m,n) - i), \quad i = 0, 1, \dots, P-1, \qquad \text{where} \quad \delta(w) = \begin{cases} 1, w = 0, \\ 0, w \neq 0 \end{cases} \tag{2.92}$$

If the histogram is normalized by the number of voxels in the image, then it becomes a type of probability distribution function (PDF). When images have high contrast and low signal non-uniformity (such as in a T_1 map), histogram thresholding can be an effective way of classifying different tissue types. An example of a T_1 histogram of the human brain is shown in Figure 2.20. Since different tissue classes generally have distinct T_1 values, (with the exception of muscle and gray matter), a T_1 histogram can be used to find optimal thresholds for segmenting a brain or other parts of the anatomy. In practice, however, tissue classification by histogram thresholding is generally not very commonly used because conventional MR images are not sufficiently uniform to yield a reliable classification. Therefore, techniques that are less sensitive to a bias field are more commonly used.

2.10.2 Pixel-based Clustering

Three popular of techniques of unsupervised pixel-based clustering include the K-means (KM), the Expectation Maximization (EM) and the Fuzzy C-means (FCM) algorithms. All three algorithms are closely related, but EM and FCM have the advantage of being able to account for partial volume effects.

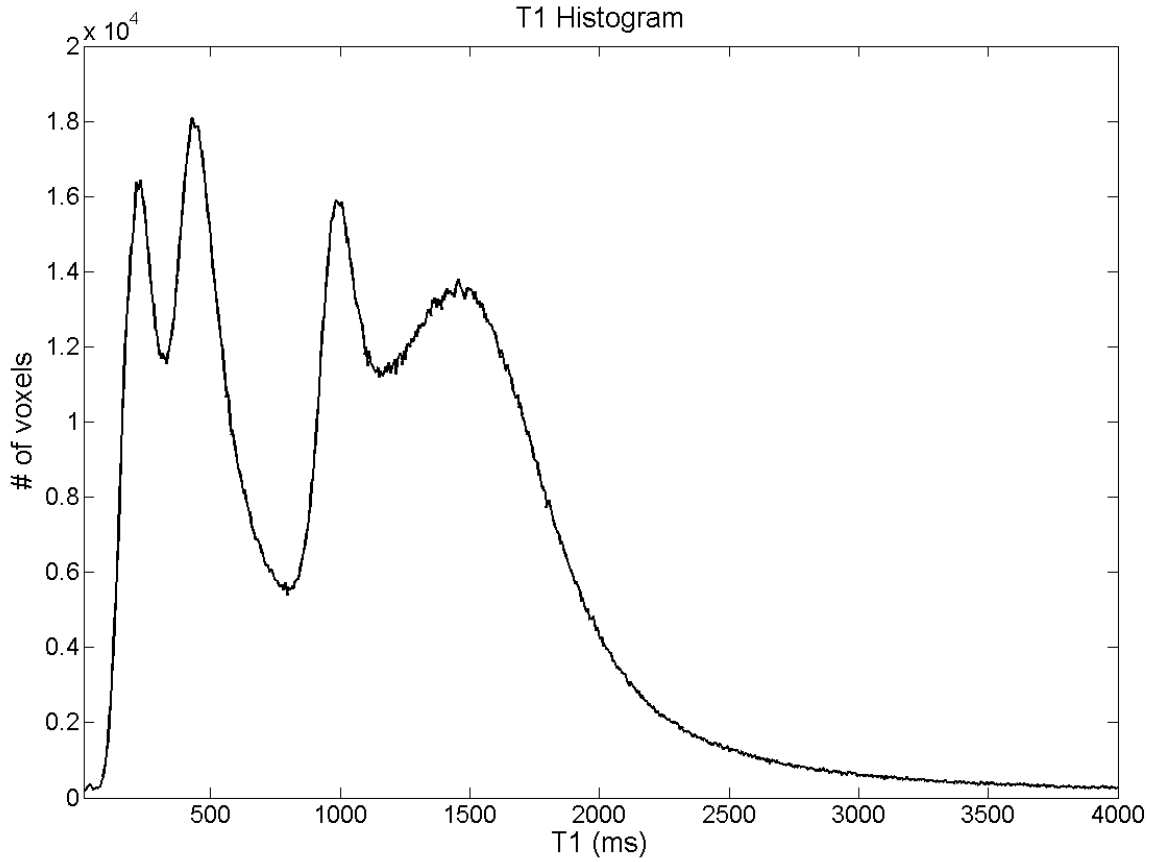

Figure 2.20: A T_1 histogram of a human head at 3T. Observe how 5 distinct tissue classes can be identified as different Gaussian-like distributions, including bone, fat, WM, GM/muscle and CSF with mean T_1 values of ~220, 450, 1000, 1500 and >3000 ms, respectively.

Let y_j be the observed intensity of pixel j (in an image with N pixels) and z_{jk} be the indicator function (i.e. the probability of pixel j belonging to tissue class k), and η_j be the additive noise term, assumed to have a Gaussian distribution with standard deviation σ. The observed pixel intensity is given by [57]

$$y_j = g_j \sum_{k=1}^{K} z_{jk} v_k + \eta_j, \;\; z_{jk} = \begin{cases} 1, & \text{if pixel } j \text{ is in class } k \\ 0, & \text{otherwise} \end{cases} \tag{2.93}$$

where g_j is the gain field (bias field) at location j and v_k is the true pixel intensity. The KM algorithm solves for g_j and z_{jk} via an optimization process, by minimizing an objective function (a.k.a. energy function) E, with two terms E_1 and E_2

$$E = \frac{1}{2\sigma^2} E_1 + \alpha E_2, \quad E_1 = \sum_{j=1}^{N} \sum_{k=1}^{K} z_{jk} \left(y_j - g_j v_k\right)^2, \quad E_2 = \sum_{j=1}^{N} \sum_{i \in N_j} z_j^T V z_i \tag{2.94}$$

The first term is the data term, while the second term is a Markov random field term that regularizes the solution by enforcing continuity in the presence of noise [57] (p. 211). V is a $K \times K$ matrix used to penalize the classification of pixel j based on its neighbor i, and N_j being the number of neighboring pixels considered (e.g. 4 in 2D or 6 in 3D). Therefore, a pixel belonging to the same tissue class as its N_j neighbors is favored over configurations consisting of different classes. The gain field g is often represented as a low-degree 3D polynomial function $g_j = \sum f_n P_n(j)$, where P_n is the choice of polynomial basis function and f_n are the coefficients.

The algorithm proceeds according to the following steps: 1) Initial estimates of the class means v_k are obtained assuming $g_j = 1$, and appropriate values for σ and α are pre-selected by the user. 2) The indicator functions z_{jk} are solved by minimizing the Energy function (Eq. (2.94)) at each pixel location. 3) The means are solved again by using the zero gradient of Eq. (2.94)

$$v_k = \frac{\sum_{j=1}^{N} z_{jk} g_j y_j}{\sum_{j=1}^{N} z_{jk} g_j^2} \tag{2.95}$$

4) The gain field g_j is estimated by solving the following matrix equation for the coefficients f_n:

$$\left[z_{jk} v_k P_n(j)\right] \cdot [f_n] = \left[z_{jk} y_j\right] \tag{2.96}$$

5) We return to step two and repeat the same procedure until convergence is reached, which occurs when $\left\| v_k^{new} - v_k^{old} \right\| < \epsilon$ where ε is also selected by the user. The FCM algorithm is very similar to KM, except that the indicator function z_{jk} is replaced by a membership function u_{jk}^q which can now take any value between 0 and 1, and represents the probability or proportion of tissue k within voxel j, given by

$$u_{jk} = \frac{\left(\left(y_j - g_j v_k\right)^2 + 2\alpha \sum_{i \in N_j} \sum_{m \neq k} u_{jm}^q\right)^{-1/(q-1)}}{\sum_{k=1}^{K} \left(\left(y_j - g_j v_k\right)^2 + 2\alpha \sum_{i \in N_j} \sum_{m \neq k} u_{jm}^q\right)^{-1/(1-q)}} \tag{2.97}$$

The exponent q is a factor that controls the degree of "fuzziness," with $q=2$ being the most common value. This type of classification is called a *soft* classification (or segmentation) because

the output classes take values in the range of [0 1] rather than being binary masks (as in KM). However, the soft classification can always be hardened via thresholding (i.e. $u_{jk} \rightarrow 1$ if $u_{jk} \geq 0.5$). Figure 2.21 shows an example of a FCM classification (both soft and hard) compared to a hard histogram-based classification performed using the T_1 map and histograms. The FCM classification was achieved via a MATLAB implementation of the bias-field corrected FCM (BCFCM) algorithm proposed by Ahmed et al. [68].The input parameters of the FCM classification were $\alpha/\sigma/\varepsilon/q$ = 0.5/0.5/0.001/2, with the input class means indicated by dotted lines in the histogram of Figure 2.21.

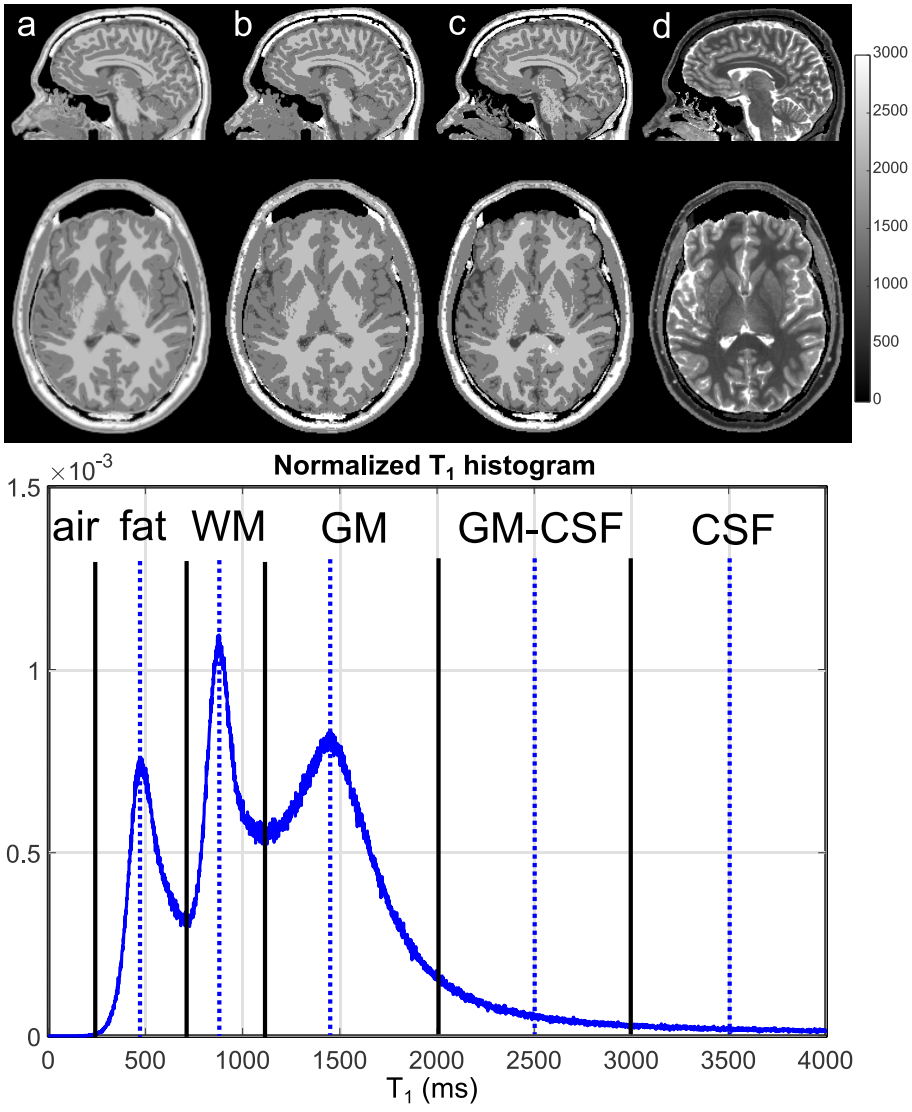

Figure 2.21: An example of a (a) soft FCM classification, a (b) hard FCM classification, a (c) hard via histogram-based classification (d) the original T_1 map. The normalized T_1 histogram with class means/thresholds are shown in blue/black respectively.

Chapter 3: SNR Efficiency of Combined Bipolar Gradient Echoes: Comparison of 3D FLASH, MPRAGE, and Multi-Parameter Mapping with VFA-FLASH and MP2RAGE[8]

"An Experiment, like every other event which takes place, is a natural phenomenon; but in a Scientific Experiment the circumstances are so arranged that the relations between a particular set of phenomena may be studied to the best advantage."

— James Clerk Maxwell,

"General Considerations Concerning Scientific Apparatus", 1876. In W.D. Niven (ed.),

The scientific Papers of James Clerk Maxwell (1890), Vol. 2, 505.

[8] A version of this chapter has been published in Magnetic Resonance in Medicine (2016) (Early View). DOI 10.1002/mrm.26306 [152]

3.1 Introduction

In recent years, bipolar multi-echo gradient echo pulse sequences have become increasingly popular for 3D structural brain imaging. The main benefits of these sequences include increased SNR and reduced susceptibility-induced geometrical distortions and water-fat shifts [69], both of which become more problematic at high fields. Mitigating these off-resonance effects is of interest in the field of Radiation Treatment Planning (RTP), where geometrical distortions can lead to errors in dose delivery [70], [4]. With current gradient performance, and the implementation of regularized parallel imaging [54], it becomes possible to execute pulse sequences such as the Fast-Low-Angle-Shot (FLASH) [71] and the Magnetization-Prepared RApid Gradient Echo (MPRAGE) [39] with high-bandwidth multi-echo trains, while maintaining equal or better SNR efficiency (defined as SNR per square-root of the total scan duration) than the traditional single-echo, low-bandwidth counterparts.

The additional information provided by the multiple echoes can be used to improve the accuracy of image segmentation algorithms [72]. For example, Fischl et al [72] have found that a multi-echo FLASH sequence out-performs a conventional single-echo MPRAGE when applied to sub-cortical brain segmentation. Van Der Kouwe et al optimized a multi-echo MPRAGE sequence and compared it to a conventional single-echo MPRAGE in a segmentation study [73], concluding that multi-echo provides considerable benefits, (such as reduced brain volume changes across different scanners) with few drawbacks.

Another common application of bipolar multi-echo sequences is multi-parameter mapping (MPM, i.e., mapping the proton-density PD, T_1 and T_2^* relaxation) using the variable flip angle (VFA) technique [74], [75], [76]. Weiskopf et al have made use of such sequences to map PD^*, T_1, T_2^* and magnetization transfer (MT) within a reasonable scan time <18 min (3 sequences each lasting 6 minutes) at 3T [11]. These quantitative parameters can then be re-combined to create synthetic images containing FLASH, MPRAGE or other arbitrary types of contrast [77], [9].

The recent "MP2RAGE" variant of the traditional MPRAGE has been proposed for structural brain imaging [44]. Its two acquisition blocks follow a shared inversion-recovery module, leading to a T_1-weighted image, and a PD-weighted image. The two complex image signals are combined analytically to obtain a real image that is both purely T_1-weighted and bias-field

corrected (fully corrected for the receive B_1 and to a first order for the transmit B_1). A T_1 map can be calculated via a look-up table and if multiple echoes are acquired, T_2^* and PD mapping are also possible. An MPM pipeline with MP2RAGE was also recently proposed to map T_1, T_2^* and quantitative susceptibility (QSM) using unipolar echoes [78].

To our knowledge, comparisons of the SNR efficiency of MP2RAGE versus the VFA technique, or of conventional single-echo vs. bipolar multi-echo MPRAGE or FLASH sequences have yet to be reported. Furthermore, the literature lacks a consensus on how multiple bipolar echoes should be combined to maximize SNR or CNR (i.e., averaging the echoes [69], a root-sum-of-squares combination [73], or a weighted linear combination [73]). Therefore, we begin our analysis by showing that the root-sum-of-squares (RSS) is optimal for combining magnitude images at different echo times (multi-echo recombined gradient echo, known in the industry as MERGE, MEDIC or mFFE), and calculate the consequent SNR gains. We then optimize and test 3D MPRAGE, MP2RAGE and FLASH sequences with high bandwidths and multiple bipolar echoes to yield superior SNR efficiency than their single-echo, low-bandwidth counterparts (each with identical scan times under 9 min). We also propose and test two MPM pipelines: one based on a multi-echo (bipolar) MP2RAGE and the second based on the VFA technique with multi-echo (bipolar) FLASH (abbreviated "VFA-FLASH"). For FLASH and MPRAGE, the measured SNR gains are compared to the theoretical predictions, while for the quantitative MPM pipelines (with MP2RAGE and VFA-FLASH) their SNR efficiency (in PD, T_1 and T_2^* maps) is compared. Both MPM pipelines are also tested in vivo on four volunteers.

3.2 Theory

3.2.1 SNR of Single-Echo Spoiled Gradient-Echo

The SNR in standard expressions is proportional to the square-root of the total acquisition time, or inversely proportional to the square-root of the readout bandwidth [79], assuming T_2^* decay is negligible within the acquisition window, T_{acq}. Without this assumption, different expressions have been reported in the literature. Vinitski et al [80] derived an expression relating SNR of a spin-echo sequence to T_2, T_2^*, T_{acq} and TE, which may be modified for a spoiled gradient-echo pulse sequence by replacing T_2 with T_2^* in the TE exponential term to yield,

$$SNR \propto \frac{2T_2^*\left(1 - e^{-T_{acq}/2T_2^*}\right)e^{-TE/T_2^*}}{\sqrt{T_{acq}}} \tag{3.1}$$

where TE is the echo time. When $T_2^* >> T_{acq}$, we can approximate the exponential terms as $e^{-T_{acq}/2T_2^*} \approx 1 - T_{acq}/(2T_2^*)$, and $e^{-TE/T_2^*} \approx 1$, such that $SNR \propto \sqrt{T_{acq}}$ as expected. Fleysher et al [81] state that $SNR \propto \sqrt{T_{acq}}e^{-T_{acq}/2T_2^*}$, which may be reconciled with Eq. (3.1) by making the first assumption above as well as $TE \approx T_{acq}/2$. Finally, Rahmer et al [82] state that $SNR \propto P_{tot}(0)\sqrt{T_{acq}}$ where $P_{tot}(0)$ is the total point-spread function (PSF) evaluated at the center a voxel, and the SNR for full-echo Cartesian sampling becomes $SNR \propto (1 - e^{-T_{acq}/T_2^*})/\sqrt{T_{acq}/T_2^*}$ for a point-like object. The optimal acquisition window for these three expressions ranges between $T_{acq}=0.6795\ T_2^*$ (Vinitski), $T_{acq}=T_2^*$ (Fleysher) and $T_{acq}=1.2564\ T_2^*$ (Rahmer). In this work we use Fleysher's expression since it is simpler and better matches phantom measurements.

3.2.2 SNR of Multi-Echo Spoiled Gradient-Echo

When images resulting from multiple echoes of the same bandwidth are acquired within a FLASH (a.k.a. SPGR, T_1FFE, GRE) sequence, Eq. (3.1) applies to each echo (if SNR is high enough so that the noise assumes a Gaussian distribution [83]). As shown in Appendix A, assuming a mono-exponential T_2^* decay the SNR gain (relative to the first echo) obtained through the RSS combination is

$$G_{SNR} = \frac{\sqrt{\sum_{n=1}^{N} e^{-2TE_n/T_2^*}}}{e^{-TE_1/T_2^*}} \tag{3.2}$$

where N is the total number of sampled echoes. In Appendix A it is also shown that the RSS combination provides the highest possible SNR gain, outperforming averaging [69]. This is not the case for multi-echo MP2RAGE (Appendix B) where, instead, a real MP2RAGE image must be calculated first for each echo, and all are then combined using a weighted average ($MP2RAGE_{wav}$).

Multiplying Eq. (3.1) by the SNR gain of Eq. (3.2) yields the SNR in the MERGE combination image,

$$SNR_{ME} \propto \frac{2T_2^*}{\sqrt{T_{acq}}}\left(1 - e^{-\frac{T_{acq}}{2T_2^*}}\right)\sqrt{\sum_{n=1}^{N} e^{-2TE_n/T_2^*}} \quad \text{(Vinitski)}$$
$$SNR_{ME} \propto \sqrt{T_{acq}}\sqrt{\sum_{n=1}^{N} e^{-2TE_n/T_2^*}} \quad \text{(Fleysher)} \tag{3.3}$$

Deriving an expression for the SNR as a function of the acquisition time requires knowledge of the limitations of scanner hardware, such as the amount of dead-time, Δ, required for the RF pulse excitation, the durations of the phase-encoding step and gradient ramp prior to the first echo, as well as the time, τ, required for the gradients to ramp up and down between successive acquisition windows. Our Philips 3T Achieva scanner uses a maximum gradient strength of ~21 mT/m and a slew rate of ~100 T/(s m). The minimum echo time can be written as $TE_{min}=\Delta+T_{acq}/2$, where $\Delta\approx1.3$ ms using a 2-lobe sinc RF excitation pulse. The nth echo time can be expressed as $TE_n=TE_{min}+(n-1)(T_{acq}+\tau)$, where $\tau\approx0.4$ ms is also essentially independent of T_{acq}. Setting $TR >> T_2^*$ (e.g., $TR >$ 200 ms) allows the acquisition of a large number of echoes and nearly full T_2^* decay before the following excitation pulse. As $N\rightarrow\infty$ Eq. (3.3) rapidly converges to (see Appendix C)

$$SNR_{ME} \propto \frac{2T_2^*}{\sqrt{T_{acq}}}\left(1 - e^{-\frac{T_{acq}}{2T_2^*}}\right)\sqrt{\frac{e^{-2\Delta/T_2^*}e^{-T_{acq}/T_2^*}}{1-e^{-2(T_{acq}+\tau)/T_2^*}}} \quad \text{(Vinitski)}$$
$$SNR_{ME} \propto \sqrt{T_{acq}}\sqrt{\frac{e^{-2\Delta/T_2^*}e^{-T_{acq}/T_2^*}}{1-e^{-2(T_{acq}+\tau)/T_2^*}}} \quad \text{(Fleysher)} \tag{3.4}$$

At sufficiently long acquisition times the SNRs of MERGE (Eq. (3.4)) and single-echo FLASH (Eq. (3.1)) with the same TR and flip angle converge as shown in Figure 3.1(a) for various values of T_2^*. In MERGE, (assuming a sufficient number of echoes for the SNR to converge), the SNR reaches a maximum theoretical value (calculated from the first derivative of Eq. (3.4)), at an optimal T_{acq} which also depends on the T_2^*, but, as illustrated in Figure 3.1(a), is significantly shorter than that of a single echo, especially for longer T_2^* values. This permits significant SNR gains while using short acquisition windows to minimize image distortions induced by B_0 inhomogeneity and other off-resonance effects.

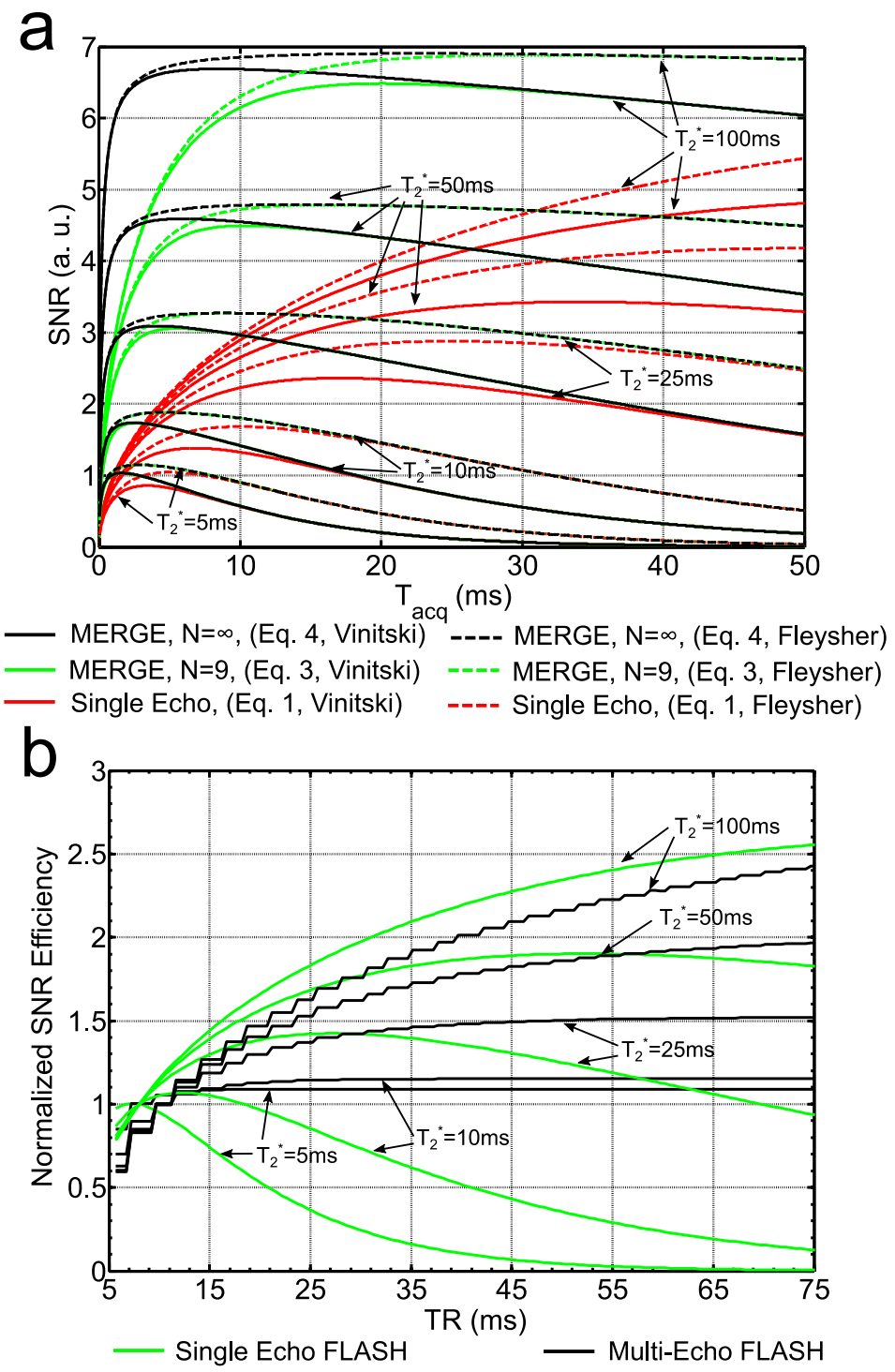

Figure 3.1: (a) Relative SNR as a function of the acquisition time, T_{acq}, for a single echo (Eq. (3.1), red curves) and SNR for a Multi-Echo Recombined Gradient Echo image (MERGE, Eq. (3.4)) with 9 echoes (Eq. (3.3), green curves) and an infinite number of echoes (black curves) at T_2^*= (100, 50, 25, 10 and 5 ms), with dead times Δ=1.3 ms, and τ=0.4 ms. Both Vinitski's and Fleysher's expressions are plotted for comparison. (b) SNR efficiency ($\propto SNR/\sqrt{TR}$) as a function of TR for a bipolar multi-echo FLASH

sequence (black) and single-echo FLASH (green) normalized to that of a typical single-echo FLASH with TR=8 ms, T_{acq}=5.7 ms (as long as possible), and T_1=1200 ms. The bipolar echo sequence has a fixed T_{acq}=1.93 ms, and enough echoes to fill the TR. Flip angles are equal to the Ernst angle. Dead times are the same as in (a), with an additional spoiler gradient duration of 1 ms.

3.2.3 Comparison to Signal Averaging and TR increases in FLASH

The signal in an ideally-spoiled gradient echo (SPGR) or FLASH is given by [29], p. 587

$$S(TR, TE, \alpha) \propto PD \frac{(1 - E_1)\sin\alpha}{1 - E_1\cos\alpha} e^{-TE/T_2^*} \tag{3.5}$$

where α is the flip angle, $E_1 = \mathrm{e}^{-TR/T_1}$ and PD is the proton density. This proportionality also holds for the n^{th} echo in MERGE by substituting TE with TE_n, and the combined MERGE signal is given by multiplying Eq. (3.5) by Eq. (3.2).

Signal averaging yields an SNR gain of $\sqrt{NEX}$ (since noise in different datasets is uncorrelated), while total scan time increases in proportion to the number of experiments or averages (NEX). Another way to increase the SNR in Eq. (3.5) is to increase the TR and readjust the flip angle so that it remains equal to the Ernst angle (or the same ratio relative to the maximum signal), for a given T_1 of interest. This yields an SNR gain $\approx \sqrt{TR_2/TR_1}$, where $TR_2 > TR_1$ assuming $TR << T_1$ (see [29], p. 691), and consequently does not confer any SNR advantage over averaging for the same total scan time. However, increasing the TR creates room for sampling more echoes, which provides an additional SNR boost through Eq. (3.2).

Using Fleysher's simplification of Eq. (3.1), and accounting for the parallel imaging acceleration factor R and geometry factor g, the expected SNR in a FLASH sequence is

$$SNR_{FLASH} \propto \frac{\sqrt{T_{acq}}}{g\sqrt{R}} \cdot \frac{(1 - E_1)\sin\alpha}{1 - E_1\cos\alpha} D(TE; T_2^*), \qquad D = \begin{cases} e^{-TE/T_2^*}, & \mathrm{N} = 1 \\ \sqrt{\sum_{n=1}^{N} e^{-2TE_n/T_2^*}}, & \mathrm{N} > 1 \end{cases} \tag{3.6}$$

In Figure 3.1(b), Eq. (3.6) was used to plot the SNR efficiency vs TR for a multi-echo bipolar FLASH compared to a typical single-echo FLASH (assuming R=1, g=1). While a single-echo FLASH with T_{acq}>6 ms would suffer from unacceptable geometrical distortions, the multi-echo FLASH (with MERGE/RSS combination) conserves SNR at short T_2^*, and predicts a ~1.6-fold

SNR gain in GM/WM tissues (T_1/T_2^*=1200/50 ms), at TR~30 ms. Similar analytical expressions can be written for the SNR in MPRAGE and MP2RAGE using the signal equation (S_{MPRAGE}) derived by Deichmann [43] and the two MP2RAGE signals (GRE_{TI1} and GRE_{TI2}) derived by Marques [44]:

$$SNR_{MPRAGE} \propto \frac{\sqrt{T_{acq}}}{g\sqrt{R}} S_{MPRAGE}(\alpha, TR, TI, TD, TR_{MP}) D(TE; T_2^*) \tag{3.7}$$

$$SNR_{MP2RAGE} \propto \frac{\sqrt{T_{acq}}}{g\sqrt{R}} \cdot \frac{\Re\left[GRE_{TI_1}^* GRE_{TI_2}\right]}{\left|GRE_{TI_1}\right|^2 + \left|GRE_{TI_2}\right|^2} D(TE; T_2^*) \Big/ \sqrt{\frac{\left(\left|GRE_{TI_1}\right|^2 - \left|GRE_{TI_2}\right|^2\right)^2}{\left(\left|GRE_{TI_1}\right|^2 + \left|GRE_{TI_2}\right|^2\right)^3}} \tag{3.8}$$

Here, $GRE_{TI} = GRE_{TI}(\alpha, TR, TFE, TA, TB, TC, TR_{MP})$, where TI is the inversion time, TR_{MP} is the shot duration, TD is the recovery (a.k.a. delay) time, and TFE is the turbo field echo factor (i.e., number of excitations per acquisition block, denoted n by Marques). TA, TB and TC are, respectively, delay times before, between and after the two acquisition blocks in MP2RAGE as defined in Ref. [44]. For a derivation of Eq. (3.8), see Appendix B and recall that in this case the optimal combination of echoes is not the RSS.

Note that the combined real MP2RAGE image is constrained within the bounds [-0.5, 0.5] (see Ref. [44] and Appendix B). Because of this scaling, SNR measurements on this image are not readily comparable to those of standard images. To compare the SNR efficiency of MP2RAGE with VFA-FLASH, it is therefore appropriate to first convert the normalized image to a T_1 map, and then compare the T_1-to-noise ratio (T_1NR), of each technique (defined as T_1 divided by its standard deviation σ_{T1}). If the look-up table is sufficiently sampled, we can assume $\sigma_{MP2RAGE} \propto \sigma_{T_1}$, and calculate a theoretical SNR gain (between two different MP2RAGE protocols) from the ratio of their $\sigma_{MP2RAGE}$. The theoretical SNR gain can then be compared to the SNR gain measured from the T_1 maps by using Eqs. (B3.3) and (B3.6).

3.2.4 Multi-Parameter Mapping with VFA-FLASH

In the VFA technique, a linearized version of Eq. (3.5) is used to solve for T_1 and PD using two optimized flip angles while keeping all other scan parameters identical [74],[84],[85],[86],[87]. The two flip angles α_1 and α_2 may be chosen to maximize the accuracy and T_1NR for a T_1 value

of interest from a simple analytical expression (see Eq. 11 in Ref. [88], or [89]). Alternatively, the flip angles can be chosen to maximize the SNR of the proton-density map *PD* [90].

To curve-fit the FLASH datasets, a procedure similar to that of Yarnykh [63] and Deoni [88] for single-echo FLASH images is used to obtain the linearized equation

$$\frac{S_{ME}}{\sin(c_{RF}^{+}\alpha_{nom})} = E_1 \frac{S_{ME}}{\tan(c_{RF}^{+}\alpha_{nom})} + c_{RF}^{-} PD(1-E_1)\sqrt{\sum_{n=1}^{N} e^{-2\,TE_n/T_2^*}}, \quad S_{ME} = \sqrt{\sum_{n=1}^{N} S_n^2} \qquad (3.9)$$

where c_{RF}^{+} is a correction factor for flip-angle inhomogeneity (B_1^{+}) given by the ratio of the actual to the nominal flip angle (i.e., α/α_{nom}) [63], c_{RF}^{-} is the correction factor for the receive sensitivity profile (B_1^{-}), and S_{ME} is the MERGE image. Equation (3.9) is a linear equation ($y=m\,x+b$) with slope E_1 and intercept given by the last term, from which T_1 and *PD*, respectively, are obtained. Note how the MERGE combination changes the y-intercept, replacing the usual exp(–*TE*/T_2^*) decay term with the new SNR gain of Eq. (3.2). Appendix D shows that this SNR gain will propagate into the final T_1 and *PD* maps, thus making the best use of available information to maximize the final T_1NR and PDNR (defined similarly to T_1NR above). Curve fitting the *N* echoes by ordinary least squares yields T_2^*, as implemented in the MPM pipeline of Weiskopf et al [11].

At lower field strengths (≤1.5 T), the B_1 inhomogeneity is often ignored and it is assumed that $c_{RF}^{+} \approx c_{RF}^{-} = c_{RF}$, provided that an optimal-SNR channel combination with uniform sensitivity is performed [91]. If T_1 and *PD* are calculated without correcting for the flip-angle non-uniformities and receiver bias, *apparent* T_1 and *PD* will result [90]

$$T_1^{app} \approx (c_{RF}^{+})^2 T_1, \qquad PD^{app} \approx c_{RF}^{+} c_{RF}^{-} PD \qquad (3.10\ a, b)$$

Two bias fields denoted by

$$\Psi_{T1} \propto (c_{RF}^{+})^2, \qquad \Psi_{PD} \propto c_{RF}^{+} c_{RF}^{-} \qquad (3.11\ a, b)$$

can be fitted from the T_1^{app} and PD^{app} map, respectively, by employing a bias field correction algorithm, followed by a calibration step [92], [93]. A scanner-dependent calibration factor $<c_{RF}>$, defined as the mean flip angle, $<\alpha_{meas}>$, measured over the brain (using a skull-stripped binary mask), divided by the nominal flip angle (α_{nom}, set on the console) is also needed to

convert the bias field into a B_1 map. (Weiskopf et al found that the assumption $<c_{RF}>=1$ holds well for a Siemens TIM Trio [92], while for our scanner we found $<c_{RF}>\approx 0.97$). This approach has the significant advantage of not requiring the acquisition of a separate B_1 map (and the associated increase in total scan time), hence maintaining the best theoretical SNR efficiency. Similarly to [92] [93], our post-processing pipeline includes a bias-field correction algorithm, N4ITK [64], which is more widely applicable because it does not rely on a human brain atlas like SPM8 used in the above references.

Since the T_2^* map tends to be noisy due to the uncertainty in curve-fitting, and the last factor of the intercept must be divided out to obtain *PD*, the T_2^* map should be filtered or de-noised (with edge-preserving techniques such as a median filter [57], p.10, or gradient anisotropic diffusion de-noising [67]) prior to solving for *PD*. Moreover, since one T_2^* map is obtained at each flip angle, the weighted average T_2^* may be calculated to improve its SNR using weights proportional to the inverse of the noise variance (see Appendix E).

$$T^*_{2,final} = \frac{w_1 T^*_2(\alpha_1) + w_2 T^*_2(\alpha_2)}{w_1 + w_2}, \qquad w_i = \frac{\sin^2 \alpha_i}{(1 - E_1 \cos \alpha_i)^2} \tag{3.12}$$

If motion is not negligible, an advanced combination procedure for the T_2^* maps has been recently proposed to minimize the resulting artifacts [94]. A summary of the post-processing steps involved in the calculation of T_1, *PD* and T_2^* is given in Figure 3.3(a).

3.2.5 Multi-Parameter Mapping with MP2RAGE

A multi-echo MP2RAGE provides two T_2^* maps: one via least-squares fitting of the $|GRE_{TI1}(TE_n)|$ images, and the second using the $|GRE_{TI2}(TE_n)|$ images. However, the presence of a null point in the $|GRE_{TI1}(TE_n)|$ images leads to very poor T_2^*NR, and in practice only the other set results in a useable T_2^* map.

The T_1 map is calculated via a 1D look-up table of the real MP2RAGE signal [44], because an explicit expression for T_1 as a function of signal and scan parameters does not exist. However, the table is not bijective for very long T_1 (the MP2RAGE signal as a function of T_1 attains a minimum at $T_{1max}\approx 2700$), and consequently the T_1 of CSF will be aliased to lower values (e.g. 2500 ms instead of the correct 4500 ms).

Once both T_2^* and T_1 are known, two different *PD* maps may be obtained in theory: one from the $GRE_{TI1}(TE_n)$ images (PD_1), and the second from the $GRE_{TI2}(TE_n)$ images (PD_2). It makes sense to first combine the multiple echoes at TI_1 or TI_2 in RSS, to yield MERGE combinations ME_{TI1} and ME_{TI2} with higher SNR. Two issues must be resolved: the PDNR in PD_1 will be very poor close to the signal null, and secondly, T_1 aliasing in CSF will bias the measured *PD*. It is reasonable to think that a weighted average combination of the two *PD* maps could improve the PDNR and mitigate the effects of the null point on PD_1. Similarly to the weighted average of the two T_2^* maps in Eq. (3.12), the best PDNR would be achieved with weights equal to the square of each corresponding signal yield (calculated from the known T_1 and assuming PD=1, $c_{RF}^{+}=c_{RF}^{-}$=1). Therefore $PD_{wav}= (w_1 PD_1+ w_2 PD_2)/(w_1+w_2)$, where $w_i=GRE_{TIi}(T_1; \alpha_i, TR, TFE, TA, TB, TC, TR_{MP})^2$. However, as verified experimentally in Figure 3.2 below, the resulting PDNR of this combination yields $PDNR(PD_{wav}) \approx PDNR(PD_2)$, regardless of the T_1. This puzzling result is counter-intuitive because if the noise in PD_1 and PD_2 were uncorrelated and $w_1=w_2$=0.5, we would expect $PDNR(PD_{wav}) \approx \sqrt{2}\ PDNR(PD_2)$. However, because T_1 is derived from both GRE_{TI1} and GRE_{TI2}, its noise (σ_{T1}) is correlated to that from both inversion times, which leads to a noise correlation between PD_1 and PD_2 (since T_1 is used to solve for both PD_1 and PD_2). Therefore, there is no practical advantage in performing a weighted average *PD* combination to obtain PD_{wav} as opposed to just using PD_2. Moreover, the PD_{wav}, PD_1, or PD_2 in CSF will still be biased to PD_{wav}<100%, PD_1^{CSF}>100% or PD_2^{CSF}<100%, since the overestimation in PD_1 and the underestimation in PD_2 do not cancel out perfectly. Therefore we choose a threshold $T_1^{ref}< T_{1max}$, and set $PD=PD_2$ if $T_1 \leq T_1^{ref}$ and $PD=PD_1$ if $T_1>T_1^{ref}$, accepting that in CSF an overestimated *PD* is preferable over an underestimated *PD*, because it prevents CSF from being confounded with surrounding tissues.

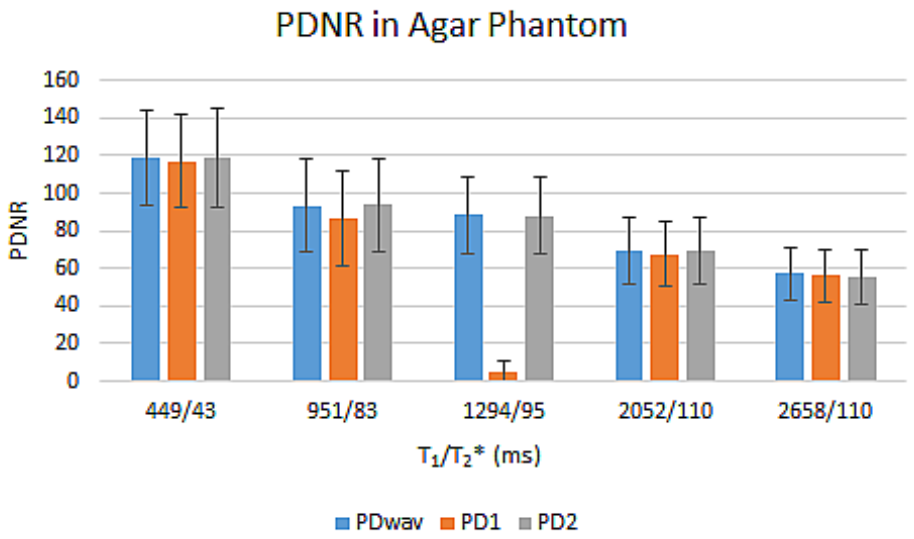

Figure 3.2: Measured PDNR in the multi-layered agar phantom for PD_1, PD_2 and PD_{wav}. The error bars correspond to the standard deviation of the 5 SNR measurements (ROIs) in each layer. As expected, the null point in PD_1 yields PDNR≈0 (middle layer, orange bar). ROI locations are the same as those in Figure 3.6 below.

In summary, using the equations derived by Marques et al [44], the final expression for the proton density is then:

$$PD = \begin{cases} \dfrac{ME_{TI_1}}{c_{RF}^{-}\sin(c_{RF}^{+}\alpha_1)\sqrt{\sum_{n=1}^{N} e^{-2TE_n/T_2^*}}}\left[\dfrac{-\epsilon_{inv}\, m_{ss}\, EA + (1-EA)}{(\cos(c_{RF}^{+}\alpha_1)E_1)^{1-TFE/2}} + (1-E_1)\dfrac{1-(\cos(c_{RF}^{+}\alpha_1)E_1)^{TFE/2-1}}{1-\cos(c_{RF}^{+}\alpha_1)E_1}\right]^{-1}, & T_1 > T_1^{ref} \\ \dfrac{ME_{TI_2}}{c_{RF}^{-}\sin(c_{RF}^{+}\alpha_2)\sqrt{\sum_{n=1}^{N} e^{-2TE_n/T_2^*}}}\left[\dfrac{m_{ss}-(1-EC)}{EC\ (\cos(c_{RF}^{+}\alpha_2)E_1)^{TFE/2}} - (1-E_1)\dfrac{(\cos(c_{RF}^{+}\alpha_2)E_1)^{-TFE/2}-1}{1-\cos(c_{RF}^{+}\alpha_2)E_1}\right]^{-1}, & T_1 \le T_1^{ref} \end{cases} \quad (3.13)$$

where $m_{ss}=m_{z,ss}/PD$ is the normalized steady-state longitudinal magnetization derived in Ref. [44], ε_{inv} is the inversion efficiency, $EA=exp(-TA/T_1)$ and $EC=exp(-TC/T_1)$. We chose T_1^{ref}=2000 ms, and employed N4ITK to estimate the bias field on the PD^{app} image and remove the c_{RF}^{+} and c_{RF}^{-} inhomogeneity. As in the case of the MPM pipeline with VFA-FLASH, the T_2^* map must be filtered to prevent adding noise to the PD map. The post-processing steps for MPM with MP2RAGE are shown in Figure 3.3(b).

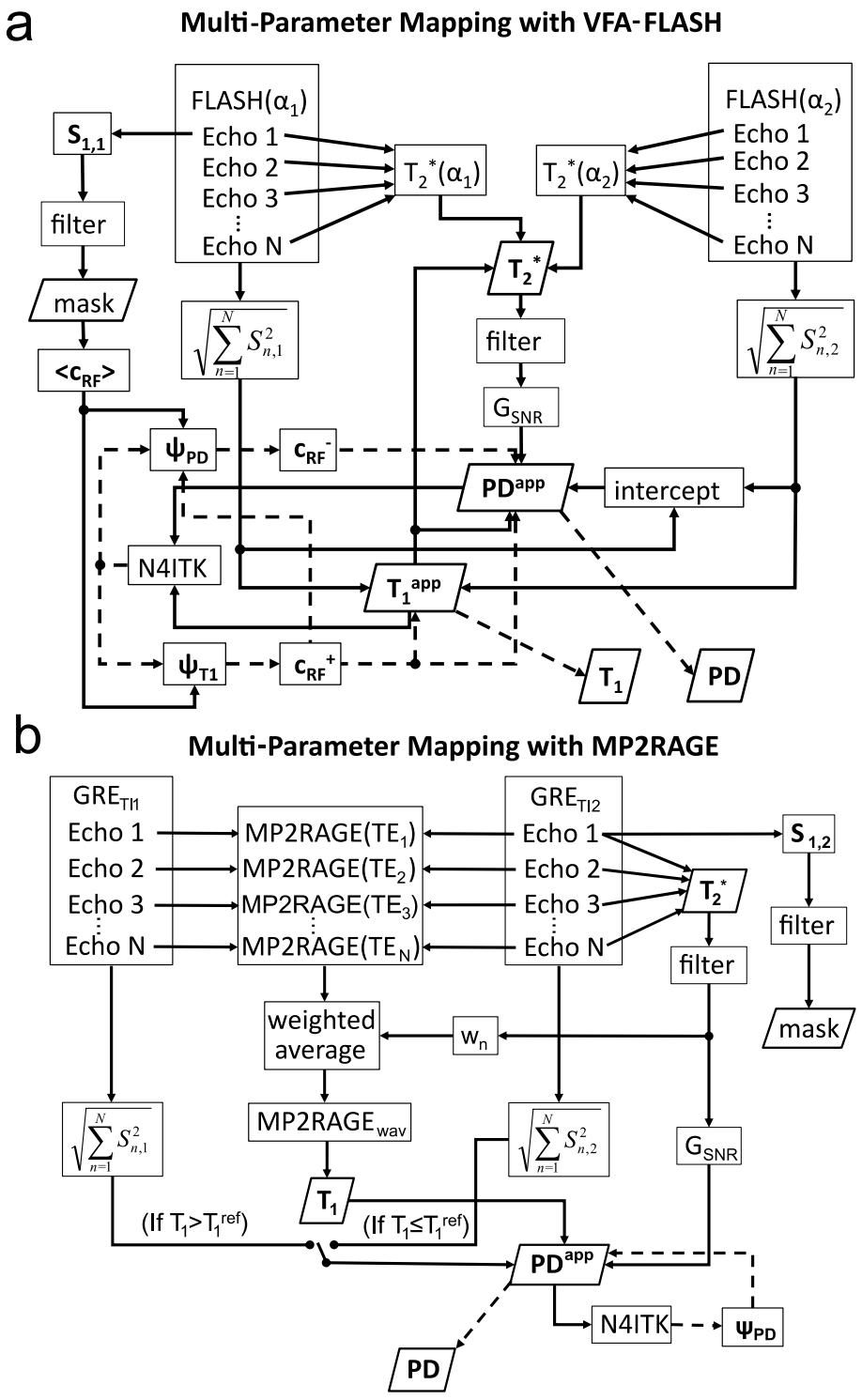

Figure 3.3: Multi-parameter mapping pipeline for (a) VFA-FLASH and (b) MP2RAGE. Note that the mean flip angle over the brain (excluding air cavities), $<c_{RF}>$, is needed to convert the bias field Ψ_{T1} into the correct c_{RF}^{+} map. The post-processing steps after N4ITK are shown as dashed arrows for clarity. See the Methods section for further details.

3.3 Methods

3.3.1 SNR Measurements Using 2D MERGE in Beakers with a Range of T_2^*

To verify Eqs. (3.1)–(3.4), SNR measurements were performed on four uniformly-filled beakers containing deionized water, 30 g/L porcine skin gelatin (300 bloom) doped with 0.5 g/L NaN_3 (to prevent bacterial growth or molding) and four different concentrations of $MnCl_2$ (100, 200, 400, and 800 μM), which decreases both the T_1 and T_2^* significantly. The beakers were scanned in a Philips 3T Achieva using a single-slice multi-echo FLASH sequence with $\Delta \approx 1.3$ ms, $\tau \approx 0.4$ ms, TR=200 ms, and flip angle α=50°, all kept constant, but varying T_{acq} from 1.12–25 ms to isolate the effect of T_2^* on the final SNR of different MERGE images (containing between 1 and 32 echoes). The number of acquired echoes was the maximum that fit within TR for each given T_{acq}.

These SNR measurements were performed with an 8-channel head array coil used in quadrature (single-channel) mode, to eliminate the effect of noise bias on T_2^* [95]. Three image dynamics (the last dynamic being a noise scan without RF pulses) were acquired to enable different SNR calculation techniques: the image-subtraction method (from the first and second dynamic) and the noise-scan method (from the first and third dynamic), as prescribed in NEMA Standard MS1-2008 [96], and the iterative method of Preibisch and Deichmann (called here "*ROI-FFT method*") based on a single acquisition [85].

3.3.2 Optimization of MPRAGE, FLASH, MP2RAGE and VFA-FLASH

All 3D MRI protocols were optimized based on a total scan time constraint of ~8:30 min, except for the single-echo and 8-echo FLASH sequences, as shown in Table 3.1. In all cases, the field-of-view (FOV) was 240×240×170 mm^3, with 1 mm isotropic resolution and non-selective RF pulses. The bandwidth of the single-echo protocols was chosen (175 or 180 Hz/pix depending on system timing constraints) based on the maximum geometrical distortion and water-fat shifts considered tolerable for RTP at 3T [6]. (Howarth et al recommend a bandwidth ≥100 Hz/pix in structural brain imaging at 1.5T [97]). Except for the single-echo MP2RAGE, all echo times were selected to have water in-phase with fat (TE=n×2.3 ms), and for the multi-echo bipolar sequences, the bandwidths (517 or 540 Hz/pix, respectively) were adjusted to maximize the sampling efficiency (ε, defined as total sampling time divided by total scan time) within the limits of the system's gradient performance.

Both the single-echo and the 6-echo MPRAGE (denoted as MPR1 and MPR6) were optimized to yield a similar contrast and signal evolution (for best gray- and white-matter CNR) by performing simulations based on the recursive solution of the Bloch equations as done in Ref. [40]. For MP2RAGE, the protocol optimized by Marques et al (protocol #1 in Table 1 of Ref. [44]) was taken as a starting point. Using similar Bloch equation simulations TR_{MP}, TFE, TI_1 and TI_2 were re-optimized so that the resulting multi-echo protocol (MP2R6) would suffer minimal off-resonance effects, have high SNR efficiency and enable T_2^* and PD mapping, without exceeding the maximum amount of SENSE acceleration (2.5 × 2 = 5-fold) possible with the 8-channel head array. A phantom T_1NR comparison of the MP2R1 protocol (listed in Table 3.1) with the 5 protocols of Marques et al [44] is provided in Figure 3.4.

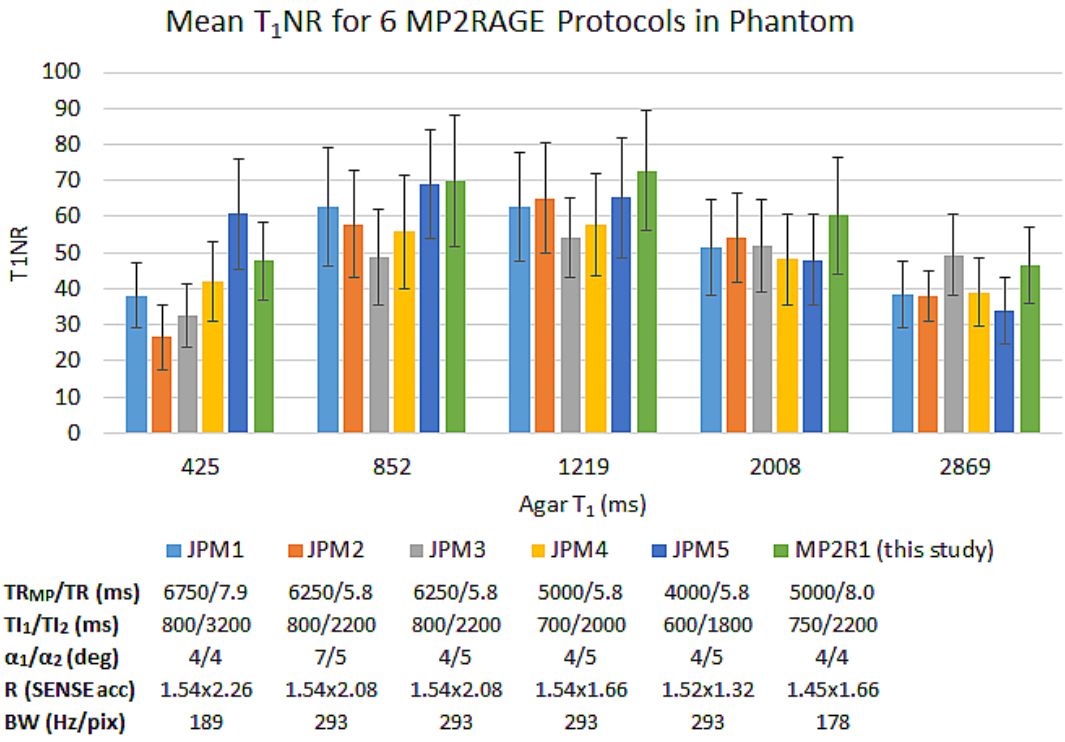

	JPM1	JPM2	JPM3	JPM4	JPM5	MP2R1 (this study)
TR_{MP}/TR (ms)	6750/7.9	6250/5.8	6250/5.8	5000/5.8	4000/5.8	5000/8.0
TI_1/TI_2 (ms)	800/3200	800/2200	800/2200	700/2000	600/1800	750/2200
α_1/α_2 (deg)	4/4	7/5	4/5	4/5	4/5	4/4
R (SENSE acc)	1.54x2.26	1.54x2.08	1.54x2.08	1.54x1.66	1.52x1.32	1.45x1.66
BW (Hz/pix)	189	293	293	293	293	178

Figure 3.4: Mean T_1NR (average of 5 ROIs per layer) in 5 different agar T_1 layers at 3T for the five MP2RAGE protocols proposed by J.P. Marques et al (for a 3T scanner), compared to the MP2R1 protocol re-optimized in this study (identical scan time of 8:30 min per protocol). The MP2R1 protocol of this study slightly outperforms those proposed by Marques et al, most probably because of its lower bandwidth of ~180 Hz/pix. The acquisition bandwidth of all protocols was chosen as low as possible on our scanner. N.B.: Phantom T_1 values are different from Figure 3.7 because the MP2RAGE measurements were performed several weeks earlier.

For VFA-FLASH, four different protocols were tested with varying number of echoes *N*, and SENSE acceleration factors (~1.44-fold, 2-fold, 3-fold and 4-fold) to assess their effects on the quality (and SNR) of the quantitative maps. The nominal flip angles were selected to maximize the T_1NR at a reference T_1 of ~1200 ms (between GM and WM at 3T), using an analytical expression (Eq. 11 in Ref. [88], or [89]), while for the conventional FLASH protocols (FLASH1 and FLASH8), the higher flip angle (α2) multiplied by a factor of ~1.2 was used to yield good T1-weighting and SNR. An elliptical phase-encoding k-space shutter was employed in all FLASH sequences to help reduce the total scan time.

Protocol Name	α_1/α_2 (°)	*N*	$TE_1/\Delta TE/TR/TI_1/TI_2$ (ms)	BW (Hz/ pix)	SENSE factor AP × RL	*TFE* / TR_{MP} (ms)	Scan dur. (min:s)	ε (%)
	MPRAGE Protocols							
MPR1	7/-	1	4.6/ - /8.8/1100/ -	175	1 × 1	240/3000	8:32	46
MPR6	9.5/-	6	2.3/2.3/16/1100/ -	517	2 × 1	123/3000	8:32	48
	FLASH Protocols							
FLASH1	22/-	1	4.6/ - /11/ - / -	175	1 × 1	-	5:56	52
FLASH8	31/-	8	2.3/2.3/22/ - / -	517	2 × 1	-	6:02	70
	MP2RAGE Protocols							
MP2R1	4/4	1	3.8/ - /8.0/750/2200	180	1.45 × 1.66	170/5000	8:40	36
MP2R6	6/6	6	2.3/2.3/16/750/2200	540	2.4 × 2	85/5000	8:40	38
	VFA-FLASH Protocols*							
VFA-FLASH1	3.5/20	1	4.6/ - /11/ - / -	175	1.2 × 1.2	-	8:46	52
VFA-FLASH6	4.5/25	6	2.3/2.3/16.5/ - / -	517	1.45 × 1.47	-	8:38	70
VFA-FLASH9	5.3/30	9	2.3/2.3/24/ - / -	517	1.75 × 1.77	-	8:33	73
VFA-FLASH12	6.0/34	12	2.3/2.3/31/ - / -	517	2 × 2	-	8:26	75

Table 3.1: MRI protocols with their relevant scan parameters optimized for a Philips 3T Achieva scanner. In all cases, the profile order was linear, non-selective RF excitation pulses were used, and the field-of-view (FOV) was 240 × 240 × 170 mm^3 with 1 mm isotropic resolution. *Note that both FLASH acquisitions (~4 min at α_1 and ~4 min at α_2) are counted as part of the total scan duration.

3.3.3 SNR, T_1, PD and T_2^* Measurements in a Multilayered Agar Phantom

A phantom consisting of 5 differentially-doped agar layers (designed to mimic fat, WM, GM, GM-CSF and CSF) was built to make T_1, T_2^* and SNR measurements with the 10 protocols

given in Table 3.1. Phantom composition was inspired from Ref. [98] (Fixed agar/NaN_3 concentrations of 10/0.5 g/L and varying $MnCl_2$ concentrations of 200, 64, 32, 10 and 0 μM, separated by cellophane wrap to avoid diffusion across the 5 layers). The T_1 of each layer was measured using a gold-standard 2D IR-EPI sequence (FOV=120×172 mm^2, axial slice, resolution: 1.3×1.3 mm^2, slice thickness: 5 mm, *TR/TE*=15000/17 ms, EPI factor=9, *TI*=25, 250, 500, 800, 1200, 1700, 2400 and 3200 ms) curve-fitted to solve for T_1 according to Eq. 1 in Ref. [99]. The T_2^* was measured in a central slice using the 2D SPGR pulse sequence (32 echoes at the shortest T_{acq}) described in the previous section.

A B_1 map was obtained using Actual Flip Angle Imaging (AFI) [63] with the following parameters: FOV=240×240×170 mm^3, 3.5×5×5 mm^3 voxels, $TR_1/TR_2/TE$ = 25/125/2.8 ms, α=60°, RF phase cycle increment ϕ=150°, *BW*=220 Hz/pixel, scan time=3 min. The AFI source images were first zero-padded to 128×128×68, c_{RF}^+ was calculated and smoothed using the *smooth3* function in MATLAB (5×5×5 3D Gaussian filter), and finally resampled to 256×256×180 pixels. The calibration constant $<c_{RF}>$ needed to correctly scale Ψ_{T1} into a c_{RF}^+ map was obtained by measuring the mean flip angle $<\alpha_{meas}>$ over the AFI B_1 map (excluding the air cavities) relative to the nominal value α_{nom} (i.e., $<c_{RF}>=<\alpha_{meas}>/\alpha_{nom}$) and found to be $<c_{RF}>$=0.84. N4ITK was unable to remove the inhomogeneity in the T_1^{app} map (since the "staircase" contrast features of the phantom were not sufficiently sparse and got confounded with the B_1 field), therefore in this case the PD^{app} was used to estimate Ψ_{T1} instead, and RF symmetry assumed (i.e., $c_{RF}^+ \approx c_{RF}^- = c_{RF,}$ and $\Psi_{T1}=\Psi_{PD,}$ which holds well because of the low conductivity of agar [100]).

The T_1 measured with VFA-FLASH (VFA-FLASH1, 6, 9 and 12) were compared to MP2RAGE (MP2R1 and 6) and 2D IR-EPI. The SNR of each layer was measured as the ratio of mean signal *S* (or the mean T_1, *PD*, T_2^*, as applicable), and noise standard deviation σ (or σ_{T1}, σ_{PD}, σ_{T2*}), in five 3D ROIs of 31×31×5 pixels (taken, respectively, at the center and at the four corners of the phantom as shown in Figure 3.6) of each agar layer using the ROI-FFT method. The standard deviation of the five SNR measurements was used as error estimate in each layer. The SNR gains from FLASH8 over FLASH1 and from MPR6 over MPR1 were measured and compared to the predicted values using Eqs. (3.6), (3.7), and (3.8), assuming an idealized average geometry factor of *g*=1 using regularized SENSE [54]. Prior to measuring SNR, the MPRAGE images were bias-

corrected approximately by dividing them by c_{RF}^2. The SNR in the parametric maps (T_1NR, T_2^*NR and PDNR) were also compared across the various MPM protocols, and T_1NR gains were compared to the theoretical predictions for MP2R6 over MP2R1 and for VFA-FLASH6, 9 and 12 over VFA-FLASH1 (using the equations in Appendix B and D).

3.3.4 In Vivo Brain Imaging on Four Volunteers

The effectiveness of MPM was assessed in vivo on four healthy male volunteers (ages: 26, 31, 41 and 43) after institutional ethics approval and informed consent were obtained. The two MP2RAGE and four VFA-FLASH protocols (total scan time of ~55 min) were tested on volunteer v1. For the remaining volunteers only MP2R1, MP2R6 and VFA-FLASH9 were tested (~29 min scan time). Slight geometrical mismatches can occur when combining even and odd echoes due to the opposite polarity of B_0-induced geometrical distortions. Helms et al recommend using a sampling bandwidth greater than 350 Hz/pixel to minimize such mismatches [69]. As a precaution, the even and odd echoes were combined separately to form "even" and "odd" MERGE (or $MP2RAGE_{wav}$ – see Appendix B and Figure 3.3) images which were then co-registered using deformable B-spline image registration in 3D Slicer (www.slicer.org) [101] prior to combining them to obtain a final MERGE (or $MP2RAGE_{wav}$) image. To compensate for possible slight head motion between the successive MERGE datasets at the two nominal flip angles, a rigid registration was also performed to ensure best possible geometrical match between the two final MERGE and T_2^* images. The windowed sinc interpolation kernel was used in every case to avoid loss of resolution or blurring in the final registered images.

Quantitative T_1, T_2^* and PD maps were calculated based on the post-processing workflow summarized in Figure 3.3. The optimal spline distance and number of iterations of the N4ITK algorithm were determined previously (by minimizing the standard deviations $std(T_1)$ and $std(PD)$ over the corrected WM/GM reference tissues, similarly to Ref. [65]), using data from 8 additional volunteers (4 males and 4 females) scanned with a protocol similar to VFA-FLASH9. To improve the accuracy of the bias field calculation, only soft tissues, (i.e., excluding air cavities and CSF from the Ψ_{T1} calculation, and also adipose from the Ψ_{PD} calculation) were included, as done in Ref. [65] with the older N3 algorithm. The mask was derived from a fuzzy c-means segmentation [68] of the T_1^{app} image in MATLAB and exported into 3D Slicer. Optimal spline distances were found to be 185 mm for Ψ_{PD}, and 210 mm for Ψ_{T1} with 400, 320, and 240

iterations (eight times the default number: 50, 40, 30). All other parameter settings were left to their default values.

The *PD* map is usually normalized with respect to CSF. However, simulation-based correction factors for non-ideal RF spoiling in CSF are then required [93], [102]; moreover, the T_2^* of CSF (needed to solve for *PD*) is usually too long to be accurately measured using a few echoes, and as mentioned previously, MP2RAGE cannot yield accurate *PD* or T_1 measurements in CSF. Therefore, we opted instead to normalize the *PD* map with respect to the mid-point between the average WM and GM peaks of the *PD* histogram (71±1% and 81±1%, respectively measured by various authors and techniques [90], [93], [103]. After multiplication by 0.76, the mid-points align correctly at $<PD>$=76%. Finally, *PD*, T_1 and T_2^* histograms (normalized to the total number of head voxels, excluding air cavities) were calculated for each volunteer (excluding the slices below the cerebellum) to provide an overall assessment of the image quality. Measurements of mean *PD*, T_1 and T_2^* were made in manually-contoured ROIs in various brain regions for comparison with previously reported literature values.

3.4 Results

3.4.1 SNR Measurements Using 2D MERGE in Beakers with a Range of T_2^*

Figure 3.5(a) displays the MERGE SNR in the $MnCl_2$-doped gelatin beakers as a function of the number of incorporated echoes. The three SNR measurement techniques (image subtraction, noise scan, and ROI-FFT) give results that agree within ~8%, except in the gelatin with long T_2^*=75.6 ms where the differences are larger. The SNR measurements were found to be less consistent at long echo times (low bandwidth) and long T_2^*, likely due to the effects of static field (B_0) inhomogeneity.

The SNR of the first point in Figure 3.5(a) (single echo, calculated using the noise scan) and T_2^* were used to extrapolate the SNR of the MERGE combinations of 2–32 echoes using Eq. (3.2) (dashed curves). Remarkably, this equation predicts the SNR behavior (within ~8%) to echo times 15 times larger than the first point, thus confirming the theory. We note that SNR convergence is achieved when $TE_{max} \geq 2 \times T_2^*$; i.e., 32 echoes at the highest bandwidth are sufficient to reach maximum SNR for the shorter T_2^* samples (10.1 and 20.9 ms).

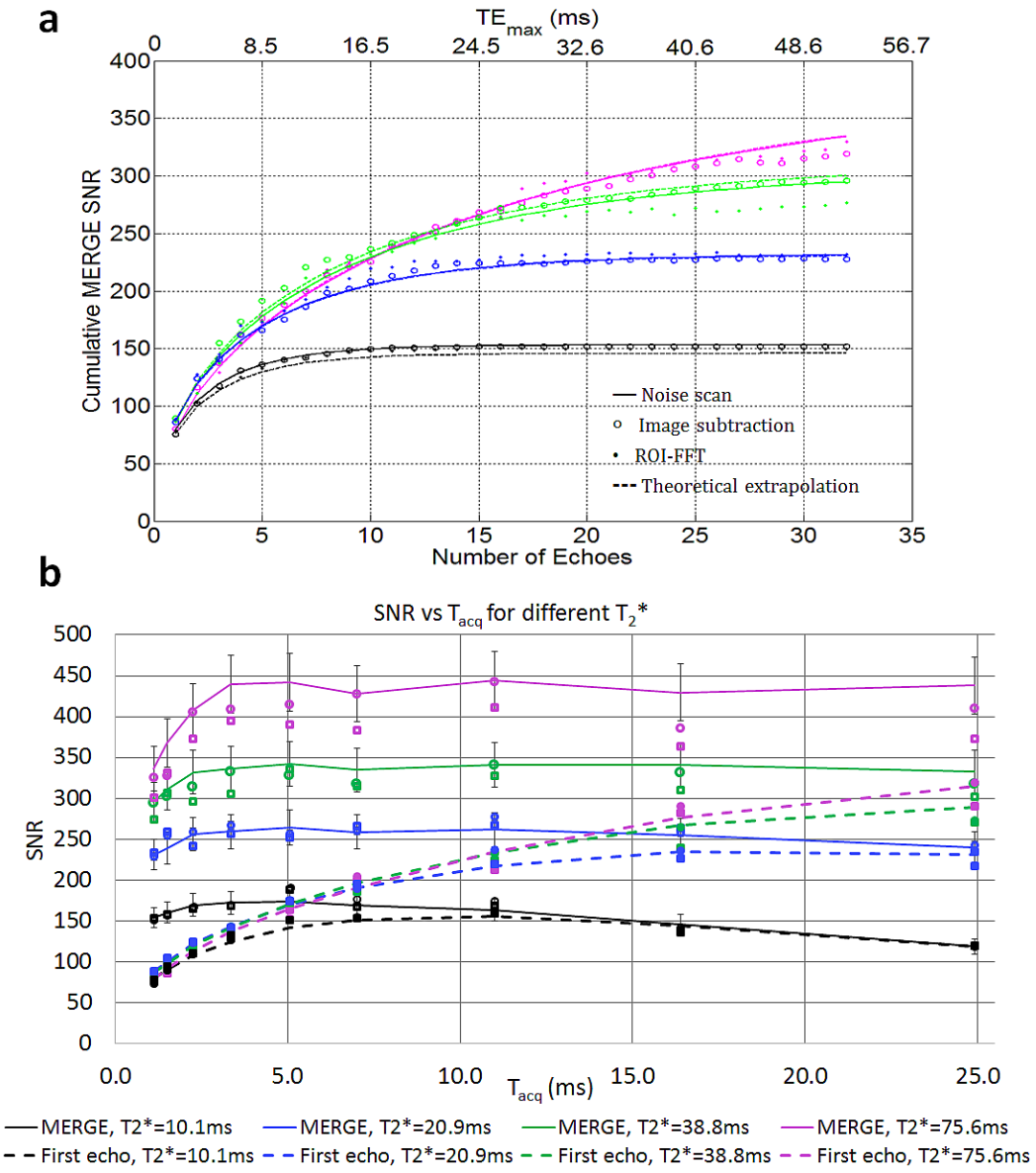

Figure 3.5: (a) SNR vs. the number of echoes (or TE_{max}) included in the MERGE combination (at the minimum T_{acq}=1.12 ms) for four different concentrations of $MnCl_2$-doped gelatin. The solid lines correspond to the SNR measured using the noise-scan method, the circles to the image-subtraction method, and the dots to the ROI-FFT method. The dashed curves are theoretical SNR extrapolations using Eq. (3.2) based on the T_2^* and the SNR of the first echo, showing excellent agreement with measurements. (b) SNR of the first echo (minimum TE) versus T_{acq} for the four different concentrations of $MnCl_2$-doped gelatin (dashed curves and filled circles/squares) and SNR of the MERGE image consisting of all 32 echoes combined (solid curves and empty circles/squares) for the same four $MnCl_2$-doped gelatin beakers.

The effect of increasing T_{acq} on SNR is illustrated in Figure 3.5(b). As expected from Eq. (3.1), the single-echo SNR approaches a $\sqrt{T_{acq}}$ dependence when T_2^* is sufficiently long, while the MERGE SNR becomes significantly less dependent on T_{acq} when all 32 echoes are included (i.e., SNR converges to its maximum value). These results agree with our theoretical predictions (**Figure 3.1**) and the optimal T_{acq} (≈11 ms/5ms) observed for a single echo or MERGE at T_2^*=10.1 ms agrees best with Fleysher's approximation of Eq. (3.1).

3.4.2 SNR, T_1, PD and T_2^* Measurements in the Phantom

Results for the SNR measurements on conventional T_1-weighted images (MPR1, MPR6, FLASH1 and FLASH8) are given as bar graphs in Figure 3.7(a), along with the SNR gains of the multi-echo protocols over their single-echo counterparts in (b).The measured SNR gains agree with the theory, except in the bottom layer (short T_1/T_2^* mimicking fat) of the FLASH8 image, probably owing to a higher B_1 non-uniformity than in other layers. SNR gains of 1.28 and 1.52 for MPR6 and FLASH8, over MPR1 and FLASH1, respectively, are achieved in layer 3 (T_1/T_2^*=1294/95 ms). Sagittal images of the phantom are shown in **Figure 3.6**. Note how the contrasts in MPR6/ FLASH8 at TE_1 are equivalent to those in MPR1/FLASH1, respectively, despite significantly different scan parameters.

Measured T_1NR of the various MPM protocols are shown in Figure 3.7(c). It is noteworthy that (except in the bottom and top layers) MP2R1 achieves comparable T_1NR to VFA-FLASH1 in the same total scan time, and likewise, MP2R6 has comparable T_1NR to VFA-FLASH6. However, at short or long T_1=449/2658 ms, VFA-FLASH1/6 slightly outperforms MP2RAGE1/6. Scan times are nearly identical so similar conclusions can be drawn for T_1NR efficiency. The measured gains in T_1NR (multi-echo over single-echo protocols) are compared to the predicted values in Figure 3.7(d). The measured gains (in layers with T_1=951 and 1294 ms which mimic WM/GM) for the VFA-FLASH12 and MP2R6 protocols are both more modest (~1.69 and 1.33) than predicted (~1.82 and 1.48), but as can be deduced from the error bars, some of the ROIs agreed more closely with the predicted values. The deviation may be due to the large parallel imaging acceleration factors of 4-fold and 4.8-fold in these two protocols, respectively, which strongly violate the assumption g≈1.

Measured PDNR and T_2^*NR of the different protocols are shown in Figure 3.7(e) and (f), respectively. Note that *PD* from the single-echo protocols (VFA-FLASH1 and MP2R1) was

corrected for T_2^* decay using the T_2^* map derived from the VFA-FLASH9 protocol. As previously predicted in the Theory, the SNR in the *PD* and T_2^* maps derived from MP2RAGE is significantly lower than that from VFA-FLASH. This is well explained by the lower sampling efficiency of MP2RAGE (~36–38%) compared to VFA-FLASH (~70–75%), and the fact that only the second image $|GRE_{TI2}|$ is used to solve for T_2^* and *PD*.

Measured T_1 and T_2^* (using the same ROIs), from the various protocols are compared in Figure 3.8. There is generally very good agreement across the measurements, and slightly larger differences in the top layer with longest T_1/T_2^*=2658/110 ms. Within that layer, IR-EPI measures a lower T_1 than in all the MPM protocols, likely due to the fact that the approximation $T_1^{app} \approx (c_{RF}^+)^2 T_1$ in Eq. (3.10a) biases the corrected T_1 to longer values at long T_1 and low c_{RF}^+.

Sagittal *PD*, T_1 and T_2^* maps of the different protocols are shown in Figure 3.9. The green arrows point to overestimated *PD* at the phantom edges, arising from strong susceptibility effects. The bias field Ψ_{PD} estimated from the PD^{app} in MPR1, as well as the c_{RF} map estimated from PD^{app} in VFA-FLASH are also shown.

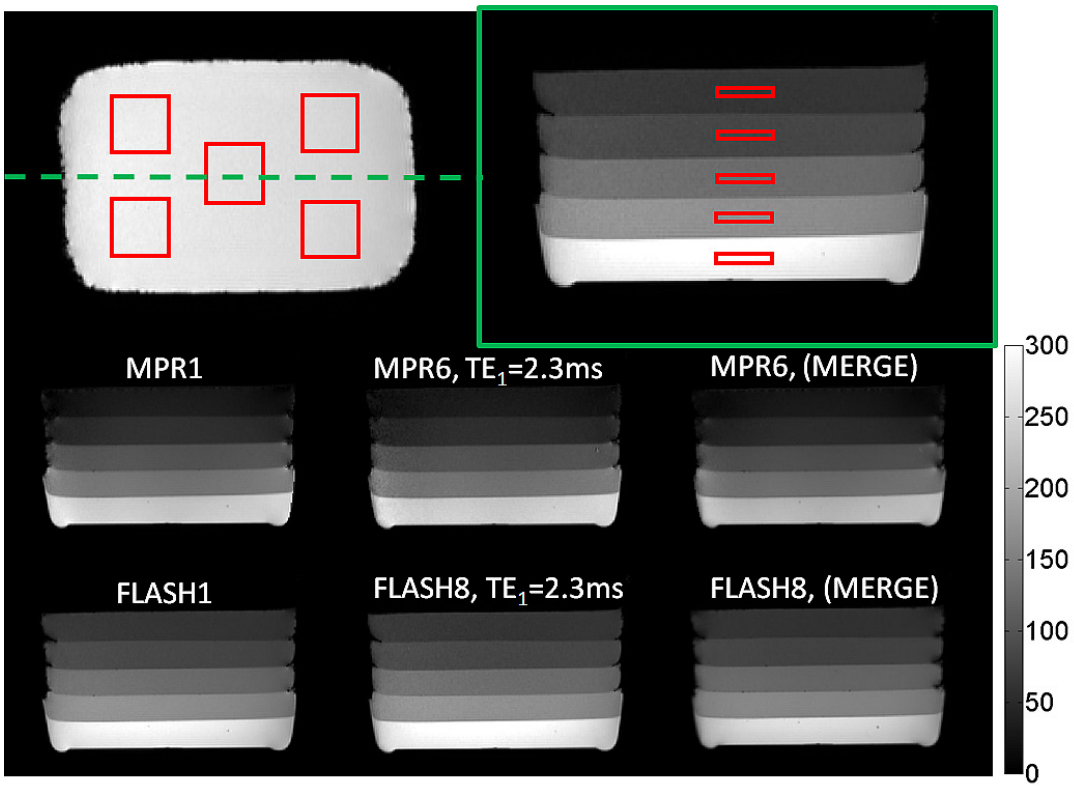

Figure 3.6: Phantom sagittal images (arbitrary units) of conventional single-echo MPRAGE and FLASH, compared to the first echo (TE_1=2.3 ms) image and the MERGE combination of the corresponding multi-echo protocols. MPRAGE images are approximately corrected for flip angle inhomogeneity by dividing them by c_{RF}^2, while FLASH images are left uncorrected. ROI locations for all phantom measurements are displayed at the top.

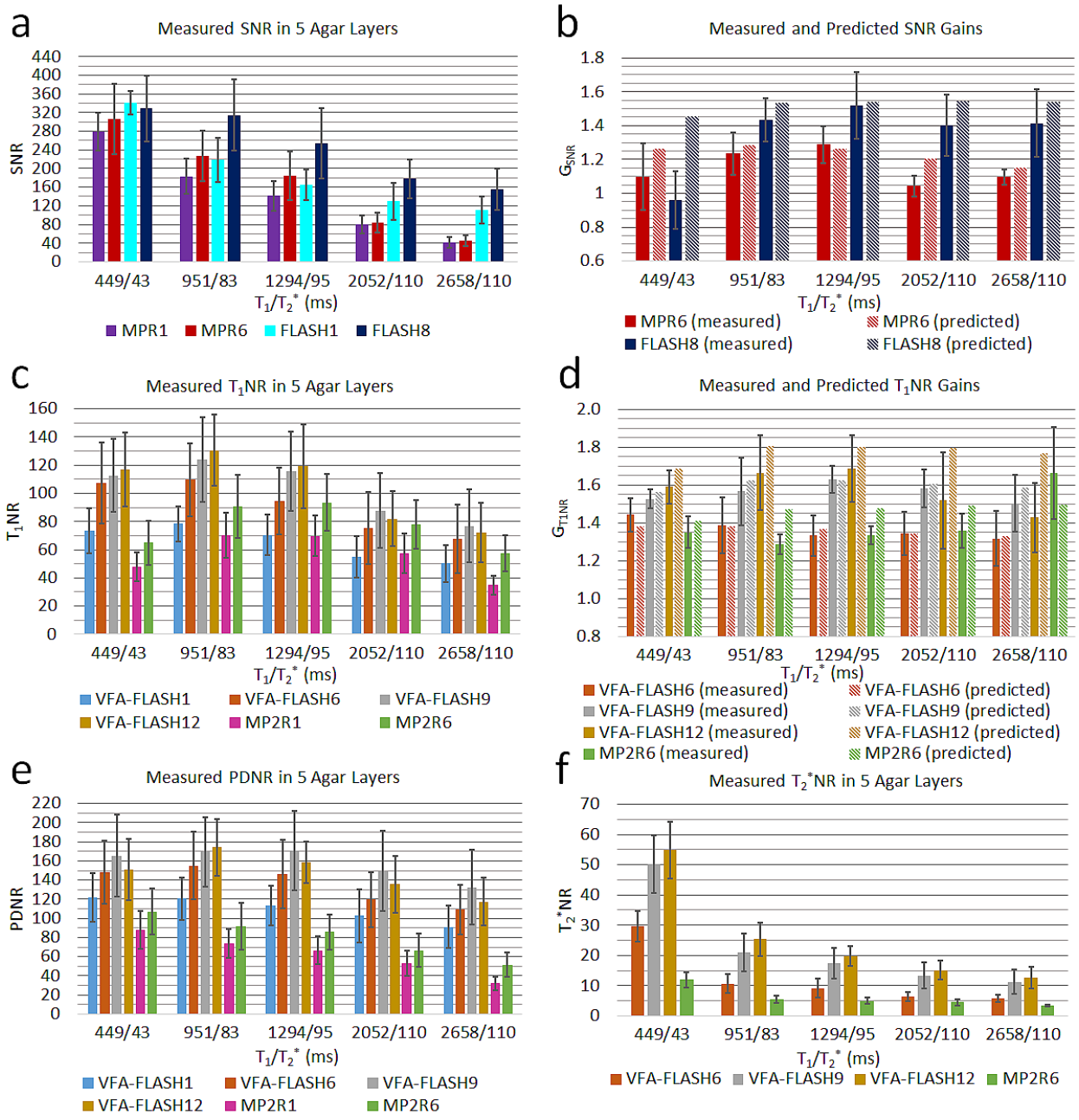

Figure 3.7: a) Measured SNR in 5 agar phantom layers using single-echo and multi-echo FLASH and MPRAGE sequences. (b) Measured and predicted SNR gains for the multi-echo FLASH and MPRAGE with respect to their single-echo counterparts. (c) Measured T_1NR with the different MPM protocols. (d) Measured and predicted T_1NR gains of the multi-echo MPM protocols with respect to their single-echo counterparts. (e) Measured PDNR with the different MPM protocols. (f) Measured T_2^*NR with the different multi-echo MPM protocols. Error bars correspond to the standard deviation from 5 SNR measurements in each layer (an estimate of SNR uniformity).

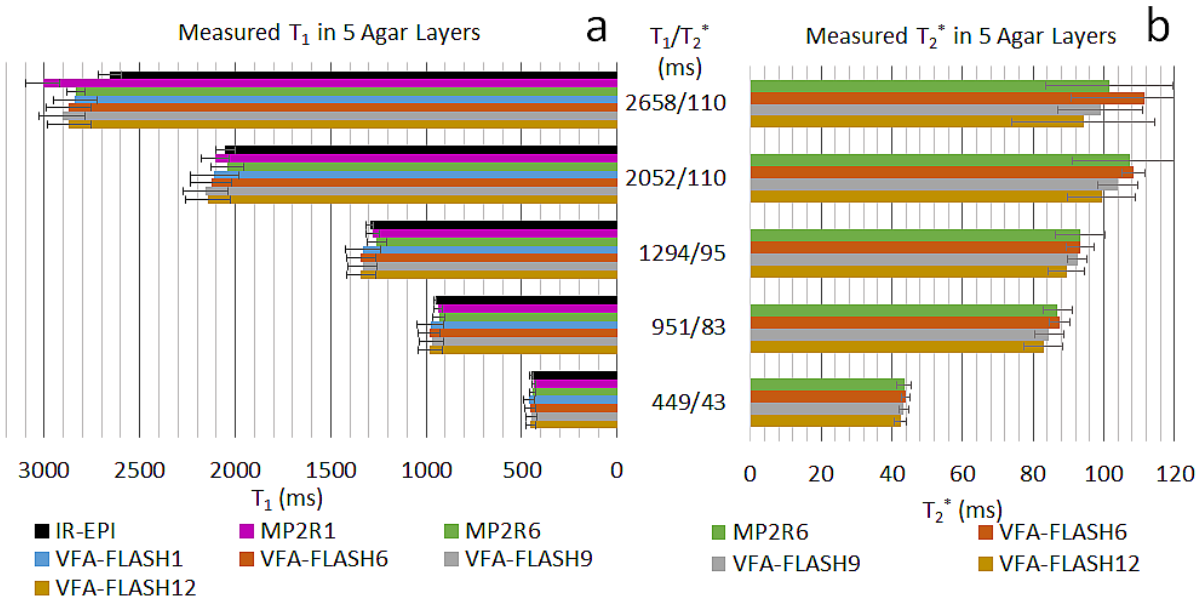

Figure 3.8: Comparisons of the T_1 (a) and T_2^* (b) measurements within each agar layer of the multi-layered phantom. Note that (except for IR-EPI), the error bars correspond to the standard deviation of the 5 ROI measurements in each layer (yielding an estimate of the T_1 or T_2^* uniformity over the phantom).

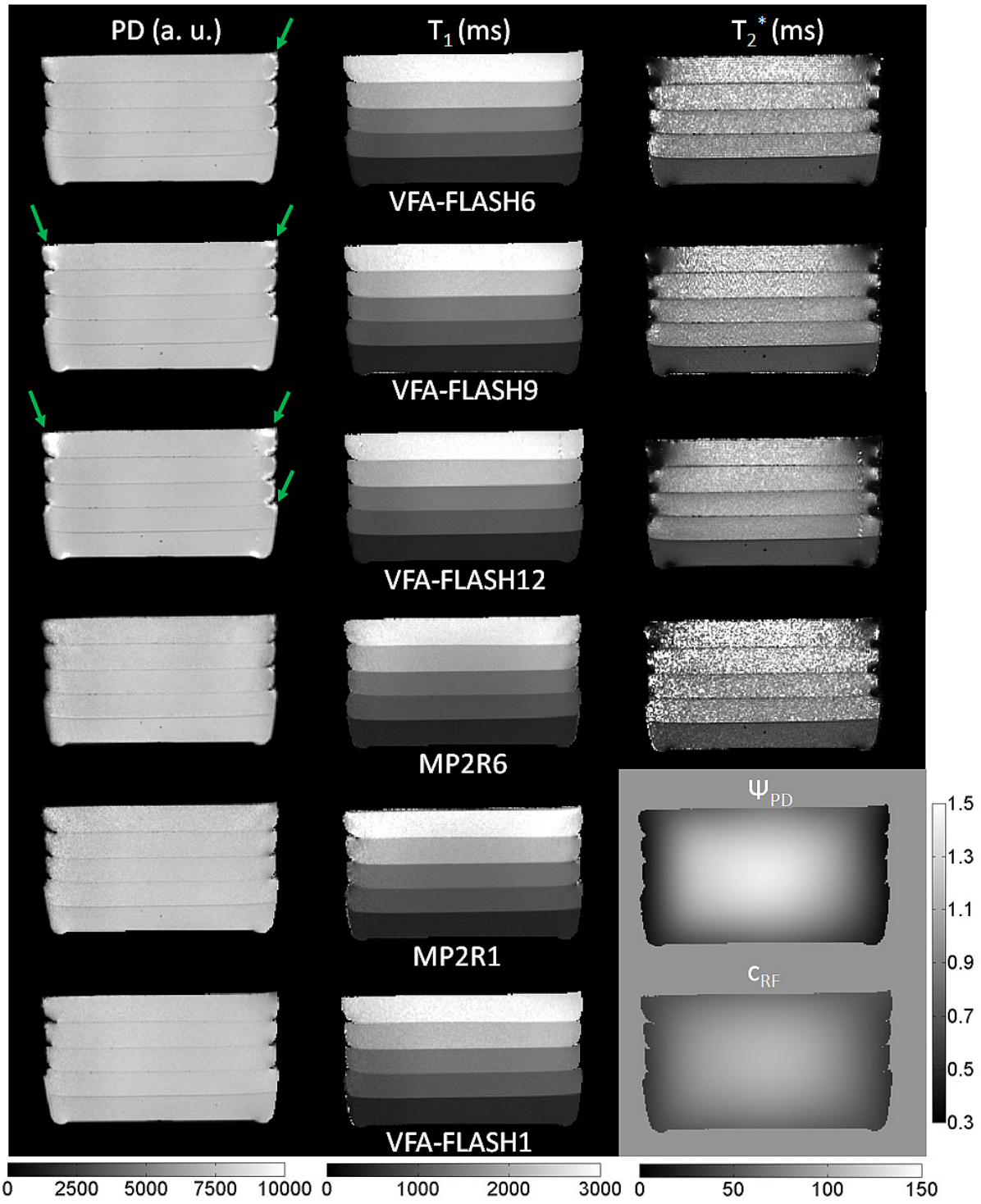

Figure 3.9: Phantom sagittal *PD*, T_1 and T_2^* maps derived from the various MP2RAGE and VFA-FLASH protocols, as well as an example of the bias field Ψ_{PD} corresponding to MP2R1, and the c_{RF} corresponding to VFA-FLASH1. The green arrows point to an overestimation in the proton density arising from susceptibility effects at the phantom edges.

3.4.3 In Vivo Results

3.4.3.1 Quantitative Maps

An axial slice of each quantitative (T_1, PD and T_2^*) map derived from 4 different MPM protocols is displayed in Figure 3.10. The MP2R6 protocol clearly yields lower SNR in PD and T_2^* than VFA-FLASH6. In fact, the T_2^* map is unusable, therefore the T_2^* map from the VFA-FLASH9 protocol was used instead to correct the proton density for T_2^* decay. Good-quality T_2^* mapping from *unipolar* multi-echo MP2RAGE was recently reported [78], but the total scan time was more than twice as long (~18 min), and the field strength was 7T, which alone provides a significant SNR advantage compared to the present study. The VFA-FLASH12 protocol yields the highest T_2^*NR, but lower-quality PD and T_1 maps. This finding suggests that recovering pure proton-density and T_1 from heavily T_2^*-weighted MERGE datasets is more challenging than with single-echo FLASH images, especially with a large acceleration factor of 2×2. However, if a more advanced curve-fitting procedure (such as a multi-component T_2^* fit) and a high-density receiver coil array (e.g., 32-channel array) were employed, better quantitative maps with higher SNR could be obtained.

The VFA-FLASH9 protocol achieves the best compromise between good T_2^* and PD image quality, and was thus tested on 3 additional volunteers. Sagittal slices of the parametric maps from all four volunteers are shown in Figure 3.11. The red arrows indicate an overestimation in PD arising from susceptibility effects in the frontal sinuses (resulting in non-exponential T_2^* decay and incorrect G_{SNR} in Eq. (3.2)). The effect is less pronounced on the VFA-FLASH6 PD maps (not shown in vivo, but visible in Figure 3.9).

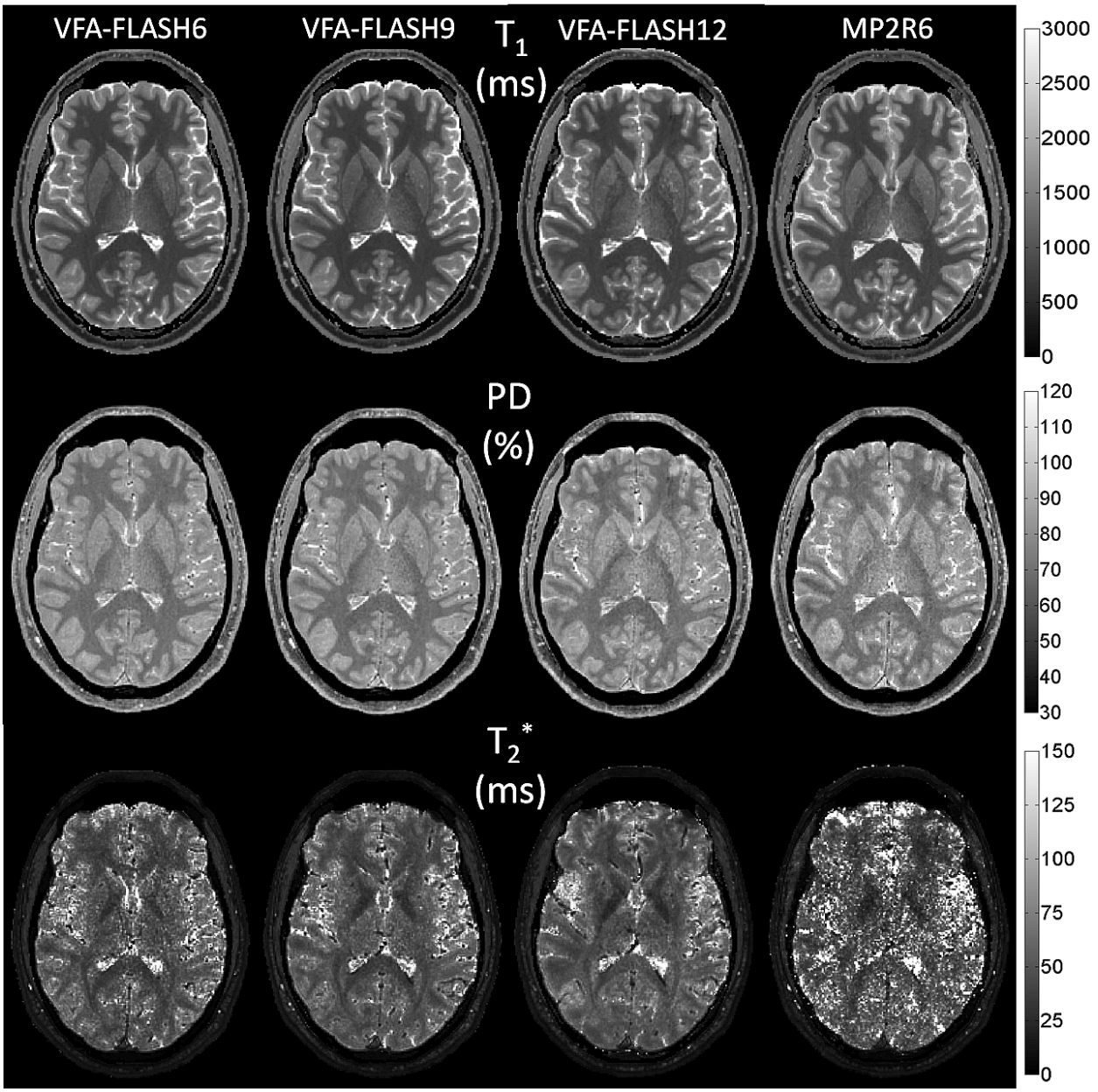

Figure 3.10: Axial T_1, PD and T_2^* maps of the first volunteer (v1) derived from the four MPM protocols (~8:30 min each) at the same slice location.

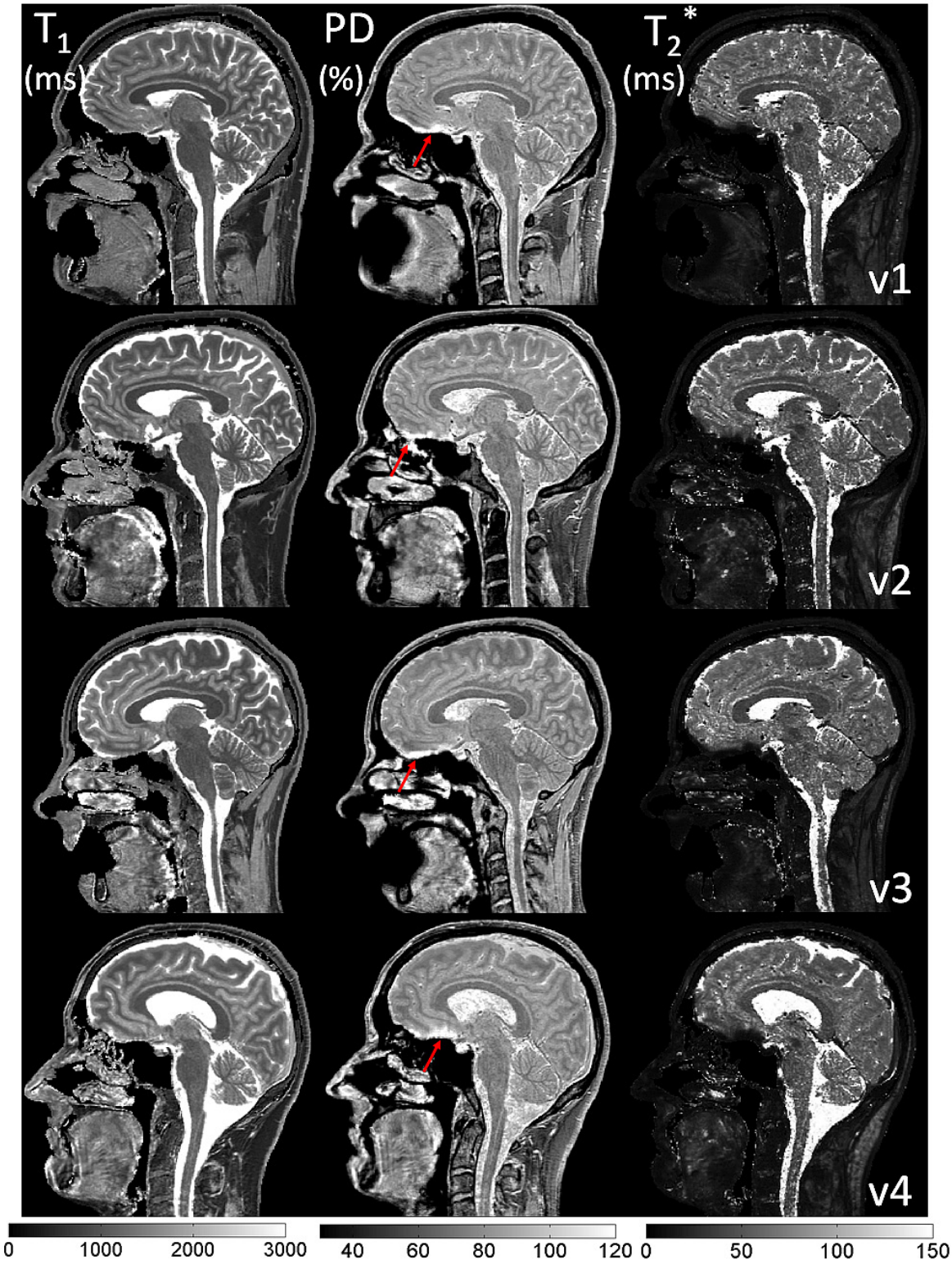

Figure 3.11: Sagittal parametric maps (*PD*, T_1 and T_2^*) of the 4 volunteers derived from the VFA-FLASH9 protocol. Susceptibility effects in the frontal sinuses tend to result in an overestimation of the proton density at the bottom surface of the frontal lobe (red arrows).

3.4.3.2 Histograms (*PD*, T_1 and T_2^*)

Histograms of the parametric maps derived from all MPM protocols tested on volunteer v1 are shown in Figure 3.12 (a–c), and those from the VFA-FLASH9 protocol tested on four different subjects are displayed in (d–f). The *PD* histograms (Figure 3.12b) of the 9-echo and 12-echo VFA-FLASH protocols are slightly more broadened than those of the 6-echo protocol, which confirms the challenge of recovering pure *PD* from heavily T_2^*-weighted MERGE images. A further explanation is that later echoes are more motion-sensitive than early ones [94]. The *PD* histogram from both the VFA-FLASH1 and MP2R1 protocols is also broader, despite excellent WM/GM peak separation. This might be due to the effect of non-ideal RF spoiling previously observed [93], to which a shorter *TR* (=8–11 ms) would be more susceptible because less T_2^* decay can occur between consecutive RF pulses.

The T_1 histogram of MP2R6 also has less GM/WM peak separation than that of MP2R1. Both MP2R1 and MP2R6 were consequently tested on the other three volunteers to confirm this observation (see the *PD* and T_1 histograms of all four volunteers in Figure 3.13). A plausible explanation is that because MP2RAGE is a phase-sensitive technique, it is more prone to phase errors (inconsistencies between the corresponding echoes at TI_1 vs TI_2), which may be present in such a bipolar multi-echo sequence [104]. As shown in Figure 3.14, both MP2R6 and VFA-FLASH6 show similar trends when separately plotting a T_1 histogram generated from each echo. In both cases, the fat peak shifts significantly depending on the *TE*, with $TE_2 \approx 4.6$ ms yielding the longest and $TE_4/TE_5 \approx 9.2/11.4$ ms both yielding the shortest adipose T_1. This effect might be explained by the existence of different proton pools within adipose. The T_1 histograms also tend to broaden at longer *TE*, most likely because of reduced SNR. However, the GM peak of the MP2R6 protocol also shows a slight plateau (or second hump) around $T_1 \sim 1400$ ms, which disappears beyond the third echo. Intra- versus extra-cellular water compartments could also be at play, resulting in varying TE-dependent biases in T_1 [105]. The effect of B_1^+ inhomogeneity on the T_1 look-up tables of both MP2R1 and MP2R6 is shown in the **Figure 3.15**. Both MP2RAGE protocols were optimized to yield a comparable effect of B_1^+ homogeneity on T_1, and thus the significant differences in histogram shapes must be explained by higher-order effects.

The T_2^* histograms of Figure 3.12(c) and (f) show that for the MP2R6 protocol the histogram is skewed relative to the VFA protocols because of poor SNR (see bottom-right T_2^* map in Figure 3.10).

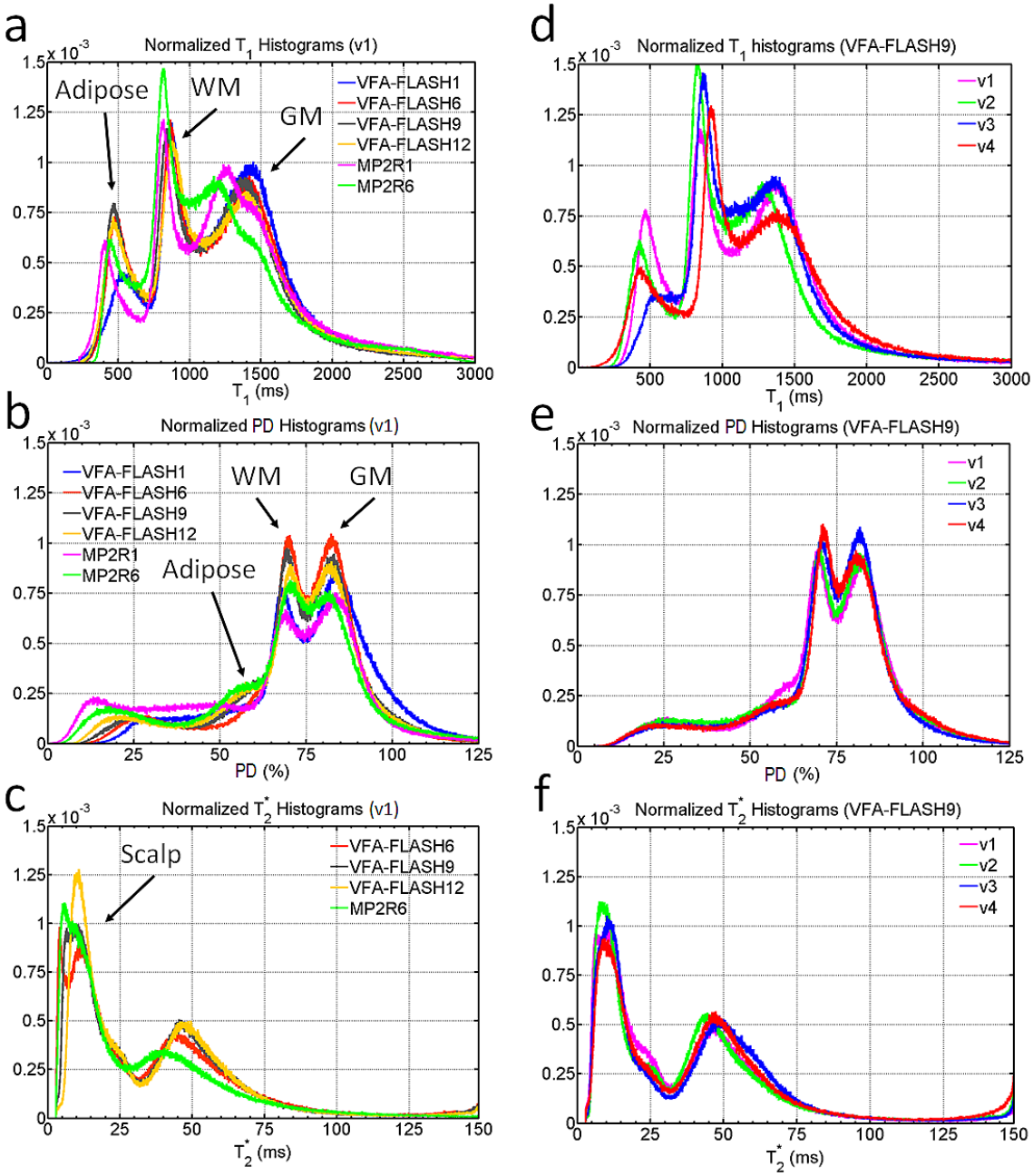

Figure 3.12: Normalized T_1, PD and T_2^* histograms of volunteer v1 derived from all 6 MPM protocols (a-c), and normalized T_1, PD and T_2^* histograms of the four volunteers for the VFA-FLASH9 protocol (d-f).

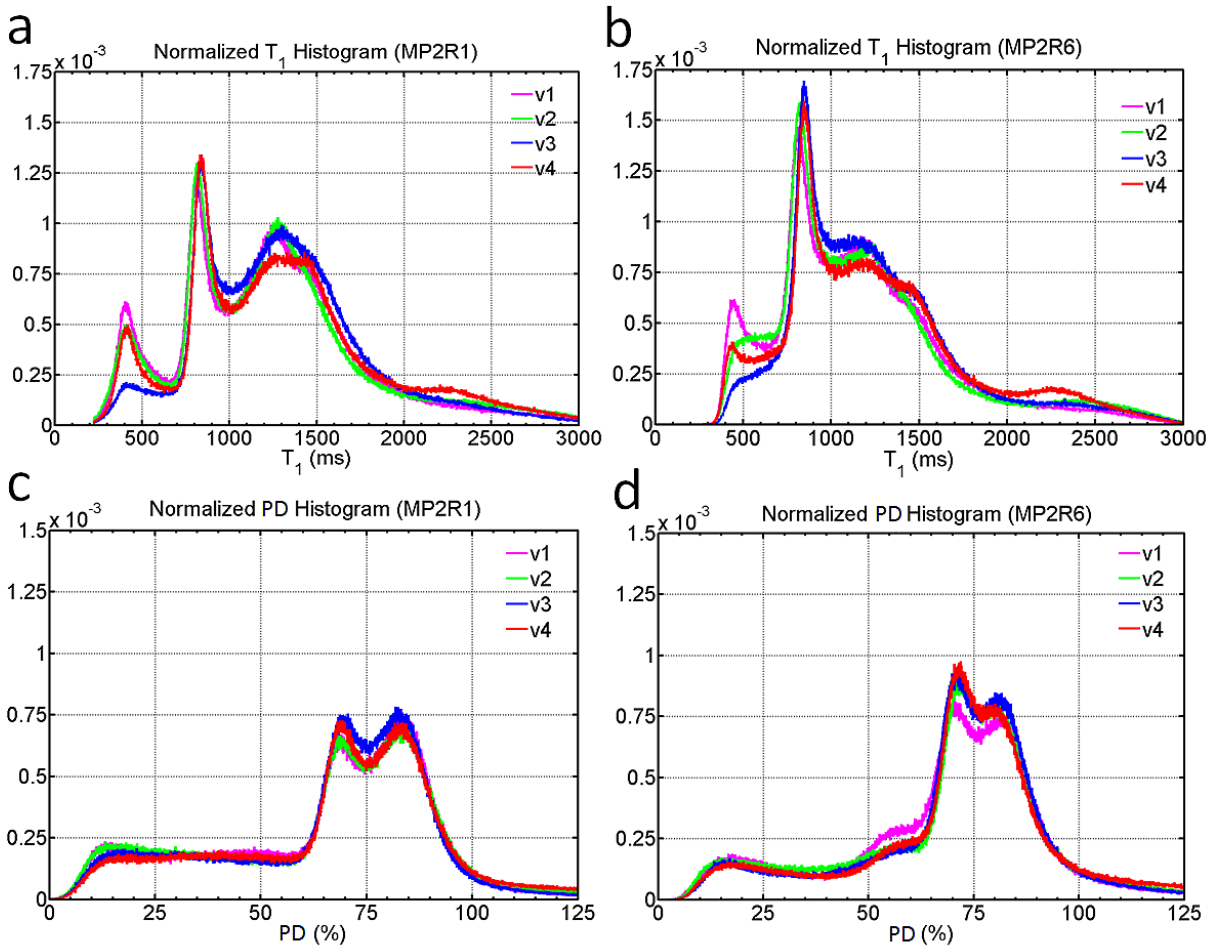

Figure 3.13: Normalized T_1 and PD histograms from MP2R1 (a, c), and MP2R6 (b, d), for all four volunteers. Notice the smaller GM-WM peak separation of the histograms derived from MP2R6.

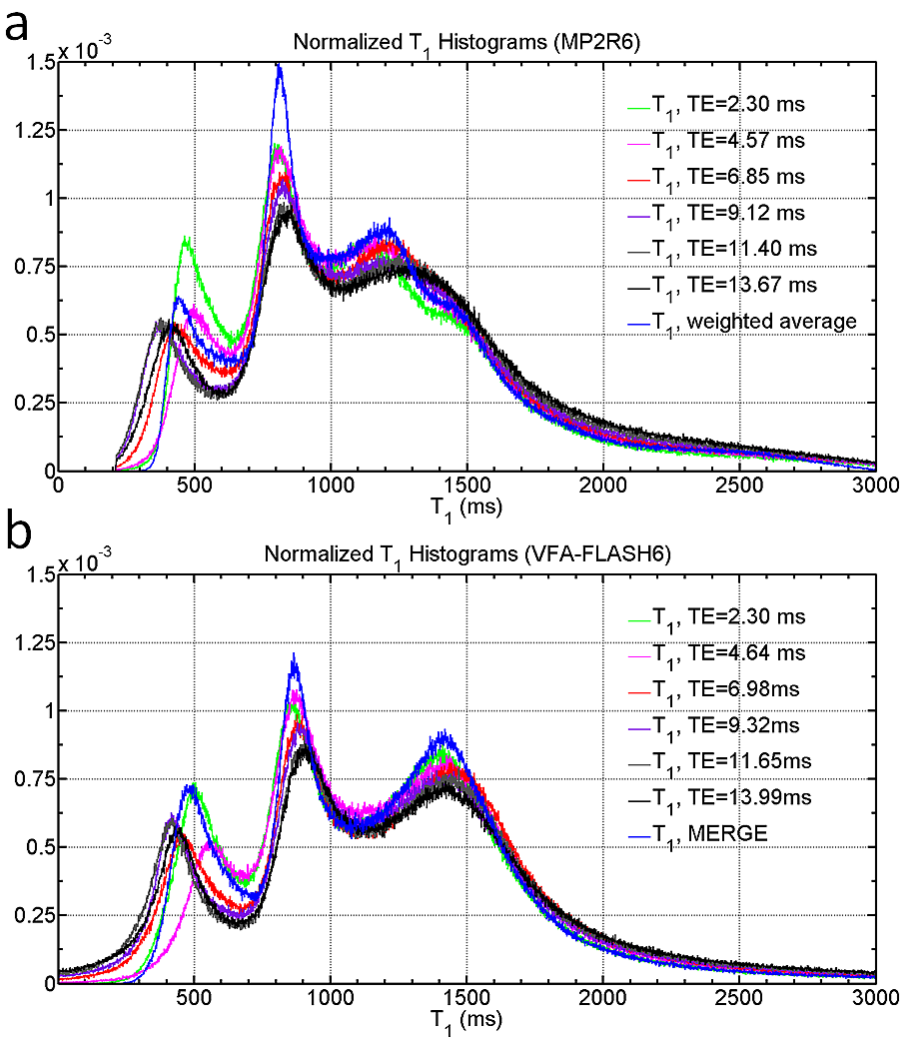

Figure 3.14: Normalized T_1 histograms of volunteer v1 derived from each separate echo of (a) the MP2R6 protocol, and (b) the VFA-FLASH6 protocol.

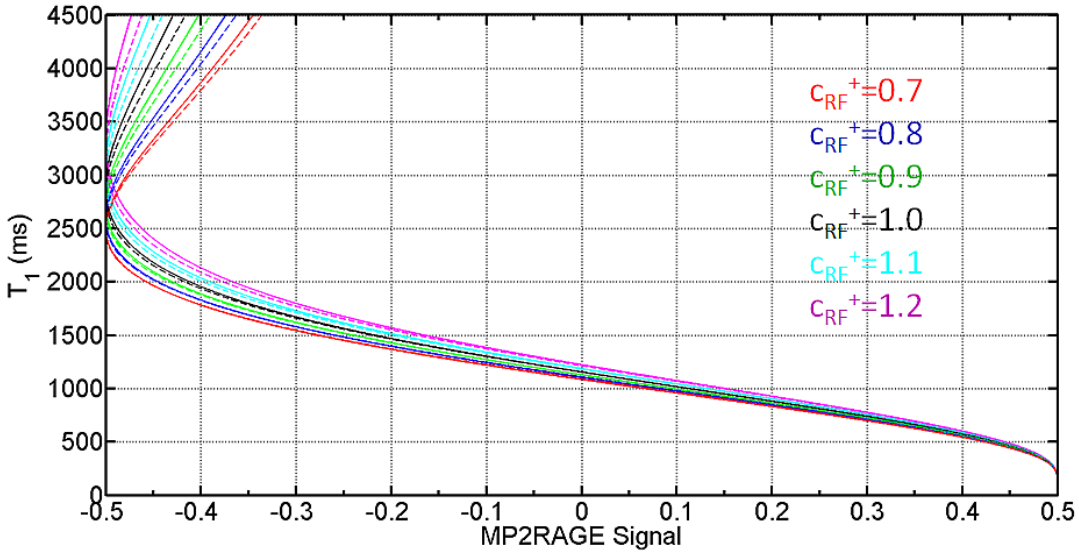

Figure 3.15: Effect of B_1^+ inhomogeneity (for a typical c_{RF}^+ range observed at 3T) on the T_1 look-up table of MP2R1 (dashed lines) and MP2R6 (solid lines). Note that, in practice, the table was made bijective by limiting the maximum T_1 to T_{1max}.

3.4.3.3 Brain ROI Measurements (*PD*, T_1 and T_2^*)

Relaxometry measurements in various brain ROIs are listed in **Table 3.2** for the three protocols tested on all four volunteers, along with two reported literature values (representative lower and higher bounds, when available). Except in CSF (i.e., ventricles) *PD* and T_2^* measurements agree well with the literature, and the T_1 measurements also agree with those reported by Marques et al [44] (who use the same MP2RAGE technique).

In general, VFA-FLASH yields ~4% longer T_1 than that from MP2RAGE. The lower T_1 standard deviations measured across the different subjects in MP2RAGE are due to the automatic B_1 bias field correction intrinsic to MP2RAGE, which, unlike VFA-FLASH, is robust to random or subject-dependent fluctuations in RF power calibration in the successive flip angle acquisitions. The proton density in CSF is overestimated by ~25–27% by MP2R1 and MP2R6, and much less (~10 %) by VFA-FLASH9 (due to a combination of non-ideal RF spoiling [93], and underestimated T_2^* which is clipped at 150 ms instead of the true ~2000 ms). As noted above, in CSF *PD* cannot be measured accurately with MP2RAGE because of the inability to correctly solve for long T_1. The MP2R1 protocol also underestimates *PD* in frontal/occipital WM (~66–67%) compared to the MP2R6 and VFA-FLASH9 (~69–71%).

Protocol/ ROI Location	VFA-FLASH9			MP2R1		MP2R6		Reported Literature		
	***PD* [%]**	***T_1* [ms]**	***T_2^** [ms]**	***PD* [%]**	***T_1* [ms]**	***PD* [%]**	***T_1* [ms]**	***PD* [%]**	***T_1* [ms]**	***T_2^** [ms]**
Putamen L	82.3 (1.5)	1204 (22)	42.2 (4.4)	81.9 (2.5)	1207 (32)	83.4 (1.3)	1187 (33)	81.9[g], 83.2[h]	1337[a], 1140[b]	41.3[j]
Putamen R	82.5 (1.5)	1245 (49)	41.8 (6.0)	81.1 (1.5)	1212 (28)	84.8 (1.0)	1221 (35)	81.9[g], 83.2[h]	1321[a], 1140[b]	41.3[j]
Globus Pallidus L	77.0 (2.0)	962 (39)	28.6 (3.7)	75.3 (1.3)	916 (37)	78.6 (2.6)	931 (41)	76.8[i]	888[b], 1043[c]	26.7[j]
Globus Pallidus R	77.4 (1.1)	973 (38)	28.5 (3.3)	75.6 (1.4)	931 (34)	79.0 (0.5)	942 (34)	76.8[i]	888[b], 1043[c]	26.7[j]
Caudate L	84.8 (1.6)	1409 (46)	50.6 (4.9)	88.6 (2.5)	1345 (28)	85.2 (1.8)	1333 (10)	81.5[g], 84.8[h]	1524[a], 1464[e]	54.9[d] 47.4[j]
Caudate R	84.8 (1.7)	1372 (55)	52.3 (6.1)	88.4 (1.6)	1342 (11)	88.5 (1.5)	1403 (32)	81.5[g], 84.8[h]	1437[a], 1464[e]	54.9[d] 47.4[j]
Splenium	67.6 (0.6)	828 (41)	37.3 (0.4)	71.5 (1.2)	777 (15)	71.3 (0.9)	783 (18)	70.1[g], 66.2[h]	730[b], 773[f]	–
Genu	69.2 (1.5)	835 (66)	38.4 (1.6)	66.9 (1.6)	755 (24)	70.3 (0.9)	771 (27)	69.6[g], 69.0[h]	898[a], 720[b]	40[e],
Frontal WM L	69.1 (0.8)	854 (51)	43.1 (1.8)	66.0 (0.4)	807 (17)	69.1 (0.8)	798 (31)	70.1[g], 69.1[h]	947[a], 838[d]	44.7[d]
Frontal WM R	69.2 (0.8)	854 (45)	43.1 (1.8)	66.0 (0.9)	810 (18)	69.5 (1.5)	830 (16)	70.4[g], 69.1[h]	921[a], 847[c]	44.7[d]
Occipital WM L	69.5 (1.5)	838 (55)	44.1 (1.2)	66.6 (1.7)	811 (15)	71.0 (1.5)	832 (17)	69.0[g], 66.9[h]	954[a], 832[d]	48.4[d]
Occipital WM R	69.9 (1.3)	856 (50)	43.9 (1.4)	66.6 (1.3)	813 (17)	71.1 (0.8)	813 (22)	69.5[g], 66.9[h]	940[a], 832[d]	48.4[d]
Ventricle L	110 (2.8)	4424 (476)	145 (4.9)	127 (7.2)	2369 (57)	125 (2.7)	2345 (61)	99.9[i]	4306[f]	–
Ventricle R	110 (3.4)	4413 (478)	143 (4.3)	126 (3.0)	2378 (27)	126 (3.2)	2325 (51)	99.9[i]	4306[f]	–

Table 3.2: Measured *PD*, T_1 & T_2^* (with standard deviations) in various brain ROIs (in axial slices) averaged across 4 volunteers. Note that the T_2^* from MP2R6 was not measured because of its poor SNR and accuracy (Figure 3.10 or Figure 3.12c). Literature references are: [a] [85], [b] [106], [c] [107], [d] [108], [e] [11], [f] [109], [g] [93], [h] [110], [i] [111], [j][112]. Most authors average the left and right hemisphere measurements, except in [85], and [93]. N.B.: *PD* is normalized with respect to the midpoint between WM and GM histogram peaks, and then multiplied by 76% (see text). PD/T_1 mapping techniques employed include VFA (a, f, g, i), Look-Locker (b, c, h), Saturation Recovery (d), while for T_2^*, multi-echo SPGR is used by all.

3.5 Discussion and Conclusions

This study compares the SNR efficiency and image quality of bipolar multi-echo gradient echo sequences over their single-echo counterparts (FLASH and MPRAGE). The theory predicts that at 3T, optimized multi-echo sequences can enable SNR and T_1NR gains of 1.3–1.8, despite 3-fold higher bandwidths, depending especially on the sequence parameters, and on the T_2^*. These gains arise from a combination of increased signal yields (by using longer *TR* and higher flip angles), and the combination of multiple echoes (MERGE). The measured SNR (or T_1NR) gains in the agar phantom agree well with the theory, as long as moderate regularized 2D SENSE accelerations are employed (≤3-fold with an 8-channel head array) which ensures that g ≈ 1. This hypothesis is confirmed by Lin et al [54] where average g-factors of 0.72, 0.84 and 1.52 were observed for regularized 1D SENSE acceleration with *R*=2, 2.67, and 4, respectively, using an 8-channel array. Therefore, the lower-than-expected SNR observed in the two protocols with *R*≥2×2 (VFA-FLASH12 and MP2R6) is consistent with g>1. The 9-echo VFA-FLASH technique was found to achieve the best overall image quality with T_1NR gains of ~1.6, which is comparable to the gain of ~1.67 obtained by a hybrid FLASH-EPI VFA T_1 mapping technique [85].

The SNR efficiency of two MPM pipelines (based on VFA with FLASH, and MP2RAGE) were compared, finding that MP2RAGE yields comparable T_1NR efficiency to that of VFA-FLASH in relevant brain tissues (i.e., WM/GM), despite having only about half the sampling efficiency (35–38% for MP2RAGE, compared to 70–75% for VFA-FLASH). This is readily explained by the fact that the T_1 in MP2RAGE is calculated from a 1D look-up table of the real MP2RAGE signal, which has better T_1-weighting and contrast-to-noise than a standard FLASH image [44]. However, since both *PD* and T_2^* must be calculated from magnitude images in either pipeline, VFA-FLASH has a significant SNR advantage (>2-fold) over MP2RAGE for *PD* and T_2^* mapping. Therefore, MP2RAGE is less suitable for MPM applications.

It was recently observed that MP2RAGE also tends to underestimate the WM T_1 (by ~6% at 3T and ~17% at 7T) due to the effect of magnetization transfer, leading to bi-exponential T_1 relaxation [113]. In this study, we confirm that MP2RAGE underestimates T_1 by ~4% (3.5%/4.5% for MP2R6/MP2R1) compared to N4ITK-corrected VFA-FLASH (when calculating the average percent difference in the ROI measurements of MP2RAGE vs VFA-FLASH in

Table 3.2. Conversely, in this implementation MP2RAGE yields narrower T_1 variability across different subjects compared to VFA-FLASH (see also Figure 3.12(d) compared to Figure 3.8(a-b)), most likely because of an intrinsic robustness to random or subject-dependent fluctuations in RF power calibration. Data from Refs. [11], [92], and [45] also suggests that the scan-scan reproducibility of MP2RAGE is better than that of VFA (coefficients of variation (CoV) of 2–3% for MP2RAGE compared to 5–7% for VFA). Further experiments (not shown in this study) revealed that the intra-subject CoV of N4ITK-corrected T_1 from VFA-FLASH is 5.8/7.4% in WM/GM, which compares well with Weiskopf's UNICORT technique (6.5/8.7%) [92], thus ruling out additional random fluctuations due to N4ITK. Improving the scan-scan reproducibility of VFA might be possible by fine-tuning the RF power calibration, or by a subsequent correction based on the expected mean T_1 of WM/GM in the general population (as similarly done for PD normalization in this study). The latter approach, however, would suppress differences based on age, gender, and body temperature that have been reported [108], [106], [114]. Despite achieving T_1NR gains of ~1.35 over its single-echo counterpart, the 6-echo MP2RAGE results in broader T_1 histogram lines (unless corrected via improved pulse-sequence modeling), thus making it less appealing.

We recommend the use of bipolar multi-echo sequences over their single-echo, low-bandwidth counterparts in structural brain imaging applications where susceptibility-induced geometrical distortions are especially a concern (e.g., Radiation Treatment Planning). Wang et al reported mean and maximum pixel shifts of <0.5mm and <4mm, respectively, at 180 Hz/pixel bandwidth with 3D MPRAGE on 19 patients at 3T [6]. The multi-echo MPRAGE or FLASH sequences tested here reduce such geometrical distortions by ~3-fold without SNR penalty and comparable scan times. (Deformable image registration of even and odd echoes was found to be unnecessary in the four volunteers at such high bandwidth, but may be needed in subjects with more substantial susceptibility inhomogeneities such as those due to dental implants).

Despite the more sophisticated post-processing, MPM with VFA-FLASH makes the best use of the increased SNR efficiency and available information to derive parametric maps with high SNR. In closing, we strongly recommend performing SNR validations in a phantom prior to using these bipolar echo sequences routinely because local SNR in images derived from bipolar

echo sequences with parallel imaging is heavily dependent on protocol and hardware (especially the g-factors).

3.6 Appendix

3.6.1 A. Derivation of Equation (3.2)

The MERGE image is formed by the root-sum-of-squares (RSS) combination of the individual images from each echo similarly to how images from receive arrays are sometimes combined. The SNR of the RSS combination is therefore given by Eq. 9 of [115], where the noise covariance matrix $\mathbf{\Psi}$ is equal to the identity matrix times a constant (σ_0^2) because the MERGE datasets are not acquired simultaneously, but at different times, and noise is therefore uncorrelated.

For a mono-exponential T_2^* decay, the elements of the signal vector are, $S_n = S_0 e^{-TE_n/T_2^*}$, n=1, 2… N and the SNR of the MERGE combination simplifies to

$$SNR_{comb} = \frac{S_0\sqrt{\sum_{n=1}^{N}(e^{-TE_n/T_2^*})^2}}{\sigma_0} = \frac{S_0\sqrt{\sum_{n=1}^{N} e^{-2\,TE_n/T_2^*}}}{\sigma_0} \qquad \text{(A3.1)}$$

Since the signal at TE=0 (S_0) is not directly measured, we may normalize SNR_{comb} by that of the first echo, SNR_1, such that

$$G_{SNR} = \frac{SNR_{comb}}{SNR_1} = \frac{S_0\sqrt{\sum_{n=1}^{N} e^{-2\,TE_n/T_2^*}}/\sigma_0}{S_0 e^{-TE_1/T_2^*}/\sigma_0} = \frac{\sqrt{\sum_{n=1}^{N} e^{-2\,TE_n/T_2^*}}}{e^{-TE_1/T_2^*}} \qquad \text{(A3.2)}$$

It is reasonable to think that an optimal linear weighting of the echoes with weights w_n might yield a superior SNR than the simpler RSS combination. In the case of mono-exponential T_2^* decay the optimal weights are equal to the corresponding exponential factors because of the form of $\mathbf{\Psi}$ and because the exponential has the same formal role in the equations as the coil sensitivity does in array image combination [115]. We may therefore express the SNR of the combined signal using Eq. 8 or 10 of [115], which simplifies to the same result as above for the RSS combination.

3.6.2 B. Optimal Multi-echo MP2RAGE Combination

As shown by Marques et al [44], letting $x=GRE_{TI1}$, and $y=GRE_{TI2}$ be the two complex MP2RAGE image signals, the optimal signal combination for the real normalized MP2RAGE image is

$$MP2RAGE = \frac{\Re(x^* y)}{|x|^2 + |y|^2} \tag{B3.1}$$

where * denotes complex conjugation, and its noise standard deviation is given by

$$\sigma_{MP2RAGE} = \sigma_s \sqrt{\frac{(x^2 - y^2)^2}{(x^2 + y^2)^3}} \tag{B3.2}$$

where σ_s is the noise standard deviation in each GRE image (assumed to be equal). Note that $\sigma_s \propto g\sqrt{R}/T_{acq}$. If multiple echoes are acquired, the T_2^* decay still cancels out in the real normalized MP2RAGE image, but not in its standard deviation. Because the decay function is the same in both images, $x(TE)=X\ exp(-TE/T_2^*)$, and $y(TE)=Y\ exp(-TE/T_2^*)$, it can be factored out, yielding

$$\sigma_{MP2RAGE}(TE) = \frac{\sigma_s}{e^{-TE/T_2^*}} \sqrt{\frac{(X^2 - Y^2)^2}{(X^2 + Y^2)^3}} \tag{B3.3}$$

The weighted average is typically calculated by weighing each measurement x_k by the inverse-square of its uncertainty [116] (p. 175)

$$\bar{x} = \frac{\sum_k \frac{x_k}{\sigma_k^2}}{\sum_k 1/\sigma_k^2} \tag{B3.4}$$

Therefore, the optimal SNR combination of echoes for MP2RAGE is

$$MP2RAGE_{wav} = \frac{\sum_{n=1}^{N} MP2RAGE(TE_n) e^{-2TE_n/T_2^*}}{\sum_{n=1}^{N} e^{-2TE_n/T_2^*}} \tag{B3.5}$$

and its noise standard deviation is calculated from the uncertainty in a weighted average [116] (p. 176)

$$\sigma_{wav} = \frac{1}{\sqrt{\sum_{n=1}^{N} 1/\sigma_{MP2RAGE}^2(TE_n)}} = \sqrt{\frac{(X^2 - Y^2)^2}{(X^2 + Y^2)^3}} \frac{\sigma_s}{\sqrt{\sum_{n=1}^{N} e^{-2TE_n/T_2^*}}} \quad \text{(B3.6)}$$

To obtain Eq. (3.8), we simply divide Eq. (B3.1) by Eq. (B3.3) or (B3.6), for single-echo or a weighted average of multiple echoes, respectively.

3.6.3 C. Derivation of Equation (3.4)

The square of the SNR gain (Eq. (3.2)), normalized to the signal at *TE*=0 is

$$\sum_{n=1}^{N} e^{-2TE_n/T_2^*} = \sum_{n=1}^{N} e^{-2[\Delta - \tau - \frac{T_{acq}}{2} + n(T_{acq}+\tau)]/T_2^*} = e^{-2(\Delta - \tau - \frac{T_{acq}}{2})/T_2^*} \sum_{n=1}^{\infty} e^{-2n(\tau + T_{acq})/T_2^*} \quad \text{(C3.1)}$$

Letting $x = e^{-2(\tau+T_{acq})/T_2^*}$, and recalling that the result for the convergent power series is

$\sum_{n=1}^{\infty} x^n = \frac{x}{1-x}$, the above expression becomes

$$\begin{aligned} e^{-2(\Delta - \tau - \frac{T_{acq}}{2})/T_2^*} \sum_{n=1}^{\infty} e^{-2n(\tau+T_{acq})/T_2^*} &= e^{-2(\Delta - \tau - \frac{T_{acq}}{2})/T_2^*} \frac{e^{-2(\tau+T_{acq})/T_2^*}}{1 - e^{-2(\tau+T_{acq})/T_2^*}} \\ &= \frac{e^{-2\Delta/T_2^*} e^{-T_{acq}/T_2^*}}{1 - e^{-2(\tau+T_{acq})/T_2^*}} \end{aligned} \quad \text{(C3.2)}$$

Substituting this result into Eq. (3.3) yields Eq. (3.4). Note that the convergence criterion $|x| = \left|e^{-2(\tau+T_{acq})/T_2^*}\right| < 1$ is satisfied.

3.6.4 D. Noise Propagation into T_1 and PD

The propagation of noise from two FLASH images at α_1 and α_2 into the final T_1 map has been extensively studied [88], [89], and the T_1 standard deviation σ_{T1}, is related to the noise standard deviation σ_s, by [85]

$$\begin{aligned} \sigma_{\mathrm{T1}} &= \frac{T_1^2}{TR} \frac{\sin\alpha_1 \sin\alpha_2 \,|\cos\alpha_1 - \cos\alpha_2| \sqrt{S_1^2 + S_2^2}}{A_1 A_2} \sigma_s, \\ A_1 &= S_2 \sin\alpha_1 \cos\alpha_2 - S_1 \sin\alpha_2 \cos\alpha_1, \\ A_2 &= S_2 \sin\alpha_1 - S_1 \sin\alpha_2 \end{aligned} \quad \text{(D3.1)}$$

In MPM with VFA-FLASH, Eq. (D3.1) also depends on T_2^*, because the MERGE combinations (S_{ME}) at each respective flip angle (α_i) may be written as G_{SNR} (Eq. (3.2)) multiplied by the FLASH signal at TE=0 ($S_{0,i}$),

$$S_i = S_{0,i}\sqrt{\sum_{n=1}^{N} e^{-2TE_n/T_2^*}} \tag{D3.2}$$

Therefore σ_{TI} in Eq. (D3.1) becomes reduced by a factor of G_{SNR}. Likewise, the noise standard deviation σ_{PD} of the proton density map PD derived by Sabati and Maudsley [90] can be modified straightforwardly to incorporate the G_{SNR} term, yielding

$$\begin{aligned} \sigma_{PD} &= \frac{\sigma_s PD}{G_{SNR}} \frac{\sqrt{A_1^2 S_{0,2}^4 + A_2^2 S_{0,1}^4}}{S_{0,1} S_{0,2} \left| A_1 S_{0,2} - A_2 S_{0,1} \right|}, \\ A_1 &= \tan\alpha_1 \sin\alpha_1 (\sin\alpha_2 - \tan\alpha_2), \\ A_2 &= \tan\alpha_2 \sin\alpha_2 (\sin\alpha_1 - \tan\alpha_1) \end{aligned} \tag{D3.3}$$

Thus the SNR of the PD map also increases by a factor of G_{SNR} (Eq. (3.2)).

3.6.5 E. Optimal weights for the combined T_2^*

The variance of T_2^* can be calculated from the expression for the variance of R_2 derived by De Deene et al for a mono-exponential log-linear fit (Eq. 9 in [117]) by replacing R_2 with R_2^* and recalling that the relative error of inverses is identical ($\frac{\sigma_{R2^*}}{R_2^*} = \frac{\sigma_{T2^*}}{T_2^*}$), yielding

$$\sigma_{\mathrm{T2}^*} \approx \frac{(T_2^*)^2 \sigma_s}{S_0} \frac{6\, e^{R_2^* TE_1}}{N(N^2-1)\Delta TE} \Gamma \tag{E3.1}$$

Here, N is the number of echoes, ΔTE is the echo spacing, TE_1 is the first echo time, S_0/σ_s is the SNR extrapolated to $TE=0$, and Γ is a function that is independent of the flip angle. Since in this expression only S_0 depends on the flip angle, we have $1/\sigma_{\mathrm{T2}^*}^2 \propto S_0^2$. Since

$$S_{0,i} = PD \frac{(1-E_1)\sin\alpha_i}{1 - E_1 \cos\alpha_i} \tag{E3.2}$$

the weights of Eq. (3.12) simplify to

$$w_i = \frac{\sin^2 \alpha_i}{(1 - E_1 \cos \alpha_i)^2} \tag{E3.3}$$

3.7 Acknowledgments

We gratefully acknowledge financial support from the Alberta Cancer Foundation, the Alberta Cancer Research Institute, and the Natural Sciences and Engineering Research Council (Canada). We also thank Philips Healthcare for technical support, Dr. Roger Luechinger for the PATI program used for data transfer, and the anonymous referees for insightful comments.

Chapter 4: Analytical Corrections of Banding Artifacts in Driven Equilibrium Single Pulse Observation of T_2 (DESPOT2)[9]

"The theory I propose may therefore be called a theory of the *Electromagnetic Field* because it has to do with the space in the neighbourhood of the electric or magnetic bodies, and it may be called a Dynamical Theory, because it assumes that in the space there is matter in motion, by which the observed electromagnetic phenomena are produced."

— James Clerk Maxwell

"A Dynamical Theory of the Electromagnetic Field" (1865). In W. D. Niven (ed.), *The Scientific Papers of James Clerk Maxwell* (1890), Vol. 2, 527.

[9] A version of this chapter has been published in Magnetic Resonance in Medicine (2016)76(6):1790-1804. DOI 10.1002/mrm.26074 [149].

4.1 Introduction

Quantitative mapping of the T_1 and T_2 relaxation constants in vivo can provide improved sensitivity to biochemical changes in tissues associated with disease over conventional T_1-weighted and T_2-weighted MRI [118], [119], [120]. The methods of Variable Flip Angles (VFA) or Driven Equilibrium Single Pulse Observation of T_1 (DESPOT1) for fast 3D T_1 mapping have gained popularity in recent years in applications such as brain and knee imaging [74], [88], [121], [87], by virtue of their simplicity and excellent signal-to-noise ratio (SNR) efficiency. In these methods, two or more spoiled gradient recalled echo (SPGR) datasets are acquired at different flip angles and the T_1 is extracted from the slope of a linear fit of the SPGR signal. Advances in transmit B_1/flip-angle mapping have made the implementation of DESPOT1 practical at 3T [63], [86], [122], where the effect of transmit B_1 inhomogeneity is more severe than at 1.5 T and must be corrected.

Conversely, the DESPOT2 method for mapping T_2 has not achieved similar success because it relies on balanced steady state free precession (bSSFP) which is prone to banding artifacts that arise from off-resonance (ΔB_0), corrupting the T_2 map [84], [123]. More recently, magnetization transfer (MT) and finite RF pulse effects were also shown to bias the resulting T_2 [124], [125]. Consequently, T_2 mapping continues to rely on spin-echo based techniques such as dual-echo or multi-echo fast-spin echo sequences [126], [127], which, however, cannot provide whole-brain T_2 maps with high isotropic resolution (~1 mm) in a reasonable scan time. Deoni et al. proposed the "phase-cycled DESPOT2" (DESPOT2-c) [123] and "DESPOT2 with full modeling" (DESPOT2-FM) [128] techniques to address the problem of banding artifacts. Unfortunately, both approaches utilize computationally-intensive post-processing algorithms and significantly longer post-processing time than the original DESPOT1/DESPOT2 methods. (DESPOT2-FM processing may take up to 48 hours for a single 1-mm isotropic 3D brain dataset, when running on a single-core CPU [129]). Furthermore, both methods are limited to two phase cycles, while using a larger number improves the robustness of the results. The method of Wood et al. [129] removes band artifacts in DESPOT2 using the "geometric solution" for bSSFP imaging [38] and is valid for exactly four phase offsets.

In this study, we remove banding artefacts analytically by introducing the *reduced* T_2 from DESPOT2 and performing a general mathematical analysis that includes the effect of off-

resonance and is valid for any number of phase cycles greater than one. Using an even number of phase offsets, an exact mathematical solution is derived to obtain both T_2 and phase accumulation, ϕ, with computational ease. Moreover, we show that with three or more phase offsets, an approximate but accurate solution for T_2 can also be used. We finally investigate two approaches for mitigating MT effects that otherwise bias the T_2 measurement: optimization of the flip angles/ RF pulse durations to cancel the MT ratios (MTR), and lengthening the RF pulse durations. All methods are readily applied with minimal sequence development on any modern clinical scanner on which bSSFP, SPGR and B_1^+ mapping sequences are implemented.

4.2 Theory

4.2.1 Solving for T_2 Analytically

The full bSSFP signal in steady-state is given by Zur et al. [130], [131]

$$\begin{gathered} M_+ = \frac{a\, e^{-i(\phi+\phi_{RF})} + b}{c\cos(\phi+\phi_{RF}) + d} M_0 e^{-TE/T_2}\,, \\ a = -(1-E_1)\sin\alpha\, E_2,\ b = (1-E_1)\sin\alpha, \\ c = E_2(E_1-1)(1+\cos\alpha),\ \ d = 1 - E_1\cos\alpha - E_2^2(E_1-\cos\alpha) \end{gathered} \tag{4.1}$$

where, $\phi = 2\pi\, \Delta f\, TR$ is the phase accumulation arising from the static field inhomogeneity and chemical shift, $\Delta f = \gamma(1+\sigma)B(\vec{r})/2\pi - f_0$, TR is the repetition time, σ is the chemical shift constant, and ϕ_{RF} is the RF phase cycle increment. Furthermore $E_1=exp(-TR/T_1)$, $E_2=exp(-TR/T_2)$, TE is the echo time, α is the actual flip angle, and $M_+=M_x+iM_y$ is the transverse magnetization.

When the signal is perfectly on resonance ($\Delta f = 0$) and the phase cycle is $\phi_{RF}= \pi$, Eq. (4.1) simplifies to

$$S_{SSFP} = M_0 \frac{(1-E_1)\sin\alpha\, e^{-TE/T_2}}{1-(E_1-E_2)\cos\alpha - E_1E_2} \tag{4.2}$$

i.e., $S_{SSFP} = |M_+|$ which is the better-known equation that describes the magnitude of the bSSFP signal. In the DESPOT2 technique, multiple bSSFP datasets are acquired at respectively different flip angles, while keeping all other scan parameters identical. These datasets are then curve-fitted using a linearized ($y=m\,x + b$) version of Eq. (4.2), given by [88]

$$\frac{S_{SSFP}}{\sin\alpha} = \frac{E_1 - E_2}{1 - E_1E_2}\frac{S_{SSFP}}{\tan\alpha} + \frac{M_0(1 - E_1)e^{-TE/T_2}}{1 - E_1E_2} \tag{4.3}$$

where $y=S_{SSFP}/\sin\alpha$, $x=S_{SSFP}/\tan\alpha$, the slope $m=(E_1-E_2)/(1-E_1E_2)$, and the intercept $b=M_0(1-E_1)e^{-TE/T2}/(1-E_1E_2)$. Expressions and results for the proton density M_0 in the presence of banding artefacts are provided in Appendix D.

The T_2 can be determined from the slope m, the TR, and the T_1 previously determined from a technique such as DESPOT1 [88]. In practice, however, off-resonance will result in a systematic underestimation of T_2, that we define "reduced T_2"

$$\tau_2(\phi) = -TR/\log\left(\frac{E_1 - m(\phi)}{1 - m(\phi)E_1}\right) \leq T_2 \tag{4.4}$$

where $m(\phi)$ shows explicitly that the measured slope is modulated by the off-resonance phase ϕ. The relationship between τ_2 and T_2 is derived in Appendix A, resulting in a simple function of ϕ and T_2, notably independent of T_1,

$$\tau_2(\phi) = -TR/\log\left(\frac{e^{-TR/T_2} + \cos\phi}{e^{TR/T_2} + \cos\phi}\right) \tag{4.5}$$

To demonstrate the periodic nature of the banding artifacts in both the bSSFP signal and τ_2, Eq. (4.1) is plotted in Figure 4.1(a), as a function of α and ϕ, (with T_1=1000 ms, T_2=70 ms, TE=2.3 ms, TR=4.6 ms), along with Eq. (4.5) normalized by the true T_2 in Figure 4.1(b) as a function of $t=TR/T_2$ and ϕ. At low flip angles, the bSSFP signal can suffer from either bright-band or dark-band artifacts, while at high flip angles, the signal suffers from dark-band artifacts [132]. Conversely, τ_2 suffers from systematic underestimation and actually becomes complex when $E_1 - m < 0$. This region, corresponding to areas near off-resonance in Figure 4.1(b), tends to vanish for very long T_2, as $t \rightarrow 0$. The practical consequences arise in the presence of noise, and the effects in the final T_2 map can be minimized as described at the end of this section.

Banding artifacts are generally dealt with by acquiring bSSFP datasets at different phase offsets by either changing the RF phase cycle increment ϕ_{RF}, or changing the transmit frequency f_{tr} (since they have an equivalent effect on Eq. (4.1)). The total phase offset resulting from ϕ_{RF} or

Δf_{tr} is defined[10] as $\theta = 2\pi TR\Delta f_{tr} + \phi_{RF} - \pi$. Various methods for synthesizing artifact-free bSSFP images from different phase-cycled datasets have been developed and their performance has been compared [132], [133]. Generally, the quality of the synthesized image improves with an increasing number of phase offsets and for best results, the number of phase offsets must be evenly distributed over a full period. The phase offset θ corresponds to a frequency offset of [131]

$$\Delta f_0 = \frac{\theta}{2\pi\, TR} \tag{4.6}$$

Multiple bSSFP datasets are acquired with several (N) phase offsets (i.e., θ_1, θ_2, ... θ_N), each with two different flip angles α_1, α_2 (totaling $2N$ datasets). For each offset θ_i, one τ_2 map is obtained from the measured slope (from magnitude signals x and y defined below Eq.(4.3)) by substituting

$$m^{\theta}(\phi) = \frac{y_1 - y_2}{x_1 - x_2} = \frac{S^{\theta}_{SSFP}(\alpha_1)/\sin\alpha_1 - S^{\theta}_{SSFP}(\alpha_2)/\sin\alpha_2}{S^{\theta}_{SSFP}(\alpha_1)/\tan\alpha_1 - S^{\theta}_{SSFP}(\alpha_2)/\tan\alpha_2} \tag{4.7}$$

into Eq. (4.4). A method of reducing the effect of the bands in the final T_2 maps is to simply take the maximum intensity projection (MIP) of two τ_2 maps [123]. However, a systematic underestimation of the true T_2 will still remain at locations where the off-resonance lies between the two offsets. Fortunately, the derivation of Eq. (4.5) leads to an exact solution. Rearranging Eq. (4.5), we may write

$$E_2^2 - E_2\left(1 - \epsilon_2^{\theta}\right)\cos(\phi + \theta) - \epsilon_2^{\theta} = 0, \text{ where}$$
$$\epsilon_2^{\theta} = e^{-TR/\tau_2(\phi+\theta)} \tag{4.8 a, b}$$

Note that $\epsilon_2^{\theta} \in [-1,1]$ and Eq. (4.8b) is valid for both real and complex values of τ_2. Because $\cos(\phi+\pi) = -\cos(\phi)$, with two phase offsets $\theta = 0, \pi$ we have a system of two non-linear equations and two unknowns (T_2 and ϕ), the solution of which is (Appendix B):

[10] This definition is consistent with the plots shown in Figure 4.1. However, the equations throughout this chapter were derived assuming $\theta = 2\pi\, TR\, \Delta f_{tr} + \phi_{RF}$.

$$T_2^{0,\pi} = -TR \Big/ \log\left(\sqrt{\frac{2\epsilon_2^0\epsilon_2^\pi - \epsilon_2^0 - \epsilon_2^\pi}{\epsilon_2^0 + \epsilon_2^\pi - 2}}\right), \qquad \text{(4.9 a, b)}$$

$$\cos\phi^{0,\pi} = \frac{\epsilon_2^0 - \epsilon_2^\pi}{\sqrt{(\epsilon_2^0 + \epsilon_2^\pi - 2)(2\epsilon_2^0\epsilon_2^\pi - \epsilon_2^0 - \epsilon_2^\pi)}}$$

The 0, π superscript on T_2 indicates the phase offsets used. A more general form of these equations shown in Appendix B is actually valid for any pair of offsets having opposite phase, thus allowing additional estimates of T_2 to be calculated by sampling 0–2π using other pairs of offsets with opposite phases. These T_2 maps can then be combined by weighted average with optimal weights given by the square of the sine or cosine of the off-resonance phase ϕ. For example, with four phase offsets the final T_2 is

$$T_2 = \frac{\sin^2\left(\phi^{\frac{\pi}{2},\frac{3\pi}{2}}\right)T_2^{0,\pi} + \cos^2(\phi^{0,\pi})T_2^{\frac{\pi}{2},\frac{3\pi}{2}}}{\sin^2\left(\phi^{\frac{\pi}{2},\frac{3\pi}{2}}\right) + \cos^2(\phi^{0,\pi})} \qquad (4.10)$$

which we define as the "exact weighted" solution for N=4. A simple closed-form solution does not exist for odd numbers of phase offsets (e.g., θ=0, 2π/3, 4π/3). In this case it is more practical to employ a root-sum-of-squares combination (RSS):

$$T_2 \cong K_N\sqrt{\sum_{n=1}^{N}\left(\tau_2^{\theta_n}\right)^2}, \qquad N \geq 3 \qquad (4.11)$$

This approximate solution for deriving a final T_2 map is based on the assumption that $TR \ll T_2$. Thus the shorter the TR, the more accurate is the approximation. The factor K_N is calculated by substituting Eq. (4.5) into Eq. (4.11) and taking the limit as $t=TR/T_2 \rightarrow 0$. It can be proven by mathematical induction that for any (even or odd) N phase offsets $K_N = \sqrt{\frac{8}{3N}}$. Note that if using only two phase offsets this RSS combination will fail to yield an accurate final T_2 map, (because the limit depends on ϕ) and Eq. (4.9) must be used instead.

The final RSS approximation is,

$$T_2 \cong \sqrt{\frac{8}{3N}} TR \sqrt{\sum_{n=1}^{N} \left[\log\left(\frac{e^{-t} + \cos(\phi + \theta_n)}{e^{t} + \cos(\phi + \theta_n)} \right) \right]^{-2}} \tag{4.12}$$

Equation (4.12) is plotted in Figure 4.1(c), and (d) for N=3 and 4, respectively, by normalizing the calculated T_2 by the actual T_2 (as shown for a single phase offset in Figure 4.1b). The proposed RSS solution introduces negligible errors (maximum ~5% for N = 3 at T_2=TR). A flowchart of the analytical DESPOT2 post-processing pipeline is shown in Figure 4.2. Note that T_1 is also needed, along with the B_1 inhomogeneity correction c_{RF}^{+} map (defined as actual flip angle α divided by the nominal flip angle α_n) from a B_1-mapping sequence, such as Actual Flip Angle Imaging (AFI) [63].

Finally, while Eq. (4.9) is exact for both positive and negative ε_2 (real and complex τ_2, respectively), in practice ε_2<0 identifies regions near the off-resonance condition where signal is low and noise becomes significant. Also, here the bSSFP signal is sensitive to hardware imperfections (such as eddy currents, or frequency drifts) because of the presence of unstable equilibrium [134]. In these locations more reliable data from other offsets must carry a larger weight to ensure a reliable estimate for T_2. One way to achieve this is to assign values for $\varepsilon_2^{\theta} \in$ [-1, 0] in Eq. (4.9) for the exact solution or to exclude that datum from the RSS combination by assigning τ_2^{θ}=0 in Eq. (4.11) wherever E_1-$m^{\theta} \leq 0$. We have chosen ε_2^{θ} = 0 in Eq. (4.9), but with prior knowledge of the expected values of T_2 other ε_2^{θ} values may be chosen (e.g., ε_2^{θ}=–0.45, if T_2~50 ms) to minimize potential bias. We must also assign these values to voxels where $|\varepsilon_2^{\theta}| > 1$, which can only occur in noise-dominated regions (i.e. E_1-$m^{\theta} \leq 0$).

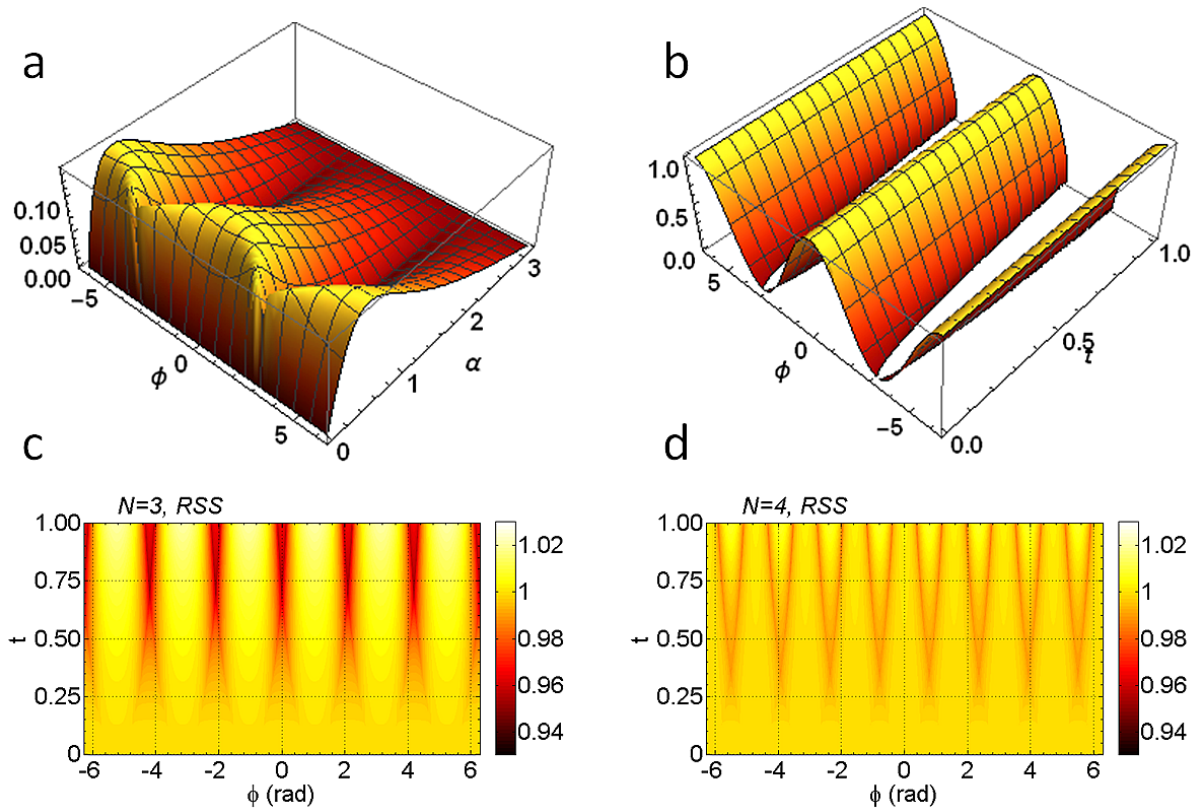

Figure 4.1: (a) Magnitude of the bSSFP signal as a function of α and ϕ for $T_1/T_2/TR$=1000/70/4.6 ms. (b) τ_2 normalized by the actual T_2, for $t=TR/T_2 \in [0, 1]$ and $\phi \in [-2\pi, 2\pi]$. (c) Plot of the approximate RSS T_2 normalized by the true T_2 using Eq. (4.11) within the range $t \in [0, 1]$ and $\phi \in [-2\pi, 2\pi]$ for N=3 and (d) for N=4.

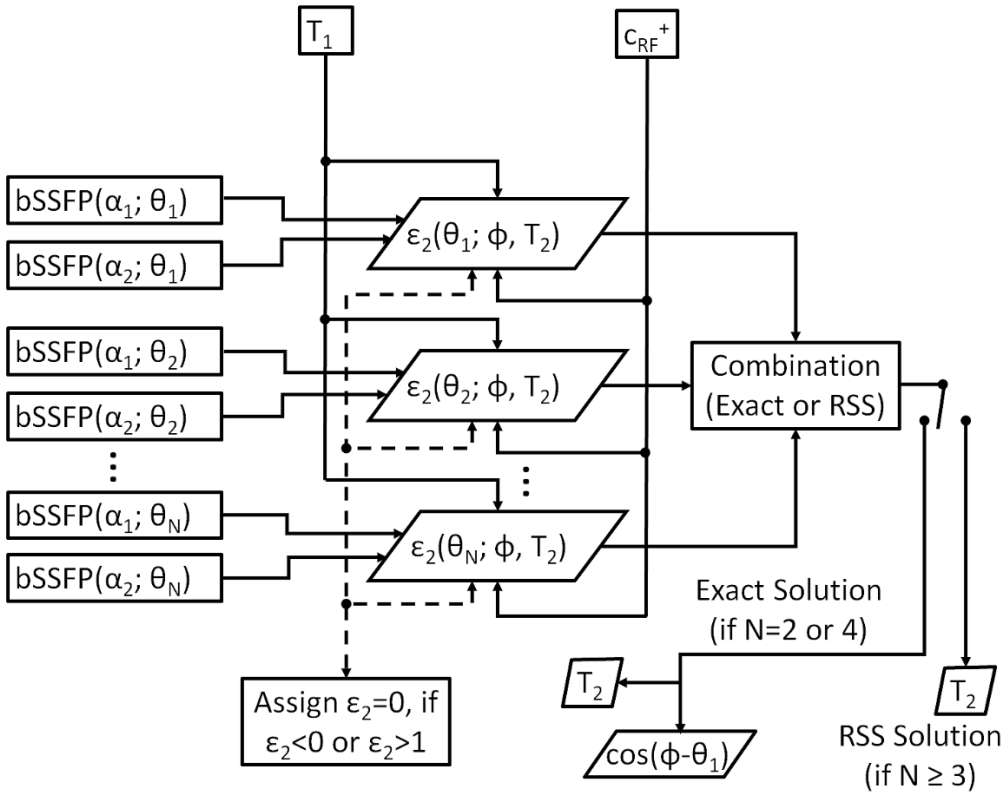

Figure 4.2: Proposed DESPOT2 post-processing pipeline, with the choice of the exact or RSS solution. In addition to the bSSFP datasets, T_1 is required from DESPOT1 and the c_{RF}^{+} (normalized B_1 inhomogeneity field) from AFI.

4.2.2 Effect of Finite RF Pulses and Magnetization Transfer on T_2

Recently, Bieri et al. have demonstrated that in vivo bSSFP is prone to on-resonance magnetization transfer (MT) effects, especially at short *TR* and high flip angles [135]. Moreover, the actual bSSFP signal may deviate considerably from that of Eqs. (4.1) and (4.2) due to the finite length of RF pulses (See Figure 4.4a). Consequently, DESPOT2 may yield incorrect white matter (WM) and gray matter (GM) T_2.

Finite RF pulse effects can be accounted for in Eq. (4.2) by the following substitution [136]:

$$E_2 \rightarrow \widetilde{E_2} = e^{-(TR-\zeta_\phi T_{RF})/T_2}, \tag{4.13}$$

$$\zeta_\phi = \zeta \cos^2\left[\frac{\phi}{2}\left(1-\frac{(1-\zeta)T_{RF}}{TR}\right)\right], \quad 2\left|\frac{\alpha}{\phi}\right| > \frac{T_{RF}}{TR} \tag{4.14 a}$$

$$\zeta \approx 0.68 - 0.125\left(1 + \frac{T_{RF}}{TR}\right)\frac{T_2}{T_1} \qquad (4.14\text{ b})$$

where T_{RF} is the RF pulse duration (for hard pulses). To avoid MT effects, Crooijmans et al. suggest using a combination of longer TR and T_{RF} [124], and a correction for the finite T_{RF} based on Eqs. (15, 16 and 20) of Ref. [136]. These corrections are exact only on-resonance, and the above DESPOT2 solutions Eqs. (4.9)-(4.10) are only valid in the limit of negligible RF pulse durations (e.g., $T_{RF}/TR \leq 0.15$). As shown in Figure 4.4b (blue curve), finite RF pulse effects will bias the calculated T_2 to longer values, as well as introducing oscillations. While the simple substitution $TR \rightarrow TR_{eff} = TR - \zeta_{corr} T_{RF}$ can be made in Eq. (4.4) or (4.9) to correct the net bias, the oscillations cannot be fully removed, even if using the phase information in Eq. (4.14a). While the finite RF pulse correction of Eqs. (4.13) and (4.14) is strictly valid only for $T_{RF1}=T_{RF2}=T_{RF}$ [136] we may use $T_{RF}=T_{RF2}$, since as shown in Figure 4.4(a), T_{RF2} dominates on both the SSFP signal bias at α_2 and the resulting T_2 bias. (The effect is also well illustrated using Bloch simulations in Fig. 2 of Ref. [125].)

There are two straightforward ways to mitigate MT effects. The first option is to significantly stretch both T_{RF1}/T_{RF2}, and increase the TR in an attempt to essentially remove the MT effects from both bSSFP signals at α_1/α_2. The main disadvantage of this approach is that stretching the RF pulses will lead to spatial spectral effects (i.e., the edges of the brain and adipose/fat tissue may no longer be properly excited [136]), and the final corrected T_2 map will contain more oscillations.

The second option [124] is to still use a short TR (~4–5 ms) and short T_{RF} (<0.7 ms), but also to select two flip angles (α_1 and α_2) such that the MT ratio (MTR) of the bSSFP signal at α_1 will be approximately equal to the MTR at α_2 in WM (or a compromise between WM and GM). This will result in the MTR cancelling out when calculating the slope in Eq. (4.3), and yield a good approximation for τ_2. This method was initially proposed with flip angles α_1/α_2=25/80˚ (assuming a short TR, and equal T_{RF} for both lower and higher flip angles) [124]. However, this choice yields a significantly suboptimal T_2NR in WM or GM, because the two flip angles are not the optimal values (optimal T_2NR is achieved with α_1/α_2≈11/57°, assuming WM T_1/T_2≈1000/52 or GM T_1/T_2≈1400/75 ms using Eq. 12 in Ref. [88]).

A better alternative that maintains the T_2NR efficiency is to let the scanner software freely adjust the T_{RF} for any given α, (to avoid exceeding maximum allowable SAR as done in Ref. [137]) and then select the lower and higher flip angles ($\alpha_1<\alpha_2$), such that they simultaneously experience the same amount of MT, while remaining close to their SNR-optimal values. As shown in Figure 4.3, in vivo MTR measurements were performed in the brain of a healthy volunteer using bSSFP images acquired in flip angle increments of 5° over a range of 5–85° (Figure 4.3(c)), obtained similarly to Gloor et al. [47]. The measured signal is curve-fitted assuming the on-resonance two-pool bSSFP equation (which accounts for MT effects) to solve for T_2, M_0, and the exchange parameters k_f and F, given the known input scan parameters (α, T_{RF}, $\omega_1(t)$, TR, TE) and the T_1 from DESPOT1[47]. The theoretical single-pool bSSFP signal is then obtained (see Figure 4.3(a) and (b)) by substituting the measured T_1, T_2 and M_0 into Eq. (4.2). Finally, the MTR is calculated as the percent difference between the single-pool and the two-pool bSSFP signals. The flip angles at which the MT effects are equal are found visually (Figure 4.3(c)) to be approximately α_1/α_2=11.5±1/59±2° with corresponding T_{RF1}/T_{RF2}=0.064/0.55 ms, and TR=4.8 ms. This choice simultaneously minimizes MT effects while optimizing the T_2NR efficiency defined as the T_2NR divided by the square-root of the scan time [88].

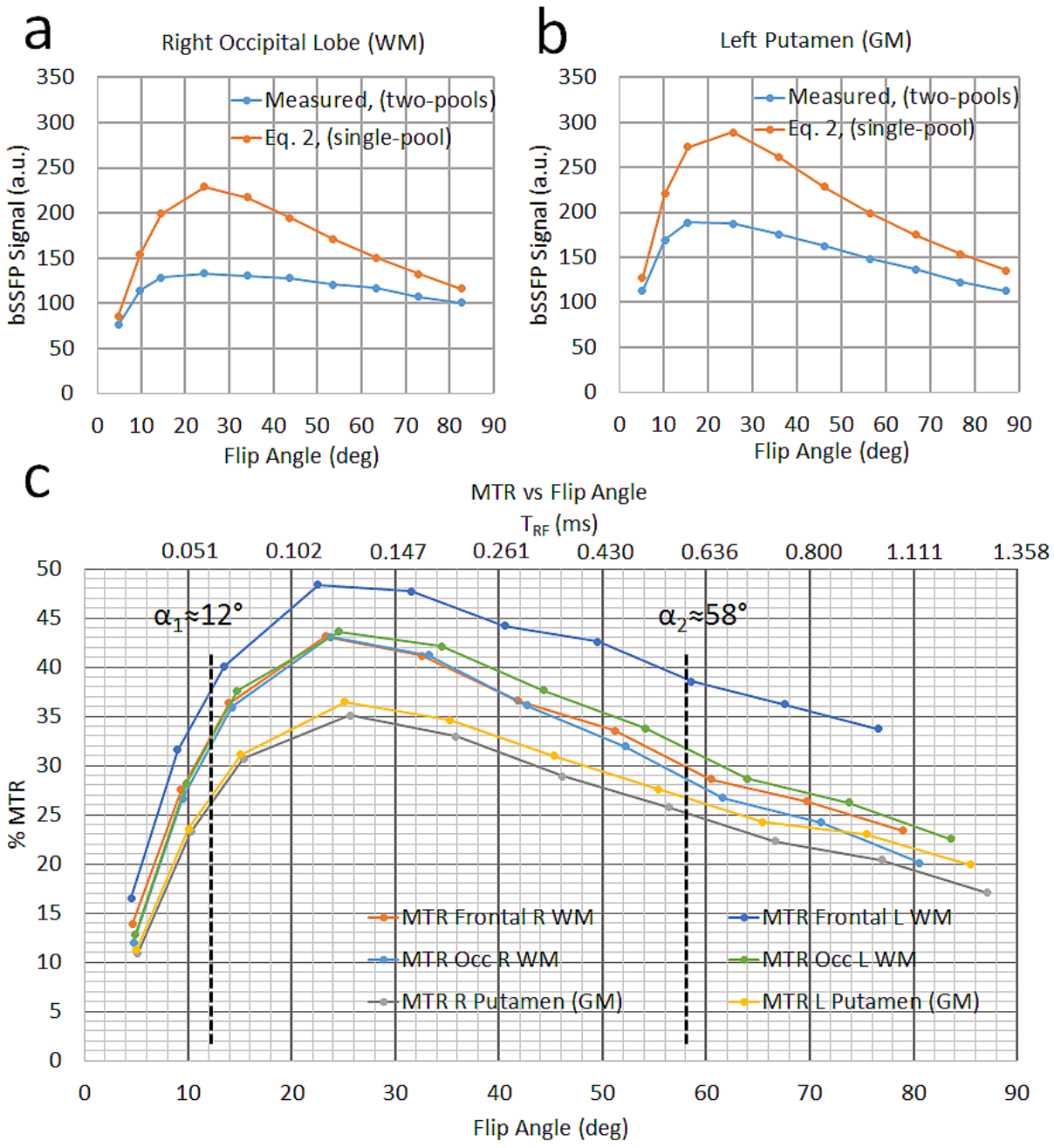

Figure 4.3: Measured bSSFP signal (blue) and predicted signal from Eq. (4.2) (orange), from an ROI in (a) the right occipital lobe, and in (b) the left putamen. (c) MTR curves as a function of flip angle and T_{RF} calculated as the percent difference between the two-pool and the single-pool signals. Two optimized flip angles (dashed vertical lines) can then be located to approximately cancel the MT effects in both WM and GM.

4.2.3 Effect of Image Noise on T_2

It is important to study how noise in both the T_1 map and in the bSSFP datasets propagates into the final T_2 map, as well as how to choose phase offsets, flip angles, and/or the number of averages (NEXs) to maximize the T_2NR efficiency. Deoni et al. have shown that taking multiple averages at two optimized flip angles yields a higher T_2NR (at a reference T_2) than curve-fitting multiple datasets of varying flip angles [88]. They also found that the optimal examination protocol dedicates 75% of the total scan time to DESPOT1 and the remaining 25% to DESPOT2. However, this analysis assumes a perfect on-resonance condition with only one phase offset (θ=0). We now investigate how noise will propagate into the final T_2 map, when 2, 3 or 4 phase offsets are used (Eqs. (4.9), (4.10), or (4.11)), including off-resonance effects while ignoring finite RF pulse effects.

In the simplest case of two on-resonance bSSFP datasets S_1 and S_2 with respective flip angles α_1, α_2, and a T_1 map previously derived from DESPOT1, the noise standard deviation σ_2 in the final T_2 may be calculated by standard error propagation (assuming the SNR is sufficiently high and uncorrelated Gaussian noise)

$$\sigma_2 = \sqrt{\left(\frac{\partial T_2}{\partial S_1}\right)^2 \sigma_s^2 + \left(\frac{\partial T_2}{\partial S_2}\right)^2 \sigma_s^2 + \left(\frac{\partial T_2}{\partial T_1}\right)^2 \sigma_1^2} \tag{4.15}$$

where σ_s is the noise standard deviation in either bSSFP dataset and σ_1 is the noise standard deviation in the T_1 map. The final result (see Appendix C) is

$$\sigma_2 = \sqrt{\frac{T_2^4(1-E_1E_2)^2}{TR^2}\frac{(1-E_1E_2+(E_2-E_1)\cos\alpha_1)^2\csc^2\alpha_1 + (1-E_1E_2+(E_2-E_1)\cos\alpha_2)^2\csc^2\alpha_2}{E_2^2(1-E_1^2)^2(S_1\cot\alpha_1 - S_2\cot\alpha_2)^2}\sigma_s^2 + \frac{E_1^2(1-E_2^2)^2T_2^4}{E_2^2(1-E_1^2)^2T_1^4}\sigma_1^2} \tag{4.16}$$

In off-resonant conditions the standard deviation for τ_2 can be obtained by substituting the T_2 for τ_2 from Eq. (4.5) into Eq. (4.16), resulting in

$$\sigma_2(\phi) = \sqrt{\frac{\tau_2^4(\phi)(1-E_1\epsilon_2(\phi))^2}{TR^2}\frac{(1-E_1\epsilon_2(\phi)+(\epsilon_2(\phi)-E_1)\cos\alpha_1)^2\csc^2\alpha_1+(1-E_1\epsilon_2(\phi)+(\epsilon_2(\phi)-E_1)\cos\alpha_2)^2\csc^2\alpha_2}{\epsilon_2^2(\phi)\left(1-E_1^2\right)^2(S_1(\phi)\cot\alpha_1-S_2(\phi)\cot\alpha_2)^2}\sigma_s^2 + \frac{E_1^2\left(1-\epsilon_2^2(\phi)\right)^2\tau_2^4(\phi)}{\epsilon_2^2(\phi)\left(1-E_1^2\right)^2T_1^4}\sigma_1^2} \tag{4.17}$$

To find the T_2NR in the analytical solution Eq. (4.9a), we must calculate

$$\sigma_2^{0,\pi}(\phi) = \sqrt{\left(\frac{\partial T_2^{0,\pi}}{\partial \tau_2^0}\right)^2 \sigma_2^0(\phi)^2 + \left(\frac{\partial T_2^{0,\pi}}{\partial \tau_2^\pi}\right)^2 \sigma_2^\pi(\phi)^2} \tag{4.18}$$

where $T_2^{0,\pi}$ and τ_2^θ are previously defined. A similar equation applies for $\sigma_2^{\pi/2,3\pi/2}(\phi)$. The final result is not algebraically concise but clearly predicts that T_2NR is a periodic function of ϕ as plotted in Figure 4.4(c).

Performing the same error analysis on the approximate solution for T_2 given in Eq. (4.11), we obtain

$$\sigma_2^{RSS}(\phi) = \sqrt{\frac{8}{3N}}\frac{\sqrt{\sum_{n=1}^N\left(\tau_2^{\theta_n}\right)^2\left(\sigma_2^{\theta_n}\right)^2}}{\sqrt{\sum_{n=1}^N\left(\tau_2^{\theta_n}\right)^2}} \tag{4.19}$$

This T_2 noise standard deviation is much more uniform with respect to ϕ than that of the exact solution calculated in Eq. (4.18) as shown in Figure 4.4(c). Note how the RSS combination of the reduced T_2 yields a more uniform T_2NR than the exact, or exact weighted analytical solutions. In fact, spikes (arising from noise in the vicinity of the singularity where E_1-1≤0) occur at regular intervals of $\phi=n\pi$ in the exact solution derived from two phase offsets (θ = 0, π), resulting in a highly non-uniform T_2NR (red curve). Using the exact weighted solution with four different phase offsets (N=4, magenta curve), and weighing the analytical T_2 by the squared sine or cosine of the phase as done in Eq. (4.10) eliminates the spikes. The T_2NR derived analytically is also verified by a Monte Carlo-based T_2NR simulation from MATLAB in Figure 4.5.

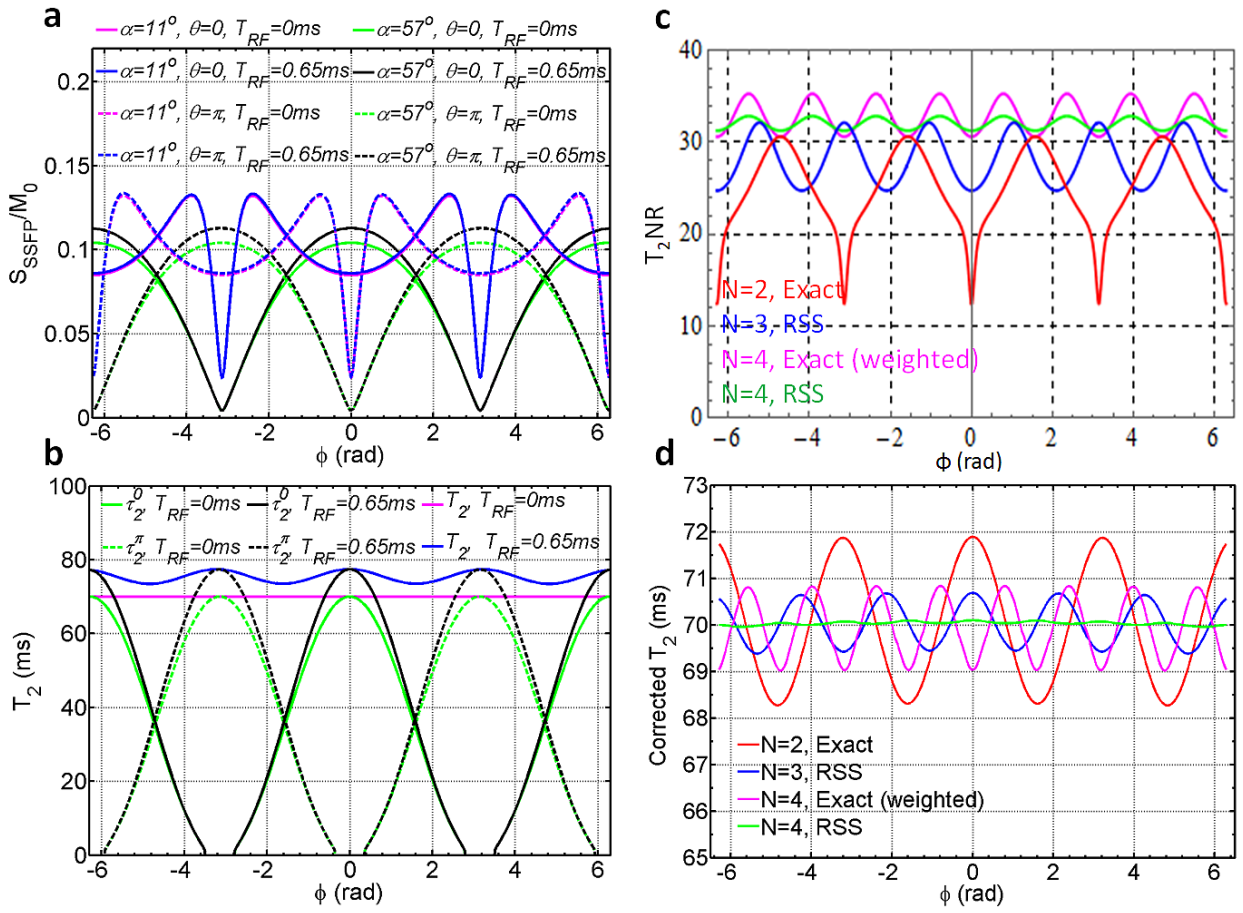

Figure 4.4: (a) Analytical plots of the bSSFP signal (using Eq. (4.1)), for two different phase offsets (θ=0/π) and flip angles (α_1/α_2=11/57°), as a function of the off-resonance phase ϕ, and with or without the effect of finite RF pulse (T_{RF}=0/0.65 ms, using Eqs. (4.13)−(4.14) for TR=4.6 ms in typical brain tissue (T_1/T_2=1000/70 ms). (b) Analytical τ_2^0, τ_2^π, and T_2 with or without finite RF pulse effects calculated from the bSSFP signals in (a) using Eqs. (4.5), and (4.9). (c) T_2NR plots (σ_1=10 ms, σ_s/M_0=0.002) calculated analytically using Eqs. (4.15)−(4.18). (d) Corrected T_2 assuming T_{RF}=0.65 ms after making the following substitutions: $TR \rightarrow TR_{eff} = TR - 0.498T_{RF}$ (in Eq. (4.9) for the exact solution with N=2 or N=4), and $TR \rightarrow TR_{eff} = TR - 0.555T_{RF}$ (in Eq. (4.4) for the RSS solution with N=3 or N=4), showing the remaining oscillations.

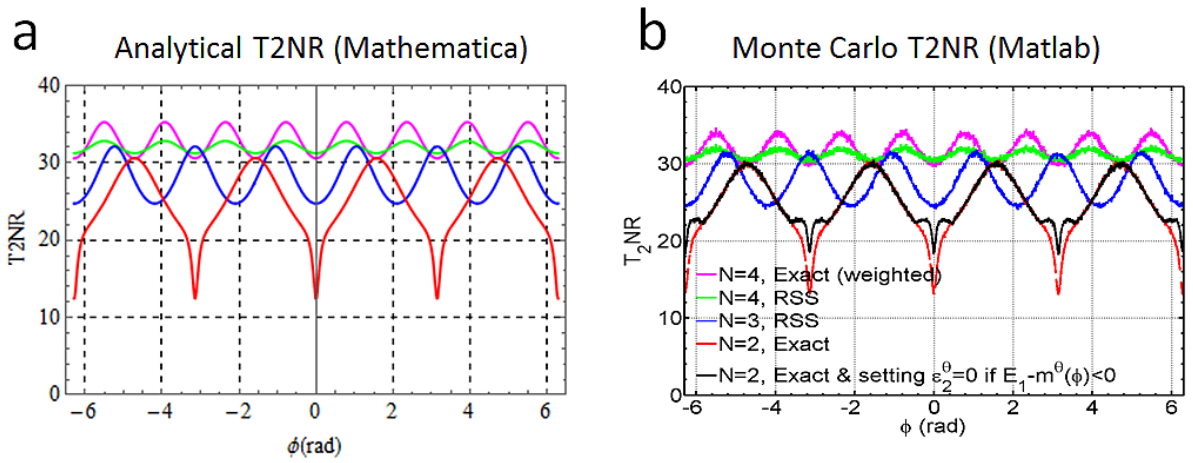

Figure 4.5: T_2NR derived analytically and plotted in Mathematical (a) compared to a Monte Carlo T_2NR simulation in MATLAB (b). Notice how assigning $\varepsilon_2^{\theta}=0$ wherever $E_1\text{-}m\leq 0$ (black curve in (b)) reduces the spike due to noise and mathematical singularity.

4.3 Methods

4.3.1 Phantom Measurements

Because banding artifacts are more easily identified in uniform gel phantoms than in vivo, DESPOT2 was first optimized on a phantom prior to being tested on volunteers. The phantom was built by pouring 7 different layers of agar solutions (7g/L) doped with varying concentrations of $MnCl_2$ (0–400 μM) into a plastic container (dimensions: 12×12×20 cm^3). Each layer was allowed to harden, then covered with cellophane wrap before pouring the next layer to prevent diffusion. The phantom was scanned on a 3T Philips Achieva scanner with an 8-channel head array, and T_1 maps were obtained using the DESPOT1 technique (scan time: 5 min per dataset) [88], utilizing a multi-echo SPGR acquisition. Flip angle non-uniformity was acquired using an Actual Flip Angle Imaging (AFI) sequence (scan time: 3 min) [63]. First-order shimming was performed automatically by the scanner as part of the preparation phase.

Two optimized DESPOT2 protocols were tested, each containing 2 flip angles by 4 phase offsets (= 8 datasets, scan time: ~2 min per dataset). The first protocol (bSSFP1) had short TR/T_{RF}, high bandwidths (517 Hz/pix) and flip angles (α_1/α_2=12/58°) chosen to cancel the MT effects in WM/GM as previously explained in the Theory. The second protocol (bSSFP2) was devised to

minimize the MT effects by employing long TR/T_{RF}, and lower flip angles (α_1/α_2=9/35°). The bandwidth was decreased, and parallel imaging (regularized SENSE [54]) acceleration increased to yield approximately the same SNR efficiency and scan time as the first protocol. Note that the phase offsets (θ = 0, π/2, π, 3π/2) were achieved by changing the transmit frequency f_{tr} according to Eq. (4.6), rather than by changing the phase-cycling scheme, and all RF pulses were non-selective. We found that changing the transmit frequency yields more accurate T_2 maps than changing the phase-cycling scheme because slow drifts in the Larmor frequency can be compensated for by automatic transmit frequency recalibration during the preparation phase of each scan.

To verify the accuracy of T_2, the phantom was also scanned with a 32-echo CPMG sequence to obtain comparative T_2 values in a 2D axial slice at the centre of the phantom. The T_2 values were obtained by fitting using the StimFit 1.0 MATLAB toolbox (http://mrel.usc.edu/). This method assumes single-component mono-exponential T_2 decay and uses extended phase graph (EPG) simulation to correct for both stimulated echoes and B_1 inhomogeneity effects [138]. An additional DESPOT2 experiment (bSSFP0) was also tested with parameters designed to minimize the effect of finite RF pulses. All pulse sequences tested on the phantom and their respective scan parameters are listed in Table 4.1.

All datasets were reconstructed and zero-padded to 3D image matrices of 256×256×180 in MATLAB using the ReconFrame package (Gyrotools, LLC, Switzerland). T_2 and ϕ maps were calculated using both the exact analytical solutions of Eqs. (4.9)−(4.10) and the RSS solution of Eq. (4.11) as summarized in the flowchart of Figure 4.2. A correction for finite RF pulse duration was also applied using the substitution $TR \rightarrow TR_{eff} = TR - \zeta_{corr} T_{RF}$ in Eq. (4.9) with ζ_{corr}=0.498 for the exact solution (with N even) and in Eq. (4.4) with ζ_{corr}=0.555 for the RSS solution (with N=3 or 4) as done similarly by Crooijmans and Bieri for N=1 [125], [136]. The T_2 was measured in 3D ROIs of 21×21×5 pixels at both a central and an off-centre location of each layer.

Performance of the proposed analytical corrections was compared with the DESPOT2-FM technique by implementing the stochastic region contraction (SRC) algorithm in MATLAB, and using the same parameters N_1=5000, N_2=25, and initial search space $0 \leq T_2 \leq 500$ ms and $0 \leq \phi \leq 2\pi$, described in Ref. [128]. Note that DESPOT2-FM is also governed by Eq. (4.1) and

thus does not account for finite RF pulse duration and MT effects. Additionally, M_0 was also allowed to vary freely as an optimization parameter, rather than factored out by normalizing the data [128]. On average, SRC converged in 4–7 iterations, and took ~19 ms per voxel. Finally, Eqs. (4.13)–(4.14c) were used to correct the resulting T_2 for finite RF pulse effects, as described in Ref. [137].

Pulse Sequence	Voxel Resolution (mm)	TR_1/TR_2 /TE/N_{echo} (ms)	α_1/α_2 (°)	T_{RF1}/T_{RF2} (ms)	BW (Hz/ pix)	SENSE Factors (AP×RL)	Δf_0 (Hz)
AFI	3.5×5.0×5.0	25/125/2.8/1	60/–	0.294/—	221	1.0×1.0	—
SPGRa	1.0×1.0×1.3	21/—/2.3n/8	5/25	0.026/0.12	517	1.4×1.2	—
SPGRb	1.0×1.0×1.5	24/—/2.3n/9	5/25	0.026/0.12	517	1.2×1.2	—
bSSFP0	1.2×1.2×1.2	9.2/—/4.6/1	11/57	0.058/0.28	517	1.0×1.0	27.17, 81.52
bSSFP1	1.1×1.1×1.1	4.8/—/2.4/1	12/58	0.064/0.55	517	1.2×1.0	0, 52.08, 104.17, 156.25
bSSFP2	1.1×1.1×1.1	9.0/—/4.5/1	9/35	0.59/2.0	271	1.5×1.5	0, 27.78, 55.56, 83.33
bSSFP3	1.0×1.0×1.2	4.4/—/2.2/1	11/57	0.058/0.60	517	1.0×1.0	0, 75.76, 151.52
CPMG*	1.2×1.2×5.0	2000/—/15n/32	90/—	—/—	217	1.0×1.0	—

Table 4.1: MRI scan parameters used both on the phantom and in vivo. Except for the 2D CPMG scan, the field-of-view was 240×240×170 cm^3, and hard, non-selective RF pulses were used in all cases. *Note that for CPMG in vivo the echo spacing was 10 ms.

4.3.2 In Vivo Measurements

Informed consent was obtained and a healthy 30 year-old male volunteer was scanned using the same DESPOT1 and DESPOT2 protocols used on the phantom (Table 4.1). Eight volunteers (4 males and 4 females aged 21–30 years) were also scanned as part of a reduced examination protocol of ~27 min duration, comprising the same AFI sequence as in Table 4.1, but with different SPGR (T_{scan}~12 min) and bSSFP (T_{scan}~12 min) scan parameters, denoted as SPGRb, and bSSFP3. For each subject, the T_2 (calculated using the approximate RSS solution with $N=3$), the T_1 and the T_2^* were measured in ROIs of different brain regions, with and without the correction for finite RF pulse duration. The global mean T_2 was also measured in 4 different

tissue classes (GM, WM, adipose, and muscle) by segmenting the brain using thresholds based on the T_1 histogram [106]. Note that one of the volunteers was the same subject (v2) for which the protocols in Table 4.1 were tested, thus enabling further comparisons to be made between the bSSFP1 and bSSFP2 protocols. For this volunteer, 2D spin-echo (SE) images were also acquired (same transverse slice location as the CPMG) with the following parameters: FOV=170×240 mm^2, resolution=1.2×1.2×5 mm, TE=15, 30, 45, 60, 75 and 105 ms, TR=1500 ms, scan time=3:30 min per image). Images acquired at varying TEs were least-squares fitted pixelwise to a mono-exponential to obtain another T_2 map. For this volunteer SRC fitting was also performed on both bSSFP1 and bSSFP2 data using the same initial conditions as for the phantom.

Each in-vivo 3D dataset was exported into 3D slicer [101] and co-registered to correct mismatches arising from slight head motion during the examination. Curve-fitting in MATLAB takes only ~20 s per subject (excluding the image reconstruction time) on a PC with an Intel Core i7-3770 CPU and 32GB of RAM.

4.4 Results

4.4.1 Phantom Measurements

Phantom bSSFP images and profiles of the calculated T_2 are shown in Figure 4.6 for the DESPOT2 protocol with the longer TR=9.2 ms, and short T_{RF2}=0.28 ms. The resulting T_2 is compared to that of the protocol with a longer T_{RF2}=2.0 ms. As predicted by the theory, stretching the RF pulse duration leads to more significant oscillations in the final T_2 (dashed black curve). Moreover, since the measured B_1 field homogeneity is altered by the spatial-spectral effects of the long T_{RF}, the T_2 calculated from bSSFP2 with TR/T_{RF2}=9.0/2.0 ms is systematically underestimated at the edges of the phantom (Figure 4.6(d)).

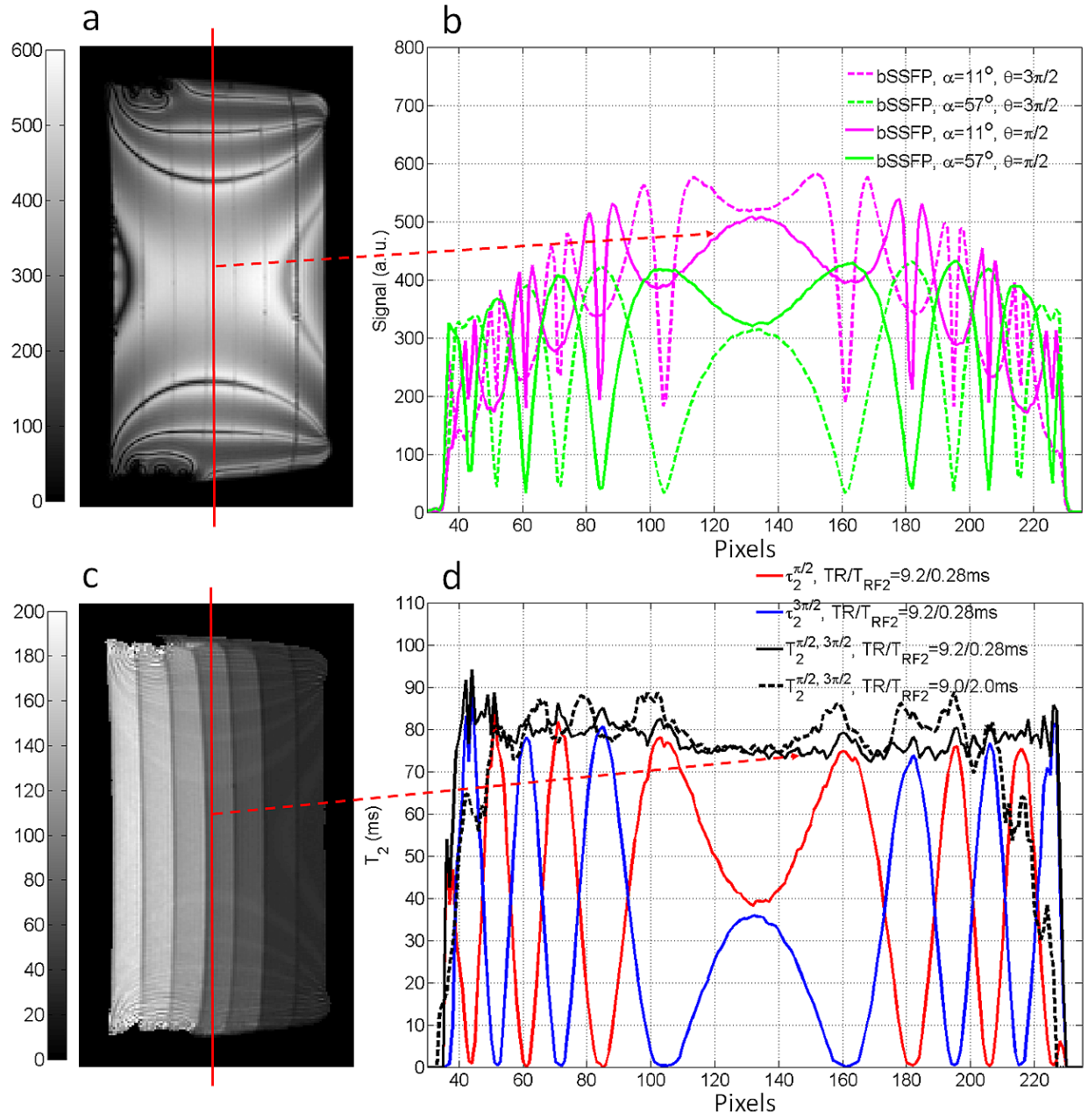

Figure 4.6: (a) bSSFP0 image at α=11°, θ=π/2 and TR=9.2 ms. (b) Signal profile through the image in (a), displaying all four bSSFP signals. (c) Analytical T_2 map (with short T_{RF}) calculated using the four bSSFP datasets, the T_1 and the c_{RF} maps. (d) Profile through the T_2 map in (c), displaying both τ_2 signals, the final T_2 with TR/T_{RF2} =9.0/0.28 ms (solid black curve) and T_2 with TR/T_{RF2}=9.0/2.0 ms (dashed black curve).

Sagittal slices of the τ_2 maps are shown in Figure 4.7, along with the T_2 calculated with the exact solution of Eq. (4.9), the exact weighted solution of Eq. (4.10), the RSS solution of Eq. (4.11), and SRC fitting technique, for both DESPOT2 protocols. A profile through a single layer (red line) is also plotted in the bottom row to visualize the differences between the analytical methods and the SRC-based T_2 fits. At short T_{RF2}=*0.55* ms (bSSFP1), and N=*2*, SRC shows fewer oscillations than the analytical methods. However, with N=*4*, these differences disappear. At long T_{RF2}=2 ms (bSSFP1), all methods exhibit oscillations, and the RSS solution performs best as predicted in Figure 4.4(d). The finite RF pulse correction applied following SRC at long T_{RF2}=2.0 ms also appears to over-correct T_2, as visible in the profiles. Furthermore, the T_2 from SRC oscillates between large over- and under-estimation in regions of spatial-spectral effects (green arrows), while the analytical solution yields a gradual under-estimation in T_2. The percent difference between the exact-weighted T_2 solution and the RSS solution with N=4 is also shown as colored intensity in both Figure 4.7(a) and (b). Differences range within ±3% for short T_{RF2} in (a) and ±6% for long T_{RF2} in (b), with the RSS solution exhibiting fewer oscillations.

The cosine or sine of the phase maps calculated from Eq. (4.9b) are displayed in Figure 4.8 for both DESPOT2 protocols. The arrows indicate minor discontinuities within the phase, caused by slight mismatches in the locations of the bands across the different bSSFP datasets (also leading to a spike or edge in the T_2 (red arrow in Figure 4.7(a)) that are attributed to hardware imperfections or drifts [124] and noise, accentuated by bSSFP signal instability (24). However, they do not appear in the RSS T_2 map of Figure 4.7 thus demonstrating that four phase offsets provide sufficient robustness against these imperfections, in addition to the expected gain in T_2NR.

Average T_2 measured in centered and off-center ROIs are displayed in Figure 4.9. In both cases the T_2 values derived from both the bSSFP1and bSSFP2 protocols compare well with CPMG with a mean absolute difference of ~4.9-7.4% for bSSFP1 and ~3.6-6.4% for bSSFP2 across all the layers, and among the four T_2 maps.

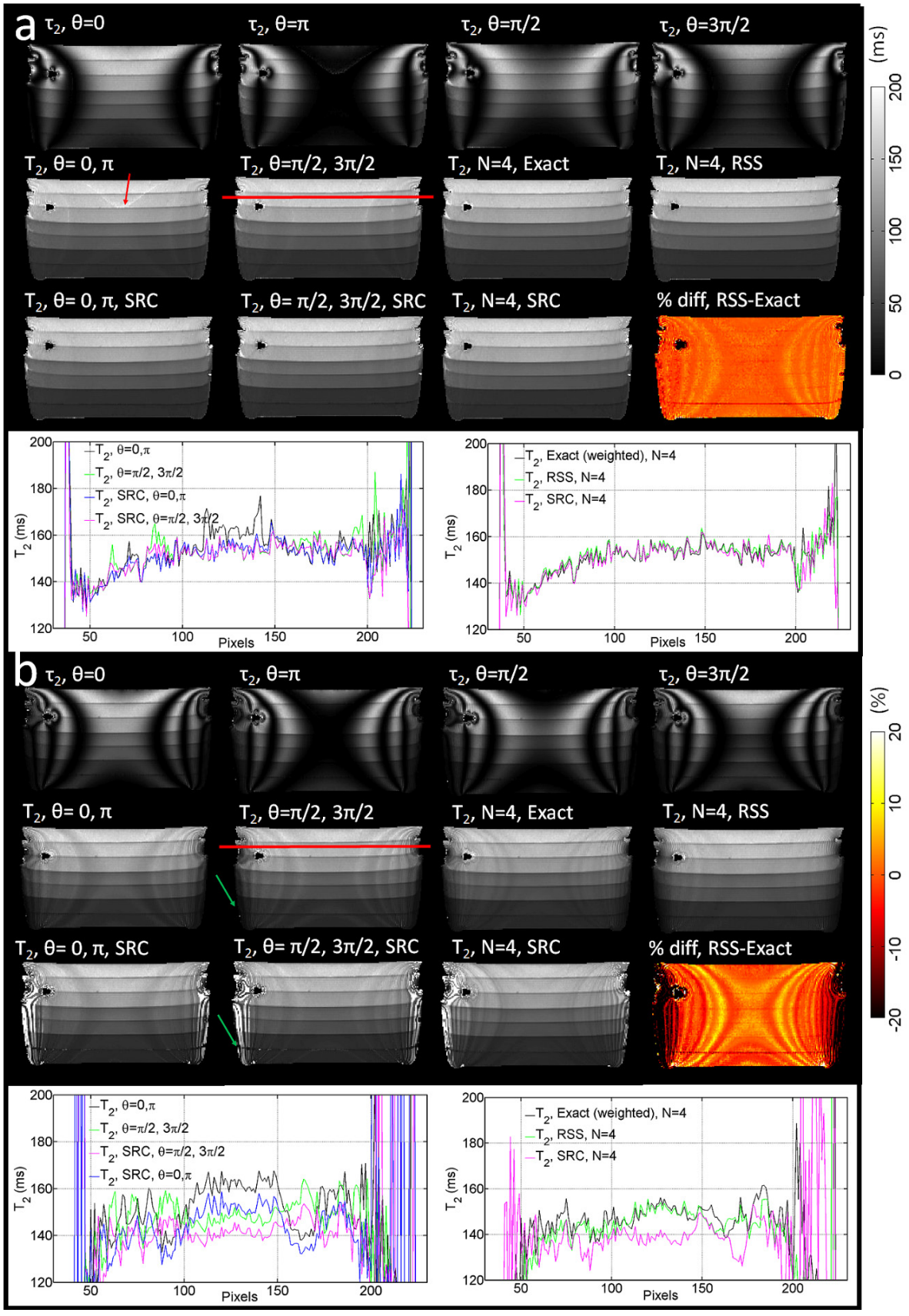
a
τ2, θ=0
τ2, θ=π
τ2, θ=π/2
τ2, θ=3π/2
T2, θ= 0, π
T2, θ=π/2, 3π/2
T2, N=4, Exact
T2, N=4, RSS
T2, θ= 0, π, SRC
T2, θ= π/2, 3π/2, SRC
T2, N=4, SRC
% diff, RSS-Exact
(ms)
T2, θ=0,π
T2, θ=π/2, 3π/2
T2, SRC, θ=0,π
T2, SRC, θ=π/2, 3π/2
T2 (ms)
Pixels
T2, Exact (weighted), N=4
T2, RSS, N=4
T2, SRC, N=4
b
(%)

Figure 4.7: (a) Sagittal phantom images of the τ_2 and T_2 maps obtained from the bSSFP1 protocol, and (b) the bSSFP2 protocol (Table 4.1). Results from SRC (DESPOT2-FM) technique are shown in the third row for both (a) and (b), and profiles through the 6th layer (red line) are shown to illustrate the differences. The colored intensity maps are percent difference between the exact-weighted and RSS solutions (N=4). The red arrow indicates an edge in T_2 arising from a combination of noise, mathematical singularity, and hardware imperfections, while the green arrows point to spatial-spectral effects.

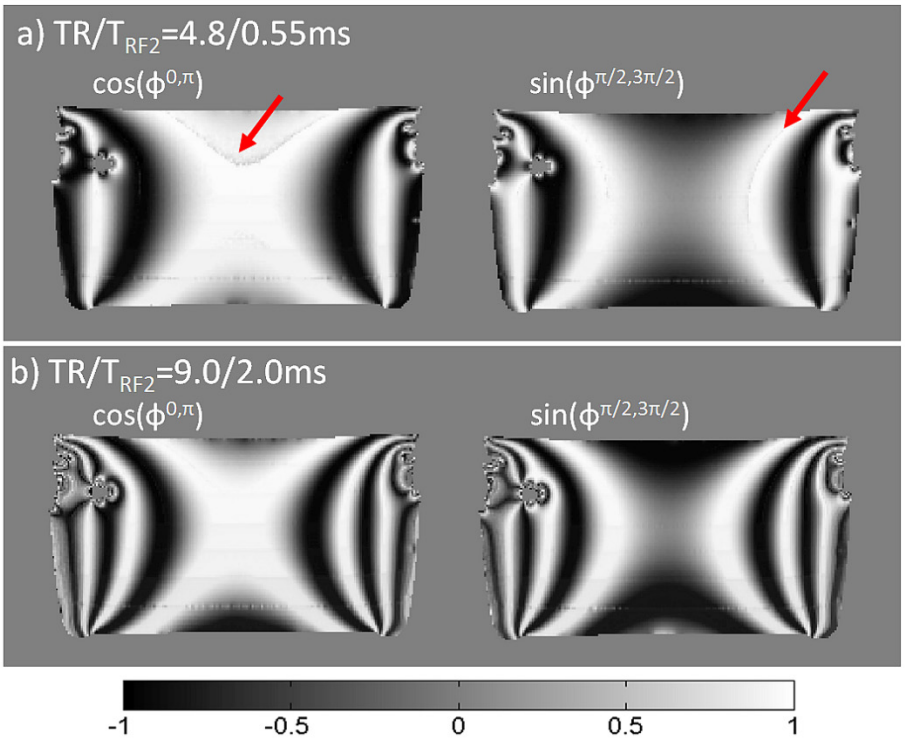

Figure 4.8: *Sin* ϕ and *cos* ϕ maps derived analytically using Eqs. (4.9)−(4.10) from (a) the bSSFP1 protocol, and (b) from the bSSFP2 protocol. Arrows indicate discontinuities (slight mismatches in band locations across the different bSSFP datasets) due to noise and hardware imperfections that are magnified by signal instabilities [134].

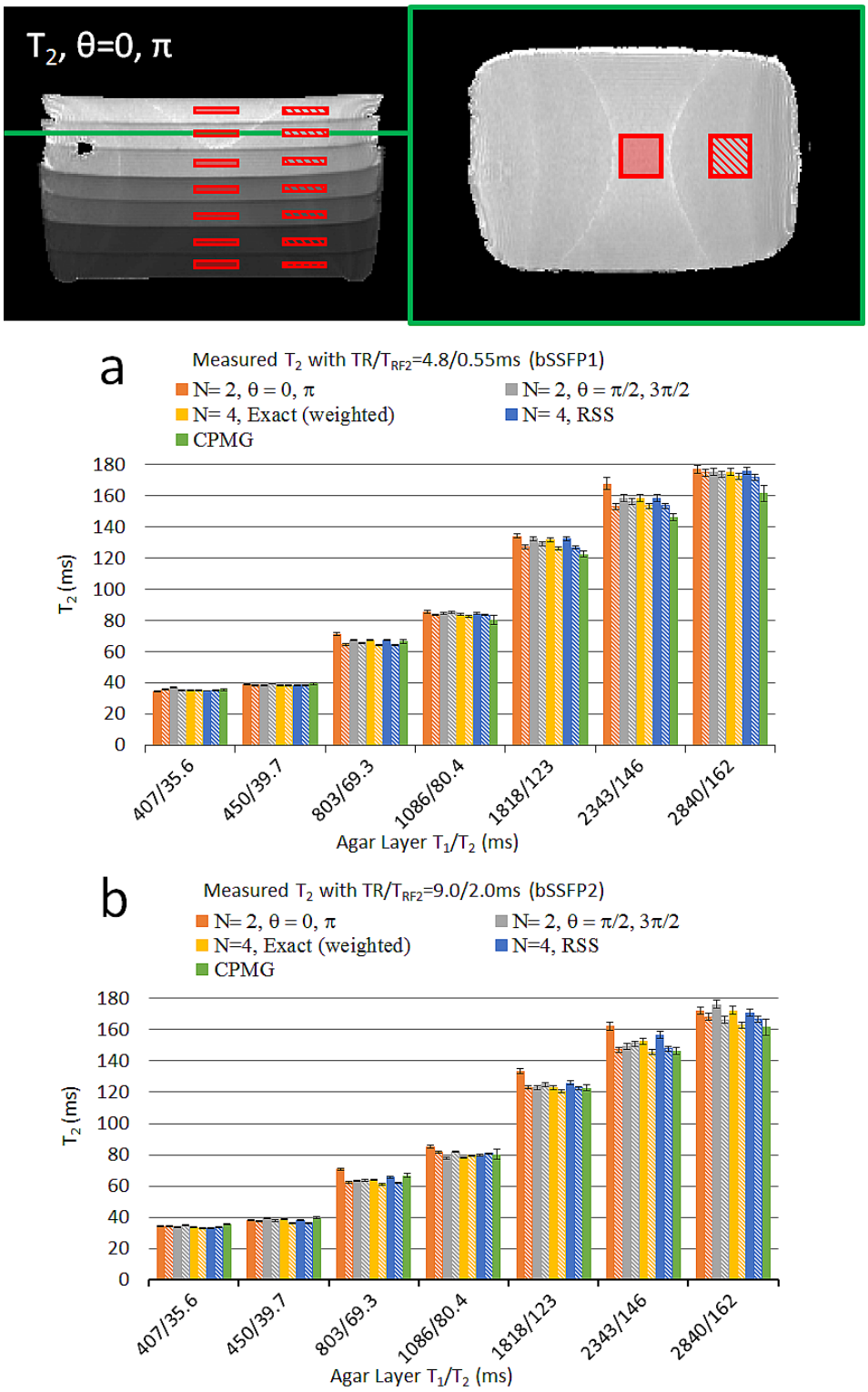

Figure 4.9: Measured T_2 in both central (solid bar) and off-center (hatched) ROIs in each layer of the phantom for the DESPOT2 protocol with (a) short TR/T_{RF} (bSSFP1) and (b) long TR/T_{RF} (bSSFP2). For comparison the T_2 measured using the 32-echo CPMG is also displayed in green.

4.4.2 In vivo Measurements

Sagittal τ_2 and T_2 maps for the two in vivo DESPOT2 protocols are displayed in Figure 4.10(a) and (b), respectively, along with T_2 from SRC. The volunteer has a metallic dental retainer which induces a signal void and tight banding artifacts within the mouth. Observe how stretching the RF pulse in (b) also acts as a fat-suppression technique, making it impossible to measure the T_2 of adipose. Equivalent SNR efficiency to the bSSFP1 protocol was achieved by decreasing the sampling bandwidth (from 517 to 271 Hz/pix). In contrast to the uniform phantom, residual oscillations within the T_2 maps obtained with long TR/T_{RF} are well below the anatomical contrast and are thus negligible, except behind the metal retainer.

Sagittal T_1 and T_2 maps of the eight volunteers are shown in Figure 4.11. Hardware imperfections result in some errors in T_2, especially in the neck area, and close to dental braces or retainers (especially in volunteers v2, v7 and v8).

Figure 4.12 compares axial T_1 and T_2 maps from the three bSSFP, the two SPGR and the CPMG protocols listed in Table 4.1. The histograms of all five T_2 images are displayed for comparison, revealing how the three different DESPOT2 protocols yield comparable mean T_2 of ~50 ms in WM, the SE-based T_2 fit yields WM T_2 ~60 ms, while the mono-exponential fit from CPMG yields a significantly longer T_2 ~70 ms (corrected using StimFit). Crooijmans et al. also reported a mean WM T_2 of ~61 ms using a similar SE-based mono-exponential T_2 fit [125]. The longer T_2 measured by CPMG, which is not observed in the agar phantom measurements (Figure 4.9), is consistent with in vivo literature values obtained using a comparable CPMG sequence and curve-fitting method [139].

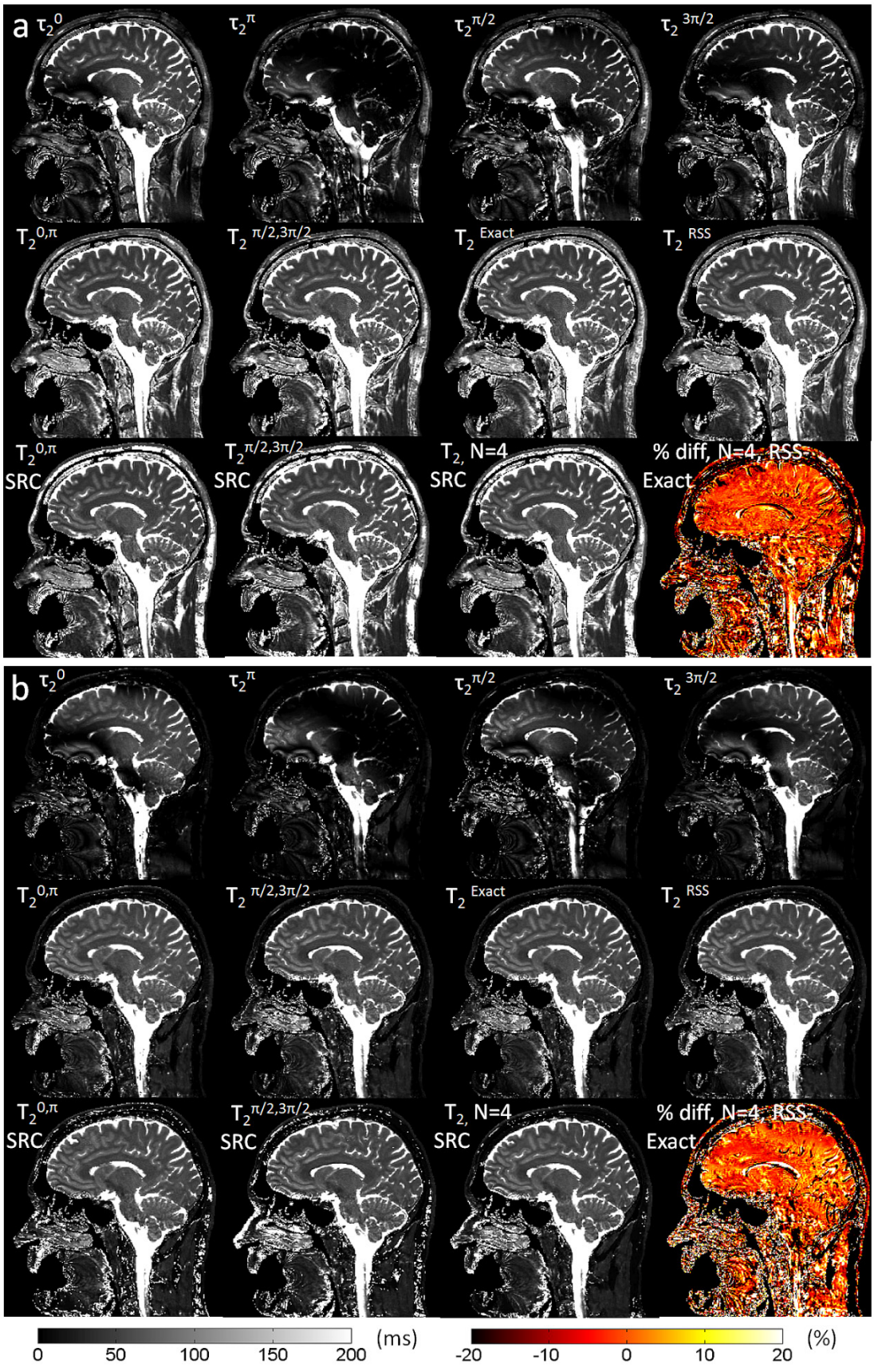
a
τ_2^0
τ_2^π
$\tau_2^{\pi/2}$
$\tau_2^{3\pi/2}$
$T_2^{0,\pi}$
$T_2^{\pi/2,3\pi/2}$
T_2 Exact
T_2 RSS
$T_2^{0,\pi}$ SRC
$T_2^{\pi/2,3\pi/2}$ SRC
T_2, N=4 SRC
% diff, N=4, RSS Exact
b
τ_2^0
τ_2^π
$\tau_2^{\pi/2}$
$\tau_2^{3\pi/2}$
$T_2^{0,\pi}$
$T_2^{\pi/2,3\pi/2}$
T_2 Exact
T_2 RSS
$T_2^{0,\pi}$ SRC
$T_2^{\pi/2,3\pi/2}$ SRC
T_2, N=4 SRC
% diff, N=4, RSS Exact
0 50 100 150 200 (ms)
-20 -10 0 10 20 (%)

Figure 4.10: (a) In vivo (volunteer v2) τ_2 corresponding to four different phase offsets (θ=0, π, π/2, and 3π/2) and T_2 maps (calculated using the same techniques, including Stochastic Region Contraction (DESPOT2-FM), as for the phantom in Figure 4.7) from bSSFP1 protocol (Table 4.1). (b) Same maps in (a) obtained from the bSSFP2 data.

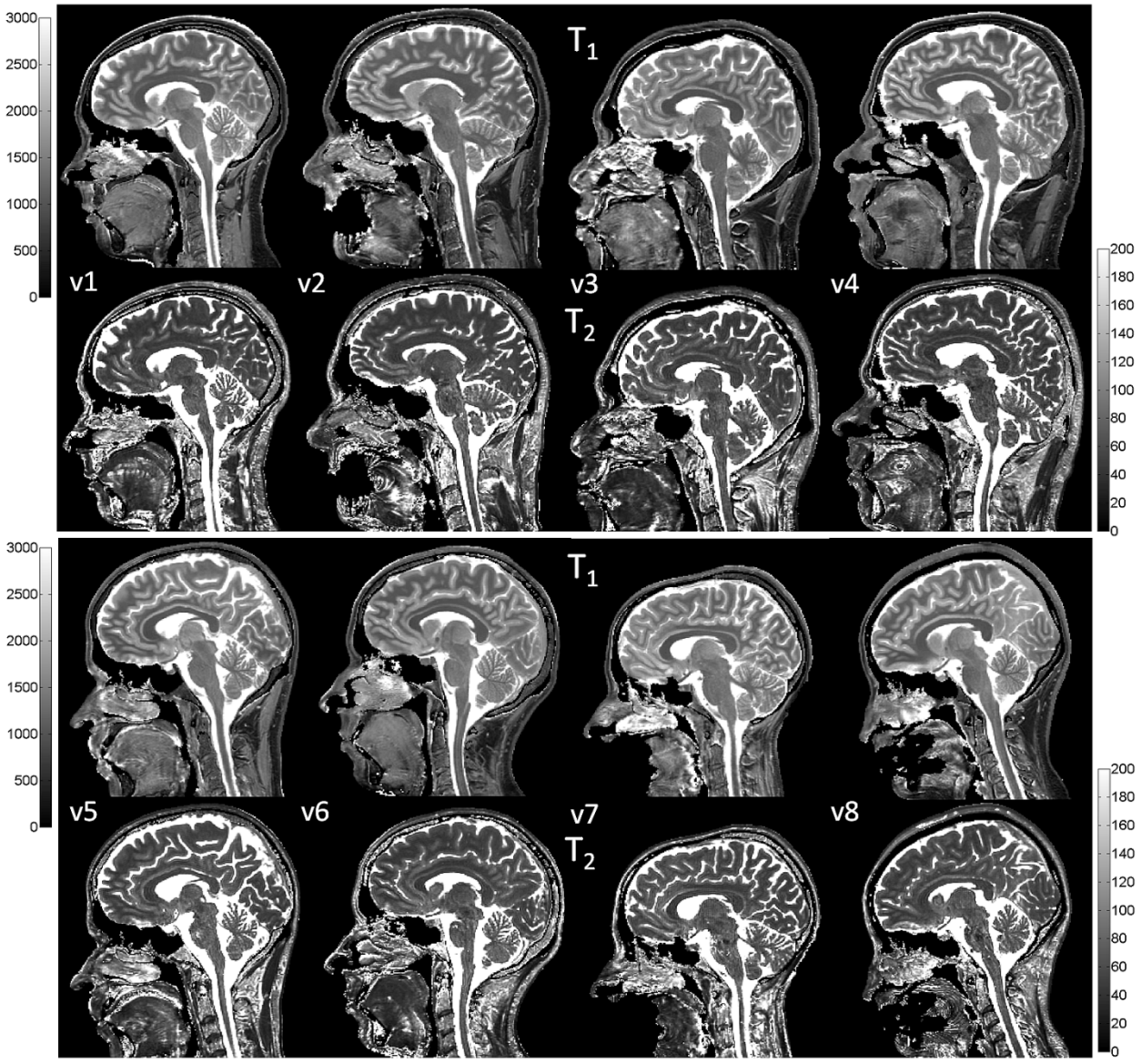

Figure 4.11: In vivo sagittal T_1 and T_2 maps (in ms) of the 8 volunteers scanned with protocols SPGRb and bSSFP3 (Table 4.1). Volunteers v2, v7, and v8 have signal voids in the mouth due to dental braces or metal retainers.

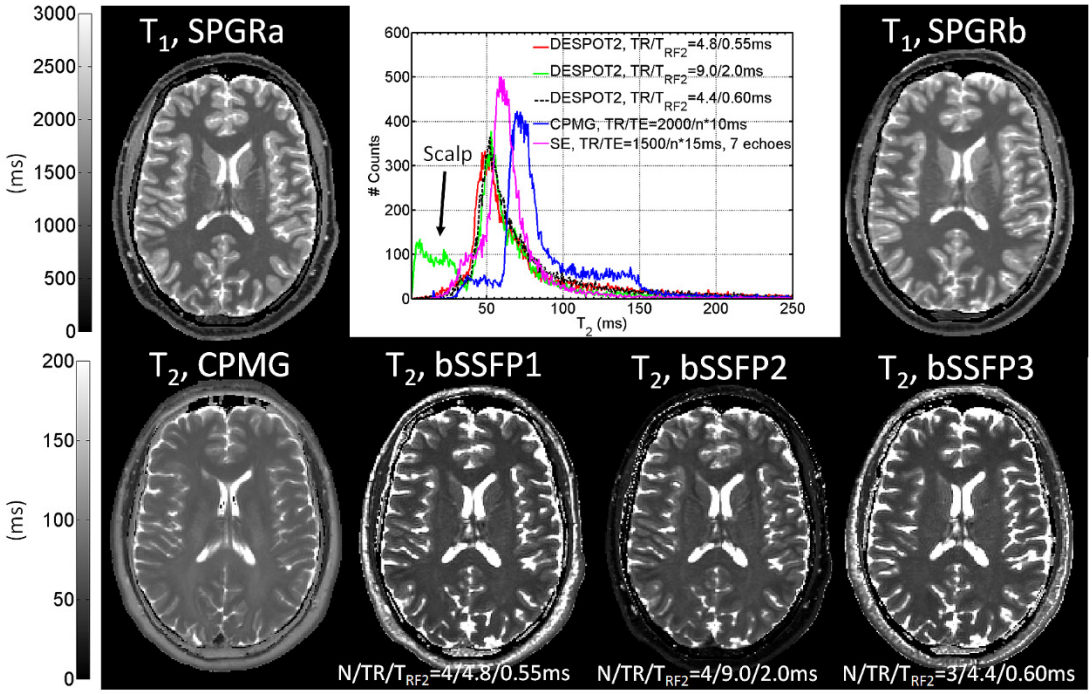

Figure 4.12: Axial T_1 maps from DESPOT1 (with SPGRa and SPGRb protocols), and T_2 from DESPOT2 (bSSFP1, bSSFP2 and bSSFP3 protocols in Table 4.1) compared to CPMG (single-component, mono-exponential fit), along with all 5 T_2 histograms for volunteer v2. Observe how the SE-based T_2 (WM T_2~60ms) lies between the DESPOT2 (WM T_2~50ms) and CPMG measurements (WM T_2~70ms). Spatial-spectral RF pulse effects in bSSFP2 cause underestimated T_2 in the scalp (arrow).

The mean T_2 and standard deviation of various tissue types and brain organs were measured and averaged across the 8 volunteers for the SPGRb and bSSFP3 protocols. They are listed (with and without finite RF pulse correction) in Table 4.2 and compared to reported literature values, including previous DESPOT2 implementations at 1.5T [84], [10], [125] and 3T [128]; and CPMG-based T_2 quantification accounting for stimulated echoes at 3T [139], and 4.7T [138]. The values reported in bold (or superscript e) correspond to the DESPOT2-FM technique of Deoni at 3T, with $\alpha_1/\alpha_2/TR$ =15/65°/4.2 ms [128]. Previous DESPOT2 implementations [84], [128], [10], did not include finite RF pulse corrections and thus they agree closely with our *uncorrected* T_2 measurements. Table 4.2 also includes the T_1 values because the accuracy of T_2 in DESPOT2 also depends on the T_1. As a consistency check we also provide the $T_2^* \leq T_2$ measured by ordinary least-squares mono-exponential fit on the multi-echo SPGR datasets as shown in Ref. [11].

Organ / Tissue	Corr. T_2 (ms)	Uncorr. T_2 (ms)	Literature T_2 (ms)		T_2^* (ms)	T_1 (ms)
			1.5 T	3 T, 4.7T[g]		
Putamen	62.7 (2.4)	67.6 (2.5)	71(7)[b]	**69(3)**[e], 57(3)[f], 55(3)[g]	45.2 (4.4)	1442 (85)
Caudate	72.9 (3.2)	78.4 (4.0)	89(6)[a], 75(8)[b], 59[c], 59(3)[d]	**82(3)**[e], 63(5)[f], 60(3)[g]	49.0 (3.9)	1563 (83)
Splenium	54.7 (3.8)	58.8 (4.2)	43(1)[d]	64(4)[g]	40.2 (1.9)	1027 (63)
Genu	48.8 (2.4)	52.4 (2.7)			38.3 (2.9)	956 (43)
Globus Pallidus	50.4 (3.3)	54.2 (3.6)		45(1)[f], 38(2)[g]	29.8 (2.8)	1212 (47)
Frontal WM R	47.7 (2.4)	51.2 (2.6)	53(4)[b], 40(2)[d]	**50(2)**[e], 53(8)[f], 53(3)[g]	41.8 (2.9)	986 (42)
Frontal WM L	47.6 (2.1)	51.1 (2.3)	53(4)[b], 40(2)[d]	**50(2)**[e], 53(8)[f], 53(3)[g]	41.7 (2.9)	983 (33)
Occipital WM R	53.8 (2.7)	57.8 (3.0)		55(1)[g]	45.1 (2.2)	1020 (35)
Occipital WM L	51.8 (1.6)	55.7 (1.8)		55(1)[g]	44.0 (1.6)	1024 (36)
WM (mean)	50.6 (1.3)	54.4 (1.4)	54(4)[a], 45[c]		45.7 (1.5)	1057 (34)
GM (mean)	67.0 (2.1)	71.8 (2.0)	71(28)[d]		56.3 (2.5)	1544 (81)
Muscle (mean)	36.5 (2.3)	39.3 (2.5)	35(4)[h]	32(2)[h]	22.8 (0.8)	1327 (49)
Adipose (mean)	99.1 (4.6)	106 (5)	165(6)[h]	133(5)[h]	NA	427 (20)

Table 4.2: Corrected and uncorrected T_2 (and standard deviations) in various brain regions across the 8 volunteers. The mean tissue values were measured from segmented T_2 histograms, while the regional values were measured in ROIs identified manually. References are: a:[84], b:[10], c:[125], d:[47], e:[128], f:[139], g:[138], h:[140]. Values in bold are from DESPOT2-FM (see text). Note that the T_2^* of adipose cannot be measured by simple mono-exponential fit due to J-coupling. T_2 mapping techniques employed include CPMG (f, g, h), and DESPOT2 (a, b, c, d, e).

4.5 Discussion and Conclusions

In this study, we have derived general analytical solutions to remove band artefacts in DESPOT2 using any number of phase offsets greater than one, along with a mathematical analysis of the T_2 and T_2NR values. These expressions reduce processing time (using a standard PC) to merely a few seconds for a volume containing ~11.8 M voxels.

We have shown that using a greater number of phase offsets increases the T_2NR both in magnitude and in uniformity with respect to the off-resonance phase ϕ. For brevity, phantom T_2 maps derived from three phase offsets ($N=3$) were not presented, but accuracy and SNR results generally lie between the $N=2$ and $N=4$ case. The technique readily accommodates additional phase offsets and more than two flip angles to improve T_2 accuracy, uniformity, and/or SNR.

In the phantom, MT effects with low concentrations of agar (7g/L) attenuate the bSSFP signal only by ~0–4% and can thus be ignored. However, in vivo MT effects are significant and two approaches were tested to remove them: selecting flip angles (α=12°/58°) to cancel the MTR of the bSSFP signals and stretching the RF pulse durations while using lower flip angles (α=9°/35°). The preferred approach depends on the application, but if more than two flip angles are to be acquired (as in mc-DESPOT [137]), then stretching the RF pulse duration is the only option (provided the spatial-spectral effects of long T_{RF} are not a concern), since cancelling the MTR is possible only using two flip angles.

The three DESPOT2 protocols tested in this study yield a comparable mean WM T_2 of ~50 ms (T_2 histogram of Figure 4.12) in volunteer v2, despite significantly different bSSFP scan parameters (N, TR, α and T_{RF}). Conversely, the mean WM T_2 measured using single-echo spin echo at varying TE, fitted to a mono-exponential model, was longer (WM T_2 ~60 ms), and that using a 32-echo CPMG was even longer (WM T_2 ~70 ms). One reason for these discrepancies is that the CPMG and SE signals are complicated functions of T_1, T_2, α, slice profiles, B_0, MT, diffusion, TE and TR. A simple mono-exponential fit with CPMG is especially prone to overestimation of the true T_2 because of the presence of stimulated echoes [138] and more elaborate fitting procedures must be employed, such as Bloch equation simulations [141], EPG simulations [138], or using a generating function [139]. A second explanation for these discrepancies lies in the existence of different water proton T_2 compartments ("pools"), known to exist especially in WM [142], [36]. Assuming a single-component T_2 relaxation in the presence of three pools yields a different *apparent* T_2 depending on the sequence, i.e., each sequence applies a stronger weighting of a different component (such as the myelin water $T_{2,M}$), over the other two components (i.e., intra-cellular and extra-cellular T_2 pools of axonal water) [10]. In fact, Crooijmans et al. [125] prefer to speak of a *spectrum* of T_2 values, and also observed that the in vivo WM single-component T_2 at 1.5 T from DESPOT2 is significantly lower (~45 ms)

than that from single-echo spin echo (~61 ms). They attribute this difference to the complex tissue microstructure that results in a broad spectrum of T_2 values, which different pulse sequences (i.e., bSSFP vs. spin echo) "see" with different weightings. In the case of simple chemical environments like agar gel, there is a single pool (or narrower spectrum) of water T_2, and thus both bSSFP and spin echo sequences measure the same T_2. This effect is also discussed by Stanisz et al. for CPMG data [143], where the T_2 from a mono-exponential fit corresponds to the arithmetic mean T_2 (~70 ms in WM) of a multi-exponential fit.

The measured T_2 values listed in Table 4.2 compare well with literature values, including those of Deoni et al. [84], [10], where finite RF pulse and MT effects were not corrected (WM T_2~54 ms), and those of Crooijmans et al. with corrections (WM T_2~45 ms) [125], [47]. We note that the latter employ only one phase offset while higher-order shimming minimizes off-resonance effects; therefore the measured T_2 is likely lower due to some residual off-resonance bias (Figure 4.1b). The application of the finite RF pulse correction systematically lowers the T_2 by about ~7.5%, further biasing it from the reported CPMG T_2 values (WM T_2~53-55ms). Although this remaining discrepancy might be explained by residual MT bias, and/or sequence-dependent weighting [125], recent work [144] has shown that T_2 mapping based on EPG simulations of CPMG still overestimates T_2 in vivo by 3–5%, with respect to the full Shinnar Le Roux-based modelling.

Finally, proton density (M_0) maps corrected for banding artifacts can also be obtained analytically from DESPOT2 using even N (see, Figure 4.14 and Figure 4.15). Moreover, field inhomogeneity maps (ΔB_0), could be obtained by taking the inverse sine or cosine of Eq. (4.9b), unwrapping the phase, and then substituting into Eq. (4.6). However, as explained in Appendix D, M_0 is more easily and accurately obtained from the DESPOT1/VFA technique [90], [93], and robust techniques for mapping ΔB_0 already exist.

4.6 Appendix

4.6.1 A. Derivation of Eq. (4.5)

The SSFP signal is defined as the magnitude of Eq. (4.1), which simplifies to

$$S_{SSFP}(\alpha,\phi,TR)=\frac{M_0\sqrt{E_2}(1-E_1)\sin\alpha\sqrt{1+2E_2\cos\phi+E_2^2}}{E_2(1-E_1)(1+\cos\alpha)\cos\phi+1-E_1\cos\alpha-E_2^2(E_1-\cos\alpha)} \quad \text{(A4.1)}$$

To calculate the slope m, assuming the on-resonance linearized equation (Eq. (4.3)), we must simplify

$$m(\phi,\alpha_1,\alpha_2,TR)=\frac{\frac{S_{SSFP}(\alpha_1,\phi,TR)}{\sin\alpha_1}-\frac{S_{SSFP}(\alpha_2,\phi,TR)}{\sin\alpha_2}}{\frac{S_{SSFP}(\alpha_1,\phi,TR)\cos\alpha_1}{\sin\alpha_1}-\frac{S_{SSFP}(\alpha_2,\phi,TR)\cos\alpha_2}{\sin\alpha_2}} \quad \text{(A4.2)}$$

Assuming $-\pi\le\phi\le\pi$, and $0\le\alpha_{1,2}\le\pi/2$, the above simplifies to

$$m(\phi,TR)=\frac{E_1-E_2^2-E_2(1-E_1)\cos\phi}{1-E_1E_2^2+E_2(1-E_1)\cos\phi} \quad \text{(A4.3)}$$

Substituting m into Eq. (4.4), yields Eq. (4.5).

4.6.2 B. Derivation of Eq. (4.9)

Rearranging Eq. (4.5) to remove the logarithm, and accounting for a phase offset θ_n we have

$$\epsilon_2^{\theta_n}=\frac{E_2+\cos(\phi+\theta_n)}{E_2^{-1}+\cos(\phi+\theta_n)} \quad \text{(B4.1)}$$

which can be rearranged as $E_2^2+E_2\left(1-\epsilon_2^{\theta_n}\right)\cos(\phi+\theta_n)-\epsilon_2^{\theta_n}=0$. Choosing θ_1=0, and θ_2=π, we obtain a system of two equations

$$\begin{aligned}E_2^2+E_2(1-\epsilon_2^0)\cos(\phi)-\epsilon_2^0=0\\ E_2^2-E_2(1-\epsilon_2^\pi)\cos(\phi)-\epsilon_2^\pi=0\end{aligned} \quad \text{(B4.2 a, b)}$$

Subtracting the equations we obtain

$-E_2\cos\phi\,(1-\epsilon_2^0)-E_2\cos\phi\,(1-\epsilon_2^\pi)=\epsilon_2^0-\epsilon_2^\pi \implies -E_2\cos\phi\,(2-\epsilon_2^0-\epsilon_2^\pi)=\epsilon_2^0-\epsilon_2^\pi.$

Solving for cos ϕ from the top equation and substituting results in

$$E_2^2=\frac{\epsilon_2^0-2\epsilon_2^0\epsilon_2^\pi+\epsilon_2^\pi}{2-\epsilon_2^0-\epsilon_2^\pi} \quad \text{(B4.3)}$$

Taking the logarithm on both sides and rearranging yields Eq. (4.9a), while Eq. (4.9b) is obtained by substituting for E_2 in the expression for cos ϕ. It can be shown in general that for any two phase offsets θ_1 and θ_2, such that $\theta_2-\theta_1=\pi$, the solution is

$$T_2 = -TR \Big/ \log\left(\sqrt{\frac{2\epsilon_2^{\theta_1}\epsilon_2^{\theta_2} - \epsilon_2^{\theta_1} - \epsilon_2^{\theta_2}}{\epsilon_2^{\theta_1} + \epsilon_2^{\theta_2} - 2}}\right),$$

$$\cos(\phi - \theta_1) = \frac{\epsilon_2^{\theta_1} - \epsilon_2^{\theta_2}}{\sqrt{\left(\epsilon_2^{\theta_1} + \epsilon_2^{\theta_2} - 2\right)\left(2\epsilon_2^{\theta_1}\epsilon_2^{\theta_2} - \epsilon_2^{\theta_1} - \epsilon_2^{\theta_2}\right)}} \quad \text{(B4.4 a, b)}$$

While $\cos(\phi\text{-}\theta)$ is elegantly expressed above solely in terms of ε_2^{θ}, the following solution (obtained by simply rearranging Eq. (4.5)) is preferred to avoid phase-wrapping in regions of low SNR:

$$\cos(\phi - \theta_1) = \frac{\epsilon_2^{\theta_1} - E_2^2}{E_2(1 - \epsilon_2^{\theta_1})} \quad \text{(B4.5)}$$

4.6.3 C. Derivation of Eq. (4.16)

The partial derivative (with respect to T_1) in Eq. (4.15) is calculated from Eq. (4.4)

$$T_2 = \tau_2(0) = -TR/\log\left(\frac{m - E_1}{mE_1 - 1}\right) \quad \text{(C4.1)}$$

Obtaining

$$\frac{\partial T_2}{\partial T_1} = \frac{E_1(m^2 - 1)TR^2}{(1 - mE_1)(m - E_1)T_1^2 \log^2\left(\frac{m - E_1}{mE_1 - 1}\right)} \quad \text{(C4.2)}$$

Substituting into the above $m = (E_1 - E_2)/(1 - E_1E_2)$, and simplifying results in

$$\frac{\partial T_2}{\partial T_1} = \frac{E_1(1 - E_2^2)T_2^2}{E_2(1 - E_1^2)T_1^2} \quad \text{(C4.3)}$$

For the other two derivatives with respect to *S*, we apply the chain rule:

$$\frac{\partial T_2}{\partial S_i} = \frac{\partial T_2}{\partial m}\left(\frac{\partial m}{\partial y_i}\frac{\partial y_i}{\partial S_i} + \frac{\partial m}{\partial x_i}\frac{\partial x_i}{\partial S_i}\right) \quad \text{(C4.4)}$$

The derivatives of the slope with respect to x or y are: $m = \frac{y_2 - y_1}{x_2 - x_1}$, $\frac{\partial m}{\partial y_1} = \frac{-1}{x_2 - x_1}$, $\frac{\partial m}{\partial y_2} = \frac{1}{x_2 - x_1}$, $\frac{\partial m}{\partial x_1} = \frac{y_2 - y_1}{(x_2 - x_1)^2}$, $\frac{\partial m}{\partial x_2} = -\frac{y_2 - y_1}{(x_2 - x_1)^2}$. Moreover, using: $y_i = S_i/\sin\alpha_i$, and $x_i = S_i/\tan\alpha_i$, we have $\frac{\partial y_i}{\partial S_i} = \frac{1}{\sin\alpha_i}$, and $\frac{\partial x_i}{\partial S_i} = \frac{1}{\tan\alpha_i}$. Finally, $\partial T_2/\partial m$ is obtained similarly to $\partial T_2/\partial T_1$, resulting in

$$\frac{\partial T_2}{\partial m} = \frac{(1-E_1^2)TR}{(1-mE_1)(m-E_1)\log^2\left(\frac{m-E_1}{mE_1-1}\right)} \tag{C4.5}$$

Substituting all these results into Eq. (4.15) and simplifying, we obtain Eq. (4.16).

$$\sigma_2 = \sqrt{\frac{T_2^4(1\text{-}E_1E_2)^2}{TR^2}\frac{(1\text{-}E_1E_2+(E_2\text{-}E_1)\cos\alpha_1)^2\csc^2\alpha_1+(1\text{-}E_1E_2+(E_2\text{-}E_1)\cos\alpha_2)^2\csc^2\alpha_2}{E_2^2(1\text{-}E_1^2)^2(S_1\cot\alpha_1\text{-}S_2\cot\alpha_2)^2}\sigma_s^2 + \frac{E_1^2(1\text{-}E_2^2)^2T_2^4}{E_2^2(1\text{-}E_1^2)^2T_1^4}\sigma_1^2}$$

4.6.4 D. Solving for the Proton-Density M_0 in DESPOT2

To find the dependence of the y-intercept (b) on TR, T_1, T_2, and ϕ, we substitute the expression for m derived in Appendix A into $y - m\,x = b$, (with either $y_1=S_1/\sin(\alpha_1)$, $x_1=S_1/\tan(\alpha_1)$ or $y_2=S_2/\sin(\alpha_2)$, $x_2=S_2/\tan(\alpha_2)$). After simplifying, we obtain:

$$b^{\theta_1,\theta_2} = \frac{M_0(1-E_1)\sqrt{1+E_2\pm 2E_2\cos(\phi-\theta_1)}}{1-E_1E_2^2\pm E_2(1-E_1)\cos(\phi-\theta_1)} \tag{D4.1}$$

The discontinuity that occurs in τ_2 and in b will also lead to a noise spike in M_0, unless we set $\varepsilon_2=0$ wherever $E_1-m\leq 0$. In that case, however, dark bands of missing proton-density will appear in the image and $\cos(\phi-\theta_1)$ will be clipped such that $|\cos(\phi-\theta_1)|<1$. Therefore, in practice we acquire at least two proton-density maps $M_0^{\theta 1}$, and $M_0^{\theta 2}$, which must be correctly "stitched" together to get the final M_0. A MATLAB plot of the measured M_0 and $\cos\phi$ obtained using θ=0, π under the influence of Gaussian noise is shown in Figure 4.13.

A possible piece-wise solution derived from the above two equations is

$$M_0 = \frac{b^\theta\left(1-E_1E_2^2+(1-E_1)\frac{\epsilon_2^\theta-E_2^2}{1-\epsilon_2^\theta}\right)}{c_{RF}^-(1-E_1)\sqrt{1+E_2^2+2\frac{\epsilon_2^\theta-E_2^2}{1-\epsilon_2^\theta}}}, \qquad \theta=\begin{cases}\theta_1, & \cos(\phi-\theta_1)\geq -1/2\\ \theta_2, & \cos(\phi-\theta_1)<-1/2\end{cases} \tag{D4.2}$$

Note that c_{RF}^-, is a correction factor that accounts for the receive B_1 inhomogeneity. Another option is to average the portions that are well-behaved (in the range $-1/2\leq\cos(\phi-\theta)\leq 1/2$). Averaging inside the bands of low M_0 is also possible with $N=4$. Phantom and in vivo M_0 maps are shown in Figure 4.14, and Figure 4.15, respectively. The c_{RF}^- factor was obtained from

AFI for the phantoms (by assuming $c_{RF}^{+} = c_{RF}^{-}$), and by using a bias-field correction algorithm for the in vivo datasets (N4ITK module in 3D Slicer). The proton-density derived from the DESPOT1 technique has no banding artefacts but some susceptibility-induced artifacts (for instance, in the upper corners of the phantom), caused by an imperfect correction of the T_2^* decay. Phase errors arising from flow in CSF and/or pulsations in the brain stem tend to corrupt the M_0 images (red arrows pointing to dark pixels) derived from DESPOT2. Moreover, the proton density is biased by MT effects in DESPOT2 (especially in Figure 4.15a), and by non-ideal spoiling in DESPOT1, resulting in $M_0 > 100\%$ in CSF. Correction for non-ideal spoiling in the VFA technique can be performed as shown by Volz et al. [93], but MT effects are more problematic. In conclusion, using DESPOT2 for M_0-mapping is challenging.

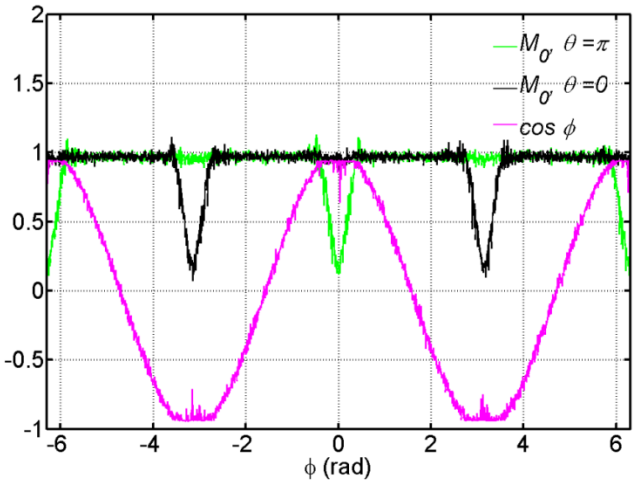

Figure 4.13: Simulated relative M_0 and cos ϕ derived using bSSFP scan parameters $\theta_1/\theta_2/\alpha_1/\alpha_2/TR$= 0/π/11/57°/4.6 ms, and physical parameters $M_0/T_1/T_2$=1.00/1000/70 ms with same Gaussian noise variances σ_1=10, σ_S=0.002 defined in Eq. (4.13) and used in Figure 4.4.

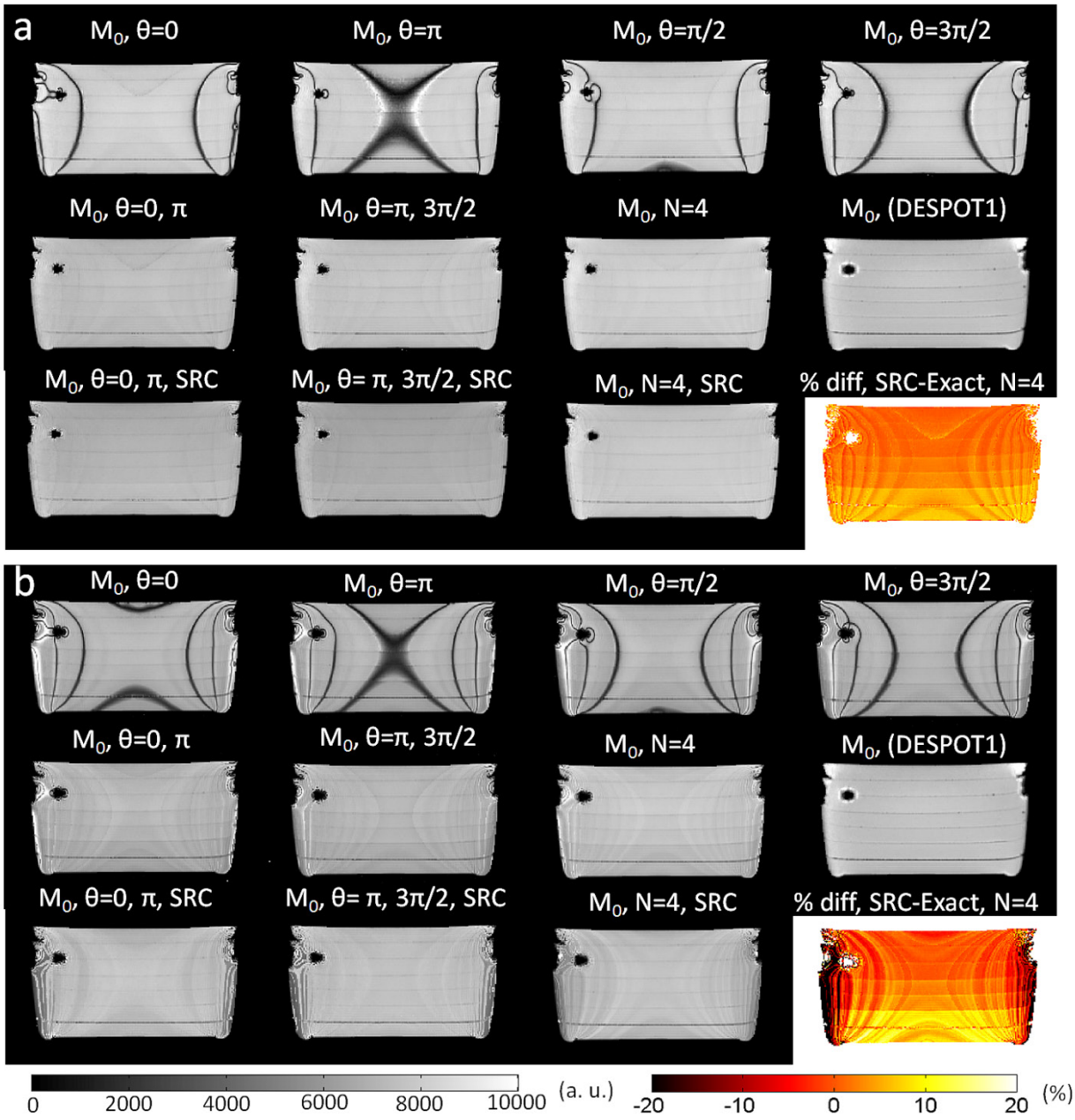

Figure 4.14: (a) Phantom M_0 maps (in arbitrary units) derived from the bSSFP1 protocol with short TR/T_{RF2}=4.8/0.55 ms. (b) M_0 maps obtained from the bSSFP2 protocol with long TR/T_{RF2}=9.0/2.0 ms. SRC results are displayed in the third row, along with a difference map between SRC and the exact solution with N=4. The M_0 calculated from the DESPOT1 (a.k.a. VFA) technique is also shown for comparison. Note that B_1^- correction was applied by assuming RF symmetry: $c_{RF}^+ = c_{RF}^-$.

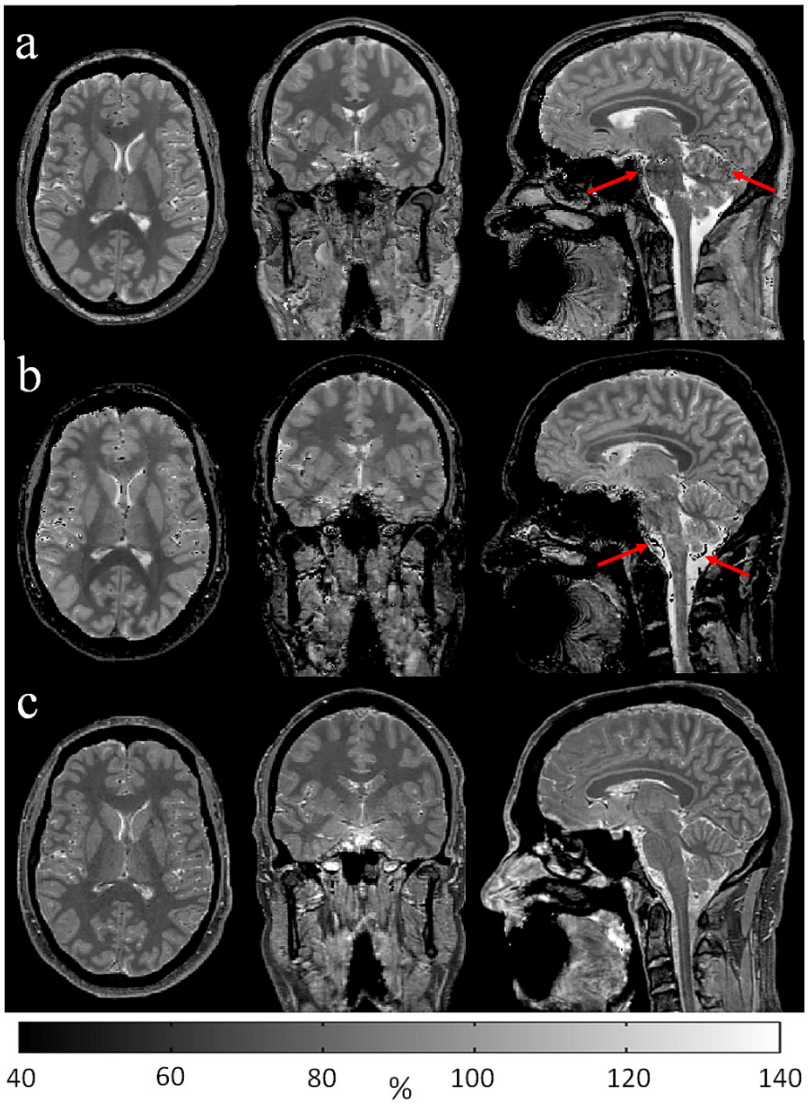

Figure 4.15: (a) M_0 maps (in % H_20) of volunteer v2 derived from the bSSFP1 protocol, (b) the bSSFP2 protocol, and (c) the SPGRa protocol (via DESPOT1/VFA technique). Note that c_{RF}^{-} correction was performed using the N4ITK bias-field correction algorithm in 3D Slicer.

4.7 Acknowledgements

We gratefully acknowledge financial support from the Alberta Cancer Foundation, and the Alberta Cancer Research Institute. We also thank Philips Healthcare for technical support and Dr. Roger Luechinger for the PATI program used for data transfer.

Chapter 5: Retrospective RF Inhomogeneity Correction with N4ITK for 3D Multi-Parameter Mapping of the Brain at 3T: Comparison with B_1 Mapping

"The popularisation of scientific doctrines is producing as great an alteration in the mental state of society as the material applications of science are effecting in its outward life. Such indeed is the respect paid to science, that the most absurd opinions may become current, provided they are expressed in language, the sound of which recals [sic] some well-known scientific phrase."

— James Clerk Maxwell

"Introductory Lecture on Experimental Physics" (1871). In W. D. Niven (ed.), *The Scientific Papers of James Clerk Maxwell* (1890), Vol. 2, 242.

5.1 Introduction

Structural magnetic resonance imaging of the human brain is routinely used in image-guided surgery (IGS), radiation treatment planning (RTP), as well as in research applications like brain morphometry studies [119]. The pulse sequence of choice for achieving high-resolution, 3D T_1-weighted images of the brain is the well-known Magnetization-Prepared Rapid Gradient Echo (MPRAGE) [39], [43], while for T_2-weighting, the 3D turbo spin echo (TSE) technique remains popular [25]. Despite their popularity, multi-center studies are difficult to implement with these sequences because conventional MR images are scaled arbitrarily and the signal strongly depends on the pulse sequence parameters, receiver-coil sensitivity and the MR manufacturer [145]. There is hope that quantitative parametric (T_1, T_2, etc.) maps could serve as a universal imaging standard across different MR manufacturers where conventional MRI fails to provide quantitative pixel-wise information [10], [11]. Indeed, parametric mapping, including T_1, proton-density (M_0), T_2, T_2^* and magnetization transfer (MT) is proving useful in the study of many diseases [146], such as multiple sclerosis [120], Parkinson's [147], Alzheimer's [148], and cancer [9]. Depending on the sequence or technique employed, certain parametric maps may require a consistent and robust RF inhomogeneity correction, especially M_0 and T_1 which is the most commonly studied parameter.

In recent years, the fast acquisition of 3D T_1 maps has become possible in a reasonable scan time with techniques such as Variable Flip Angle (VFA), (a.k.a. Driven Equilibrium Single Pulse Observation of T_1 (DESPOT1)) [88], and more recently the MP2RAGE sequence [44]. A closed-form analytical expression to remove banding artifacts in bSSFP-based T_2 mapping (i.e., "DESPOT2") was also recently reported, enabling the fast calculation of T_2 from a set of 4 or more additional bSSFP images [149]. Unfortunately, large discrepancies exist across global mean T_1 values reported in both white matter (WM) and gray matter (GM) of the normal human brain at 3T [150], and the range appears to be larger at 7T [113]. To demonstrate the discrepancies at 3T, we have collected the mean reported T_1 values of healthy human brain WM and GM from 23 different studies from the past 16 years and displayed them in a histogram in Figure 5.1(a). Figure 5.1(b) is a second histogram of the T_1 measured in 5 specific regions of the brain, (where given among the same 23 studies). These large discrepancies suggest various degrees of T_1 bias. In general, T_1-mapping techniques that rely on an inversion-recovery module (e.g., IR-EPI, Look-Locker, IR-bSSFP) tend to yield lower T_1 than techniques based on steady-

state spoiled gradient echo sequences (e.g., DESPOT1/VFA, or the Method of Slopes [151]). The deviations cannot be explained by variability within the human population, since, in all cases, the standard deviation across the different subjects is significantly smaller than the standard deviation in reported T_1 across the different studies.

Fast 3D techniques such as VFA and MP2RAGE yield some of the higher voxel resolutions and T_1-to-Noise Ratio (T_1NR) efficiency (defined as T_1NR divided by the square-root of the total scan time), making them attractive for 3D T_1 mapping in a clinical setting. While MP2RAGE has the advantage of yielding T_1 maps automatically corrected for B_1 field inhomogeneity [44], it is not ideal for multi-parameter mapping (MPM) applications due to its low sampling efficiency [152]. Conversely, VFA requires a robust and accurate B_1 map if reliable T_1, and additional parameters are to be calculated [86].

Further problems arise when relying on B_1-mapping sequences (besides the increase in total scan time). Many different B_1-mapping pulse sequences exist [153], each of which makes various assumptions when solving for the transmit B_1^+ or flip angle, such as ideal RF spoiling and $TR<<T_1$ in Actual Flip Angle Imaging (AFI), [33], [63], or perfect saturation in the Saturated Double Angle Method (SDAM) [62], just to name a few. These assumptions can translate into various biases in B_1 maps among the different methods [154]. Moreover, B_1-mapping is sensitive to susceptibility differences, geometrical distortions, and partial volume effects arising from coarse voxel resolutions (3–5 mm voxels), low sampling bandwidths, and/or the use of echo-planar imaging (EPI) readouts. These problems are worst at tissue-air boundaries, or where susceptibility differences tend to be significant (i.e., nasal cavity/ inferior surface of the frontal lobe).

A solution may be to correct B_1 inhomogeneity via RF simulations or retrospective bias-field methods, neither of which adds scan time. Recently, the "UNICORT" retrospective technique, which uses the bias-field correction algorithm in the SPM8 toolbox (http://www.fil.ion.ucl.ac.uk/spm/software/spm8/), was applied to correct R_1 brain maps derived from the VFA technique [92]. UNICORT was also successfully employed to correct the receive B_1^- field in quantitative proton-density (a.k.a. absolute water-content mapping, M_0) [93], [102]. In this study, we reproduce the UNICORT technique using the N4ITK bias-field correction algorithm [64], which is available in the ITK image-processing C++ library and within 3D Slicer

(www.slicer.org [101]). The N4ITK algorithm provides advantages over that in the SPM8 (or the upgraded SPM12) toolbox, including faster execution times, and the fact that it is not limited to the brain, but can be applied to other parts of the human anatomy and even phantoms (it relies on B-spline fitting rather than atlas-based image registration and segmentation).

The goals of this study were, firstly, to find the optimal N4ITK parameters and calibration procedure that most successfully remove both B_1^+ and B_1^- inhomogeneity in the parametric brain maps (esp. T_1, M_0 and T_2) of healthy volunteers; secondly, to test both the intra-subject (11 time-points) and inter-subject (8 volunteers) reproducibility of the method; thirdly, to compare it to commonly used B_1-mapping sequences and the previous UNICORT method and, fourthly, to assess its performance on patients with primary brain tumors.

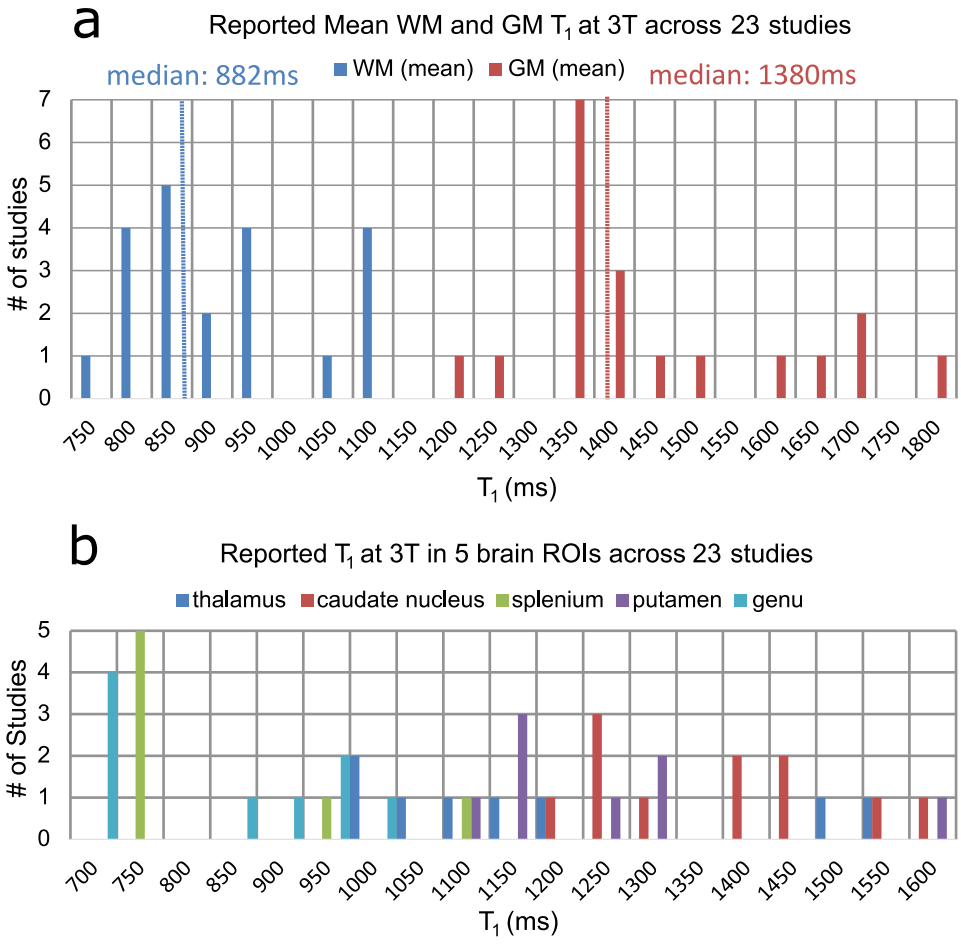

Figure 5.1: (a) Mean white matter (WM) and grey matter (GM) T_1 reported across 23 studies (published in 1999–2015) involving healthy volunteers. The median T_1 (across the studies) is given by the dotted vertical lines. (b) Reported T_1 measured in ROIs of specific brain regions for the same studies.

References: [44], [113], [151], [86], [35], [155], [92], [122], [106], [156], [157], [158], [85], [109], [159], [108], [160], [161], [143], [162], [11], [163], [164]. T_1 mapping techniques include: MP2RAGE, VFA, IR-FSE, MoS, IR-bSSFP, IR-GRASE, MPRAGE, PRESS (Spectroscopy), and MRF.

5.2 Theory

In the Variable Flip Angle (VFA) technique [74], two or more spoiled gradient echo (SPGR) images are acquired using different flip angles, while keeping all other scan parameters identical. The original VFA technique can be modified to acquire simultaneously T_1, M_0 and T_2^* using two multi-echo (bipolar) SPGR sequences, resulting in SNR gains of ~1.6 over a conventional single-echo low-bandwidth SPGR protocol of the same scan duration [152].

The multi-echo SPGR signal can be cast into the following linear ($y=m\,x+b$) equation [152]:

$$\frac{S_{ME}}{\sin(c_{RF}^{+}\alpha_{nom})} = E_1 \frac{S_{ME}}{\tan(c_{RF}^{+}\alpha_{nom})} + c_{RF}^{-} M_0 (1-E_1) \sqrt{\sum_{n=1}^{N} e^{-2\,TE_n/T_2^*}}, \quad S_{ME} = \sqrt{\sum_{n=1}^{N} S_n^2} \qquad (5.1)$$

where S_n is the signal from each echo at time TE_n, S_{ME} is the multi-echo signal (multi-echo images combined by root-sum-of-squares (RSS) to preserve optimal SNR in the presence of T_2^* decay as explained in [17]), α_{nom} is the nominal flip angle, $y=S_{ME}/\sin(c_{RF}^{+}\alpha_{nom})$, $x=S_{ME}/\tan(c_{RF}^{+}\alpha_{nom})$, the slope is $E_1=exp(-TR/T_1)$, the y-intercept is $c_{RF}^{-} M_0 (1-E_1)\sqrt{\sum_{n=1}^{N} e^{-2\,TE_n/T_2^*}}$, c_{RF}^{+} is the normalized B_1^{+} transmit field (given by the ratio of the actual to the nominal flip angle: $c_{RF}^{+}=\alpha/\alpha_{nom}$), and c_{RF}^{-} is the normalized B_1^{-} receive field. Note that the same principles (with a very similar equation) apply for single-echo VFA implementations [93], [90]. The main difference is that in a single-echo implementation, T_2^* must be either ignored [90] or measured from a separate sequence [93] when solving for M_0, rather than obtained via ordinary least-squares fit (and combined by weighted average) of the same two multi-echo SPGR acquisitions [152], [94].

If Eq. (5.1) is solved for T_1 and M_0 while ignoring the flip angle inhomogeneity, c_{RF}^{+}, and receive sensitivity profile, c_{RF}^{-} , the resulting T_1 and M_0 will be an "apparent" T_1^{app} or M_0^{app} approximately related to the true T_1 or M_0 according to $T_1^{app} \approx (c_{RF}^{+})^2\, T_1$, $M_0^{app} \approx c_{RF}^{+} c_{RF}^{-}\, M_0$, [109], [90]. A limitation of this approximation (also present in Eq. (5.1)) is that the corrected T_1 remains biased by the effect of non-ideal RF spoiling in the SPGR datasets. Equations have been

proposed in Preibisch and Deichmann [35] to relate the biased T_1 to the true unbiased T_1, by denoting $T_1^{app} \approx (c_{RF}^{+})^2\, T_1'$ and $T_1 = A(c_{RF}^{+}) + B(c_{RF}^{+})\, T_1'$, where the coefficients A and B are quadratic functions of c_{RF}^{+} that depend on ϕ_0 (the RF phase-cycle increment), α_1, α_2, TR, T_2 and must be estimated from Bloch equation simulations. In this study, we propose instead to combine the error arising from both B_1 inhomogeneity and non-ideal RF spoiling into a new term, $c_{RF,s}^{+}$, yielding two bias fields Ψ_1 and Ψ_0

$$T_1^{app} \approx \left(c_{RF,s}^{+}\right)^2 T_1, \quad M_0^{app} \approx c_{RF,s}^{+} c_{RF}^{-}\, M_0 \tag{5.2 a, b}$$

$$\Psi_{T1} \propto \left(c_{RF,s}^{+}\right)^2, \qquad \Psi_{M_0} \propto c_{RF,s}^{+} c_{RF}^{-} \tag{5.3 a, b}$$

A calibration factor c_{cal}^{Ω} that depends on the hardware and transmit-gain setting, defined as the mean inhomogeneity measured over a specified region (volume) Ω (e.g., the entire head, or a skull-stripped binary mask), is also needed to convert the bias fields into correctly normalized $c_{RF,s}^{+}$ and c_{RF}^{-} maps:

$$c_{RF,s}^{+} = \frac{\sqrt{\Psi_1}}{\langle \Psi_1 \rangle_\Omega} c_{cal}^{\Omega}\,, \qquad c_{RF}^{-} = \frac{\Psi_0 \left(c_{cal}^{\Omega}\right)^2}{\langle \sqrt{\Psi_0} \rangle_\Omega^2\, c_{RF,s}^{+}} \tag{5.4 a, b}$$

The calibration factor should be selected to minimize the bias in T_1 arising from RF inhomogeneity and imperfect spoiling in the final estimated T_1 (of different tissue types, e.g. WM/GM) within the average human population. Once the two bias fields have been obtained (see below) and converted into the $c_{RF,s}^{+}$ and c_{RF}^{-} fields following the calibration step, they are substituted back into Eq. (5.1), to obtain the final corrected M_0 and T_1. As a last note, M_0 remains in arbitrary units until normalized against a known standard. A common choice is to use the cerebrospinal fluid (CSF) signal, assuming M_0^{CSF} =100%. However, [93] have shown that a correction for non-ideal spoiling in SPGR is then required (based on simulations). A simpler option that avoids this correction is to find the mid-point between the WM and GM peaks on the corrected M_0 histogram, and normalize the M_0 map such that this midpoint lies at M_0=76% [152]. This calibration assumes that the mean WM/GM M_0 in the normal human population is ≈ 71/81% (with respect to pure H_20 or CSF [93], [103], [111]), and also minimizes biases arising from non-ideal RF spoiling.

Once T_1 and $c_{RF,s}^{+}$ are obtained pixel-wise, a T_2 map can be calculated from a minimum of 4 bSSFP images (assuming $c_{RF}^{+} \approx c_{RF,s}^{+}$), as shown in Jutras et al [149]. A magnetization transfer (MT) saturation MT_{sat} map can also be obtained by acquiring a third SPGR sequence with an MT module positioned after the first N echoes, as shown in Helms et al [49].

5.3 Materials and Methods

5.3.1 Phantom Study

To examine the performance of various B_1 mapping methods, two large acrylic (PMMA) phantoms of inner dimensions 25.0×15.2×14.0 cm^3 were built and scanned in a Philips 3T Achieva scanner using a transmit/receive (T/R) quadrature birdcage head coil (see below). The phantoms were filled with 4.5 L of agar solution (deionized water, 1.00% agar and 0.05% NaN_3, 1% = 1g/100 mL). Different NaCl concentrations (a "lossy" phantom 1 with [NaCl]=0.2%, and a "low-loss" phantom 2 [NaCl]=0%) were used to examine the effect of conductivity σ on the B_1^{+} and B_1^{-} fields. The concentration of $MnCl_2$ (phantom 1: [$MnCl_2$]=35 μM and phantom 2: [$MnCl_2$]=31 μM) was adjusted to approximately match the T_1/T_2 (~1400/100 ms) of GM at 3T [165].

5.3.1.1 Experiments

Both phantoms were scanned using two 3D B_1-mapping sequences – Actual Flip angle Imaging (AFI) [63] and Saturated Double Angle Method (SDAM) [62], – with the scan parameters listed in Table 5.1. Two multi-echo SPGR scans with isotropic 1 mm voxel resolution were acquired to obtain T_1 and M_0 maps via the VFA technique ($\alpha_1/\alpha_2/TR/\Delta TE/N$ =4.5/25/16.5/2.3/6). A T_1 map from an MP2RAGE sequence was also acquired using the same optimized parameters listed in Marques et al [44] (5th entry of Table 1: $\alpha_1/\alpha_2/TI_1/TI_2/TR/TE/TR_{MP2RAGE}$ = 4/5°/600/1800/5.8/2.7/4000 ms), to assess how well it corrects for B_1^{+} inhomogeneity in T_1 in comparison with the B_1-corrected VFA technique. Finally, a 2D inversion recovery gradient echo sequence (IR-EPI) was acquired to serve as a T_1-mapping gold-standard using an adiabatic inversion pulse, TI=20, 200, 500, 800, 1200, 1700, 2300 and 3000 ms, TR/TE=3500/10 ms, EPI factor=3, 1.2×1.2×5 mm^3 voxel size, and scan time = 3 min per TI) All 3D datasets were reconstructed from raw k-space data, zero-padded and/or resampled to 3D arrays of 256×256×180 pixels in MATLAB using the MRecon toolbox (GyroTools, Switzerland). Corrected T_1 and M_0 maps were obtained using Eqs. (5.1) and (5.2 a, b) for VFA with the two different B_1 maps: AFI, and SDAM, as well as the

two bias-field algorithms N4ITK and SPM12. The spline distance was optimized in N4ITK (with a fixed number of 400/320/240 iterations at levels 1–3 of the algorithm) by minimizing the full-width at half-maximum (FWHM) of the phantom T_1 and M_0 histogram peaks. The optimal N4ITK spline distance for the phantom was 150 mm, while the optimal SPM12 settings were a regularization of 10^{-3} and a smoothing distance of 50 mm. The Ψ_1 and Ψ_0 bias fields were converted to approximate c_{RF}^{+} and c_{RF}^{-} maps by matching the mean flip angles measured by AFI ($<c_{RF}^{+}>_{AFI}$=0.82, 0.75 for phantoms 1 and 2, respectively) with those from N4ITK (i.e., $<c_{RF}^{+}>_{AFI} = < c_{RF,s}^{+}>_{N4ITK} = c_{cal}^{phantom}$). Note that in this case we are assuming that the effect of non-ideal RF spoiling is negligible, thus $c_{RF,s}^{+} \approx c_{RF}^{+}$. The inversion recovery data was curve-fitted to solve for T_1 using the robust MATLAB toolbox provided by [166].

5.3.1.2 B_1 Field Simulations of a T/R Birdcage Coil

The coil used in the phantom experiments consists of a 12-element hybrid birdcage 30 cm in diameter and 21 cm in length with a circular end cap at the superior end (Figure 5.2(a)). Full-wave simulations were performed using HFSS V.15 (ANSYS, USA) to acquire scattering (S) parameters of the coil and all field quantities. Quadrature excitation was achieved using a 50 Ω port at the 4 and 7 o'clock positions each with 1.0 W of incident power. The coil was centered within a cylindrical perfect electrical conductor closed by circular radiation boundaries to simulate the system's RF shield and openings, respectively. The capacitors at the end cap were adjusted to tune the empty coil's uniform mode to the Larmor frequency (127.8 MHz).

An accurate model of the phantom (within ±1 mm) was positioned inside the coil, as shown in Figure 5.2 (a). One end of the phantom extends out of the coil to ensure a large range of B_1 amplitudes. For the simulations, the relative permittivity ε_r and the conductivity σ of the agar solutions were estimated from the salt concentrations using the tabulated measurements and empirical formula of [100], yielding ε_r=75.8, σ=0.587 *S/m* for phantom 1 with 0.2% NaCl and ε_r=75.4, σ=0.297 *S/m* for phantom 2 without NaCl. The phantom walls (PMMA) and acetal (POM) support for the phantom were assigned data sheet values of ε_r=2.6, and ε_r=4, respectively. The auxiliary magnetic fields **H** were exported from HFSS to MATLAB and the magnitude B_1^{+} field calculated using Eq. 14 in Hoult [61]. This field magnitude squared was exported into 3D Slicer to be manually registered with the T_1^{app} map of the phantom. Because $T_1^{app} \propto (B_1^{+})^2 T_1$ (Eq. (5.2 a, b)), assuming a perfectly uniform T_1 over the agar gel phantom (and ideal RF

spoiling in the SPGR datasets) enables an accurate comparison of the measured and simulated B_1 fields following a rigid (3DOF) registration. This B_1 measured from T_1^{app} was termed "expected B_1," to distinguish it from the "simulated B_1" and those measured with AFI or SDAM. Thus four c_{RF}^{+} maps were compared for both phantom 1 and 2.

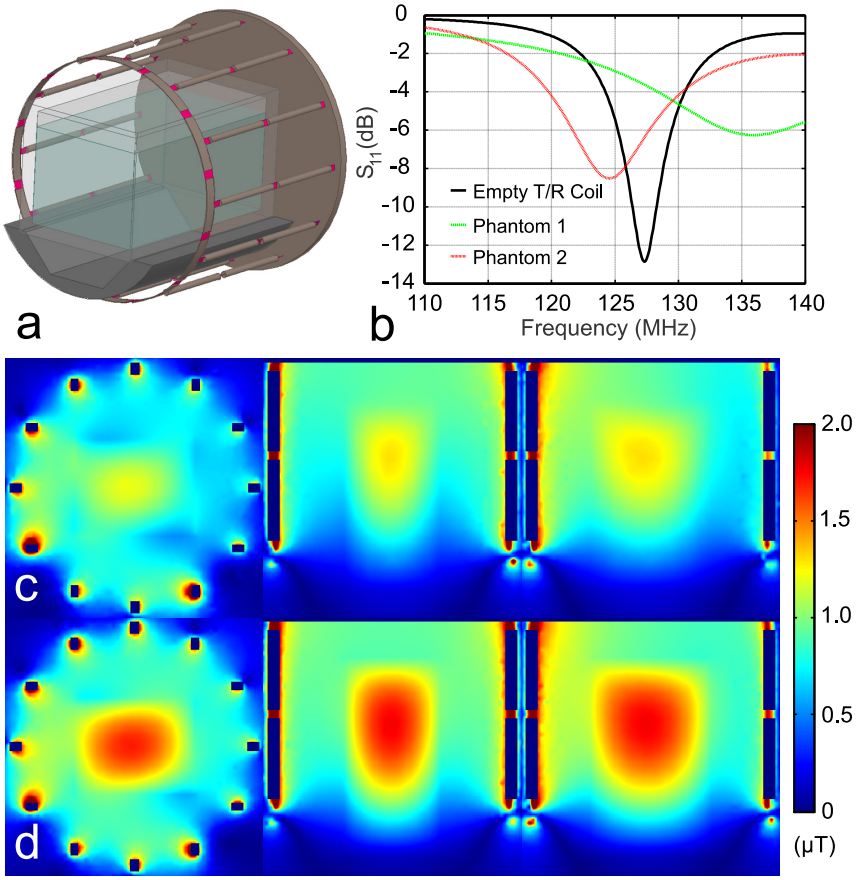

Figure 5.2: (a) Phantom and T/R birdcage coil model setup for HFSS simulation. (b) Plots of S_{11} (reflection at input) for the tuned empty coil and when loaded with phantom 1 (lossy) or phantom 2 (low-loss). (c) Simulated B_1^{+} field images (transverse, sagittal and coronal images) of phantom 1 and (d) of phantom 2 using an input power of 1.0W.

5.3.2 In vivo Brain N4ITK Optimization and Measurements

5.3.2.1 Multi-Parameter Mapping protocol on 8 in vivo volunteers

For the in vivo optimization of N4ITK, 8 healthy volunteers (4 males and 4 females, ages: 21–30) were scanned following approval by the local ethics committee and obtaining informed consent. For all in vivo scans, the body coil was used for excitation and an 8-channel head array

was used for reception. The scan protocol consisted of two B_1-mapping sequences (AFI and SDAM), two multi-echo SPGR sequences (2 flip angles), and 6 bSSFP sequences (2 flip angles by 3 phase offsets). Important scan parameters are listed in Table 5.1, and the total examination time was ~32 minutes per subject. The B_1 sequences were optimized to have similar scan duration (~3 min), and voxel resolution ($3.5\times5\times5 mm^3$). For AFI, the default Philips spoiler gradient areas were employed (A_{G1}/A_{G2}=76.2/561.2 mT·ms/m), as they yielded the best B_1 map quality (i.e., narrowest T_1 peak FWHM) on the agar phantoms. The RF phase-cycle increment for SPGR and AFI was the default Philips value of ϕ_0=150°.

All datasets were reconstructed in MATLAB as described previously for the phantom datasets, with the exception that a uniform-sensitivity coil combination normalized to that of the body coil was applied to yield optimal SNR and correct for the B_1^- sensitivity profiles of the 8-channel head array (Roemer reconstruction) [91]. Following image reconstruction, datasets were exported to 3D Slicer [101] and co-registered to correct slight mismatches arising from head motion during the examination. A windowed sinc interpolation was used to avoid loss of image sharpness in the final resampled datasets.

The parametric maps (M_0, T_1 and T_2) were curve-fitted in MATLAB using the magnitude images according to Eqs. (5.1)–(5.3 a, b) and Eq. 11 in Jutras et al [149] using the normalized flip angle/B_1 maps (c_{RF}^+) obtained from AFI and SDAM (see Fig. 2a in Ref. [152] and Fig. 2 in Ref. [149]) . Uncorrected T_1^{app} and M_0^{app} maps of the eight volunteers were generated and used to optimize and calibrate N4ITK as described in the following sections. The T_2^* maps used to solve for M_0 were not corrected for B_0 inhomogeneities.

5.3.2.2 Optimization of N4ITK for Ψ_1

The optimization of the N4ITK-derived Ψ_1 field was based on the assumption that the WM tissue of the human brain forms a single tissue class with a sharp distribution on a T_1 histogram. Therefore, the N4ITK-estimated $c_{RF,s}^+$ field that is closest to the true $c_{RF,s}^+$ field will yield the narrowest WM T_1 peak on a T_1 histogram. A similar approach was previously used to optimize the N3-MNI algorithm for bias field correction in conventional MPRAGE and SPGR imaging [65]. The main difference is that the normalized variance of the image intensity in WM was used instead of the width of the WM peak in a T_1 histogram (used in this work). We refer to our approach as a "histogram-sharpening" (*H-S*) technique. The two most sensitive N4ITK

parameters – the spline distance (d_s), and number of iterations (n_i) – were optimized by testing them over a wide range (d_s=10–350mm, and n_i=50–400) on all 8 brain T_1^{app} datasets. Other parameters (e.g. FWHM, shrink factor, etc…) were assigned their default values because they did not significantly impact the bias field. Note that axial slices below the nose and cerebellum were excluded from the T_1 histogram to avoid adding significant contribution from adipose and muscle tissues in the neck. N4ITK also requires a mask as input to exclude hypo- or hyper-intense signal in air cavities and CSF, respectively, (where T_1 is either undefined or long and noisy) from biasing the calculation [65]. Therefore, a Ψ_1 mask that excludes these regions was generated in MATLAB using a bias-field corrected fuzzy c-means segmentation [68] on T_1^{app} (5 classes with initial inputs: 10, 450, 950, 1500 and 3000ms) and exported into 3D Slicer.

5.3.2.3 Optimization of N4ITK for Ψ_0

To obtain corrected proton density M_0, the Ψ_0 bias field must also be optimized such that the c_{RF}^- field yields both the narrowest WM and GM M_0 histogram distributions when substituted into the y-intercept of Eq. (5.1). An *H-S* technique similar to that above was used beginning with the optimal N4ITK-derived $c_{RF,s}^+$ and T_1 maps previously obtained (n_i=400, 320, 240 and d_s=210 mm), but varying n_i and d_s for each Ψ_0 field calculation, yielding a corrected M_0 map. Next, both GM and WM were segmented by global thresholding on the T_1 histogram (with thresholds of ~[750–1050 ms] for WM and [1150–1700 ms] for GM, but optimized for each subject). The segmented WM and GM were displayed as separate M_0 histograms following the calculation of the corrected M_0. In this case, the FWHM of both the WM and GM M_0 histograms were measured (rather than that for WM only). The FWHM of the WM and GM M_0 were measured (in arbitrary units) across the 8 volunteers as a function of spline distance (in 20 mm increments) for varying numbers of iterations as done for Ψ_1, to identify the global minimum across the 8 subjects.

To generate a Ψ_0 mask as required by N4ITK, first the Ψ_1 mask above was used to obtain an initial Ψ_0 field estimate and corrected M_0. Then both the corrected T_1 and M_0 were thresholded globally to mask out air, adipose and CSF using the following bounds: $50<M_0<90\%$ and $700<T_1<2000$ ms. This Ψ_0 mask provided equivalent or superior accuracy in the Ψ_0 field (and c_{RF}^-) calculation (especially in subjects with much adipose), but was found to bring little improvement (if any) on the Ψ_1 field calculation compared to the initial Ψ_1 mask.

5.3.2.4 Calibration of Ψ_1 / Ψ_0 Fields to yield $c_{RF,s}^{+}/c_{RF}^{-}$

To obtain the calibrated $c_{RF,s}^{+}$ /c_{RF}^{-} fields from the N4ITK-fitted Ψ_1 /Ψ_0 fields, two different choices of region Ω were compared. In the first, Ω was the entire visible head volume and c_{cal}^{head} was chosen such that the mean N4ITK-based $c_{RF,s}^{+}$ over the head matches that measured by AFI (i.e.: $<c_{RF}^{+}>_{AFI} =< c_{RF,s}^{+}>_{N4ITK}=c_{cal}^{head}$) as described previously for the phantom. In the second scheme, Ω was a skull-stripped brain mask, as done in [92] and [152]. Skull-stripping was implemented using the BET tool in FSL (http://www.fmrib.ox.ac.uk/fsl). The second calibration factor c_{cal}^{brain} was chosen such that the mean WM T_1 of the 8 volunteers (=905 ms) would remain unchanged with respect to first calibration scheme. Recall that the calibration factor of the Ψ_0 field is not critical because the corrected M_0 must be normalized with respect to a known standard such as CSF.

5.3.2.5 M_0, T_1 and T_2 Histograms and Measurements in Brain ROIs

Once the optimal N4ITK parameters were found (n_i=400, 320, 240, and d_s=210 mm for Ψ_1 and 185 mm for Ψ_0) they were used to create final M_0, T_1 and T_2 maps using the calibrated $c_{RF,s}^{+}$ and c_{RF}^{-} fields. The M_0, T_1, and T_2 maps corrected with N4ITK were compared to those obtained using the AFI and/or SDAM-based B_1^{+} correction (c_{RF}^{+}) by displaying of the M_0, T_1 and T_2 histograms, and also via measurement of mean and standard deviation in specific brain ROIs. Where applicable, ROIs of the left and right brain hemispheres were measured separately to detect potential RF asymmetry.

5.3.2.6 Scan-Scan Reproducibility of T_1 Mapping on a Volunteer

To assess the intra-subject reproducibility of the technique, a single volunteer (v1) was scanned 11 times over a period of approximately 18 months. Each examination included an AFI B_1 map (same parameters listed in Table 5.1) and two SPGR datasets (VFA technique) with different scan parameters ($\alpha_1/\alpha_2/N/TR$) and voxel resolutions ranging from 1×1×1 mm^3 to 1×1×2 mm^3. For each time point, a T_1 map was calculated and corrected using both AFI and optimized N4ITK. The global mean WM T_1 peak (and its width) was measured on a T_1 histogram of each time point using the approach previously described and the standard deviation of the means obtained with AFI was compared with that obtained from N4ITK. All 11 T_1 maps (corrected with both AFI and N4ITK) as well as the 11 M_0 maps (corrected with N4ITK only) were co-registered using 6 DOF rigid registration in 3D Slicer (including only the skull-stripped brain to avoid biases arising

from tissue deformations that are common in the scalp and neck). Coefficients of variation (CoV) were then calculated voxel-wise in both the T_1 and M_0 maps to measure reproducibility. The mean CoV was also calculated in WM, GM and CSF following image segmentation performed by thresholding on the T_1 histogram.

5.3.3 In Vivo Comparison of N4ITK-corrected T_1 with Inversion Recovery and SPM

In order to compare the N4ITK-corrected T_1 with a gold-standard inversion recovery technique, four of the same eight volunteers (v1, v4, v5 and v6) were re-scanned with different AFI, SDAM, and SPGR parameters (but the same flip angles and TR), as well as the same IR-EPI sequence tested on the phantoms (see Table 5.1). A single axial slice with identical in-plane resolution as the SPGR sequences (1.2 ×1.2 mm^2) and 5 mm thickness was positioned to encompass relevant brain ROIs, including the caudate nucleus, putamen, frontal/occipital WM, genu and splenium. The 2D IR-EPI T_1 map was co-registered with the 3D VFA T_1 map (N4ITK-corrected) to compare the percent difference voxel-wise. Both a weakly-spoiled (A_{G1}/A_{G2}=148.6/633.6 mT·ms/m) and a strongly-spoiled (A_{G1}/A_{G2}=424.5/909.5 mT·ms/m) AFI sequence were tested (with coarser resolution of 7.5 mm isotropic) to investigate the effect of the gradient spoiling on the B_1 and T_1. The AFI and SPGR sequences had a different phase-cycle increment of ϕ_0=117° to investigate how it would affect the VFA T_1 corrected using the different c_{RF}^{+} or $c_{RF,s}^{+}$ maps with respect to the previous experiments (with ϕ_0=150°) on 8 volunteers. Finally, the SPM12 bias-field correction algorithm was also tested on the R_1^{app} and the $1/M_0^{app}$ maps (both with and without skull-stripping) using the same parameters optimized by Weiskopf et al [92] to obtain $c_{RF,s}^{+}$ and c_{RF}^{-}. Therefore, a total of five 3D T_1 maps derived from different correction schemes (weakly-/strongly-spoiled AFI, SDAM, N4ITK and SPM12), and the 2D T_1 map (from IR-EPI) where compared for each subject.

Pulse* Sequence	Voxel Resolution (mm)	$TR_1/TR_2/TE_1/\Delta TE/N_{echo}$ (ms)	α_1/α_2 (°)	BW (Hz/ pix)	SENSE Factors AP×RL	$\phi_0/\Delta f_0$ (°/Hz)	Scan Time (min)
Protocols for the 8 volunteers (FOV=240×240×170 mm^3)							
AFI	3.5×5.0×5.0	25/125/2.8/–/1	60/–	221	1.0×1.0	150/–	3:15
SDAM[1]	3.5×5.0×5.0	177/–/2.8/–/1	60/120	260	1.0×1.0	0/–	3:20
SPGR	1.0×1.0×1.5	24/–/2.3/2.3/9	5/25	517	1.2×1.2	150/–	12:00
bSSFP	1.0×1.0×1.2	4.4/–/2.2/–/1	11/57	517	1.0×1.0	–/0, 75.8, 151.5	12:00
Protocols for the 4 volunteers (FOV=240×240×180 mm^3)							
AFI[2]	3.5×7.5×7.5	25/125/1.54/–/1	60/–	500	1.0×1.0	117/–	1:30
SDAM[1]	3.5×8.0×7.5	175/–/2.1/–/1	60/120	422	1.0×1.0	0/–	1:35
SPGR	1.2×1.2×1.2	24/–/2.3/2.3/9	5/25	517	1.4×1.4	117/–	10:00
IR-EPI[3]	1.2×1.2×5	3500/–/10/–/1	180/90		1.0×1.0	0/–	3:00

Table 5.1: Scan parameters of the in vivo examination protocols. [1]SDAM had an EPI factor of 3. Hard non-selective RF pulses were used for the AFI, SDAM, SPGR and the bSSFP sequences. [2]This AFI sequence was run at two different spoiling regimes (see text). [3]IR-EPI was run 8 times with TI=20, 200, 500, 800, 1200, 1700, 2300 and 3000 ms. *All sequences were Philips implementations, with parameters optimized for this study.

5.3.4 Imaging of Primary Brain Tumor Patients

The robustness of the proposed N4ITK-based RF inhomogeneity correction was tested in the presence of abnormal brain anatomy using an MPM protocol similar to that described in [11]. With local Research Ethics Board approval, informed consent was obtained from 5 patients following surgical resection of primary brain tumors. The scan parameters for this study are listed in Table 5.2, including a multi-echo SPGR sequence with a magnetization-transfer module (MT-SPGR) to enable the calculation of MT_{sat} maps in addition to M_0, T_1, T_2 and T_2^*. The MT module contained a Gaussian pulse envelope with a duration of 4.2 ms, 2 kHz frequency offset and a flip angle of 340°, positioned after the 8th echo with echo times identical to those of the other two SPGR sequences (T_1- and M_0-weighted).

Pulse Sequence*	Voxel Resolution (mm)	$TR/TE_1/\Delta TE/N_{echo}$ (ms)	$\alpha_1/\alpha_2/\alpha_{MT}$ (°)	BW (Hz/ pix)	SENSE Factors AP×RL	$\phi_0/\Delta f_0$ (°/Hz)	Scan Time (min)
MT-SPGR	1×1×1	31.5/2.3/ 2.3/8	6.5/-/340	517	1.7×1.7	50/–	6:00
SPGR	1×1×1	31.5/2.3/ 2.3/12	6.5/35/-	517	1.7×1.7	50/–	12:00
bSSFP	1×1×1	4.8/2.4/—/1	12/58/-	517	1.2×1.0	–/52.08, 156.25	8:50

Table 5.2: Scan parameters of the MPM patient study. The field of view was 240×240×170 mm^3 and hard non-selective RF pulses were used in all cases. Note that only two bSSFP phase offsets (rather than 3 used for healthy volunteers) were acquired. *All sequences were Philips product implementations, except for the MT-FLASH, where the MT pulse angle, shape and resonance offset were manually selected via the sequence development user interface.

The parametric maps (M_0, T_1, T_2 and T_2^*) of the patients were reconstructed using the same pipeline as for the healthy volunteers, with the following exceptions: Only the first 6 echoes were combined in RSS prior to solving for M_0 and T_1, while all 12 echoes were included in the T_2^* fit. To reduce motion artifacts, the T_2^* was weighted voxel-wise by its inverse variance (inverse squared uncertainty of each fit). These choices were made because later echoes are more motion-sensitive [94] and in general the patient datasets contained more motion artifacts than those of the volunteers. Therefore, a trade-off between SNR and image sharpness was made based on the severity of the artifacts. The N4ITK calibration over the skull-stripped brain was used to derive the parametric maps of the patients after confirming that it yields lower inter-subject variability in measured T_1 (see the Discussion). The MT_{sat} maps were calculated and also c_{RF}^+-corrected as described in [11] and [49], using all 8 echoes of the MT-weighted and the first 8 echoes of the M_0-weighted SPGR combined in RSS.

5.4 Results

5.4.1 Phantom Experiments and Simulations

The T_1 and M_0 histograms of the two phantoms (normalized to the phantom volume) are shown in Figure 5.3, under different B_1 correction schemes. Because the phantom is sealed and has no thermal or concentration gradients, it can be assumed that both T_1 and M_0 are uniform over the entire phantom, and thus the corresponding histograms are expected to appear as sharp Gaussians (i.e., narrow peaks). In all cases, N4ITK yields significantly sharper histograms than those resulting from corrections using AFI, SDAM, MP2RAGE, or the HFSS simulations. SPM12 is

also able to remove the B_1 inhomogeneity in the phantom, except at the very edge of the field-of-view where the remaining bias is more significant than with N4ITK, leading to more asymmetric T_1/M_0 histograms with longer "tails". The correction using the expected B_1 field (from Eq. (5.2)) yields the narrowest T_1 peaks. Moreover, the assumption of RF symmetry (i.e., $c_{RF}^{+} = c_{RF}^{-}$), which must be made if correcting M_0 with AFI or SDAM, clearly does not hold well in either phantom, but holds better in the low-loss phantom 2.

Maps and profiles of the simulated, expected (from T_1^{app}) and measured (from AFI/SDAM) phantom B_1^{+} maps are shown in Figure 5.4. Interestingly, the simulated B_1 field agrees more closely with AFI or SDAM than with the expected B_1. A close look at the profiles in Figure 5.4 (b) reveals that AFI, SDAM and the simulated B_1 all tend to underestimate the expected B_1 field, especially at the center of each phantom. The effect is also more pronounced in the low-loss phantom 2, and explains the broader FWHM of the histograms in Figure 5.3(b). This result confirms the prediction that non-ideal RF spoiling is happening in the SPGR images of the phantom, thus violating the assumption $c_{RF,s}^{+} \approx c_{RF}^{+}$. In fact, if we plot the equations for T_1^{app} as a function of c_{RF}^{+} and a fixed T_1=1400 ms provided by Preibisch and Deichmann [85], non-ideal RF spoiling is expected to make the bias field more convex, which is observed in both phantoms, although to a greater degree in the low-loss phantom 2 (given the greater B_1 inhomogeneity). The mean absolute error (in %) between the N4ITK-fitted (not shown due to nearly perfect overlap) and the expected $c_{RF,s}^{+}$ field was a mere 1.23% for lossy phantom 1 and 1.93% for low-loss phantom 2. The T_1 measured by IR-EPI (mean ± standard deviation) was 1362±34/1486±50 ms for phantom 1/2, in close agreement (+0.66/1.3%) with the AFI-corrected mean VFA T_1 of 1353/1471 ms. The IR-EPI result revealed that the T_1 was indeed highly uniform throughout the phantom, although a slight gradient toward shorter T_1 was visible closer to the surface, which is in contact with air and thus possibly some moisture may have been lost from the agar. However, the inhomogeneity in the VFA-corrected T_1 clearly did not follow the same trend; instead the T_1 was ~9/19% longer than the mean at the center of phantom 1/2, which is an effect of non-ideal RF spoiling [35].

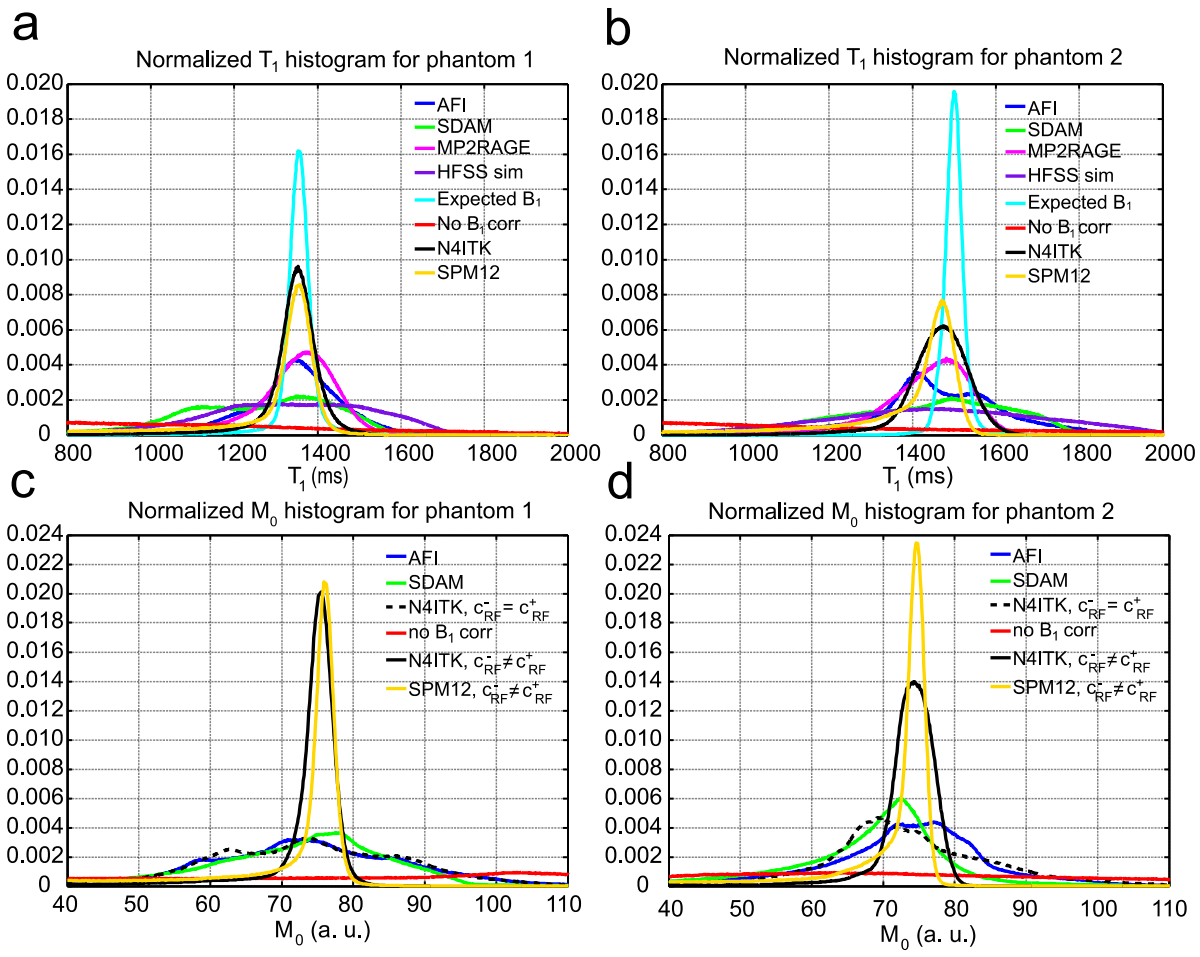

Figure 5.3: (a) Normalized T_1 histograms of lossy phantom 1 corrected by 6 different methods (AFI, SDAM, N4ITK, MP2RAGE, simulation and the expected B_1. (b) T_1 histograms of low-loss phantom 2 and the same correction schemes. (c) M_0 histograms of phantom 1 corrected with AFI, SDAM and N4ITK assuming RF symmetry ($c_{RF}^{+}=c_{RF}^{-}$), and with N4ITK without assuming RF symmetry. (d) M_0 histograms of phantom 2 and the same correction schemes.

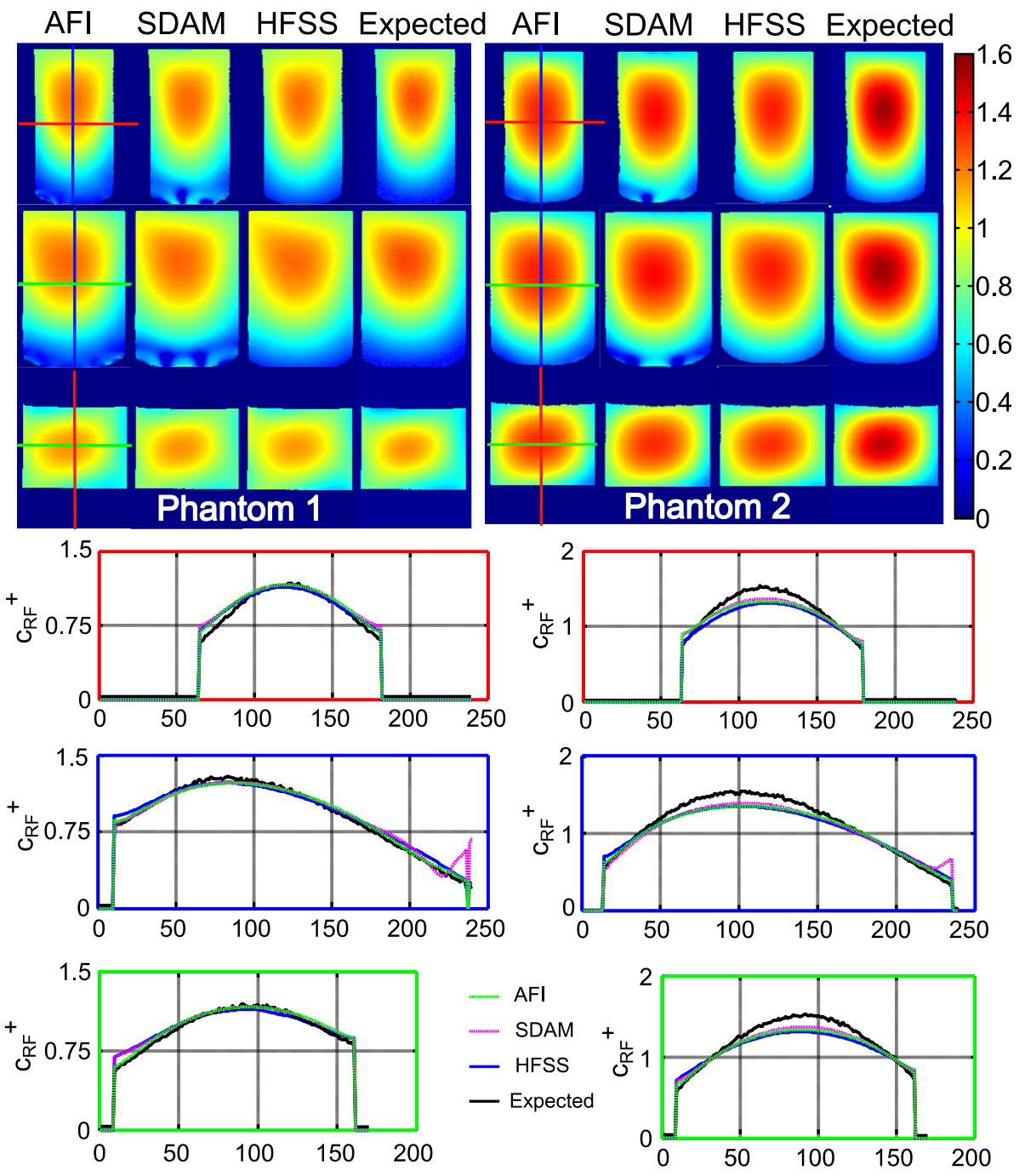

Figure 5.4: Images (sagittal, coronal, and axial slices, respectively) of the measured and simulated c_{RF}^+ maps in phantoms 1 and 2, along with corresponding profile plots (red, blue and green). The expected B_1 is calculated by assuming uniform AFI-corrected T_1 (=1353/1471 ms for phantom 1/2) throughout the phantom and using Eq. (2). The mean absolute error (in %) between the N4ITK-fitted (not shown due to nearly perfect overlap) and the expected c_{RF}^+ field is merely 1.23% for phantom 1 and 1.93% for phantom 2.

5.4.2 In vivo Experiments on 8 subjects

5.4.2.1 Optimization of N4ITK for Ψ_1 and Ψ_0

Results for the Ψ_1 optimization are plotted in Figure 5.5(a) as WM T_1 peak width versus spline distance, for four different numbers of iterations. Slightly narrower WM T_1 peak widths can clearly be achieved by increasing the number of iterations, with the best parameters being n_i/d_s=400/210 mm (yellow arrow), or n_i/d_s =200/170 mm (gray arrow). Note that the sharp decrease in WM T_1 peak width at d_s<70mm corresponds to an over-fitting of the bias field to include intrinsic image contrast.

Results for the optimization of the Ψ_0 field are displayed in Figure 5.5(b) and (c) for the WM and GM M_0 histogram peak widths, respectively. Interestingly, the optimal spline distance for WM M_0 (d_s=170 mm) differs slightly from that of GM (d_s=200 mm), therefore their midpoint (d_s=185mm) was selected as the optimal value for the Ψ_0 bias field. Figure 5.5(c) also demonstrates that 400/320/240 iterations yields the best corrected M_0 maps (compared to those with fewer iterations). Using such a large number of iterations, however, has the disadvantage of longer computation times (0.3 s per iteration of the first level on an Intel i7-3770 CPU (3.4 GHz) with 32 GBytes of RAM).

Sagittal $c_{RF,s}^+$ maps of volunteer v1 obtained using 5 different N4ITK parameter settings as well as SPM12 are displayed in Figure 5.6(a–f) along with c_{RF}^+ maps measured with AFI and SDAM (g, h). A corrected T_1 map using the optimal N4ITK settings of n_i/d_s=400/210 mm for Ψ_1 (corresponding to the $c_{RF,s}^+$ map shown in (e)) is also displayed, with $c_{RF,s}^+$ profiles shown in (i). As previously observed in the phantom, both the AFI and SDAM measure a more moderate RF inhomogeneity of c_{RF}^+≈1.14, while the optimal N4ITK setting (black curve) fits a much higher combination of RF and spoiling inhomogeneity of $c_{RF,s}^+$≈1.25. Errors in the measured B_1 field arising from off-resonance, partial volume or other effects are readily visible in the nasal cavity, and also at the top of the skull for SDAM in Figure 5.6 (h), while the $c_{RF,s}^+$ field from N4ITK is immune to such errors. The $c_{RF,s}^+$ map in (a) demonstrates the effect of over-fitting with a short spline distance of 30 mm, which causes image contrast to appear in the *bias field*. Finally, the $c_{RF,s}^+$ field fitted using SPM12 compares generally well with that from N4ITK inside the brain, but differs quite significantly within the scalp and neck. This is not a surprising result, given the fact that SPM is an atlas-based correction.

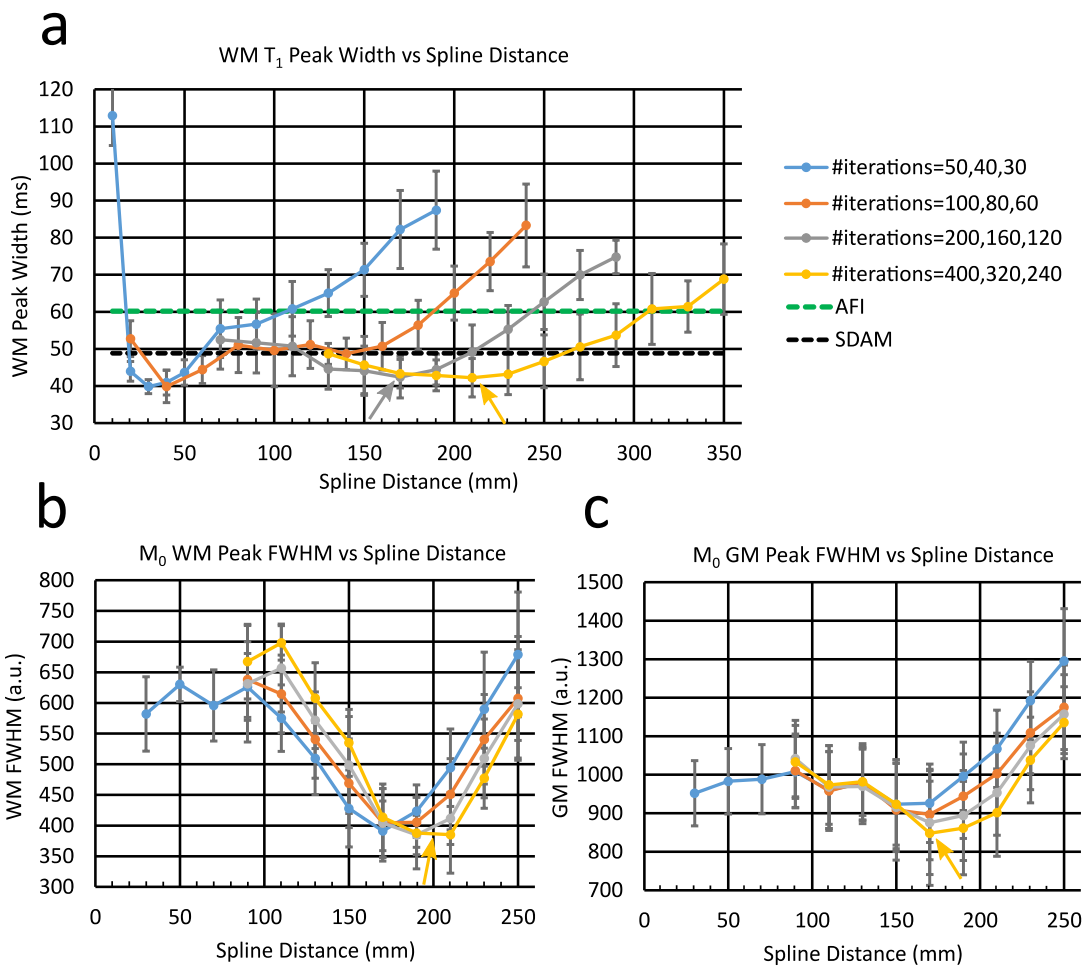

Figure 5.5: Optimization of the N4ITK bias fields for the brain in vivo at 3T. (a) Optimization of the Ψ_1 field by plotting WM T_1 peak width versus spline distance for four different numbers of iterations. The average WM T_1 peak widths obtained with SDAM and AFI are shown in dotted black and green lines, respectively. (b) Optimization of the Ψ_0 field by plotting WM M_0 peak FWHM versus spline distance, and (c) the GM M_0 peak FWHM versus spline distance. Optimal points are shown by the arrows.

5.4.2.2 M_0, T_1 and T_2 Histograms

Histograms of all parametric maps normalized by the head volume of each volunteer are shown in Figure 5.7. Parametric maps corrected with the optimal N4ITK settings are given in a, c, and e, and compared to those corrected with AFI in b, d and f. Both T_1 and M_0 histograms from the N4ITK-based correction show significantly better WM/GM peak separations, while the T_2 histograms show few differences. In general, the AFI sequence yields better WM/GM peak separations in smaller brains (e.g. v7 vs. v1), where the RF and spoiling inhomogeneity is less

significant (i.e.: $c_{RF,s}^{+}$ is closer to c_{RF}^{+}). As previously noted by [93], RF symmetry holds poorly in vivo, making the c_{RF} correction via AFI (in b) rather inadequate to clearly separate WM from GM on the M_0 histogram.

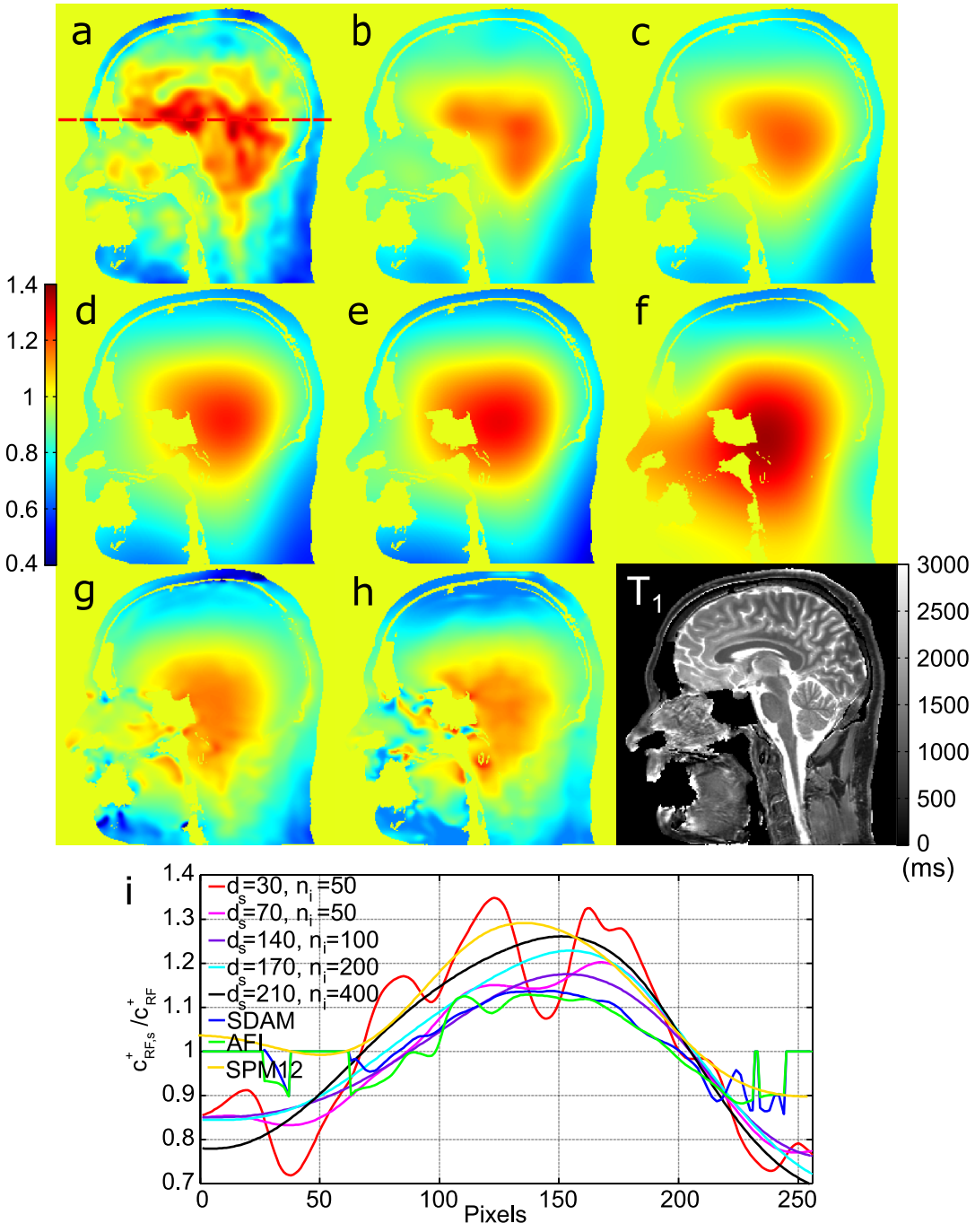

Figure 5.6: Sagittal in vivo $c_{RF,s}^{+}$ field (volunteer v1) derived from N4ITK with (a) n_i/d_s =50/30mm, (b) n_i/d_s=50/70mm, (c) n_i/d_s=100/140mm, (d) n_i/d_s=200/170mm, (e) n_i/d_s=400/210mm, (f) SPM12 with

κ/FWHM=10^{-3}/60 mm, (g) c_{RF}^{+} fields with SDAM and (h) AFI. A mask was applied to display the outline of the head. (i) Profiles through the c_{RF}^{+} and $c_{RF,s}^{+}$ fields (red line in (a)), but without any masking.

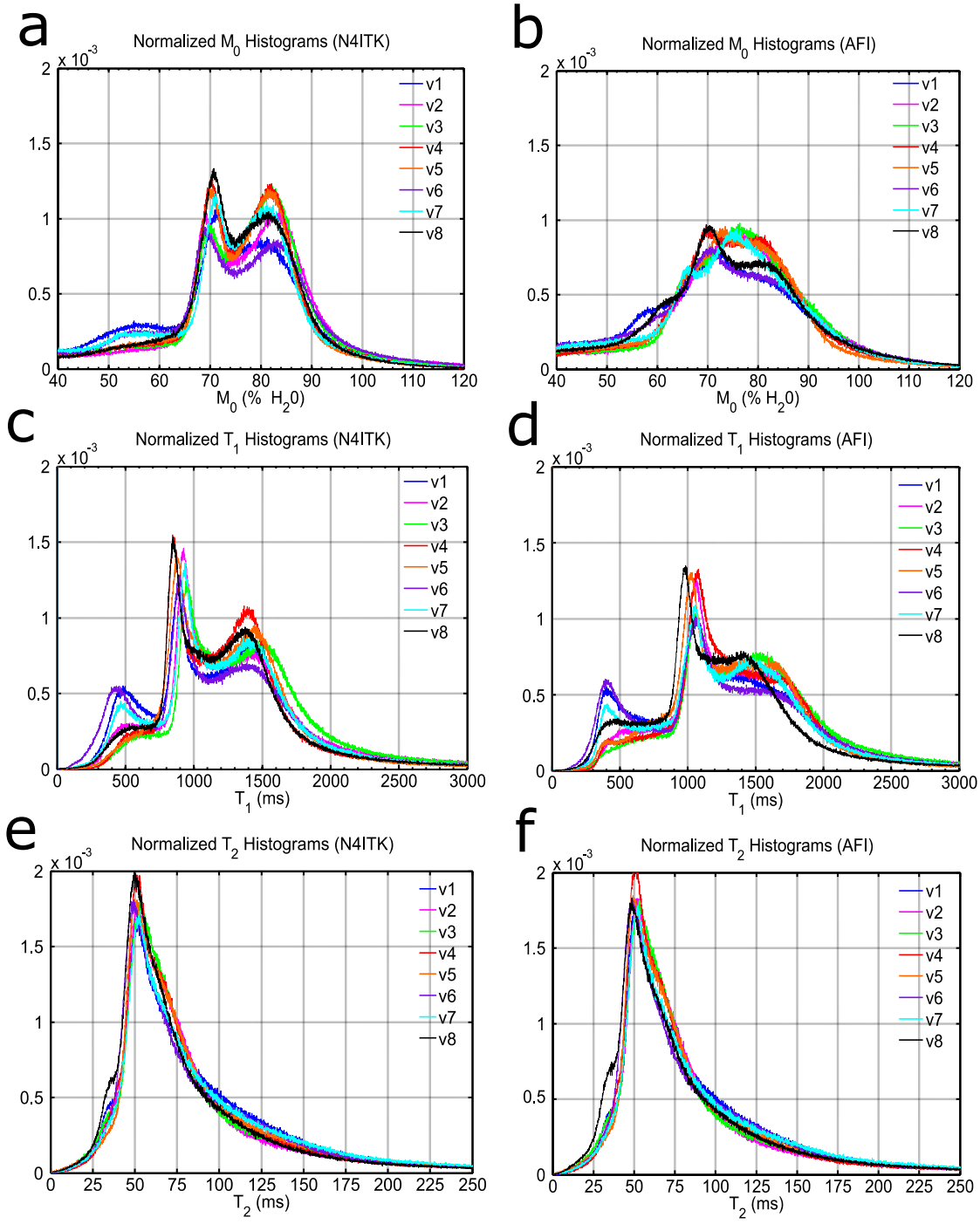

Figure 5.7: (a) Normalized M_0 histograms of the 8 volunteers corrected using N4ITK, and (b) AFI assuming RF symmetry: $c_{RF}^{+}=c_{RF}^{-}$. (c) Normalized T_1 histograms corrected using N4ITK, and (d) AFI. (e)

Normalized T_2 histograms corrected using N4ITK, and (f) AFI. The left-most peak in (c) and (d) at ~450 ms corresponds to adipose within the skull.

5.4.2.3 Measurements in Brain ROIs

Measured M_0, T_1 and T_2 in brain ROIs of the 8 volunteers are listed in Table 5.3 corrected with N4ITK, AFI, and SDAM. For comparison, IR-EPI T_1 measurements from the second examination session on 4 volunteers are also listed (see section 5.4.4). Since the c_{RF}^- inhomogeneity in M_0 could not be corrected using AFI or SDAM (by assuming RF symmetry, $c_{RF}^-=c_{RF}^+$), only T_1 and T_2 are listed for these two methods. A lower- and an upper-bound reported literature value is also listed for each ROI and parameter. Where possible, the lower-bound T_1 was taken from an IR-based technique, while the higher-bound T_1 was from a VFA technique. In general, the N4ITK-based T_1 measurement falls within the two bounds, while the AFI and SDAM measurements exceed the higher bound. The average percent difference (over all ROIs) in measured T_1 between N4ITK and the two B_1-mapping techniques are +16.7% for AFI and +12.8% for SDAM, while those of in T_2 are only -1.6% for AFI and -1.3% for SDAM. N4ITK (using c_{cal}^{head}) underestimates the T_1 by ~3.6% with respect to IR-EPI. This bias may be compensated by re-adjusting (decreasing) c_{cal}^{head} or c_{cal}^{brain} on the entire population of subjects.

5.4.3 Scan-scan Reproducibility of T_1 and M_0 Mapping

The mean c_{RF}^+ measured over the brain of each volunteer as a function of head volume V_{head} (in L) reveals a linear correlation of $\langle c_{RF}^+ \rangle_{AFI}$=0.914–0.012 V_{head} with R^2=0.92 for AFI, and $\langle c_{RF}^+ \rangle_{SDAM}$=0.941–0.012 V_{head} with R^2=0.80 for SDAM. Following this observation, the linear relationship between head volume and $\langle c_{RF}^+ \rangle_{AFI}$ was used to obtain a subject-specific c_{cal}^{head} when calibrating the N4ITK-fitted B_1^+ field such that $\langle c_{RF,s}^+ \rangle_{N4ITK} = \langle c_{RF}^+ \rangle_{AFI} = c_{cal}^{head} \approx 0.865$. Accounting for such variations in head sizes was found to slightly reduce the inter-subject variability in N4ITK-corrected T_1 from a WM T_1 peak standard deviation of ~43 ms to ~36 ms (see "WM (mean) T_1" in Table 5.2). In the calibration over the skull-stripped brain, the c_{RF}^+ field was normalized to yield the same mean WM/GM T_1 among the 8 subjects as in the calibration over the whole head, resulting in c_{cal}^{brain}=0.97 (i.e. c_{cal}^{brain}=0.97 was used on every subject, rather than using a subject-specific value that depends on the head size). For the skull-stripped brain, there was no observable dependence on brain size, and the standard deviation in measured WM T_1 peak across the 8 subjects was further reduced from ~36 ms to ~22 ms.

B_1 corr/ ROI Location	AFI (weakly spoiled)		SDAM		N4ITK			IR-EPI*	Reported Literature @ 3T		
	T_1 [ms]	T_2 [ms]	T_1 [ms]	T_2 [ms]	M_0 [%]	T_1 [ms]	T_2 [ms]	T_1 [ms]	M_0 [%]	T_1 [ms]	T_2 [ms]
Putamen R	1418 (95)	62.7 (2.4)	1385 (49)	62.8 (2.4)	83.3 (1.6)	1222 (72)	63.6 (2.5)	1250 (54)	81.9[g], 83.2[h]	1337[a], 1140[b]	69[j], 57[k]
Putamen L	1468 (61)	62.7 (2.6)	1384 (46)	63.0 (2.4)	83.7 (2.0)	1182 (55)	64.1 (2.5)	1232 (63)	81.9[g], 83.2[h]	1321[a], 1140[b]	69[j], 57[k]
Globus Pallidus R	1190 (62)	48.2 (3.2)	1150 (32)	48.1 (3.2)	80.2 (2.6)	1003 (54)	48.9 (3.2)	–	76.8[i]	888[b], 1043[c]	45[k]
Globus Pallidus L	1236 (36)	48.0 (2.1)	1158 (36)	48.2 (1.9)	80.3 (3.4)	983 (40)	49.2 (1.9)	–	76.8[i]	888[b], 1043[c]	45[k]
Caudate R	1544 (105)	75.3 (5.1)	1538 (71)	75.3 (4.8)	86.2 (2.2)	1338 (68)	76.3 (5.0)	1432 (94)	81.5[g], 84.8[h]	1524[a], 1464[e]	82[j], 63[k]
Caudate L	1606 (71)	73.2 (4.3)	1555 (74)	73.5 (4.2)	85.2 (2.8)	1392 (71)	74.3 (4.4)	1438 (16)	81.5[g], 84.8[h]	1437[a], 1464[e]	82[j], 63[k]
Splenium	1016 (52)	53.6 (3.1)	988 (43)	53.9 (3.0)	70.9 (2.2)	867 (58)	54.6 (2.9)	906 (30)	70.1[g], 66.2[h]	730[b], 773[f]	–
Genu	959 (48)	48.9 (2.8)	960 (61)	48.9 (2.6)	69.7 (0.6)	845 (44)	49.5 (2.7)	872 (22)	69.6[g], 69.0[h]	898[a], 720[b]	–
Frontal WM R	992 (44)	47.6 (2.5)	973 (43)	47.7 (2.3)	69.7 (0.6)	875 (40)	48.1 (2.4)	902 (43)	70.1[g], 69.1[h]	947[a], 838[d]	50[j], 53[k]
Frontal WM L	1004 (32)	48.0 (2.1)	972 (37)	48.2 (2.0)	69.6 (0.7)	885 (45)	48.6 (2.0)	908 (38)	70.4[g], 69.1[h]	921[a], 847[c]	50[j], 53[k]
Occipital WM R	1020 (31)	52.8 (2.8)	985 (44)	52.9 (2.5)	69.9 (1.0)	892 (44)	53.4 (2.5)	910 (52)	69.0[g], 66.9[h]	954[a], 832[d]	–
Occipital WM L	1025 (41)	51.2 (1.7)	969 (47)	51.4 (1.5)	69.9 (1.0)	861 (35)	51.9 (1.5)	902 (28)	69.5[g], 66.9[h]	940[a], 832[d]	–
WM (mean)	1054 (31)	50.2 (1.3)	1004 (21)	50.4 (1.2)	70.4 (0.5)	905 (36)	51.1 (1.2)	–	71 (1)	912*, 882**	48[l]
GM (mean)	1567 (51)	66.1 (2.4)	1503 (47)	66.9 (2.3)	81.5 (0.6)	1403 (55)	67.6 (1.9)	–	81 (1)	1445*, 1380**	64[l]

Table 5.3: Measured M_0, T_1 and T_2 in various brain ROIs using B_1 inhomogeneity corrections based on N4ITK, AFI, or SDAM. Lower and upper bound literature values are listed in each case for comparison. *Mean and **median values calculated from the 23 publications in Figure 5.1. Literature references are: [a][85], [b][106], [c][107], [d][108], [e][11], [f][109], [g][93], [h][110], [i][111], [j][128], [k][139], [l][164]. Note that most authors average over corresponding ROIs in the left and right brain hemispheres. *The IR-EPI T_1 measurements listed here only include $TI \geq 200$ ms, to avoid bias from the faster-relaxing components as recommended by Rioux et al [113]. T_1 mapping techniques include VFA (a, e, f, g, i, j), Look-Locker (b, c, h), Saturation Recovery (d), and T_2 mapping techniques include DESPOT2 (j), CPMG (k) and MRF (l).

Voxel-wise CoVs of the 11 datasets of volunteer v1 are displayed in Figure 5.8(a-c) as well as the 11 corresponding T_1 histograms in (d) and (e). Mean CoVs over WM/GM/CSF tissue classes

are 6.3/8.4/12.2% for AFI-corrected T_1, 5.8/7.4/11.2% for N4ITK-corrected T_1, and 3.4/4.7/6.6% for N4ITK-corrected M_0. The neck and scalp have much higher CoVs (>20%) because of tissue deformations and the fact that only a 6DOF rigid registration was employed (excluding the skull and neck via masking).

Corrected axial M_0, T_1, T_2 and T_2^* images of two female (v3, v5) and two male volunteers (v6, v8) are shown in Figure 5.9, along with the corresponding N4ITK-fitted $c_{RF,s}^{+}/c_{RF}^{-}$ fields (and input Ψ_1/Ψ_0 masks) in Figure 5.10.

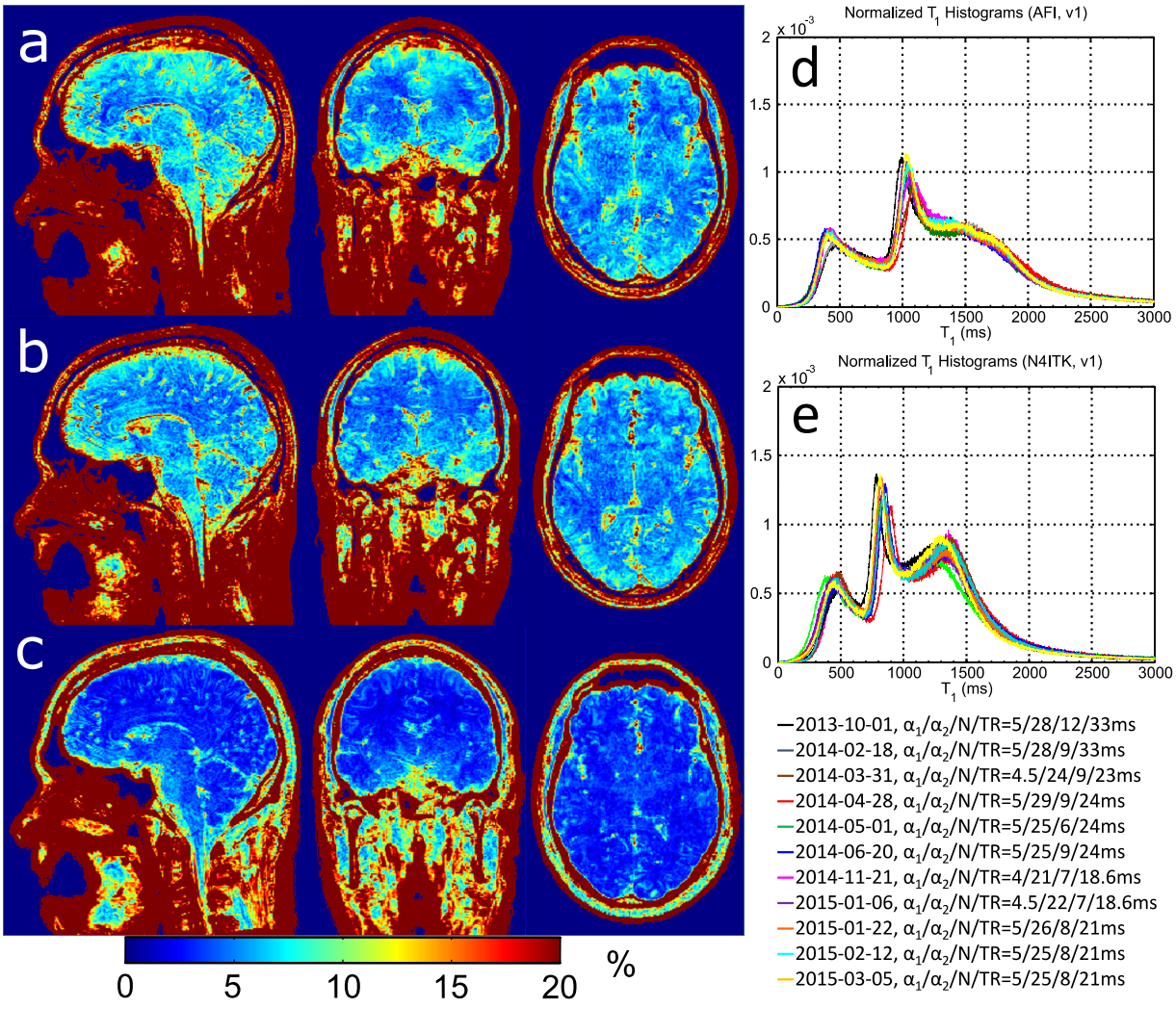

Figure 5.8: Measured coefficients of variation (CoV=<X>/σ_X×100%) describing measurement reproducibility in (a) T_1 corrected with AFI, (b) T_1 corrected with N4ITK, and (c) M_0 corrected with N4ITK. Eleven T_1 histograms corresponding to the CoVs in (a) and (b) are shown in (d) and (e), respectively.

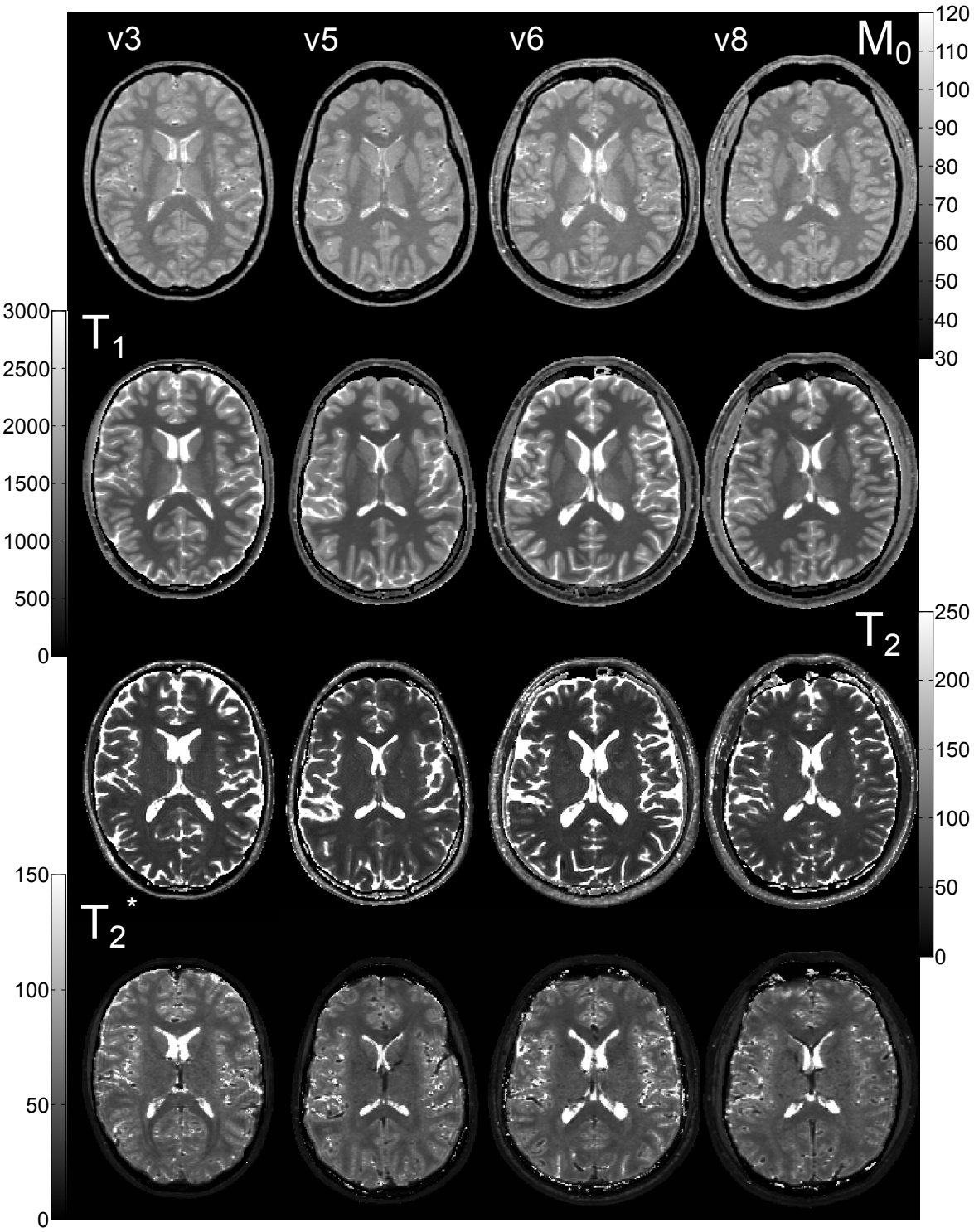

Figure 5.9: Axial in vivo M_0 [%], T_1 [ms], T_2 [ms] and T_2^* [ms] maps of four volunteers, after correction for $c_{RF,s}^{+}$ and c_{RF}^{-} (shown in Figure 5.10) with optimal N4ITK parameters.

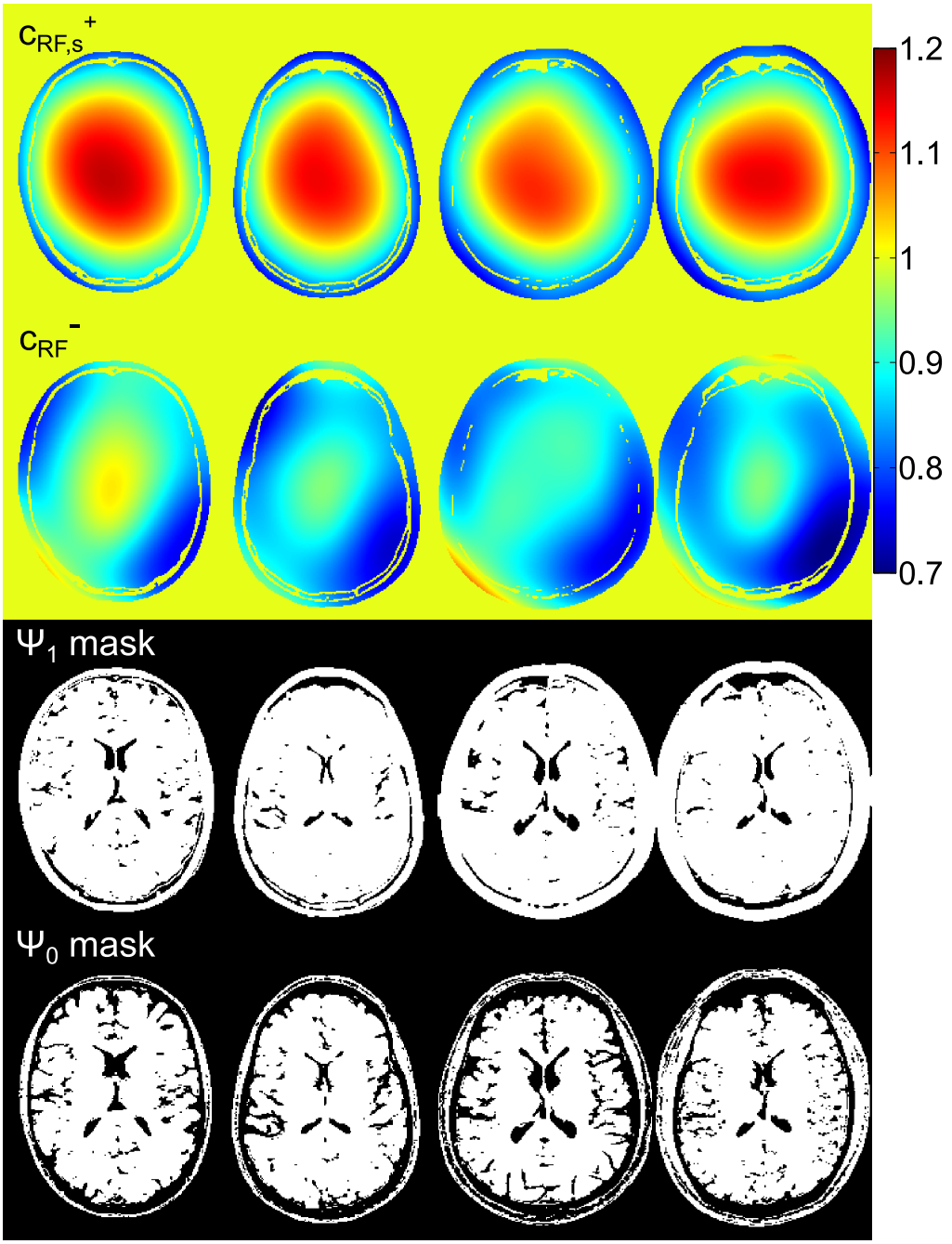

Figure 5.10: Axial $c_{RF,s}^{+}$ and c_{RF}^{-} maps fitted from N4ITK, within the same axial slices shown in Figure 5.9 for the same 4 volunteers, as well as the masks used in conjunction with the T_1^{app} and M_0^{app} images to estimate the fields. Observe the similarity in field patterns among the different head sizes and shapes.

5.4.4 In vivo Comparison of N4ITK-corrected T_1 with Inversion Recovery and SPM

Normalized image histograms of T_1 and M_0 are shown in Figure 5.11 for three volunteers (v1, v4 and v6) under the three different B_1 correction schemes (weakly-/strongly-spoiled AFI and

SDAM), and the two different bias-field correction methods (N4ITK and SPM12). In all four volunteers, the B_1 correction using the weakly-spoiled AFI results in a gross overestimation of T_1 with broader WM/GM peaks at ~1100/1700 ms. The strongly-spoiled AFI correction and the SDAM correction both yield a lower T_1 of ~1000/1550ms. The B_1 maps are accurate, but the non-ideal RF spoiling inhomogeneity intrinsic to the SPGR sequence remains uncorrected. Finally, N4ITK and SPM remove both sources of inhomogeneity simultaneously, yielding WM/GM T_1~875/1400ms. Interestingly, the SPM12 correction with c_{cal}^{brain}=1.00 (same calibration factor used by Weiskopf et al [92]) makes the WM T_1 peaks match very closely with those of N4ITK with c_{cal}^{brain}=0.97. There is however a tendency for SPM to yield slightly lower GM T_1 or M_0 than N4ITK. We may therefore conclude that the value of c_{cal} is also algorithm-dependent and not only hardware- and subject-dependent. The SPM12 algorithm results in an even greater inhomogeneity than N4ITK at the center of the brain (see Figure 5.6 (f) and (i)), thus requiring a higher c_{cal} value. As noted earlier, SPM12 cannot accurately remove the RF inhomogeneity within the skull or neck, therefore, the SPM12-corrected T_1/M_0 histograms were also plotted after skull-stripping the T_1/M_0 images for comparison.

A comparison of the IR-EPI and the N4ITK-corrected VFA T_1 map is shown in Figure 5.12 for the same three volunteers, along with histograms of each corresponding T_1 and the voxel-wise percent difference (also shown for the fourth volunteer v5). Note that some systematic discrepancies between both techniques are visible, and it may be observed that N4ITK removes most but not all the inhomogeneity, thus still yielding somewhat broader WM T_1 peaks than the gold-standard IR-EPI technique. The systematic percent differences (-4.4, +4.5, -6.1 and -7.2%) are most likely due to our choice of using an identical c_{cal}^{brain}=0.97 for all subjects, when in practice the true $c_{cal}^{brain}$is unknown and may be somewhat subject-dependent (e.g., temperature, head size, physiology, etc…) and potentially even fluctuate over time, for example due to calibrations like the scanner's transmit gain (TG).

5.4.5 Imaging of Primary Brain Tumor Patients

Axial slices taken through the five parametric maps of the tumor patients are given in Figure 5.13. Transmit and receive B_1 inhomogeneity (c_{RF}^{+} and c_{RF}^{-} maps) fitted by N4ITK are given in Figure 5.14, for the same corresponding axial slice location of each patient. The binary masks that were input into N4ITK for fitting Ψ_1 and Ψ_0 are also shown below the fields. In spite of the

large masses, or cavities following surgical resection, the algorithm is still able to provide a robust estimate of the bias fields and correct for RF inhomogeneity leading to sharp M_0/T_1 histograms (not shown for brevity).

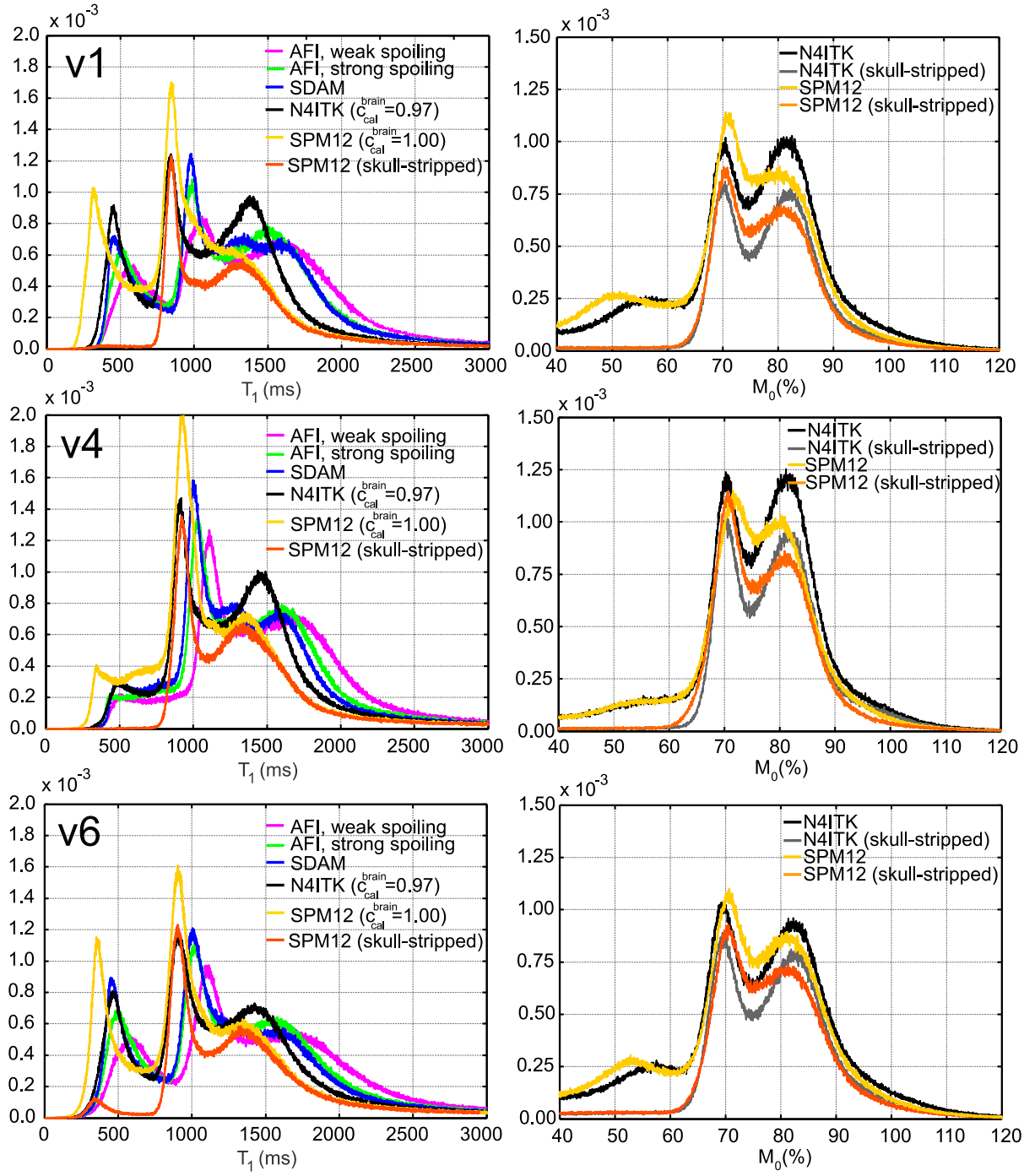

Figure 5.11: Comparison of normalized T_1 and M_0 histograms for 3 of the 4 volunteers scanned with the different B_1 correction techniques.

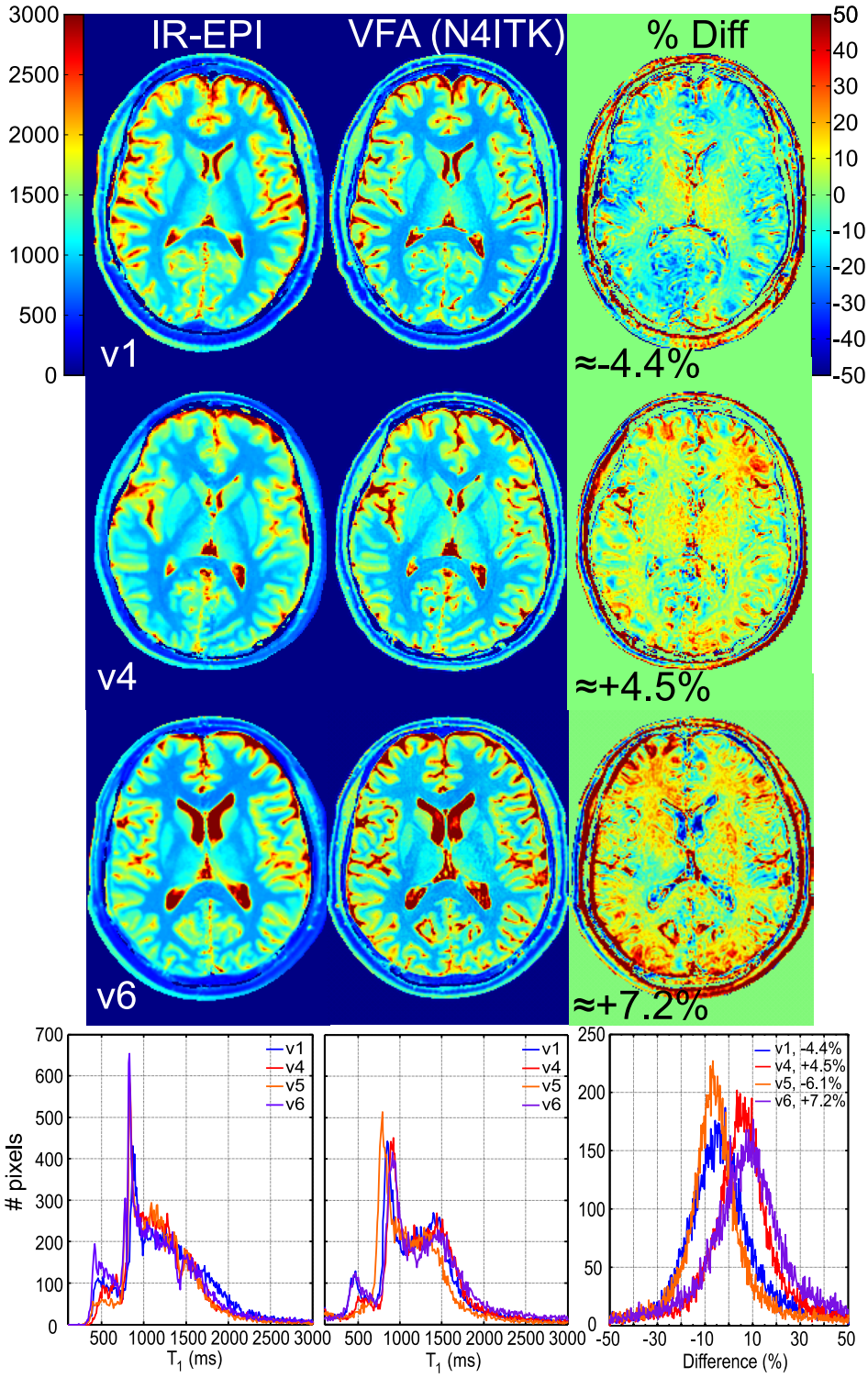

Figure 5.12: A single-slice T_1 comparison of IR-EPI with VFA (corrected using N4ITK) for 3 out of the 4 volunteers. Histograms from all volunteers are shown. All 8 TIs were included within the fit of these IR-EPI T_1 maps.

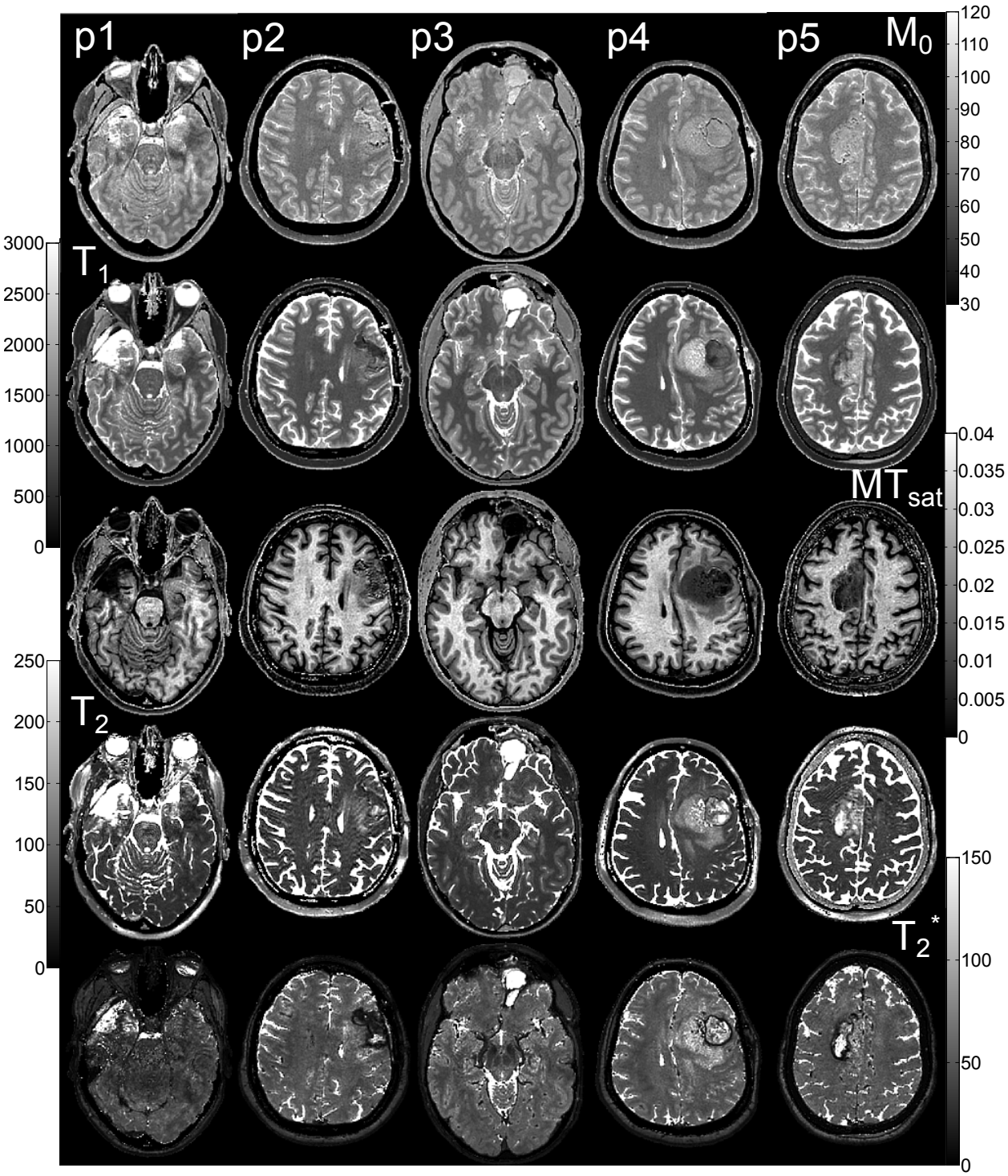

Figure 5.13: Axial slices of the parametric maps taken through primary brain tumors in 5 patients. Note that M_0 is in percent (%), MT_{sat} is unitless, while T_1, T_2 and T_2^* are in milliseconds (ms). The tumors are clearly defined, despite motion artifacts being present in the M_0 and T_2^* maps of p1 and in the T_2 maps of p3 and p5.

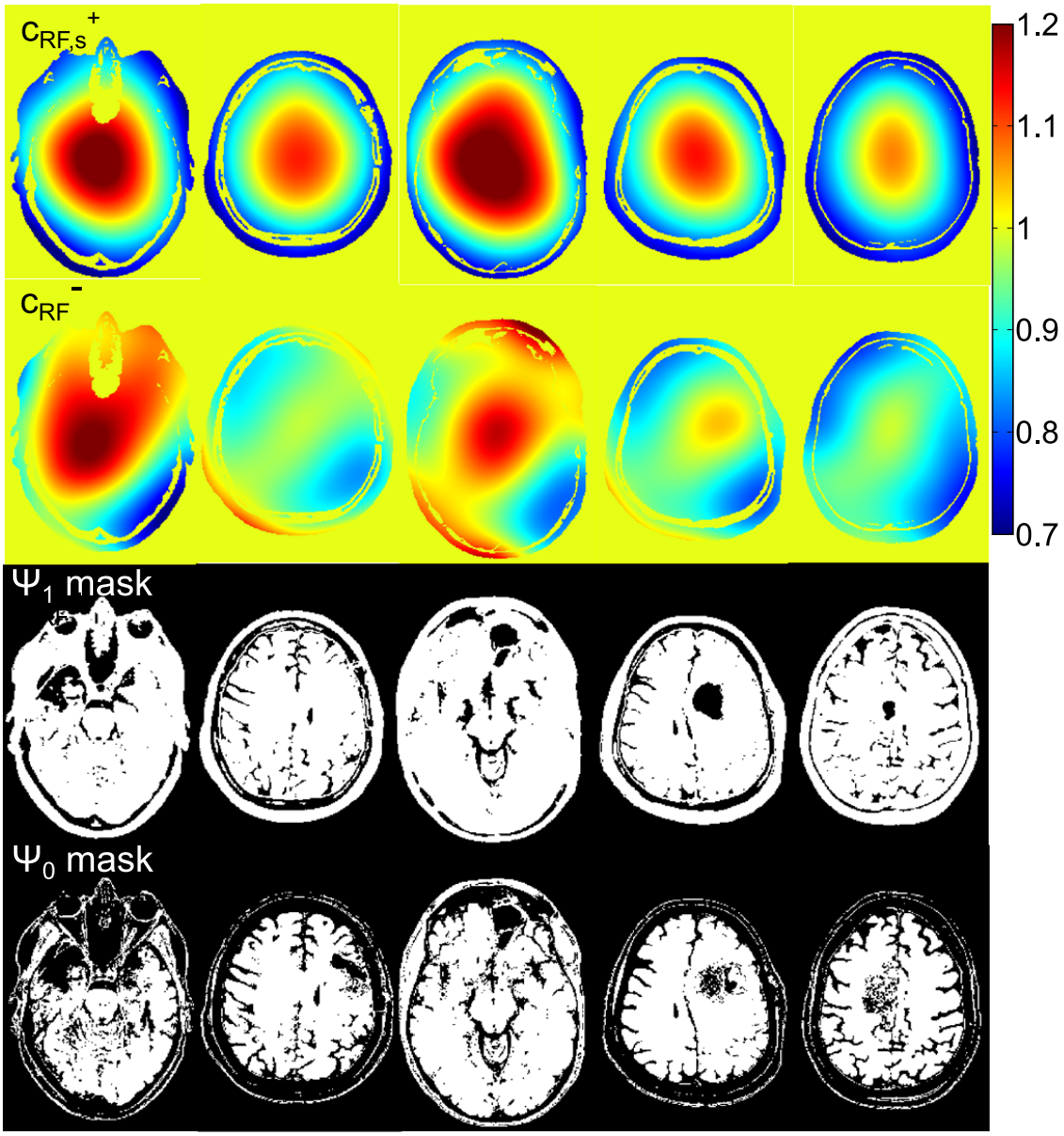

Figure 5.14: Axial $c_{RF,s}^{+}$ and c_{RF}^{-} maps fitted from N4ITK, within the same axial slices shown Figure 5.13 for the 5 patients, as well as the masks used in conjunction with the T_1^{app} and M_0^{app} images to estimate the fields.

5.5 Discussion

In this work, N4ITK was optimized via a histogram-sharpening (H-S) technique for fitting both transmit and receive RF inhomogeneity in T_1^{app} and M_0^{app} brain maps, yielding two bias fields, Ψ_1 and Ψ_0. This optimization needs to be performed only once for a given imaging configuration (anatomy, coil, field strength) and need not be repeated for each subject. In all cases, the N4ITK-based RF inhomogeneity correction yields narrower WM/GM T_1 histogram peaks than two

conventional B_1 mapping techniques, because the additional bias from non-ideal RF spoiling is also removed.

Unlike the B_1^+ field, there is no existing method to accurately map the B_1^- field in absolute terms. As explained in Volz et al [93], and also confirmed in this work (see Figure 5.7b), the assumption of RF reciprocity ($c_{RF}^+ \approx c_{RF}^-$) fails in vivo, and a bias field correction algorithm or a polynomial fit [102] is necessary to accurately map M_0 at 3T. As listed in Table 5.3, the N4ITK-corrected M_0 agrees closely with values reported in the literature, with mean values of ~70.4/81.5% in WM/GM. The M_0 histograms following the N4ITK-based correction also compare well with those of SPM12-based correction in Figure 5.11.

In contrast to M_0 and T_1, T_2 mapping via the VFA technique (DESPOT2) is relatively robust to RF inhomogeneity and/or errors in T_1, provided that the same c_{RF}^+ (or $c_{RF,s}^+$) is used consistently in the calculation of both T_1 and T_2. This effect is illustrated via the brain ROI T_2 measurements shown in columns 3, 5 and 8 of Table 5.3, where, despite T_1 differences of 100−200 ms between AFI/SDAM and N4ITK, the differences in T_2 are only ~1 ms. This effect is due to a partial cancellation of the effect of RF inhomogeneity when T_2^{app} is calculated from T_1^{app}. In fact, the T_2 histograms and maps remain relatively unaffected in the complete absence of B_1 correction (not shown), but instead are quite sensitive to motion and pulsation effects (i.e., where dB/dt≠0).

The scan-scan reproducibility of T_1 and M_0 mapping was assessed in this work via voxel-wise statistics on 11 VFA scans of volunteer v1. The large number of time points over many months, with some variations also in scan parameters, provide stronger CoV measurements than those in other studies where CoVs are estimated from only a few time points separated by hours or days. The CoVs in M_0 were 3.4/4.7/6.6% (in WM/GM/CSF, respectively), which compare well with those reported by [90] (2.7/3.9/5.2%). Likewise, the CoVs in T_1 were 5.8/7.4/11.2% for N4ITK, which are comparable to those of UNICORT [92] (6.5/8.7/– %), and also slightly superior to those of AFI-corrected T_1 reported here (6.3/8.4/12.2%).

The N4ITK-based RF inhomogeneity correction technique requires a careful choice of calibration factor c_{cal}^{Ω} to obtain the correctly normalized $c_{RF,s}^+$ and c_{RF}^- fields. We found that normalizing the bias fields over the skull-stripped brain with the assumption of a fixed and identical c_{cal}^{brain}=0.97 for all subjects yielded the lowest inter-subject variability in T_1, and also

yielded T_1 maps in excellent agreement with [92]'s UNICORT technique with c_{cal}^{brain}=1.00. The intra-subject T_1 comparisons with IR-EPI highlight some subject-specific systematic bias in the range of ±7%. Moreover, we also observed that the choice of RF phase cycle increment ϕ_0 (=50/117º) has a systematic impact on the resulting T_1 (under a fixed c_{cal}^{brain}=0.97), yielding systematic shifts (≈+5/–4%) of the WM/GM T_1 peaks with respect to system's default value of ϕ_0 =150º. Therefore, we conclude that c_{cal} is a function of several variables, including the transmit gain (TG) setting, the coil loading, (CL), and ϕ_0, and could potentially depend on other hardware or subject-dependent variables. We also found that using the same TG setting (RF power optimization step) on both the lower and higher SPGR flip angles (α_1/α_2) was crucial in reducing both the intra-subject and inter-subject fluctuations in T_1.

We observed the MT-induced bi-exponential T_1 relaxation reported by Rioux et al [113] in the IR-EPI T_1 measurements on 4 subjects. Excluding the shortest TI=20 ms from the fit resulted in WM/GM T_1 values that were systematically 8/6% longer, while this effect was negligible within the agar phantom, with an average systematic increase of only ~0.3%. Finally, using the same T_1 curve-fitting toolbox designed by Barral et al [166] and including the shortest TI within the fit resulted in the same mean WM T_1 of ~830 ms reported by Stikov et al [150]. Since T_1-mapping via the VFA technique is not expected to be sensitive to MT effects [137], we are a step closer to reconciling the differences in reported WM/GM T_1 across different studies and techniques.

The parametric maps and RF fields calculated on the 5 cancer patients demonstrate that N4ITK can still estimate the RF inhomogeneity in the presence of highly abnormal brain anatomy. It was previously observed that large tumors can alter the ability to accurately map and correct for c_{RF}^- in M_0 mapping, and that UNICORT (SPM8) performance in such cases was inferior to polynomial-fitting via pseudo proton densities [102]. While for brevity's sake, we do not compare N4ITK to the SPM12 correction on the patients, there was no evidence of any significant visible perturbations within the N4ITK-derived $c_{RF,s}^+/c_{RF}^-$ fields of the 5 brain cancer patients compared with those of the healthy volunteers. From our observations, certain tumors contain a region of short T_1~500 ms, surrounded by a wider surrounding area of longer T_1~1500−2500 ms (usually identified as peritumoral edema), while others generally show little change in T_1, but a significantly longer T_2>75−150 ms. By virtue of the flow effects on T_2^* maps, the tumor vasculature is clearly distinguished from the edema by its very short T_2^* (<30 ms).

Unlike T_1, the MT_{sat} of tumor always decreases to values below that of normal GM or WM (<0.014/0.03), signifying a decrease in the macromolecular pool while proton density tends to increase or remain unchanged.

One concern of using bias field correction algorithms in quantitative MR applications (as proposed in this work) is whether such techniques are robust against artificially eliminating either physiological or pathological non-uniformities that are not associated with RF field non-uniformities. Indeed, comparison with the IR-EPI standard shows that the N4ITK correction is not perfect, although the long spline distance of ~185–210 mm is essential to prevent the removal of local pathological and physiological deviations in T_1. Further investigation and comparisons with B_1-mapping techniques applied to different types of pathologies will be required in the future to address these remaining inconsistencies.

5.6 Conclusion

The primary aim of this work was to optimize the N4ITK bias-field correction algorithm to remove the effects of both transmit and receive RF inhomogeneities (B_1^+/B_1^-) in multi-parameter mapping via the VFA technique at 3T. We hypothesized that N4ITK may provide a more robust RF inhomogeneity correction than B_1-mapping or RF simulation techniques and thus could serve as a standard with which to implement quantitative studies longitudinally or across different imaging centers. Our optimization and calibration of the N4ITK algorithm remove RF inhomogeneities in maps of M_0, T_1 and T_2 of the normal and diseased brain at 3T. We have shown that N4ITK significantly outperforms AFI, SDAM and B_1 simulations because it also simultaneously compensates for the inhomogeneity in non-ideal RF spoiling, yielding T_1 measurements that agree significantly better with the mean/median values reported in the literature as well as our IR-EPI T_1 measurements. While robust M_0 mapping was also achieved, T_2 was shown to be quite insensitive to the choice of RF inhomogeneity correction. Our N4ITK-based B_1 correction can be readily implemented in VFA T_1, T_2, MT_{sat} and M_0 mapping on any MRI scanner, provided that a scanner-specific calibration factor c_{cal}^{head} or c_{cal}^{brain} is first determined for typical human heads or skull-stripped brains, respectively. The N4ITK parameters optimized in this study may be used to correct RF inhomogeneity in the human brain at 3T; however, at different field strengths, with substantially different coil configurations, or in other parts of the human anatomy, the optimization should be repeated because the optimal

spline distance depends on the RF wavelength [65] and the anatomy [64]. The reproducibility of the method was also shown to be slightly superior to B_1-mapping with AFI and shown to compare well with typical reported M_0 and T_1 CoVs of similar studies. Multi-parameter mapping with N4ITK-based RF inhomogeneity correction was largely unaffected by the presence of abnormal anatomy such as large primary brain tumors and cavities following tumor resection.

5.7 Acknowledgements

This work was supported by the Alberta Cancer Foundation, the Natural Sciences and Engineering Research Council (Canada) and the Alberta Cancer Research Institute. We also thank CMC Microsystems for software access, Philips Healthcare for technical support, Dr. Guillaume Gilbert for implementing the MP2RAGE sequence, Dr. Roger Luechinger for the PATI program used for data transfer, Mr. Bryson Dietz for assistance using the SPM12 and FSL software and Mr. Ken Hennig for building the phantoms and supports.

Chapter 6: Automatic Tissue Classification and Generation of Synthetic CT from Ultra-short TE (UTE) MRI

"The true logic of this world is the calculus of probabilities."

— James Clerk Maxwell

In James Clerk Maxwell and Peter Michael Harman (ed.), *The Scientific Letters and Papers of James Clerk Maxwell*, Vol. 1, 1846-1862-(1990), 197.

6.1 Introduction

Computed Tomography (CT) is an imaging modality that generates image contrast based on the linear attenuation coefficient of X-rays. The intensity of CT pixels is usually given in Hounsfield units (HU), defined as $N_{CT} = (\mu - \mu_w)/\mu_w \times 1000$ HU, where μ_w, is the average linear attenuation coefficient of water (given the X-ray spectrum), and μ is the measured attenuation coefficient of the voxel. Since the human body is about 75% water, this scaling minimizes the variability in CT pixel values across different scanners and scan parameters. Hounsfield units have the useful property of being approximately linearly proportional to the electron density. Since X-ray dose deposition is governed primarily by the Compton Effect, which in turn depends on the electron density, CT datasets are used for tissue inhomogeneity corrections in Radiation Treatment Planning (RTP), as well as for linear attenuation corrections in Positron Emission Tomography (PET). Unlike MRI, however, CT is at a disadvantage for its ionizing radiation exposure and poor soft-tissue contrast. Consequently, there is a strong research interest in replacing CT with MRI in both RTP and PET imaging, but before this can become clinically routine, a fast MRI-based tissue classification technique is required so that electron densities can be automatically assigned to MRI voxels[11]. The classified image is often called a "synthetic-CT" (a.k.a. "pseudo-CT" or "substitute-CT"). One promising technique for fast MRI-based tissue classification uses an ultra-short echo time sequence (UTE).

Before UTE imaging started gaining momentum in the early 2000s, proposed methods for classifying (or segmenting) bone/air MRI voxels included manual segmentation [3] and segmentation based on level sets (a.k.a. geodesic snakes), of which the brain-extraction tool (BET) in FSL is an example [4], [167]. The segmentation of gray-matter (GM), white-matter (WM), and cerebrospinal fluid (CSF) on T_1-weighted images, was already well established, as well as the segmentation of water/fat content using Dixon's method [29], (pp. 857–887). Unfortunately, manual segmentation is too time-consuming for routine clinical use. As for Atlas-based segmentation, it is generally inaccurate for patients with abnormal anatomy [168]. Since it is not uncommon for cancer patients to have undergone surgery, altering their normal anatomy, routine use of an Atlas-based segmentation approach may not be the most viable option.

[11] In CT, electron densities can be assigned via a simple calibration using a phantom containing materials (inserts) of known densities. However, because no correlation exists between electron density (or atomic number Z) and MRI signal intensity, a tissue classification is required prior to assigning electron densities.

An ultra-short echo (UTE) pulse sequence is usually a gradient-spoiled, RF-spoiled or balanced gradient echo pulse sequence, with a radial (center-out k-space) sampling trajectory. By virtue of its ultra-short TE, UTE can detect signal in cortical bone, which has short T_2^* in the range of 0.4–0.5 ms and a proton density ~20% that of pure water. Excellent bone-to-tissue contrast is usually generated by comparing the ultra-short echo to a longer echo, (usually in the range of 2–5ms). The segmentation of bone using a double-echo or triple-echo UTE pulse sequence has now clearly become the gold standard for MRI-based bone segmentation, and has already proved to be quite successful in enabling automatic linear attenuation corrections on hybrid PET-MRI scanners [18], [168], [169], [170].

Since 2010, at least seven different UTE-based segmentation methods have been published. Keereman et al [168] were the first to propose a simple threshold-based segmentation technique on a T_2^* map derived from a double-echo UTE dataset, and yielding a 3-class segmentation (bone, air, and soft-tissue). Unfortunately, their method does not enable the segmentation of fat, nor the distinction between hard cortical bone (CT#: 600–1500 HU) versus porous bone (CT#: 100–600HU). Catana et al [169], published a similar approach (3-classes), but using an image-subtraction method (using two echoes) in place of T_2^*. Their method was also easy to implement, but the results were quite comparable to those of Keereman's. The required UTE scan time was about 5 min in both cases. In 2011, Johansson et al published a more sophisticated classification method based on two double-echo UTE images acquired at two different flip angles (α_1/α_2=10°/60°), and a 3D T_2-weighted (3D turbo spin echo) Cartesian MRI dataset. Training data was obtained by registering the 5 MRI datasets to CT and using a Gaussian mixture model with expectation-maximization to predict CT numbers from MRI pixels. Their method was reported to achieve a mean absolute error (MAE) of 137 HU (between actual and predicted CT numbers over the brain) based on five patients [171]. Unfortunately, their method is more difficult to reproduce, because of the complex post-processing and the total scan time (~11 minutes) was especially criticized by other authors for being too long.

In 2012, Berker et al [18] published a new 4-class segmentation method (soft-tissue, adipose, bone and air) based on a UTE triple-echo Dixon sequence (UTILE-Dixon). Their method is elegant, in that a single pulse sequence acquired in 3-4 min scan time can enable a 4-class segmentation (bone, air, fat and soft-tissues), which none of the previous methods could achieve.

In 2013, Navalpakkam et al proposed a technique that appears to incorporate ideas from both Johansson and Berker to create continuous-valued attenuation maps [170]. The main difference with respect to the UTILE-Dixon method, was that a separate Cartesian 2-point Dixon (0.5min) and a double-echo UTE sequence (1.5min) were acquired instead of a triple-echo UTE. Their regression method (pattern recognition approach ε-SVR) was also different from Johansson's but required the same CT training data. Recently (in 2014), a sixth method was proposed by Delso et al [172] (cluster-based segmentation) and shown to outperform both Keereman's and Catana's methods. Finally a seventh method based on fuzzy c-means classification using a combination of T_1w, T_2w, Dixon, and UTE MRI was also tested in radiation therapy dose computation for head and neck (on one patient) [173]. Despite segmentation results that do not appear to outperform previous UTE-based techniques (see Fig. 10 in Ref. [173]), their MRI-based heterogeneity correction was quite comparable to the CT-based correction on a dose-volume histogram.

As far as the MRI acquisition strategy (i.e. the choice of pulse sequence(s)) is concerned, Berker's and Navalpakkam's methods are definitely the most promising, given the short scan duration of under four minutes. While combining Cartesian T1w/T2w MRI data to the UTE may certainly help further refine the final classification, it is preferable to seek to achieve a robust classification from a single sequence alone, for the sake of time constraints, simplicity and potential standardization of the method across different scanners and imaging centers. A single sequence also avoids the need for inter-sequence MR image registration prior to the classification. Therefore, Berker's technique should serve as a starting point from which further refinements can be made. Navalpakkam et al did demonstrate that a continuous-valued synthetic CT yielded more accurate linear attenuation corrections in PET-MR (see their Fig. 6 [170]). However, their method employed two sequences (a Cartesian Dixon and a radial double-echo UTE), and could therefore be sensitive to interscan motion.

Therefore, in this work we combine the strengths of both Navalpakkam's [170] and Berker's [18] previous techniques by further refining Berker's UTILE-Dixon tissue classification method to obtain continuous-valued attenuation maps via a simple fuzzy c-means (FCM) classification algorithm. The new technique is compared (both in vivo and in a phantom) to Berker's original (discrete) method in terms of MEA (between the actual CT and the synthetic CT). We also

compare the accuracy of the dose simulation on the traditional CT versus the synthetic CT (sCT) via dose volume histograms (DVHs).

6.2 Theory

6.2.1 Berker's Original UTILE-Dixon Method

At 3T (~128 MHz), the three echo times (TE's) selected within a UTILE-Dixon (spoiled gradient echo UTE) sequence should be as close as possible to $TE_1/TE_2/TE_3$=0/1.15/2.30 ms to enable Dixon decomposition based on the chemical shift ($\Delta\omega_f/\omega$=3.4 ppm) between water and fat. In practice, however, TE_1 cannot be perfectly zero, due to hardware constraints (minimum coil switching time), and thus a value of TE_1=0.07−0.10 ms is more typical on most systems (N.B. Berker et al used TE_1=0.09ms). The "zero-TE" (ZTE) imaging sequence does achieve TE_1=0 ms and was recently employed for the purpose of tissue classification. However, it cannot simultaneously achieve Dixon water/fat classification [174] because only a single echo is acquired.

Most UTE implementations use a flip angle of α=10°, and TR~4-6 ms. However, to minimize errors in bone, air and CSF classification, an optimal flip angle for UTILE-Dixon should be found to yield about the same signal intensity within both bone and CSF based on their intrinsic proton-density, T_1, and T_2^*. This is because bone and CSF yield about the same SNR, which is lower than that of other tissues. The CSF signal tends to be noisy in a UTE image due to its long T_1 ~4300 ms, while the bone signal is noisy due to its low proton density M_0 ~20% and short T_2^*~0.4–0.5 ms.

The optimal flip angle is found by using the modified spoiled gradient echo signal equation in steady-state, which takes into account T_2^* decay during the RF pulse [175]:

$$S_{UTE} = \frac{M_0(1-E_1)b}{1-E_1 a} e^{-\frac{TE}{T_2^*}}, \tag{6.1}$$

$$a = e^{-\tau}\left[\cos\beta + \frac{\tau}{\beta}\sin\beta\right], \qquad b = a\frac{\sin\beta}{\beta}, \qquad \beta = \sqrt{\alpha^2-\tau^2}, \qquad \tau = \frac{T_{RF}}{2T_2^*}$$

Here, T_{RF} is the time duration of the RF pulse, E_1=exp*(-TR/T1)*, α is the flip angle and TR is the repetition time. Notice that taking the limit of $\tau\rightarrow 0$ reduces Eq. (6.1) to the well-known spoiled gradient echo equation (SPGR) with b=sin α and a=cos α. In practice a hard non-selective RF

pulse is used to minimize *TE*, and because the maximum achievable B_1 is limited (on our system ~13μT, to avoid damaging the eight-channel head receiver array), the pulse length increases as the flip angle increases. Taking all this into account for our Philips 3T MRI scanner with *TR*=6ms, yields the following plot in Figure 6.1. The optimal flip angle is ~7.5°, where the signal magnitude curves for bone and CSF intersect.

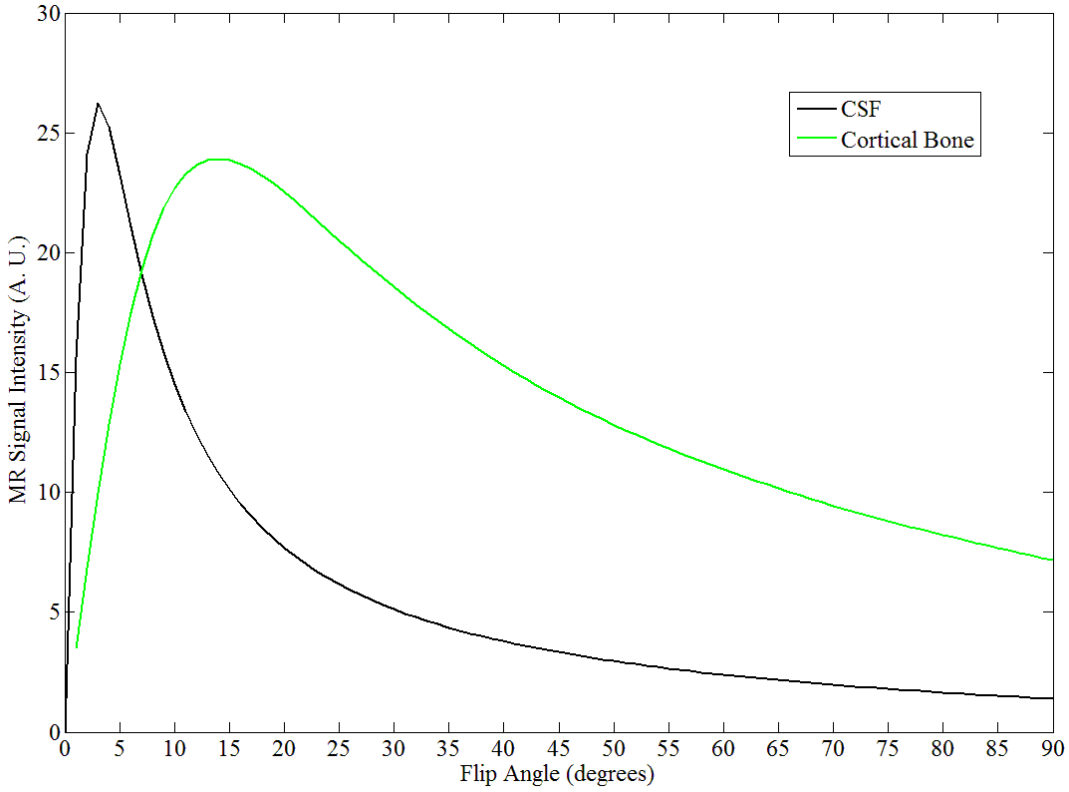

Figure 6.1: Plot of the bone and CSF signal as a function of flip angle for *TR*=6ms on our Philips Achieva 3T scanner, assuming M_0=0.23, T_1=220 ms, T_2^*=0.5 ms for bone, and M_0=1.00, T_1=4300 ms, T_2^*>150 ms for CSF.

In a voxel containing both water and fat the complex signal can be expressed as [18]

$$I_n = \left[M_w + M_f\, e^{i\,\Delta\omega_f\, TE_n}\right] e^{i(\phi_s + \gamma \Delta B_0 TE_n)} \tag{6.2}$$

Here $\Delta\omega_f$ is the chemical shift between water and fat (3.4 ppm ≈ 447 Hz at 3T), ϕ_s is an unknown static phase offset, ΔB_0 is the static field inhomogeneity, M_w is the water magnitude and M_f is the fat magnitude signal. Since water and fat will be out of phase at the second echo, $exp(i\,\Delta\omega_f\, TE_2)$ = -1, and in-phase again at the third echo, $exp(i\,\Delta\omega_f\, TE_2)$ = +1, we can obtain a linear system of 6 equations and 4 unknowns by assuming $TE_1 \approx 0$.

$$
\begin{aligned}
I_1 &= \left(M_w + M_f\right) e^{i\phi_s} \\
I_2 &= \left(M_w - M_f\right) e^{i(\phi_s + \gamma \Delta B_0 TE_2)} \\
I_3 &= \left(M_w + M_f\right) e^{i(\phi_s + \gamma \Delta B_0 TE_3)}
\end{aligned} \tag{6.3}
$$

Before solving this system of equations, however, it is necessary to unwrap the phase of all three UTE images. Phase-unwrapping was performed using the algorithm of Cusack and Papadakis implemented in MATLAB, and freely available online (http://www.cusacklab.org/) [176]. Once M_w and M_f are known, they can be combined to obtain a water-fat fraction,

$$
r = \frac{M_w - M_f}{M_w + M_f} \tag{6.4}
$$

which ranges from r=-1 (pure fat) to r=+1 (pure water). Finally, the linear attenuation coefficient μ_r is calculated as a linear combination of that of soft-tissue μ_{soft} and adipose $\mu_{adipose}$:

$$
\mu_r = \frac{1+r}{2}\mu_{soft} + \frac{1-r}{2}\mu_{adipose} \tag{6.5}
$$

To segment bone from soft-tissues, Berker et al applied a threshold (t=0.55) to the following difference image, derived from the first M_1 and third M_3 echo UTE magnitude image:

$$
d_{UTE} = 2\frac{M_1 - M_3}{M_1 + M_3} \tag{6.6}
$$

As in both Berker's, and Navalpakkam's processing pipeline [170], we also performed morphological filtering and connected-component analysis to clean up the false-positive "bony signal" that arises at skin-air boundaries from gradient-delay/eddy-current effects. To achieve this, a mask was generated from the M_3 image using the Foreground masking (BRAINS) module in 3D Slicer with the following parameters[12]: Otsu Correction Factor=0.6, Closing Size=4 mm, ROIAuto Dilate Size=0. This mask was then eroded using the BinaryErodeImageFilter (Simple Filters module[13]) with a kernel radius of [3 3 3], and a ball kernel type. As shown in Figure 6.3, this mask is used to correctly classify the susceptibility-induced and gradient-delay-induced "bony" edges at skin-air interfaces as soft-tissue instead. Finally, air-cavities are distinguished

[12] For an explanation of these parameters, see https://www.slicer.org/wiki/Documentation/4.6/Modules/ForegroundMasking.
[13] See https://www.slicer.org/wiki/Documentation/4.6/Modules/SimpleFilters.

from the other 3 tissue classes (bone, adipose and soft-tissue) by globally thresholding M_1, M_2 and M_3 (i.e. $mask_{air} = \{p | \{M_1(p) \leq t_{air}\} \cap \{M_2(p) \leq t_{air}\} \cap \{M_3(p) \leq t_{air}\}\}$, where t_{air} is the threshold and p is the pixel intensity value).

6.2.2 Proposed Improvements to UTILE-Dixon Technique

Potential improvements to the original UTILE-Dixon classification technique include accounting for partial volume effects among different tissue classes, or distinguishing between varying bone densities. As shown in Figure 6.2, plotting the histogram of the CT and d_{UTE} images reveals some interesting trends concerning bone density. Patient 5 (in black) clearly has more porous bone with a peak at ~750 HU, while patient 2 (in blue) has more cortical bone with a peak at ~1250 HU. The peaks are not quite as visible on the d_{UTE} histogram (in b), most likely because of noise, and the fact that the correlation between d_{UTE} and the CT numbers may not be linear. Therefore, to improve the bone classification, a bias-field corrected fuzzy c-means clustering (FCM) algorithm can be applied to the d_{UTE} image using 6 initial class estimates of 0, 0.20, 0.39, 0.68, 1.1, 1.4, corresponding to air, GM/WM, fat/CSF/muscle, soft, medium and hard bone, respectively. This algorithm outputs a "soft" segmentation of N classes, with each voxel receiving N values in the range of [0, 1], each corresponding to a probability P_k of belonging to class k, with the obvious constraint $\sum_k P_k = 1$. (For an overview of how FCM classification works, please refer to section 2.10.2).

Although not used for the soft-tissue classification, the first three classes (air, WM/GM and fat) are still assigned to better distinguish bone from other tissues, as may be justified from the d_{UTE} histogram peaks shown in Figure 6.2(c). Next, to more accurately segment tissues from air, FCM is also applied to the M_1 image using 4 initial class estimates of ~0.137, 0.320, 0.626 and 0.870 of the maximum intensity corresponding to air, bone/CSF, WM/GM/muscle and adipose, respectively. (Note that the M_1 image is first scaled linearly on a 16-bit integer scale (0-65536) after truncating the intensity at 99.5% of the cumulative image histogram).

Although bone and CSF have approximately the same M_1 image intensity, they can be distinguished from each other after bone has been segmented using d_{UTE}. In summary, bone is distinguished from non-bone using d_{UTE}, air is distinguished from non-air using M_1, adipose is distinguished from other soft-tissues using r (Eq. (6.4)), and once bone is identified, CSF can be distinguished from bone using the second class in M_1. To obtain a final synthetic CT, it suffices

to take the weighted summation of the CT number assigned to each class (or attenuation coefficients μ) with each weight corresponding to the class probability:

$$sCT = \sum_{k=1}^{N} P_k \, CT_k \tag{6.7}$$

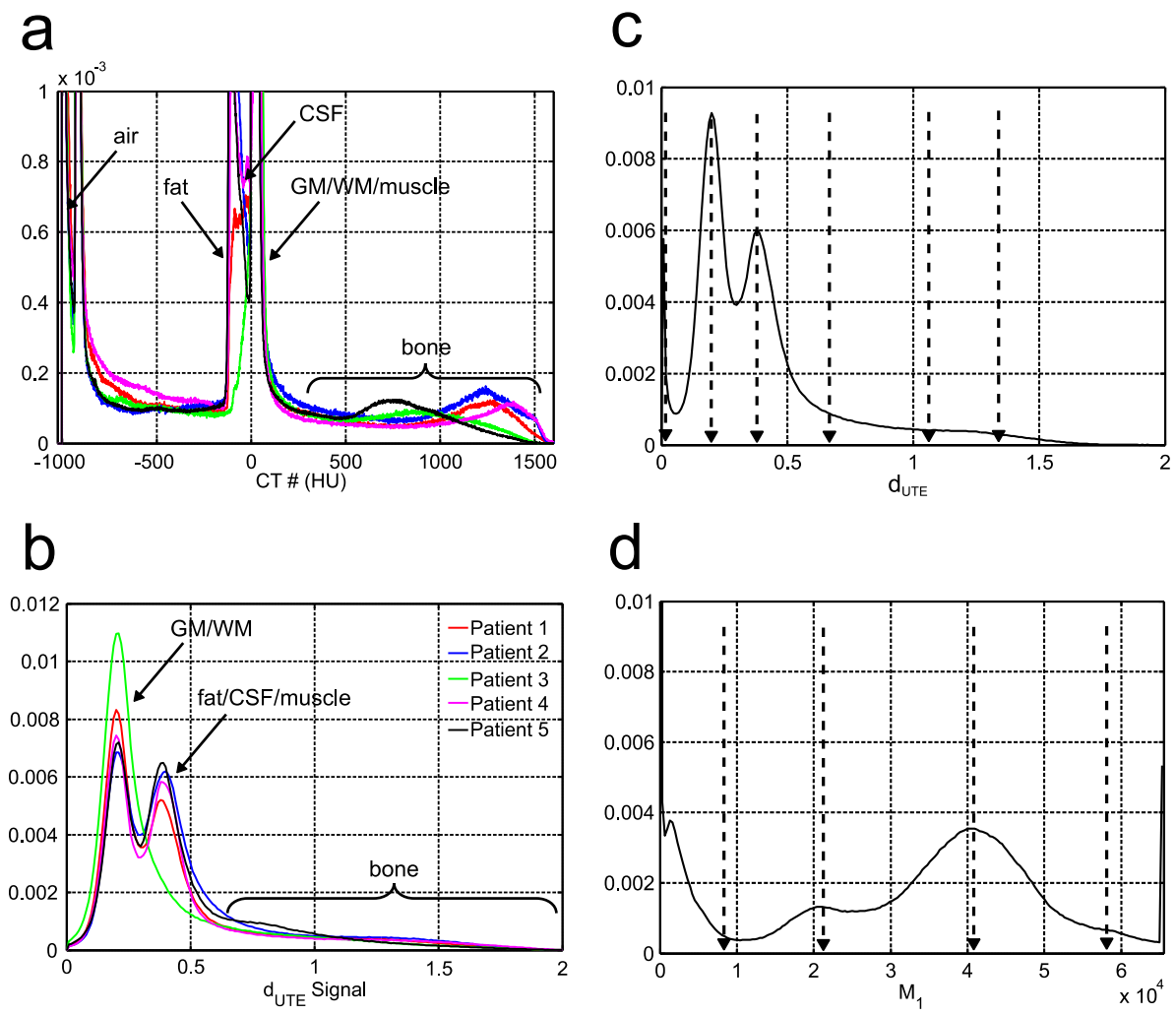

Figure 6.2: (a) CT histograms of 5 patients, with labelled tissue classes. (b) d_{UTE} histograms of the same 5 patients with corresponding tissue classes labelled (except for air/background). Note that patient 3 had very little adipose, causing its histogram (green curve) to lack a second peak. (c) d_{UTE} histogram of one patient with the 6 starting class estimates and (d) M_1 histogram with 4 starting class estimates shown as downward arrows.

A final improvement can be brought to the pipeline by attempting to directly predict bone CT number from d_{UTE} signal (shown in Figure 6.3(c)). This can be added to the algorithm by adding

an IF statement to Eq. (6.7). If a voxel has a sufficiently high probability of being bone (e.g. $P_{bone}=\{P_{soft}+P_{med}+P_{hard}\} \geq 0.3$), then a direct conversion of d_{UTE} to CT number is applied using a quadratic fit ($y=Ax^2+Bx+C$). However, to obtain the coefficients A, B and C, joint histograms of CT vs d_{UTE} must first be plotted and a quadratic fit measured over a sufficiently large number of patients, following registration.

6.3 Experimental Methods

6.3.1 Phantom Experiment

A limitation of this study is that patients could not be scanned in the MRI in the exact same position as in the planning CT. We hypothesize that this inconsistency and the consequent non-rigid tissue deformations (especially in the neck) might inflate the MAEs (measured between the CT and sCT). Therefore, to eliminate this effect a rigid phantom was built, consisting of a 2 L plastic container filled with two layers of agar solution (bottom layer with $MnCl_2$ doping for short T_1 and the top layer without $MnCl_2$ for long T_1), a beef bone, three ping-pong balls and petroleum jelly. These materials mimicked, respectively, muscle or WM, CSF, bone, air and adipose.

The phantom was scanned in a Philips Brilliance CT scanner using a high-resolution protocol (FOV=25×25cm^2, ultra-sharp filter, axial mode, 120 kVp, 800 mAs, 512×512 matrix, slice thickness: 0.75 mm, 272 slices). The phantom was also scanned at 3T using the same eight-channel head array and UTILE-Dixon scan with parameters (flip angle, TEs and bandwidth) similar to those used for the patients, except that four different samplings densities were tested: 37300, 30640, 22350, and 10950 radial spokes, with corresponding scan durations of 4, 3, 2 and 1 min. All three classification pipelines were tested on the phantom data, including Berker's, FCM1 and FCM2, as well as three different image registration methods, including manual (6DOF), automatic affine (12DOF) and automatic B-Spline deformable (>27DOF). The MAEs were measured for each undersampling, classification and registration scheme.

6.3.2 In Vivo Patient Study

6.3.2.1 CT Imaging

Twelve primary brain tumor patients who were scheduled to undergo radiation therapy were recruited as part of this study, following informed consent and approval by the Health Research Ethics Board of Alberta. Each patient was scanned on a Philips Brilliance Big Bore CT as part of

the clinical preparation for radiation therapy, which included mask fixation. The CT scan parameters were: 120 kVp, 284 mAs, FOV=53.4×53.4 cm^2, 2 mm slice thickness, and matrix size = 512×512. About 200 slices were acquired for each patient to cover the entire head and neck region, including a small portion of the shoulders and abdomen.

6.3.2.2 MR Imaging

Within a week of starting their radiation therapy treatment, patients were scanned on a Philips 3T Achieva using an eight-channel head receiver array. No mask fixation was employed because of insufficient room inside the coil. The MRI examination consisted of a 3D Multi-Parameter Mapping protocol (containing a series of 3 Cartesian multi-echo FLASH and 4 bSSFP sequences), followed by a 3D UTILE-Dixon sequence. (Note that only the UTE scan is relevant to this chapter, while the MPM data is analyzed and discussed in the previous chapters 3, 4 and 5). The FOV, voxel resolution, sampling bandwidth and echo spacing were optimized to achieve the best image quality and SNR in a practical scan time given the limits of our system's gradient performance, yielding: 1.7 mm isotropic resolution, FOV=25×25×25 cm^3, BW=1300 Hz/pix, α/TR=8°/6.1 ms, $TE_1/TE_2/TE_3$=6.1/0.09/1.32/2.54 ms. Note that these scan parameters are different than those chosen by Berker et al ($TE_1/TE_2/TE_3$=0.09/1.09/2.09 ms, 1.75 mm resolution, and FOV=28×28×28 cm^3), although the total scan time (~4 min) and voxel resolution were comparable. UTE images were reconstructed to a final matrix size of 256×256×256 with an optimal-SNR coil combination with uniform sensitivity [91].

6.3.2.3 Image Processing and Registration

The three magnitude and three phase UTE images were post-processed to create a final synthetic CT dataset according to both the original UTILE-Dixon classification pipeline shown in Figure 6.3(a) and the improved version shown in Figure 6.3(b). For the original implementation, air, fat, soft-tissues and bone were assigned bulk CT numbers of -1000, -110, 30 and 1000 HU, respectively, while for the FCM implementation, up to seven tissue classes were taken into account, including air, fat, CSF, soft-tissues (i.e., WM/GM/muscle), soft bone, medium bone and hard bone: -1000, -110, 30, 0, 600, 1200, 1600 HU, respectively. The CT numbers of the different tissue classes were estimated based on the first five patient CT datasets (all obtained from the same CT scanner with the same 120 kVp).

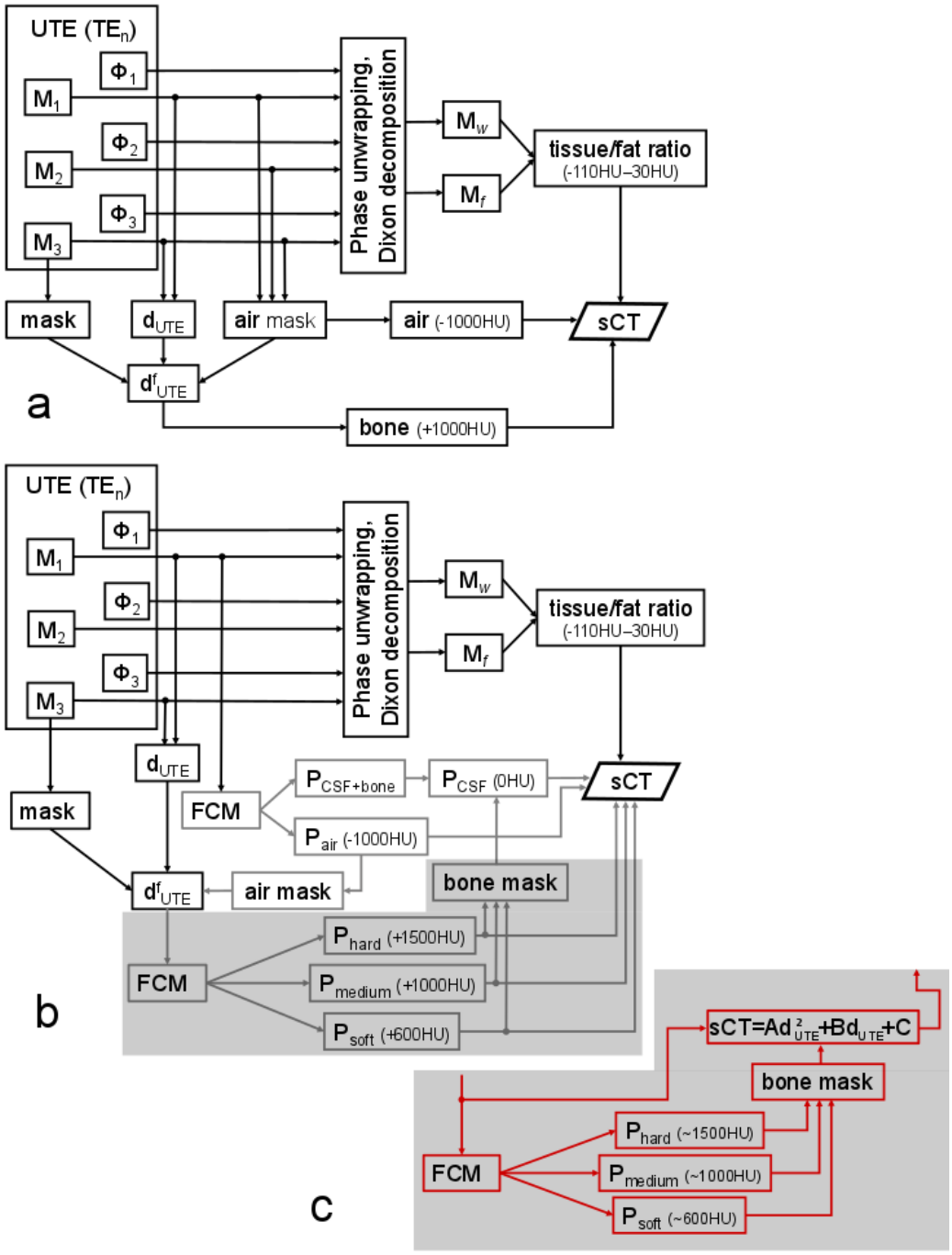

Figure 6.3: (a) Flow-chart of the original UTILE-Dixon implementation, and (b) the improved implementation with FCM1 with differences in gray. (c) FCM2 option shown within the gray mask.

The synthetic CT images obtained from each pipeline, denoted as sCT_{Berker} and sCT_{FCM1}, were exported to 3D Slicer, to be co-registered to the planning CT dataset. First, a manual (6 DOF) registration was performed to bring the sCT_{FCM} and planning CT within the capture range of the registration algorithm. Both the sCT_{FCM1} and CT were masked (to exclude air cavities) via

thresholding (using the Foreground masking BRAINS module[14]) and the two masks were multiplied (logical AND) to obtain a final overlapping mask. Next an automatic rigid (6 DOF) registration was performed using samples within the mask. This mask was crucial to ensure that the registration does not converge into a local minimum as a result of tissue deformations (especially present at the back of the neck). Finally, an affine (12 DOF) image registration was also performed automatically, after applying the rigid transformation. In both automatic registrations (rigid and affine) the mean squared error (MSE) was selected as the cost metric rather than Mattes Mutual Information (the default setting)[15]. Following registration, all sCT datasets were resampled to the same output settings (origin, FOV and resolution) as the planning CT using the transform matrix. Additionally, a second set of CT and sCT datasets were created using the "Crop Volume" module[16] to reduce the FOV and exclude the neck region where non-rigid tissue deformations tend to occur. To assess the accuracy of the sCT, the mean absolute error (MAE) between the CT and sCT was calculated for both classification techniques (sCT_{Berker} and sCT_{FCM1}), both types of registrations (rigid and affine) and with and without including the neck (yielding 2×2×2=8 MAEs per subject).

6.3.2.4 Correlation between Bone CT Number and d_{UTE}

To investigate a possible correlation between the bone CT number and the d_{UTE} signal, the d_{UTE} image of each subject was also coregistered and resampled using the same rigid (6 DOF) and affine (12 DOF) image transforms. Joint histograms of d_{UTE} and CT were then plotted in MATLAB using 200 bins in the range of [0 2] for d_{UTE} and [0 2000] for CT. For each patient, 10 samples were manually selected along the center of mass of each joint histogram distribution (clusters), and all the samples were pooled across the 12 patients (120 points in total). (Manual selection avoided the difficulty of pre-conditioning the samples to achieve a stable fit). A quadratic fit ($y=ax^2+bx+c$) of the data with $y \equiv$CT and $x \equiv d_{UTE}$ was calculated in Excel. This quadratic model for mapping d_{UTE} into bone CT was used to further refine the pipeline shown in Figure 6.3(c), by assigning continuous-valued CT numbers within the bone mask. These final sCT images were denoted as sCT_{FCM2}.

[14] See https://www.slicer.org/wiki/Documentation/4.6/Modules/ForegroundMasking.
[15] See refer to https://www.slicer.org/wiki/Documentation/4.6/Modules/BRAINSFit.
[16] See https://www.slicer.org/wiki/Documentation/Nightly/Modules/CropVolume.

6.3.2.5 Dose Simulation on Synthetic CT datasets

In order to investigate the accuracy of dose simulation performed on sCT, two patients sCT datasets (already registered to their respective planning CT) were converted into DICOM images and exported into the Eclipse Treatment Planning software, used for planning all external beam RT treatments at the Cross Cancer Institute. All patients were treated with a state-of-the-art VMAT (Volumetric Arc Therapy) treatment. For every patient, the CT dataset was replaced by the sCT and the dose was re-calculated (using the same monitor units). Comparison was done primarily via dose volume histograms (DVHs) of the PTV and other relevant structures, including the body, the cerebrum, the brain stem and the eyes.

6.4 Results and Discussion

6.4.1 Phantom Experiments

Examples of M_1, d_{UTE} and sCT images of the phantom are shown in Figure 6.4, for both the lowest and highest sampling densities, (labelled with acceleration factors of R=4 and R=1, respectively). Observe how robust the M_1 image remains under 4-fold acceleration. Streaking artifacts mostly appear on the left side of the sagittal image, where the SNR is lower because it is the open end of the eight-channel head array. Both the worst (sCT_{Berker}) and best (sCT_{FCM2}) images are also shown in Figure 6.5 for comparison. A comparison of the CT and registered sCT_{FCM2} is shown in for two different sampling densities and registration schemes showing that the quality of the sCT is not significantly affected by undersampling. The measured MAEs are summarized in Figure 6.6. The fact that the B-spline deformable registration significantly lowers the MAE (from 84 HU to 45 HU), confirms our hypothesis that the observed differences between CT and sCT are governed primarily by tissue deformations in the neck rather than classification errors. Moreover, it is noteworthy that the UTE image reconstruction method and our classification pipeline are both very robust to undersampling, in that an excellent sCT dataset can still be obtained in a total scan duration of 1 min, which is very practical for MRI-based RTP applications.

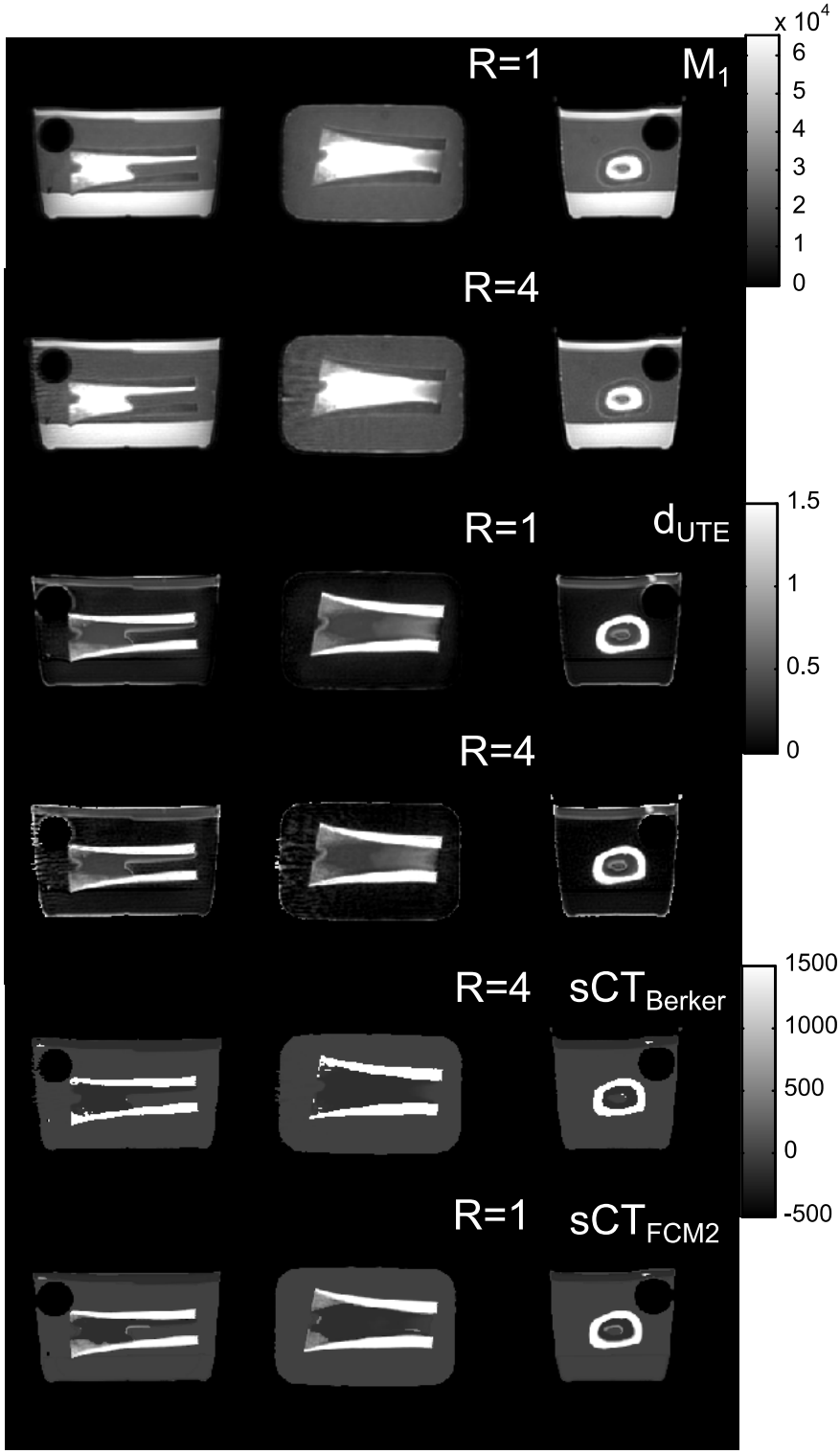

Figure 6.4: Phantom images of M_1, d_{UTE}, and sCT for 37300 spokes (R=1) and 10950 spokes (R=4). Both the worst case and best case scenario are shown for sCT (sCT_{Berker} with R=4, versus sCT_{FCM2} with R=1).

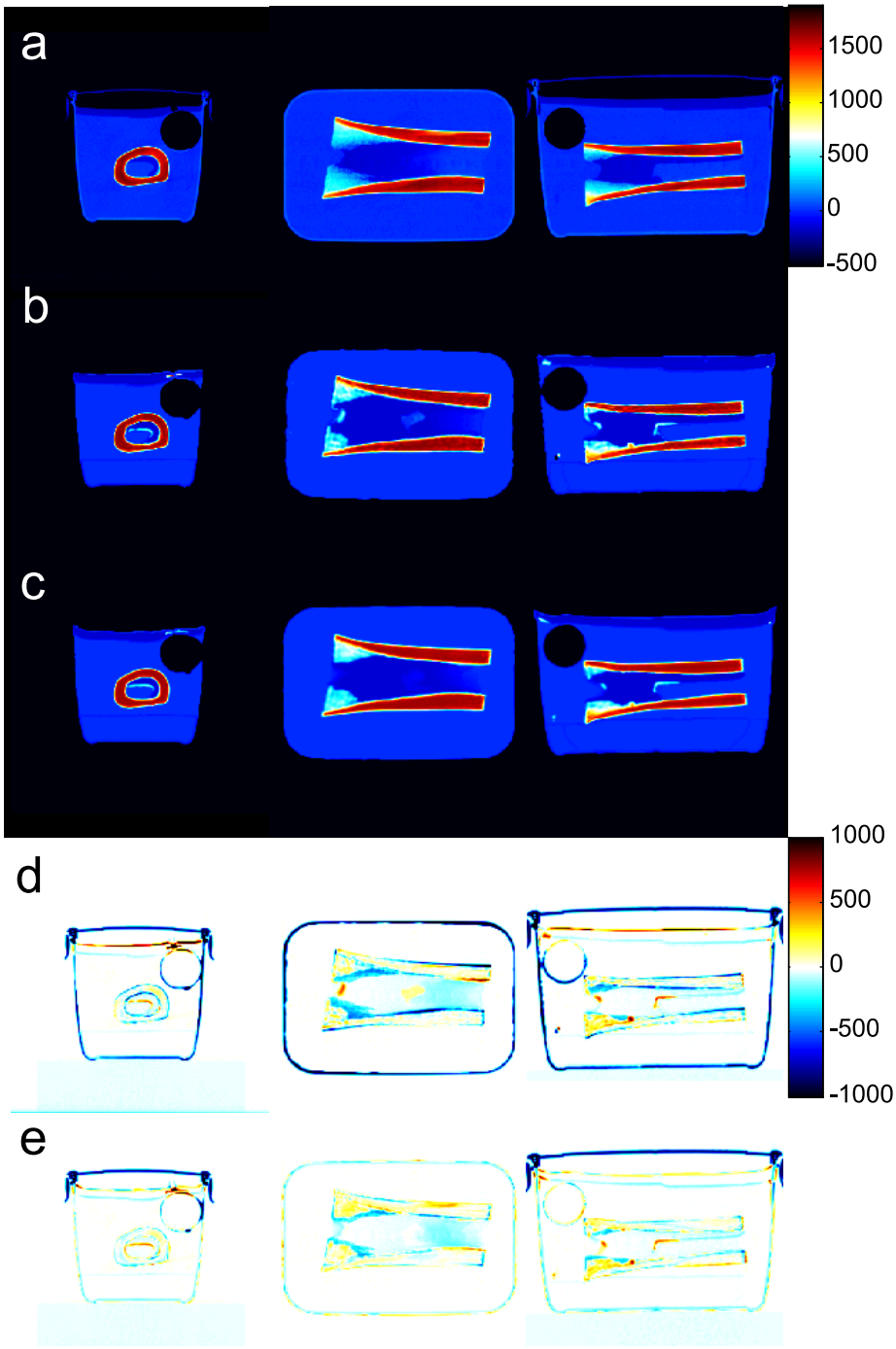

Figure 6.5: (a) CT of the phantom (in HU). (b) Registered sCT_{FCM2} for acceleration of R=4 and rigid (6 DOF) registration. (c) Registered sCT_{FMC2} for R=1 and using B-spline deformable registration. (d) Difference image (sCT-CT) between (a) and (b). (e) Difference image (sCT-CT) between (a) and (c).

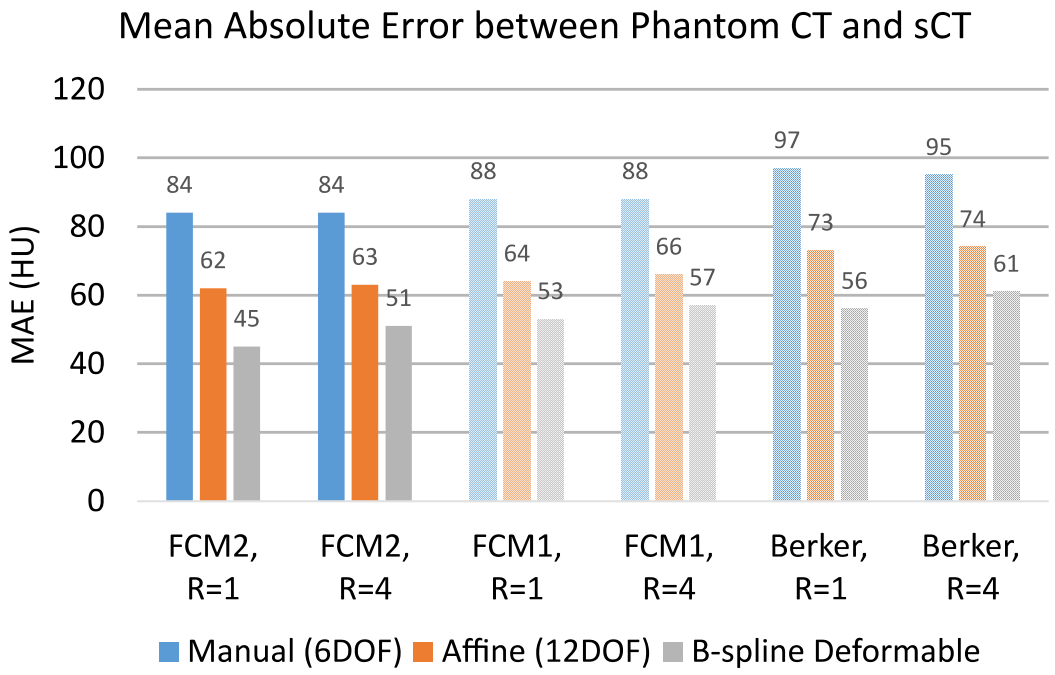

Figure 6.6: Measured MAEs for different undersampling, classification and registration schemes.

6.4.2 In Vivo Patient Study

6.4.2.1 Image Processing and Registration

An example of d_{UTE}, M_1 and sCT_{FCM1} images in sagittal, coronal and axial slice orientations are shown in Figure 6.7 for patient p1. Susceptibility effects induce short T_2^* decay and gradient-delays can create dark or bright edges in the M_1 image, especially at tissue-air interfaces, which appear as bright bony-looking edges in the d_{UTE} image. Fortunately, the eroded mask generated from the M_3 image (as shown in the pipelines of Figure 6.3) successfully prevents such errors from being mis-classified as bone in the final sCT image. Other potential methods of addressing this problem include dynamic Magnetic Field Monitoring (MFM) [177] during the UTE sequence, or the use of a modified sequence called Pointwise Encoding Time Reduction with Radial Acquisition (PETRA) [178], where the center of k-space is sampled using single-point imaging, and radial spokes are sampled beyond a minimum k-space radius k_r. Both of these methods eliminate gridding (k-space sampling trajectory) errors arising from gradient delays and eddy currents but cannot fully remove dephasing effects arising from susceptibility differences at tissue-air interfaces.

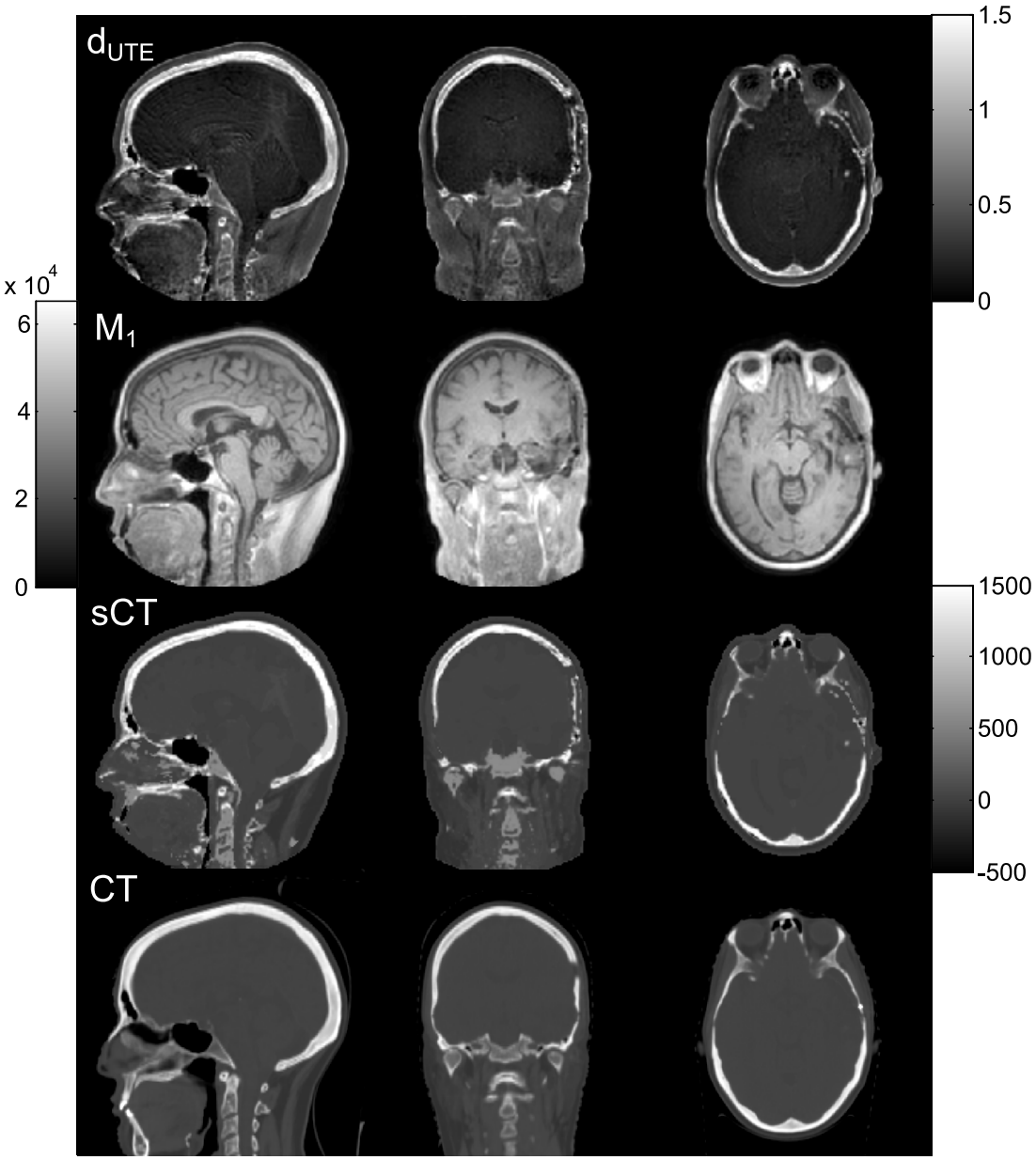

Figure 6.7: Sagittal, coronal and axial images of d_{UTE}, M_1, sCT_{FCM1}, and CT for a patient. The MAE between sCT_{FCM1} and the CT of this patient was 132 HU (neck included) or 113 HU (neck excluded).

The MAEs measured across all 12 patients are summarized in Figure 6.8. As expected, the proposed improvements to Berker's original classification technique do result in lower MAEs, but the decrease in error (<10 HU) is not significant. The fact that excluding the neck region from the comparison more significantly decreases the MAEs (~25 HU), suggests that most of the errors are attributed to non-rigid tissue deformations in the neck which rigid (6 DOF) or affine (12 DOF) registration cannot take into account. Therefore, it is reasonable to expect that if the

patients were scanned in the exact same position (using the same fixation device) in the MRI scanner as on the CT simulator, significantly lower MAEs would have been achieved. The affine registration yields the lowest MAEs, and, interestingly, Berker's original method is also more sensitive to the choice of registration (~7 HU difference between affine vs. rigid) compared to the newly proposed FCM1 classification (with ~1 HU difference). Results from the FCM2 classification are not shown, since they only decrease the MAEs by ~1 HU on average.

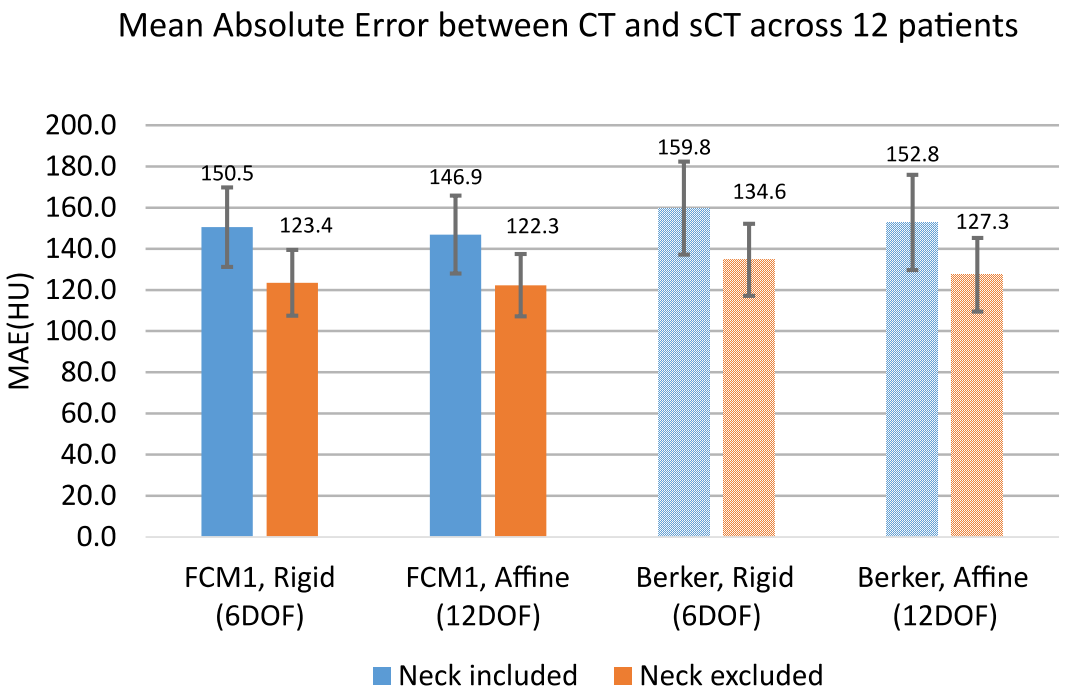

Figure 6.8: Mean absolute error (with error bars as standard deviations) measured across 12 patients.

6.4.2.2 Correlation between Bone CT Number and d_{UTE}

A correlation between MRI signal and CT number in bone was previously reported both in conventional T_1-weighted Dixon MRI of the pelvis [179] and in ZTE imaging of the head [174]. As shown in Figure 6.9(a), a joint histogram of CT number versus d_{UTE} signal for one patient reveals a strong correlation, with a high-density diagonal cluster. In (b) a quadratic fit of the CT number as a function of d_{UTE} is plotted using a subset of samples pooled from all 12 patients, yielding a correlation coefficient of R^2=0.97. A coronal sCT slice derived from the 3 different classification methods (Berker's, FCM1 and FCM2) is shown in Figure 6.10, along with the actual CT and the subtraction image (sCT-CT). The quadratic model more accurately predicts

bone CT number compared to the other two methods, with an intra-bone MEA of 214 HU, compared to 246 HU for FCM1 and 251 HU for Berker's original method.

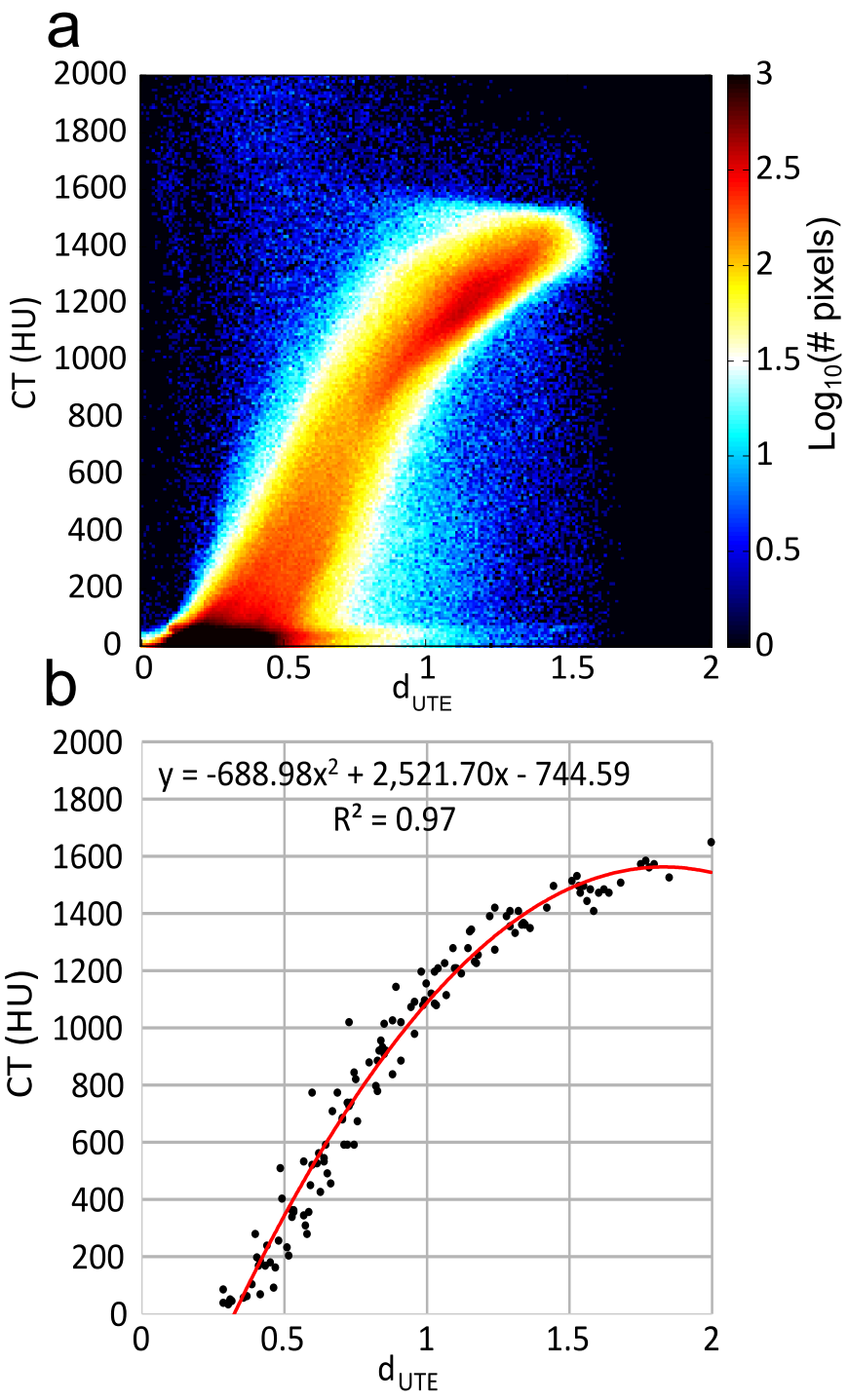

Figure 6.9: (a) Joint histogram of CT versus d_{UTE} signal for CT numbers≥0 for one patient. (b) Quadratic least-squares fit of the CT versus d_{UTE} using samples from all 12 patients pooled together.

We expect that the quadratic fit should remain approximately valid and reproducible between different imaging centres provided that similar echo times are employed across different MRI scanners, and the same kVp across different CT scanners. However, it would be appropriate to verify the reproducibility of the fit across different CT and MRI scanner manufacturers before attempting to use the same *A*, *B*, *C* coefficients across different centres.

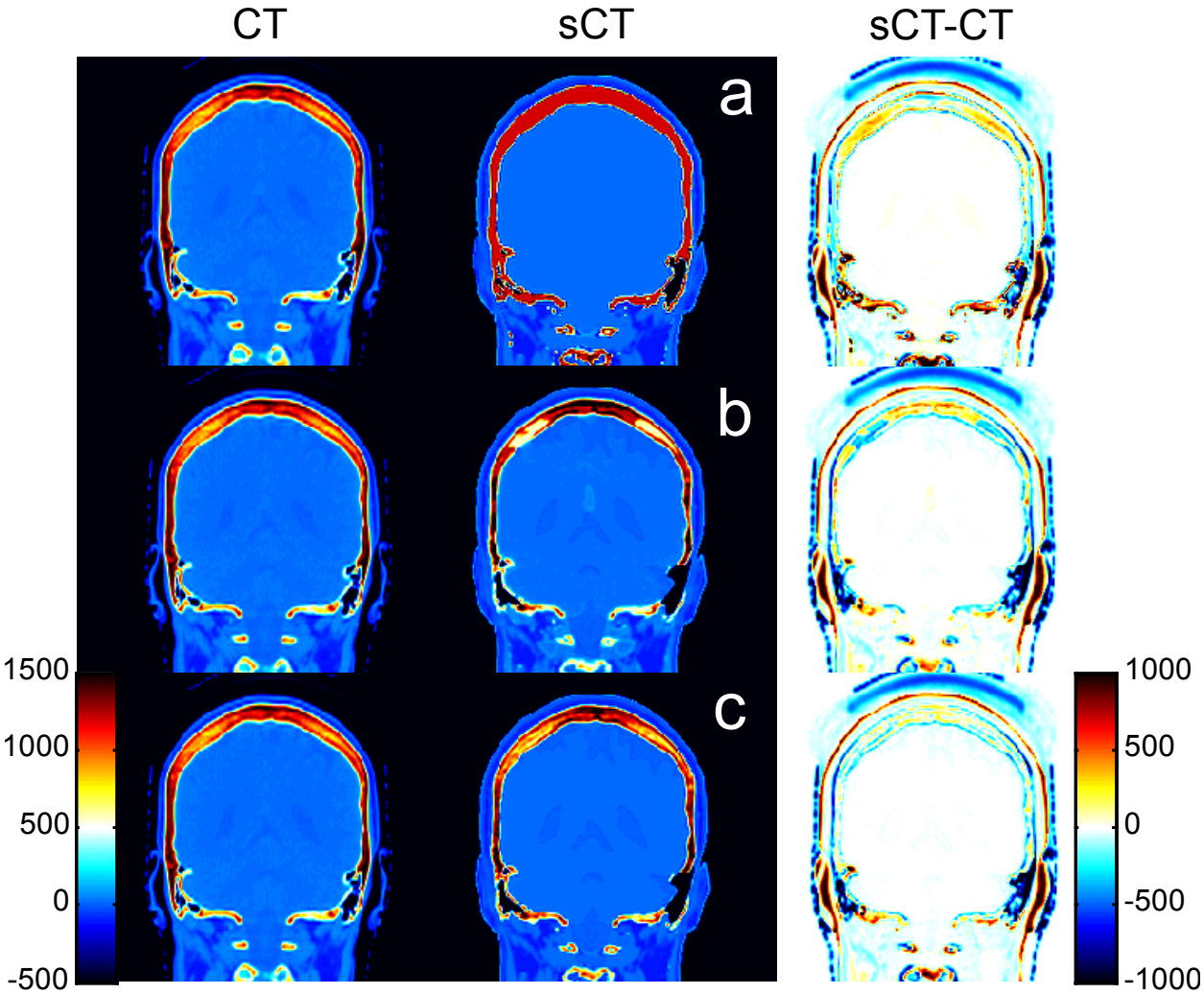

Figure 6.10: Comparison of the actual CT and the sCT generated using (a) the Berker's original method (MAE=158 HU), (b) the FCM1 pipeline (MAE=140 HU) and (c) the FCM2 pipeline (MAE=139 HU).

6.4.2.3 Dose Simulation on the Synthetic CT Datasets

Images of the CT-based versus sCT-based RT plans of patient 3 are shown in Figure 6.11 (a) and (b), respectively. The DVHs computed for two different patients are shown in Figure 6.12 (a) for patient 1 and (b) for patient 3. (A DVH is cumulative histogram of the dose distribution in a specific structure (e.g. PTV), normalized by the volume of that structure). Overall, the mean dose

(D_{mean}) to the PTV is 1.0/0.8% higher for patient 1/3, respectively. The DVHs of the organs at risk also agree closely, except for the body, which has a significantly different calculated volume on the planning system, due to the large difference in FOVs between MR vs CT (see Figure 6.12b), and because the "body" also includes the bed and mask fixation, which are invisible to the MRI. The MEA (excluding the neck) for these two patients was 114 HU and 99 HU, respectively. The higher measured dose in the sCT-based plan is likely caused partly by the exclusion of the bed and mask fixation device from the dose computation, and also by the fact that the sCT appears to slightly underestimate the skull thickness with respect to the true CT. In CT, the skull thickness can be biased by the choice of slice thickness (=2 mm in this case), and scanning mode (i.e. axial versus helical). In UTE, however, the coarser voxel resolution (=1.75 mm isotropic) tends to result in the thinner regions of the skull being misclassified as soft tissue within the sCT, while the thicker regions appear with the correct thickness. Our results show greater error in D_{mean} (between MR-based vs CT-based plans) than what was previously measured by Stanescu et al. [4] (~0%) or Hsu et al. [173]. However, this is easily explained by the simple fact that the patients in both of those studies were scanned in the RT position (with mask fixation) on the MRI, thus significantly reducing the differences in tissue deformations and skin folds (especially in the neck, ears, and at tissue air boundaries). Therefore our RT plan comparisons (CT vs sCT) serve as a worse-case scenario for brain cancer RTP. If this worse-case scenario yields acceptable dose distribution, so will the ideal case when using the same RT position and also including both the flat bed and mask fixation in the simulation. Nevertheless, the use of a different patient setup can be considered a limitation of the present study.

Finally, it is not clear at this point how successful our UTE-based tissue classification will be for RTP (or PET-MR linear attenuation corrections) in other parts of the human anatomy, especially when a larger FOV is required (as in imaging the pelvis for prostate cancer). The ability to resolve the short T_2^* of bone from susceptibility effects at tissue-air interfaces is expected to degrade at larger FOV, due to decreasing B_0 homogeneity. Consequently, tissues will tend to get mis-classified as bone. Other competing techniques such as atlas-based [180] and model-based [181] segmentation could turn out to be more robust than a UTE-based method. Nevertheless, UTE-based methods appear to be the most advantageous in terms of speed (short computation /acquisition times) and accuracy in brain RTP or PET-MR [182], [183]. Finally, the fact that

metal implants always lead to signal voids in MRI implies that CT-based RTP will always be required in certain cases.

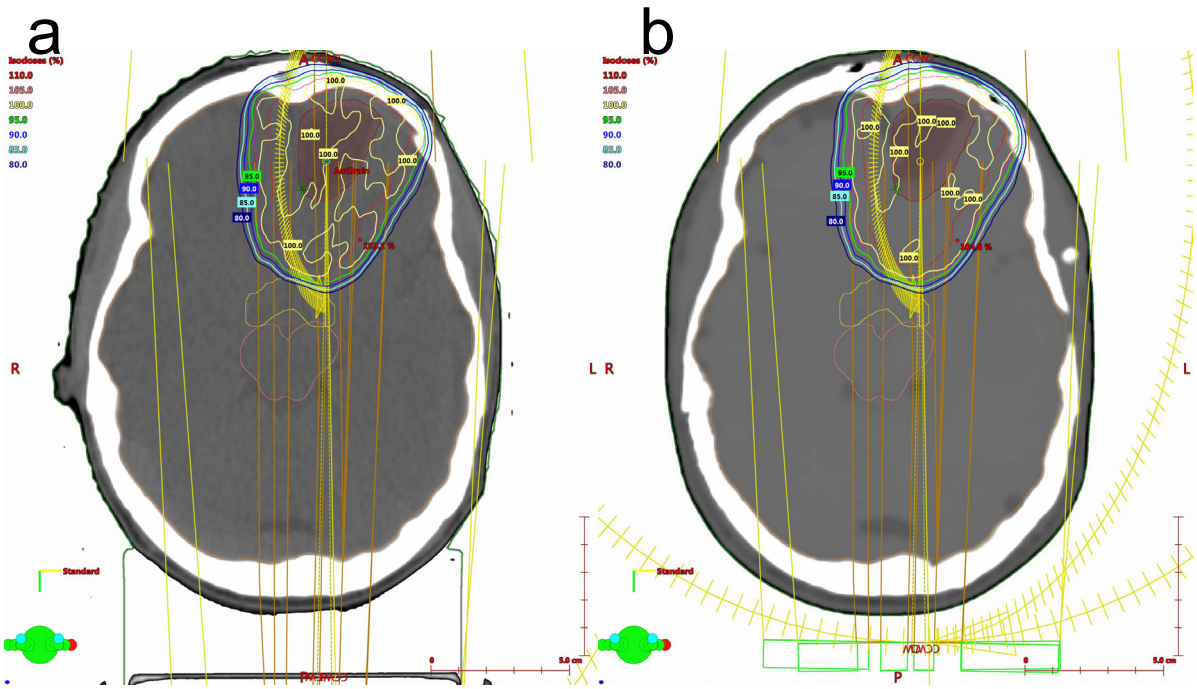

Figure 6.11: Comparison of the CT-based RT plan in (a) with the sCT-based plan in (b) for patient 3. Dosimetric differences are deemed insignificant according to the DVHs of Figure 6.12.

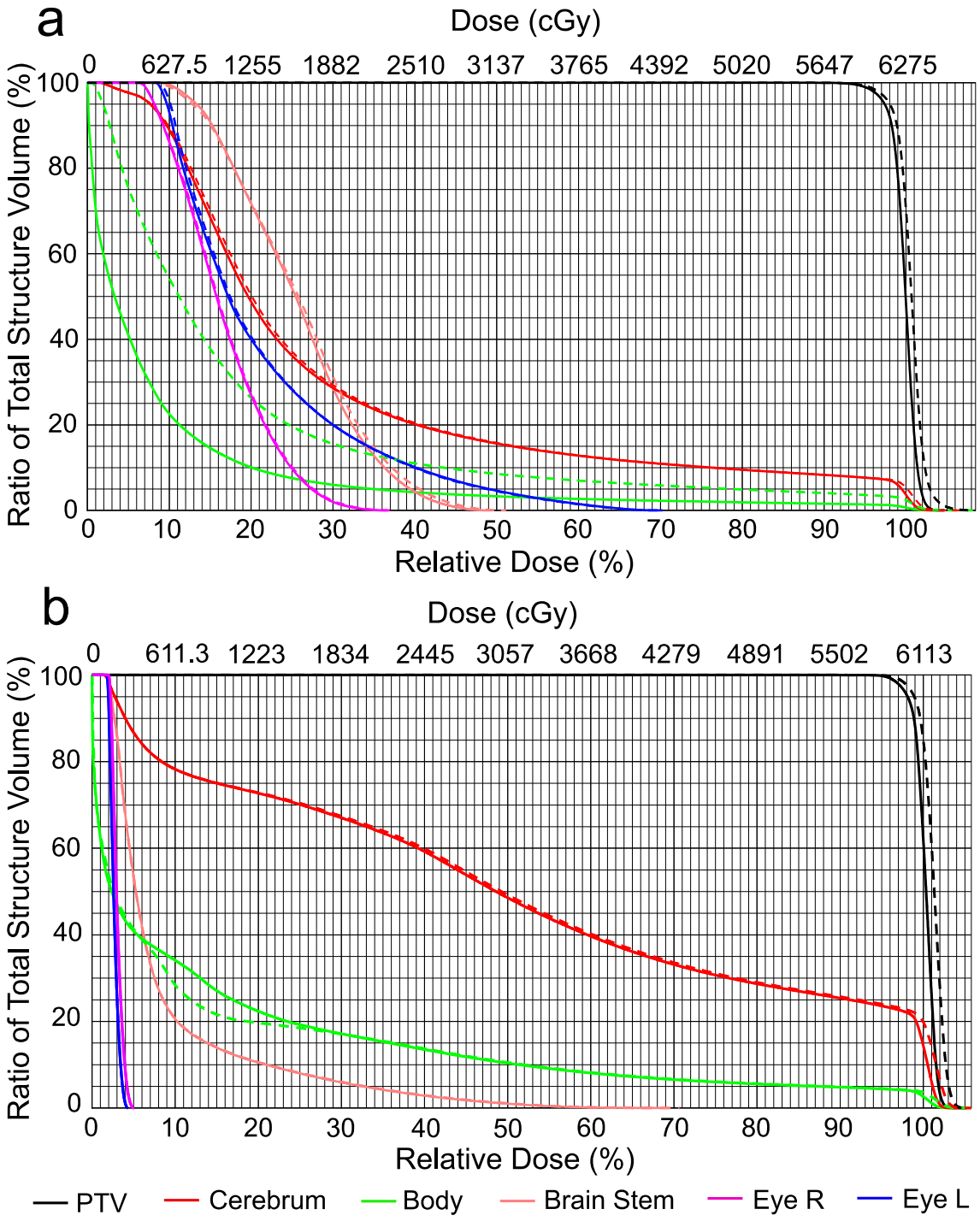

Figure 6.12: Dose volume histograms of PTV and other relevant structures calculated for patient 1 in (a) and patient 3 in (b) using the original CT (solid lines) and the new sCT (dash lines).

6.5 Conclusions

In this work, we have investigated a simple and yet robust automatic tissue classification technique based on UTE-MRI. The technique was built upon Berker's original pulse sequence and processing pipeline, with further refinements that account for partial volume effects and varying bone densities, resulting in continuous-valued attenuation coefficients (or CT numbers). Improvements to the method were confirmed by lower MAEs (measured between the CT and registered sCT) achieved both in vivo (~122±15 HU) (12 patients) and in the phantom (~62 HU). These measured MAEs (excluding the neck region) were also lower than those reported by Johannsson et al. [171] (average of ~137 HU on five patients), despite a significantly simpler post-processing pipeline and shorter scan time. It was also noteworthy that the UTE scan time could be decreased to ~1 min via mere undersampling (and partial k-space gridding reconstruction) and still result in accurate synthetic CT images of the phantom. The dose distribution computed on the sCT (using the same monitor units) of two patients also agreed well with that calculated on the traditional CT, despite the patients not having been scanned in the RT position (with head fixation and flatbed). Closer agreements (between CT vs sCT-based plans) should be expected by implementing the method using the exact same RT position and head fixation device. Since the head is primarily constrained by rigid-body motion, (which can be accounted for via rigid 6 DOF registration of the sCT to the CT), the absence of the mask-fixation device had a marginal impact on the dosimetry. However, for testing the method on head-and-neck cancer patients, the use of the mask fixation device and a larger UTE field-of-view would likely be necessary to yield a comparable dose distribution, as non-rigid tissue deformations where present in the neck (given the different patient setup). We conclude that automatic UTE-MRI tissue classification is a viable method for routine clinical MRI-based RTP of the head, replacing the planning CT scan, and thus saving time and resources to the health care system while avoiding the additional ionizing radiation dose to the patient.

Chapter 7: Conclusions and Future Work

"A strict materialist believes that everything depends on the motion of matter. He knows the form of the laws of motion though he does not know all their consequences when applied to systems of unknown complexity.

Now one thing in which the materialist (fortified with dynamical knowledge) believes is that if every motion great & small were accurately reversed, and the world left to itself again, everything would happen backwards the fresh water would collect out of the sea and run up the rivers and finally fly up to the clouds in drops which would extract heat from the air and evaporate and afterwards in condensing would shoot out rays of light to the sun and so on. Of course all living things would regrede from the grave to the cradle and we should have a memory of the future but not of the past.

The reason why we do not expect anything of this kind to take place at any time is our experience of irreversible processes, all of one kind, and this leads to the doctrine of a beginning & an end instead of cyclical progression for ever."

— James Clerk Maxwell

Letter to Mark Pattison (7 Apr 1868). In P. M. Hannan (ed.), *The Scientific Letters and Papers of James Clerk Maxwell* (1995), Vol. 2, 1862-1873, 360-1.

7.1 Summary of Findings and Limitations

This doctoral research dissertation has sought to overcome some of the primary road-blocks that have been preventing the clinical application of quantitative MRI in the field of radiation therapy and oncology. As was explained in the Overview of the Thesis, the primary motivation for replacing conventional MRI with quantitative MRI was to: 1) to improve the CNR efficiency, 2) to provide new biomarkers for disease progression or regression, and 3) to enable improved reproducibility across different imaging centers.

In Chapter 3: we proposed using multi-echo bipolar pulse sequences with parallel imaging in place of the conventional single-echo sequences with low bandwidth. We showed that these sequences have the advantage of not only enabling fast multi-parameter mapping (MPM), but also providing a substantial SNR boost of 1.3 to 1.6-fold, and a 3-fold reduction in water-fat shifts and off-resonance-induced geometrical distortions over their conventional single-echo counterparts. The main limitation of bipolar multi-echo sequences and the proposed VFA T_1, M_0 and T_2^* mapping pipeline is sensitivity to head motion, especially in the final T_2^* and M_0 maps, as longer echo times become increasingly motion-sensitive. Therefore, even if the T_2^* is long, there is an upper limit (ranging from 6−12 echoes) on how many echoes may be included in the RSS combination without degrading the final image sharpness.

In Chapter 4: we developed a new and faster technique for correcting banding artifacts in T_2 maps derived from bSSFP sequences. Abnormal T_2 relaxation within the brain has long been known to serve as an important disease biomarker [24], and the clear tumor visibility in the T_2 maps of Chapter 5 support this premise. However, banding artifacts may still occur in applications where anatomical motion or transient changes in static field inhomogeneity take place (e.g., due to heating of iron shims). Also, the hyper-intense CSF signal makes bSSFP images prone to ringing artifacts in the presence of slight head motion, especially at high flip angles. Therefore, future work may be needed to improve the quality of the T_2 maps in these situations.

In Chapter 5, we presented a new technique which uses the N4ITK bias-field correction algorithm for automatically estimating and removing both transmit and receive RF inhomogeneity ($c_{RF,s}^{+}$ and c_{RF}) in parametric maps. Such a robust RF inhomogeneity correction is especially critical to achieve accurate T_1 and M_0 mapping. The proposed technique was found

to outperform two commonly used B_1 mapping techniques – AFI and SDAM – and did not require any additional scan time. The technique was also tested on brain cancer patients and found to remain robust in the presence of large surgical resections and/or tumors. However, we should note that this new technique may be limited in its ability to resolve inter-subject differences in T_1, as some previous studies have attempted [106], [108] [184], since the RF inhomogeneity estimation may be biased by the geometry and/or anatomy of the brain, in addition to the transmit gain setting. Therefore, slight anatomy-dependent biases on the corrected T_1 appear be present across different subjects (as shown in Figure 5.12); nevertheless, the new RF inhomogeneity correction is expected to be useful for monitoring local intra-subject changes in the parametric maps.

In Chapter 6:, we refined Berker's technique [18] for performing automatic tissue classification using a triple-echo UTE MRI sequence. The technique enables the fast generation of synthetic CT images while also accounting for local variations in bone densities and partial volume effects. The method was also used to perform radiation dose simulation on two brain cancer patients, yielding clinically insignificant mean deviations of less than ~1%. A limitation of the study was that the patients were not scanned in the typical RT position using mask fixation. This had the advantage of making the MRI examination more comfortable for the patients, but also the disadvantage of introducing some non-rigid tissue deformations (mismatches), especially in the neck. An additional drawback of the technique is its sensitivity to UTE image artifacts, which tend to be hardware-sensitive (especially the issue of gradient-delays). These artifacts have to be minimized as part of the sequence optimization, image reconstruction or a post-processing step. Therefore, the robustness of the technique within the context of RTP ultimately depends on the hardware performance of the MRI scanner, and not just on the classification algorithm itself.

7.2 Extension to other Magnetic Field Strengths (e.g. 1.5T or 7T)

Although MPM via the VFA technique is developed and optimized throughout this thesis at a field strength of 3T, it could also be implemented at lower fields such as 1.5T or at ultra-high fields of 7T or greater. In fact, VFA T_1 and T_2 mapping (DESPOT1/2 of Chapters 3 and 4) were originally tested at 1.5T [84]. The primary advantage of MPM at a lower field strength lies in the better uniformity of the B_0 and B_1 (RF) fields, thus potentially translating into better reproducibility (lower systematic bias) when different B_1 mapping sequences or techniques are

used across different scanner manufacturers, while the main disadvantage of a lower field is the decreased SNR efficiency. As an example, Abbas et al [111] have recently compared proton-density mapping at 1.5T vs 3T and found a CNR improvement of 1.5-fold in the latter. It should also be feasible to implement MPM at 7T, although a complete re-optimization of the scan parameters and protocols would be needed in order to avoid exceeding SAR limits (especially in the MT-FLASH and the bSSFP sequences). The B_1 and B_0 inhomogeneity would also be greater at 7T, potentially necessitating RF-shimming, as well as higher-order B_0 shimming (at least for accurate T_2^* mapping) than the simpler automatic first-order (x, y, z,) shims employed throughout this work. Finally, the echo times would need to be more tightly spaced and higher sampling bandwidths used to achieve the same negligible water-fat shifts.

7.3 Future Work

7.3.1 Further Technical Innovations

An emerging trend in MRI is the design of high-density coil arrays, which have the potential of permitting higher parallel imaging acceleration factors without a significant SNR loss (low g-factors). Since new MRI scanners equipped with 32 and even 64 coils (for head and/or torso imaging) are now commercially available, it will be necessary to test the proposed bipolar sequences on these newer hardware systems and under higher parallel imaging accelerations (R=5–10) prior to clinical implementation, since the optimal scan parameters are expected to vary depending on the choice of hardware and parallel imaging reconstruction available (e.g. SENSE versus GRAPPA). Moreover, compressed sensing (a.k.a. sparse MRI) with iterative image reconstruction techniques have the potential to further reduce scan times [185], but further testing will be required to ensure that the parametric maps are not being biased by non-uniform noise levels within the raw images.

The need for motion correction is also becoming a hot topic in brain imaging, especially when imaging at sub-millimeter voxel resolutions. In a recent study, Weiskopf et al [186] tested a new commercially-available prospective motion correction (PMC) system on MPM (M_0, T_1, T_2^* and MT_{sat}) and found that it could effectively suppress motion artifacts in brain parametric maps. It would be worthwhile to investigate how effectively this PMC system might reduce motion artifacts in T_2 maps, especially given their sensitivity to off-resonance effects.

Following the in vivo comparison of the VFA-FLASH technique to MP2RAGE in Chapter 3 and IR-EPI in Chapter 5, it appears that VFA is sensitive to fluctuations in RF power calibration, and not just in RF homogeneity itself. Consequently, a logical new avenue of research would be to investigate how more consistent RF power calibration and more robust B_1 correction schemes could be implemented on MRI scanners, especially for imaging at ultra-high fields where RF-shimming also becomes necessary and could add further complications.

7.3.2 Clinical Application on Primary Brain Cancer Patients

Quantitative MRI will only be clinically viable if it offers at least some advantages over conventional MRI while remaining cost-effective to the health-care system. In this section, we present and discuss some preliminary results of multi-parameter mapping (MPM).

This doctoral dissertation paved the way for a clinical study that began in April 2016 at the Cross Cancer Institute, Edmonton, Canada. The study was approved by the local research ethics board (Health Research Ethics Board of Alberta) and funded by the Alberta Cancer Foundation. The purpose of the study is: 1) to investigate the potential benefits of using MPM to better monitor the cancer treatment outcome (follow-up) and 2) to test the feasibility of replacing the planning CT with a synthetic CT (derived from UTE) for the purpose of dose simulation in RTP. This second goal of the clinical study was discussed in Chapter 6: and will not be discussed here again.

In this study, 30 patients diagnosed with primary brain tumors were recruited on a voluntary basis, following written informed consent. The study consists of four MRI examinations taken at different time points, the first being before the start of the radiation therapy, (referred to as the baseline scan), and the second, third and fourth taking place approximately 3, 6, and 12 months after the end of the radiation therapy (or equivalently about 4, 7 and 13 months following the baseline scan).

Part of the challenge associated with initiating a clinical trial on MPM is that there is no gold standard yet established to ultimately use or process the parametric maps to draw the best plausible conclusions as pertaining to clinical oncology. Moreover, the challenging amount of raw data generated per scan (~10 gigabytes) add further complexity to the study, which is expected to generate a total of about 1.2 terabytes of raw data, without counting any of the post-processed data. Aspects of the image processing pipeline that were well established before the

start of the study included: 1) the raw data acquisition, 2) the reconstruction of the raw data into conventional MR images, 3) the curve-fitting of the conventional images to obtain the parametric maps (Chapters 3 and 4) and 4) the registration of the images (intra-scan registration) and maps (inter-scan registration) to compare MPM at the different time points. However, once the parametric maps have been generated for the different time points, the sky will be the limit in regard to how the maps can be analyzed. Potential fields of computer vision and machine learning that could prove useful include texture-based and histogram-based analysis of the tumors [57].

7.3.2.1 Methods

As this section of the thesis is being written, only two patients have received their second scan (4 months later), and thus the preliminary results presented here will be limited to these two cases. For each time point, five parametric maps were generated, including M_0, T_1, T_2, T_2^* and MT_{sat}. The baseline T_1 map was registered to the post-treatment T_1 using 6 DOF rigid registration in 3D Slicer. The resulting image transform was saved and used to register (and resample) all the other parametric maps. At this point, it was observed that the brain anatomy of both patients had changed significantly over 4 months, causing some significant anatomical mis-matches (of several millimeters) between the two scans. Therefore, a deformable B-spline registration (using mutual information as the cost function) was also applied following the rigid registration to quantify the amount of anatomical displacements and to yield better point-to-point anatomical alignment. The percent difference between the post-treatment and baseline parametric maps was measured voxel-wise.

7.3.2.2 Results and Discussion

Figure 7.1 shows the post-treatment T_1 map of both patients with the superposed B-spline grid following the deformable registration. Using the deformation field, it is possible to quantify both the magnitude and direction of the displacement in the patient's anatomy, yielding 2.5 mm and 3.1 mm shifts pointing towards the bulk tumor volume in both (a) and (b), respectively.

The primary motivation for obtaining geometrically accurate images (in Chapters 1 and 3) was the need for accurate dosimetry. Furthermore, if these anatomical shifts are to be accurately quantified (reported) across different scanners and imaging centers then we have an additional

motivation for using high-bandwidth bipolar multi-echo sequences in both the baseline and follow-up scans.

A voxel-based comparison of the parametric maps is presented in Figure 7.2 and Figure 7.3 for the patients in Figure 7.1 (a) and (b), respectively. For the first patient, intra-tumor T_1, T_2, and T_2^* have all increased by over 100% in certain locations, while the MT_{sat} has decreased significantly by 50–100%. The proton-density map shows a more modest increase of ~15–30% in certain locations. The edema in the frontal lobe has also clearly expanded by several millimeters in both the left and right directions. Similar trends in T_1, T_2 and T_2^* can also be observed in the second patient, except that the increase in T_1 and T_2 relaxation tends to be more localized, and little change in M_0 is observable. Contrary to the first patient, a global decrease/increase in the MT_{sat}/T_2^* is also visible. The global change in T_2^* is most likely caused by the known sensitivity to motion (and B_0 inhomogeneity), while MT_{sat} might be biased by a fluctuation in the RF power calibration.

Another application of the baseline parametric maps within the context of current trends in RTP entails searching for a correlation between the measured parameters (e.g. T_1/T_2) and the tumor cell density/activity, thus enabling the delineation of a biological clinical target volume (CTV), (a.k.a. BTV) where the dose is optimized based on the expected tumor cell density/activity [187]. BTVs derived from PET have already been shown to improve treatment outcome [188].

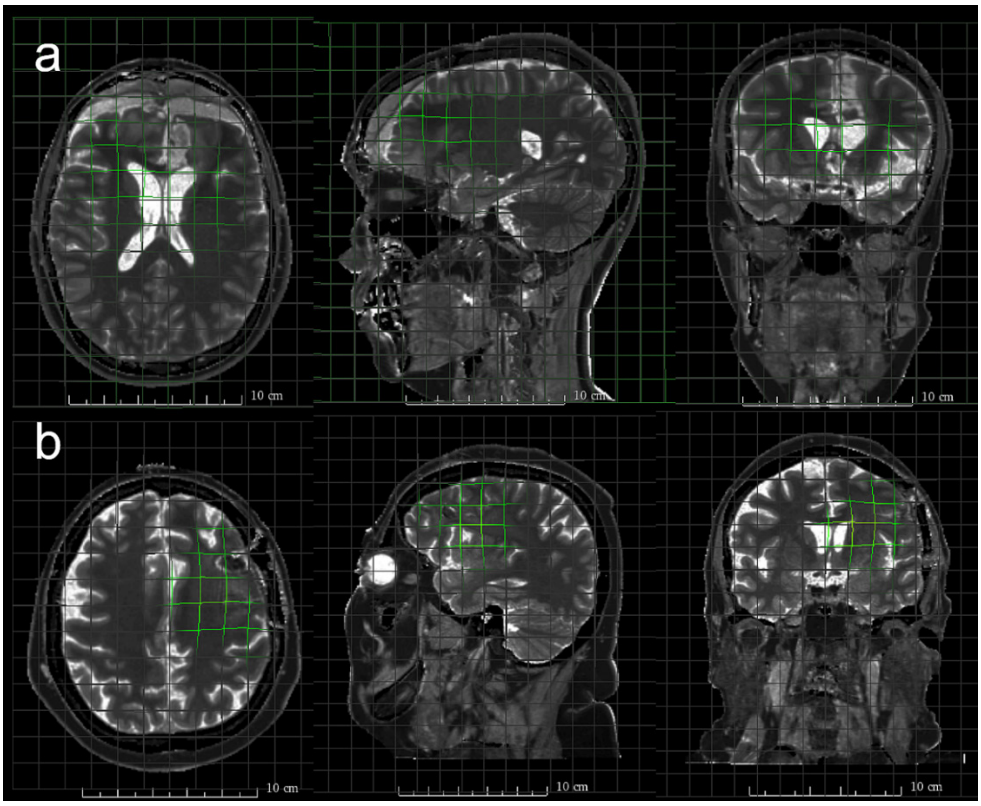

Figure 7.1: Post-treatment T_1 maps of two cancer patients showing the deformed B-spline grid following registration with the baseline T_1. The brain anatomy has shifted by ~2.5 mm in the first patient in (a) and ~3.1 mm in the second patient in (b). In both cases, the shift points towards the bulk tumor volume.

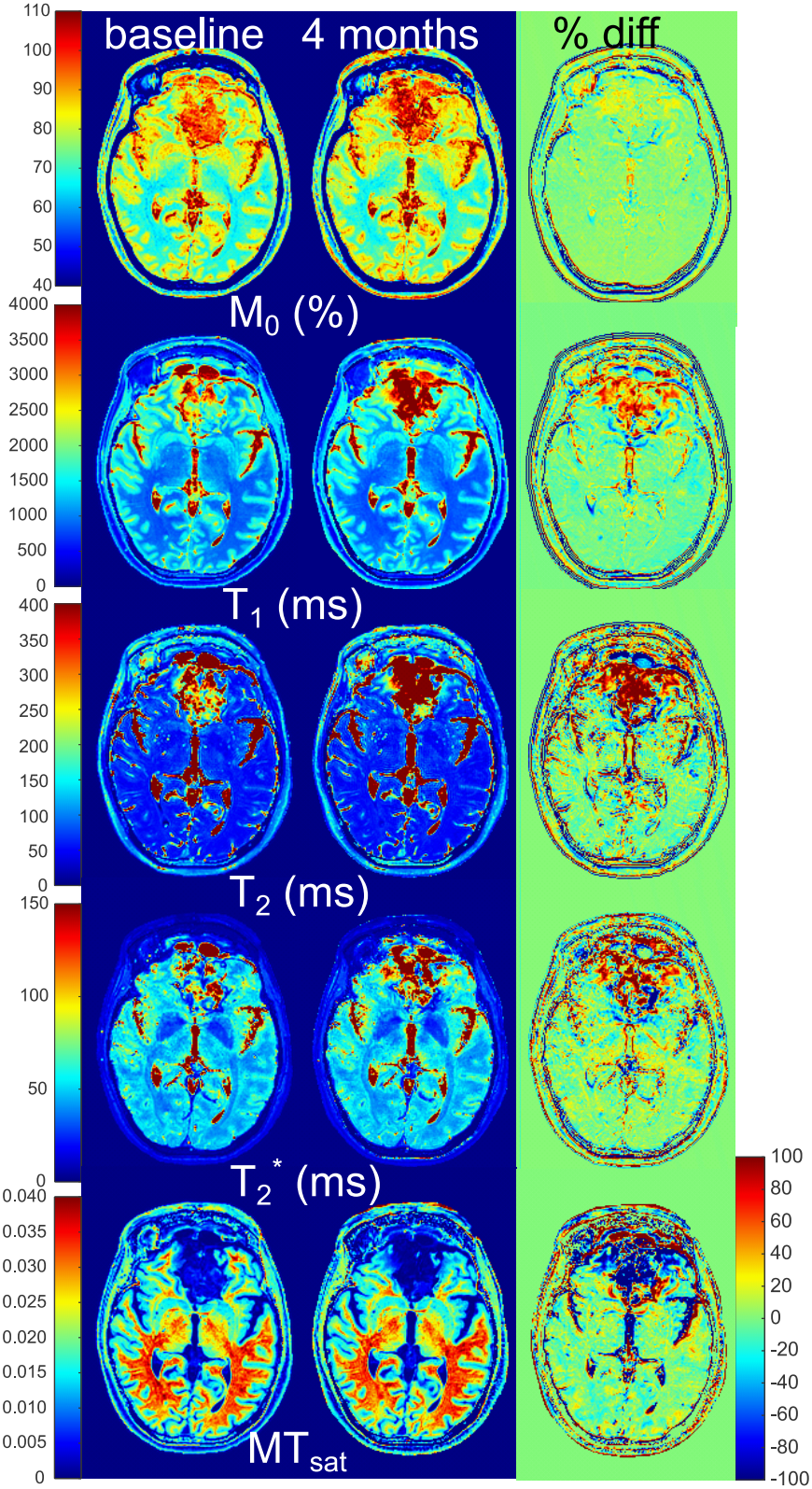

Figure 7.2: Parametric maps of patient (a) in Figure 7.1 before treatment and 4 months later, following rigid 6 DOF registration.

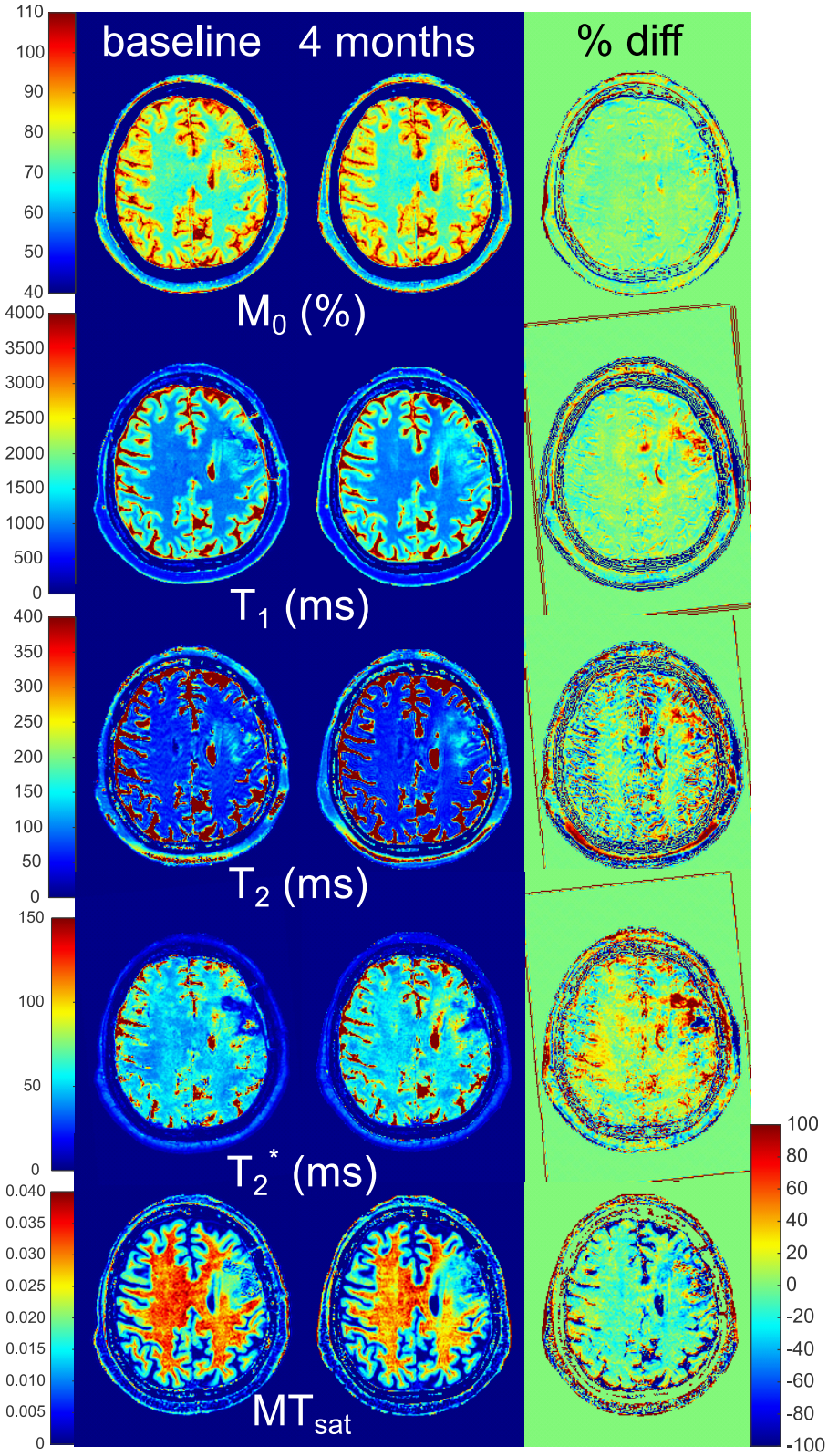

Figure 7.3: Parametric maps of patient (b) in Figure 7.1 before treatment and 4 months later, following affine and deformable B-spline registration.

7.3.2.3 Conclusion

At this point, it is too early to conclude whether the changes in relaxometry and anatomical displacements observed in both patients point toward a tumor regression, progression or pseudo-progression. What we can conclude, however, is that these techniques (without the use of contrast agent) seem sufficiently sensitive to pick out significant changes in anatomy and relaxometry between the scans before and four months after the treatment. Future research and work beyond the completion of this study will be needed to fully assess the potential benefits of MPM in clinical oncology.

7.4 Final Closing Remarks

In this concluding chapter, the major findings of this dissertation were highlighted, as well as some limitations. An application of MPM on primary brain tumors was presented with some preliminary results on two patients before and three months after radiation therapy. While it was too early to fully assess the usefulness of MPM in comparison to the standard clinical practice of using contrast-enhanced T_1-weighted images, we could nevertheless conclude that significant changes in relaxometry (>100%) and anatomical shifts (>2.5 mm) were detectable within and around the tumor, potentially providing useful diagnostic information for clinical oncology. The clinical trial will have to be completed and the data thoroughly analyzed before definite findings and conclusions can be reported.

Bibliography

[1] "Statistics about Radiation Therapy." [Online]. Available: http://www.rtanswers.org/statistics/aboutradiationtherapy/.

[2] "Equipment, Workload and Staffing for Radiotherapy in the UK 1997-2002," *R. Coll. Radiol.*, no. 5, p. 3, 2005.

[3] T. Stanescu, J. Hans-sonke, P. Stavrev, and B. G. Fallone, "3T MR-based treatment planning for radiotherapy of brain lesions," *Radiol. Oncol.*, vol. 40, no. 2, pp. 125–132, 2006.

[4] T. Stanescu, H.-S. Jans, N. Pervez, P. Stavrev, and B. G. Fallone, "A study on the magnetic resonance imaging (MRI)-based radiation treatment planning of intracranial lesions.," *Phys. Med. Biol.*, vol. 53, no. 13, pp. 3579–93, Jul. 2008.

[5] T. Stanescu, H. S. Jans, K. Wachowicz, and B. G. Fallone, "Investigation of a 3D system distortion correction method for MR images.," *J. Appl. Clin. Med. Phys.*, vol. 11, no. 1, p. 2961, Jan. 2010.

[6] H. Wang, J. Balter, and Y. Cao, "Patient-induced susceptibility effect on geometric distortion of clinical brain MRI for radiation treatment planning on a 3T scanner.," *Phys. Med. Biol.*, vol. 58, no. 3, pp. 465–77, Mar. 2013.

[7] B. Zhang, D. MacFadden, a Z. Damyanovich, M. Rieker, J. Stainsby, M. Bernstein, D. a Jaffray, D. Mikulis, and C. Ménard, "Development of a geometrically accurate imaging protocol at 3 Tesla MRI for stereotactic radiosurgery treatment planning.," *Phys. Med. Biol.*, vol. 55, no. 22, pp. 6601–15, Nov. 2010.

[8] S. P. M. Crijns, C. J. G. Bakker, P. R. Seevinck, H. de Leeuw, J. J. W. Lagendijk, and B. W. Raaymakers, "Towards inherently distortion-free MR images for image-guided radiotherapy on an MRI accelerator.," *Phys. Med. Biol.*, vol. 57, no. 5, pp. 1349–58, Mar. 2012.

[9] U. Nöth, E. Hattingen, O. Bähr, J. Tichy, and R. Deichmann, "Improved visibility of brain tumors in synthetic MP-RAGE anatomies with pure T 1 weighting," *NMR Biomed.*, vol. 28, no. April, pp. 818–830, 2015.

[10] S. C. L. Deoni, S. C. R. Williams, P. Jezzard, J. Suckling, D. G. M. Murphy, and D. K. Jones, "Standardized structural magnetic resonance imaging in multicentre studies using quantitative T1 and T2 imaging at 1.5 T.," *Neuroimage*, vol. 40, no. 2, pp. 662–71, Apr. 2008.

[11] N. Weiskopf, J. Suckling, G. Williams, M. M. Correia, B. Inkster, R. Tait, C. Ooi, E. T. Bullmore, and A. Lutti, "Quantitative multi-parameter mapping of R1, PD*, MT, and R2* at 3T: A multi-center validation," *Front. Neurosci.*, vol. 7, no. 7 JUN, pp. 1–11, 2013.

[12] D. Ma, V. Gulani, N. Seiberlich, K. Liu, J. L. Sunshine, J. L. Duerk, and M. A. Griswold, "Magnetic resonance fingerprinting.," *Nature*, vol. 495, no. 7440, pp. 187–92, 2013.

[13] R. Damadian, "Tumor detection by nuclear magnetic resonance," *Science (80-.).*, vol. 171, no. 3976, pp. 1151–1153, 1971.

[14] L. Kjaer, C. Tomsen, F. Gjerris, B. Mosdal, and O. Henriksen, "Tissue characterization of intracranial tumors by MR imaging. In vivo evaluation of T1- and T2-relaxation behavior at 1.5 T," *Acta Radiol.*, vol. 32, no. 6, pp. 498–504, 1991.

[15] P. Sanghera, J. Perry, A. Sahgal, S. Symons, R. Aviv, M. Morrison, K. Lam, P. Davey, and M. N. Tsao, "Pseudoprogression Following Chemoradiotherapy for Glioblastoma Multiforme," *Can. J. Neurol. Sci.*, vol. 37, no. 1, pp. 36–42, 2010.

[16] J.-D. Jutras, "Efficient Data Acquisition, Transmission and Post-Processing for Quality Spiral Magnetic Resonance Imaging," University of Alberta, 2011.

[17] J.-D. Jutras, K. Wachowicz, G. Gilbert, and N. De Zanche, "SNR Efficiency of Combined Bipolar Gradient Echoes: Comparison of 3D FLASH, MPRAGE, and Multi-Parameter Mapping with VFA-FLASH and MP2RAGE," *Magn. Reson. Med.*, vol. In Press, no. January, 2016.

[18] Y. Berker, J. Franke, A. Salomon, M. Palmowski, H. C. W. Donker, Y. Temur, F. M. Mottaghy, C. Kuhl, D. Izquierdo-Garcia, Z. a Fayad, F. Kiessling, and V. Schulz, "MRI-based attenuation correction for hybrid PET/MRI systems: a 4-class tissue segmentation technique using a combined ultrashort-echo-time/Dixon MRI sequence.," *J. Nucl. Med.*, vol. 53, no. 5, pp. 796–804, May 2012.

[19] N. Bloembergen, E. M. Purcell, and R. V. Pound, "Relaxation Effects in Nuclear in Nuclear Magnetic Resonance Absorption," *Phys. Rev.*, vol. 73, no. 7, pp. 679–712, 1948.

[20] R. Damadian, M. Goldsmith, and L. Minkoff, "NMR in Cancer: XVI. FONAR Image of the Live Human Body," *Physiol. Chem. & Phys.*, vol. 9, pp. 97–109, 1977.

[21] P. C. Lauterbur, "Image Formation by Induced Local Interactions: Examples Employing Nuclear Magnetic Resonance," *Nature*, vol. 242, no. 5394. pp. 190–191, 1973.

[22] P. Mansfield and P. K. Grannell, "NMR 'diffraction' in solids?," *J. Phys. C Solid State Phys.*, vol. 6, no. 22, pp. L422–L426, 1973.

[23] Z.-P. Liang and P. C. Lauterbur, *Principles of Magnetic Resonance Imaging: A Signal Processing Perspective*. New York: IEEE Press, 2000.

[24] J. V Hajnal, D. L. Hill, and D. J. Hawkes, Eds., *Medical Image Registration*. Boca Raton: CRC Press, 2001.

[25] J. P. Mugler, S. Bao, R. V. Mulkern, C. R. Guttmann, R. L. Robertson, F. A. Jolesz, and J. R. Brookeman, "Optimized single-slab three-dimensional spin-echo MR imaging of the brain," *Radiology*, vol. 216, no. 3, pp. 891–899, 2000.

[26] H. Lee, E.-Y. Kim, K.-S. Yang, and J. Park, "Susceptibility-resistant variable-flip-angle turbo spin echo imaging for reliable estimation of cortical thickness: a feasibility study.," *Neuroimage*, vol. 59, no. 1, pp. 377–88, Jan. 2012.

[27] J. Hennig, "Multiecho Imaging Sequences with Low Refocusing Flip Angles," *J. Magn. Reson.*, vol. 78, pp. 397–407, 1988.

[28] J. Park, J. P. Mugler, W. Horger, and B. Kiefer, "Optimized T1-weighted contrast for single-slab 3D turbo spin-echo imaging with long echo trains: Application to whole-brain imaging," *Magn. Reson. Med.*, vol. 58, no. 5, pp. 982–992, 2007.

[29] M. A. Bernstein, K. F. King, and X. J. Zhou, *Handbook of MRI Pulse Sequences*, vol. 32, no. 5. Burlington: Elsevier Academic Press, 2004.

[30] T. E. Yankeelov, D. R. Pickens, and R. R. Price, *Quantitative MRI in Cancer*. Boca Raton: CRC Press, 2012.

[31] Y. P. Du, Z. Jin, Y. Hu, and J. Tanabe, “Multi-echo acquisition of MR angiography and venography of the brain at 3 Tesla.,” *J. Magn. Reson. Imaging*, vol. 30, no. 2, pp. 449–454, 2009.

[32] K. Sekihara, “Steady-state magnetizations in rapid NMR imaging using small flip angles and short repetition intervals.,” *IEEE Trans. Med. Imaging*, vol. 6, no. 2, pp. 157–164, 1987.

[33] V. L. Yarnykh, “Optimal radiofrequency and gradient spoiling for improved accuracy of T1 and B1 measurements using fast steady-state techniques.,” *Magn. Reson. Med.*, vol. 63, no. 6, pp. 1610–26, Jun. 2010.

[34] Y. Zur, M. L. Wood, and L. J. Neuringer, “Spoiling of transverse magnetization in steady-state sequences.,” *Magn. Reson. Med.*, vol. 21, no. 2, pp. 251–63, Oct. 1991.

[35] C. Preibisch and R. Deichmann, “Influence of RF spoiling on the stability and accuracy of T1 mapping based on spoiled FLASH with varying flip angles.,” *Magn. Reson. Med.*, vol. 61, no. 1, pp. 125–35, Jan. 2009.

[36] C. Lenz, M. Klarhöfer, and K. Scheffler, “Limitations of rapid myelin water quantification using 3D bSSFP,” *Magn. Reson. Mater. Physics, Biol. Med.*, vol. 23, no. 3, pp. 139–151, 2010.

[37] O. Bieri, “An analytical description of balanced steady-state free precession with finite radio-frequency excitation,” *Magn. Reson. Med.*, vol. 65, no. 2, pp. 422–431, 2011.

[38] Q. S. Xiang and M. N. Hoff, “Banding artifact removal for bSSFP imaging with an elliptical signal model,” *Magn. Reson. Med.*, vol. 71, no. 3, pp. 927–933, 2014.

[39] J. P. Mugler and J. R. Brookeman, “Three-dimensional magnetization-prepared rapid gradient-echo imaging (3D MP RAGE).,” *Magn. Reson. Med.*, vol. 15, no. 1, pp. 152–7, Jul. 1990.

[40] C. Lin and M. A. Bernstein, “3D magnetization prepared elliptical centric fast gradient echo imaging.,” *Magn. Reson. Med.*, vol. 59, no. 2, pp. 434–9, Feb. 2008.

[41] T. Stocker and N. J. Shah, “MP-SAGE: A new MP-RAGE sequence with enhanced SNR

and CNR for brain imaging utilizing square-spiral phase encoding and variable flip angles," *Magn. Reson. Med.*, vol. 56, no. 4, pp. 824–834, 2006.

[42] J. R. B. Mugler, John P, Frederick H. Epstein, "Imaging Using Variable Flip Angles *," *Magn. Reson. Med.*, vol. 28, pp. 165–185, 1992.

[43] R. Deichmann, C. D. Good, O. Josephs, J. Ashburner, and R. Turner, "Optimization of 3-D MP-RAGE sequences for structural brain imaging.," *Neuroimage*, vol. 12, no. 1, pp. 112–27, Jul. 2000.

[44] J. P. Marques, T. Kober, G. Krueger, W. van der Zwaag, P.-F. Van de Moortele, and R. Gruetter, "MP2RAGE, a self bias-field corrected sequence for improved segmentation and T1-mapping at high field.," *Neuroimage*, vol. 49, no. 2, pp. 1271–81, Jan. 2010.

[45] G. Okubo, T. Okada, A. Yamamoto, M. Kanagaki, Y. Fushimi, T. Okada, K. Murata, and K. Togashi, "MP2RAGE for deep gray matter measurement of the brain: A comparative study with MPRAGE," *J. Magn. Reson. Imaging*, vol. 43, no. 1, pp. 55–62, 2016.

[46] J. G. Sled and G. B. Pike, "Quantitative imaging of magnetization transfer exchange and relaxation properties in vivo using MRI," *Magn Reson Med*, vol. 46, no. 5, pp. 923–931, 2001.

[47] M. Gloor, K. Scheffler, and O. Bieri, "Quantitative magnetization transfer imaging using balanced SSFP.," *Magn. Reson. Med.*, vol. 60, no. 3, pp. 691–700, Sep. 2008.

[48] G. Helms, H. Dathe, K. Kallenberg, and P. Dechent, "High-resolution maps of magnetization transfer with inherent correction for RF inhomogeneity and T1 relaxation obtained from 3D FLASH MRI," *Magn. Reson. Med.*, vol. 60, no. 6, pp. 1396–1407, 2008.

[49] G. Helms, H. Dathe, and P. Dechent, "Modeling the influence of TR and excitation flip angle on the Magnetization Transfer Ratio (MTR) in human brain Obtained from 3D spoiled gradient echo MRI," *Magn. Reson. Med.*, vol. 64, no. 1, pp. 177–185, 2010.

[50] K. Johansson and K. Lagerstrand, "Optimization of uTE scan protocol for human lung MR imaging," Gothenburg, 2011.

[51] S. Nielles-Vallespin, M. A. Weber, M. Bock, A. Bongers, P. Speier, S. E. Combs, J. Wöhrle, F. Lehmann-Horn, M. Essig, and L. R. Schad, "3D radial projection technique with ultrashort echo times for sodium MRI: Clinical applications in human brain and skeletal muscle," *Magn. Reson. Med.*, vol. 57, no. 1, pp. 74–81, 2007.

[52] K. P. Pruessmann, M. Weiger, M. B. Scheidegger, and P. Boesiger, "SENSE: Sensitivity encoding for fast MRI," *Magn. Reson. Med.*, vol. 42, no. 5, pp. 952–962, 1999.

[53] M. A. Griswold, P. M. Jakob, R. M. Heidemann, M. Nittka, V. Jellus, J. Wang, B. Kiefer, and A. Haase, "Generalized Autocalibrating Partially Parallel Acquisitions (GRAPPA)," *Magn. Reson. Med.*, vol. 47, no. 6, pp. 1202–1210, 2002.

[54] F.-H. Lin, K. K. Kwong, J. W. Belliveau, and L. L. Wald, "Parallel imaging reconstruction using automatic regularization.," *Magn. Reson. Med.*, vol. 51, no. 3, pp. 559–67, Mar. 2004.

[55] M. Weiger, K. P. Pruessmann, and P. Boesiger, "2D SENSE for faster 3D MRI," *Magn. Reson. Mater. Physics, Biol. Med.*, vol. 14, no. 1, pp. 10–19, 2002.

[56] J. X. Ji, J. B. Son, and S. D. Rane, "PULSAR: A MATLAB Toolbox for Parallel Magnetic Resonance Imaging Using Array Coils and Multiple Channel Receivers," *Concepts Magn. Reson. Part B Magn. Reson. Eng.*, vol. 31B, no. 1, pp. 24–36, 2007.

[57] I. N. Bankman, *Handbook of medical image processing and analysis*, 2nd ed. Amsterdam: Elsevier Academic Press, 2009.

[58] J. F. Barrett and N. Keat, "Artifacts in CT: recognition and avoidance," *Radiographics*, vol. 24, no. 6, pp. 1679–1691, 2004.

[59] J. G. Sled and G. B. Pike, "Standing-wave and RF penetration artifacts caused by elliptic geometry: an electrodynamic analysis of MRI.," *IEEE Trans. Med. Imaging*, vol. 17, no. 4, pp. 653–62, Aug. 1998.

[60] D. I. Hoult, "Sensitivity and power deposition in a high-field imaging experiment.," *J. Magn. Reson. Imaging*, vol. 12, no. 1, pp. 46–67, 2000.

[61] D. I. Hoult, "The principle of reciprocity in signal strength calculations—A mathematical

guide," *Concepts Magn. Reson.*, vol. 12, no. 4, pp. 173–187, 2000.

[62] C. H. Cunningham, J. M. Pauly, and K. S. Nayak, "Saturated double-angle method for rapid B1+ mapping.," *Magn. Reson. Med.*, vol. 55, no. 6, pp. 1326–33, Jun. 2006.

[63] V. L. Yarnykh, "Actual flip-angle imaging in the pulsed steady state: a method for rapid three-dimensional mapping of the transmitted radiofrequency field.," *Magn. Reson. Med.*, vol. 57, no. 1, pp. 192–200, Jan. 2007.

[64] N. J. Tustison, B. B. Avants, P. a Cook, Y. Zheng, A. Egan, P. a Yushkevich, and J. C. Gee, "N4ITK: improved N3 bias correction.," *IEEE Trans. Med. Imaging*, vol. 29, no. 6, pp. 1310–20, Jun. 2010.

[65] R. G. Boyes, J. L. Gunter, C. Frost, A. L. Janke, T. Yeatman, D. L. G. Hill, M. a Bernstein, P. M. Thompson, M. W. Weiner, N. Schuff, G. E. Alexander, R. J. Killiany, C. DeCarli, C. R. Jack, and N. C. Fox, "Intensity non-uniformity correction using N3 on 3-T scanners with multichannel phased array coils.," *Neuroimage*, vol. 39, no. 4, pp. 1752–62, Feb. 2008.

[66] I. Uwano, K. Kudo, F. Yamashita, J. Goodwin, S. Higuchi, K. Ito, T. Harada, A. Ogawa, and M. Sasaki, "Intensity inhomogeneity correction for magnetic resonance imaging of human brain at 7T.," *Med. Phys.*, vol. 41, no. 2, p. 22302, Feb. 2014.

[67] P. Perona and J. Malik, "Scale-space and edge detection using anisotropic diffusion.," *IEEE Trans. Pattern Anal. Mach. Intell.*, vol. 12, no. 7, pp. 629–639, 1990.

[68] M. N. Ahmed, S. M. Yamany, N. Mohamed, A. A. Farag, and T. Moriarty, "A modified fuzzy C-means algorithm for bias field estimation and segmentation of MRI data," *IEEE Trans. Med. Imaging*, vol. 21, no. 3, pp. 193–199, 2002.

[69] G. Helms and P. Dechent, "Increased SNR and reduced distortions by averaging multiple gradient echo signals in 3D FLASH imaging of the human brain at 3T.," *J. Magn. Reson. Imaging*, vol. 29, no. 1, pp. 198–204, Jan. 2009.

[70] L. N. Baldwin, K. Wachowicz, S. D. Thomas, R. Rivest, and B. G. Fallone, "Characterization, prediction, and correction of geometric distortion in 3 T MR images," *Med. Phys.*, vol. 34, no. 2, p. 388, 2007.

[71] A. Haase, J. Frahm, D. Matthaei, W. Hanicke, and K. D. Merboldt, “FLASH imaging. Rapid NMR imaging using low flip-angle pulses,” *J. Magn. Reson.*, vol. 67, no. 2, pp. 258–266, 1986.

[72] B. Fischl, D. H. Salat, A. J. W. van der Kouwe, N. Makris, F. Ségonne, B. T. Quinn, and A. M. Dale, “Sequence-independent segmentation of magnetic resonance images.,” *Neuroimage*, vol. 23 Suppl 1, pp. S69-84, Jan. 2004.

[73] A. J. W. Van Der Kouwe, T. Benner, D. H. Salat, and B. Fischl, “Brain morphometry with multiecho MPRAGE.,” *Neuroimage*, vol. 40, no. 2, pp. 559–69, Apr. 2008.

[74] H. Z. Wang, S. J. Riederer, and J. N. Lee, “Optimizing the precision in T1 relaxation estimation using limited flip angles.,” *Magn. Reson. Med.*, vol. 5, no. 5, pp. 399–416, 1987.

[75] W. Lin, R. P. Paczynski, R. Venkatesan, Y. Y. He, W. J. Powers, C. Y. Hsu, and E. M. Haacke, “Quantitative regional brain water measurement with magnetic resonance imaging in a focal ischemia model,” *Magn. Reson. Med.*, vol. 38, no. 2, pp. 303–310, 1997.

[76] R. Venkatesan, W. Lin, and E. M. Haacke, “Accurate determination of spin-density and T1 in the presence of RF- field inhomogeneities and flip-angle miscalibration,” *Magn. Reson. Med.*, vol. 40, no. 4, pp. 592–602, 1998.

[77] S. C. L. Deoni, B. K. Rutt, and T. M. Peters, “Synthetic T1-weighted brain image generation with incorporated coil intensity correction using DESPOT1.,” *Magn. Reson. Imaging*, vol. 24, no. 9, pp. 1241–8, Nov. 2006.

[78] R. Metere, E. H. Moller, G. Kruger, T. Kober, and A. Schafer, “Simultaneous Quantitative Mapping of T1 , T2*, and Magnetic Susceptibility with Multi-Echo MP2RAGE at 7 T,” in *International Society of Magnetic Resonance in Medicine*, 2015, vol. 23, p. 439.

[79] O. Ocali and E. Atalar, “Ultimate intrinsic signal-to-noise ratio in MRI.,” *Magn. Reson. Med.*, vol. 39, no. 3, pp. 462–73, Mar. 1998.

[80] S. Vinitski, R. Griffey, M. Fuka, N. Matwiyoff, and R. Prost, “Effect of the sampling rate on magnetic resonance imaging.,” *Magn. Reson. Med.*, vol. 5, no. 3, pp. 278–85, Sep.

1987.

[81] L. Fleysher, R. Fleysher, S. Liu, W. Zaaraoui, and O. Gonen, “Optimizing the precision-per-unit-time of quantitative MR metrics: examples for T1, T2, and DTI.,” *Magn. Reson. Med.*, vol. 57, no. 2, pp. 380–7, Feb. 2007.

[82] J. Rahmer, P. Börnert, J. Groen, and C. Bos, “Three-dimensional radial ultrashort echo-time imaging with T2 adapted sampling.,” *Magn. Reson. Med.*, vol. 55, no. 5, pp. 1075–82, May 2006.

[83] A. Cardenas-Blanco, C. Tejos, P. Irarrazaval, and I. Cameron, “Noise in Magnitude Magnetic Resonance Images,” *Concepts Magn. Reson. Part A*, vol. 32A, no. 6, pp. 409–416, 2008.

[84] S. C. L. Deoni, T. M. Peters, and B. K. Rutt, “High-resolution T1 and T2 mapping of the brain in a clinically acceptable time with DESPOT1 and DESPOT2.,” *Magn. Reson. Med.*, vol. 53, no. 1, pp. 237–41, Jan. 2005.

[85] C. Preibisch and R. Deichmann, “T1 mapping using spoiled FLASH-EPI hybrid sequences and varying flip angles.,” *Magn. Reson. Med.*, vol. 62, no. 1, pp. 240–6, Jul. 2009.

[86] H.-L. M. Cheng and G. A. Wright, “Rapid high-resolution T1 mapping by variable flip angles: accurate and precise measurements in the presence of radiofrequency field inhomogeneity.,” *Magn. Reson. Med.*, vol. 55, no. 3, pp. 566–74, Mar. 2006.

[87] A. Manuel, W. Li, V. Jellus, T. Hughes, and P. V Prasad, “Variable flip angle-based fast three-dimensional T1 mapping for delayed gadolinium-enhanced MRI of cartilage of the knee: need for B1 correction.,” *Magn. Reson. Med.*, vol. 65, no. 5, pp. 1377–83, May 2011.

[88] S. C. L. Deoni, B. K. Rutt, and T. M. Peters, “Rapid combined T1 and T2 mapping using gradient recalled acquisition in the steady state.,” *Magn. Reson. Med.*, vol. 49, no. 3, pp. 515–26, Mar. 2003.

[89] M. C. Schabel and G. R. Morrell, “Uncertainty in T1 mapping using the variable flip angle method with two flip angles.,” *Phys. Med. Biol.*, vol. 54, no. 1, pp. N1-8, Jan. 2009.

[90] M. Sabati and A. A. Maudsley, “Fast and high-resolution quantitative mapping of tissue water content with full brain coverage for clinically-driven studies.,” *Magn. Reson. Imaging*, vol. 31, no. 10, pp. 1752–9, Dec. 2013.

[91] P. B. Roemer, W. a Edelstein, C. E. Hayes, S. P. Souza, and O. M. Mueller, “The NMR phased array.,” *Magn. Reson. Med.*, vol. 16, no. 2, pp. 192–225, Nov. 1990.

[92] N. Weiskopf, A. Lutti, G. Helms, M. Novak, J. Ashburner, and C. Hutton, “Unified segmentation based correction of R1 brain maps for RF transmit field inhomogeneities (UNICORT).,” *Neuroimage*, vol. 54, no. 3, pp. 2116–24, Feb. 2011.

[93] S. Volz, U. Nöth, and R. Deichmann, “Correction of systematic errors in quantitative proton density mapping.,” *Magn. Reson. Med.*, vol. 68, no. 1, pp. 74–85, Jul. 2012.

[94] N. Weiskopf, M. F. Callaghan, O. Josephs, A. Lutti, and S. Mohammadi, “Estimating the apparent transverse relaxation time (R2*) from images with different contrasts (ESTATICS) reduces motion artifacts,” *Front. Neurosci.*, vol. 8, no. September, pp. 1–10, 2014.

[95] P. A. Hardy and A. H. Andersen, “Calculating T2 in images from a phased array receiver.,” *Magn. Reson. Med.*, vol. 61, no. 4, pp. 962–9, Apr. 2009.

[96] National Electric Manufacturers Association, “Determination of Signal-to-Noise Ratio (SNR) in Diagnostic Magnetic Resonance Imaging, NEMA Standards Publication MS1-2008,” 2008.

[97] C. Howarth, C. Hutton, and R. Deichmann, “Improvement of the image quality of T1-weighted anatomical brain scans.,” *Neuroimage*, vol. 29, no. 3, pp. 930–7, Feb. 2006.

[98] J. O. Christoffersson, L. E. Olsson, and S. Sjöberg, “Nickel-doped agarose gel phantoms in MR imaging.,” *Acta Radiol.*, vol. 32, no. 5, pp. 426–31, Sep. 1991.

[99] S. Nekolla, T. Gneiting, J. Syha, R. Deichmann, and A. Haase, “T1 maps by K-space reduced snapshot-FLASH MRI.,” *J. Comput. Assist. Tomogr.*, vol. 16, no. 2, pp. 327–32, 1992.

[100] H. Kato, K. Yoshimura, M. Kuroda, A. Yoshida, K. Hanamoto, S. Kawasaki, K. Shibuya,

Y. Yamamoto, M. Tsunoda, M. Takemoto, and Y. Hiraki, “Development of a phantom compatible for MRI and hyperthermia using carrageenan gel-relationship between T1 and T2 values and NaCl concentration.,” *Int. J. Hyperthermia*, vol. 20, no. 8, pp. 803–814, 2004.

[101] A. Fedorov, R. Beichel, J. Kalpathy-Cramer, J. Finet, J.-C. Fillion-Robin, S. Pujol, C. Bauer, D. Jennings, F. Fennessy, M. Sonka, J. Buatti, S. Aylward, J. V Miller, S. Pieper, and R. Kikinis, “3D Slicer as an image computing platform for the Quantitative Imaging Network.,” *Magn. Reson. Imaging*, vol. 30, no. 9, pp. 1323–41, Nov. 2012.

[102] S. Volz, U. Nöth, A. Jurcoane, U. Ziemann, E. Hattingen, and R. Deichmann, “Quantitative proton density mapping: correcting the receiver sensitivity bias via pseudo proton densities.,” *Neuroimage*, vol. 63, no. 1, pp. 540–52, Oct. 2012.

[103] H. Neeb, K. Zilles, and N. J. Shah, “A new method for fast quantitative mapping of absolute water content in vivo.,” *Neuroimage*, vol. 31, no. 3, pp. 1156–68, Jul. 2006.

[104] J. Li, S. Chang, T. Liu, H. Jiang, F. Dong, M. Pei, Q. Wang, and Y. Wang, “Phase-corrected bipolar gradients in multi-echo gradient-echo sequences for quantitative susceptibility mapping,” *Magn. Reson. Mater. Physics, Biol. Med.*, vol. 28, no. 4, pp. 347–355, 2015.

[105] D. Hwang, D.-H. Kim, and Y. P. Du, “In vivo multi-slice mapping of myelin water content using T2* decay.,” *Neuroimage*, vol. 52, no. 1, pp. 198–204, Aug. 2010.

[106] A. M. Oros-Peusquens, M. Laurila, and N. J. Shah, “Magnetic field dependence of the distribution of NMR relaxation times in the living human brain.,” *MAGMA*, vol. 21, no. 1–2, pp. 131–47, Mar. 2008.

[107] N. Gelman, J. R. Ewing, J. M. Gorell, E. M. Spickler, and E. G. Solomon, “Interregional variation of longitudinal relaxation rates in human brain at 3.0 T: Relation to estimated iron and water contents,” *Magn. Reson. Med.*, vol. 45, no. 1, pp. 71–79, 2001.

[108] J. P. Wansapura, S. K. Holland, R. S. Dunn, and W. S. Ball, “NMR relaxation times in the human brain at 3.0 tesla.,” *J. Magn. Reson. Imaging*, vol. 9, no. 4, pp. 531–8, Apr. 1999.

[109] G. Helms, H. Dathe, and P. Dechent, “Quantitative FLASH MRI at 3T using a rational

approximation of the Ernst equation.," *Magn. Reson. Med.*, vol. 59, no. 3, pp. 667–72, Mar. 2008.

[110] H. Neeb, V. Ermer, T. Stocker, and N. J. Shah, "Fast quantitative mapping of absolute water content with full brain coverage," *Neuroimage*, vol. 42, no. 3, pp. 1094–1109, 2008.

[111] Z. Abbas, V. Gras, K. Möllenhoff, A.-M. Oros-Peusquens, and N. J. Shah, "Quantitative water content mapping at clinically relevant field strengths: A comparative study at 1.5T and 3T.," *Neuroimage*, vol. 106, pp. 404–13, 2015.

[112] C. Langkammer, T. Liu, M. Khalil, C. Enzinger, M. Jehna, S. Fuchs, F. Fazekas, Y. Wang, and S. Ropele, "Quantitative susceptibility mapping in multiple sclerosis.," *Radiology*, vol. 267, no. 2, pp. 551–9, 2013.

[113] J. A. Rioux, I. R. Levesque, and B. K. Rutt, "Biexponential longitudinal relaxation in white matter: Characterization and impact on T 1 mapping with IR-FSE and MP2RAGE," *Magn. Reson. Med.*, vol. 0, p. n/a-n/a, 2015.

[114] G. Diakova, J.-P. Korb, and R. G. Bryant, "The magnetic field dependence of water T1 in tissues.," *Magn. Reson. Med.*, vol. 68, no. 1, pp. 272–7, 2012.

[115] B. Keil and L. L. Wald, "Massively parallel MRI detector arrays.," *J. Magn. Reson.*, vol. 229, pp. 75–89, Apr. 2013.

[116] J. R. Taylor, *An introduction to error analysis*, 2nd ed. Sausalito: University Science Books, 1997.

[117] Y. D. Deene, R. V. De Walle, E. Achten, and C. D. Wagter, "Mathematical analysis and experimental investigation of noise in quantitative magnetic resonance imaging applied in polymer gel dosimetry," *Signal Processing*, vol. 70, no. 2, pp. 85–101, Oct. 1998.

[118] J. M. Walker and J. W. M. Bulte, *Magnetic Resonance Neuroimaging: Methods and Protocols*. Springer, 2011.

[119] J. Ashburner and K. J. Friston, "Voxel-based morphometry--the methods.," *Neuroimage*, vol. 11, no. 6 Pt 1, pp. 805–21, Jun. 2000.

[120] M. A. van Buchem, J. C. McGowan, and R. I. Grossman, "Magnetization transfer

histogram methodology: its clinical and neuropsychological correlates.," *Neurology*, vol. 53, no. 5 Suppl 3, pp. S23–S28, 1999.

[121] L. Wang, M. E. Schweitzer, A. Padua, and R. R. Regatte, "Rapid 3D-T1 mapping of cartilage with variable flip angle and parallel imaging at 3.0T.," *J. Magn. Reson. Imaging*, vol. 27, no. 1, pp. 154–61, Jan. 2008.

[122] S. C. L. Deoni, "High-resolution T1 mapping of the brain at 3T with driven equilibrium single pulse observation of T1 with high-speed incorporation of RF field inhomogeneities (DESPOT1-HIFI).," *J. Magn. Reson. Imaging*, vol. 26, no. 4, pp. 1106–11, Oct. 2007.

[123] S. C. L. Deoni, H. A. Ward, T. M. Peters, and B. K. Rutt, "Rapid T2 estimation with phase-cycled variable nutation steady-state free precession.," *Magn. Reson. Med.*, vol. 52, no. 2, pp. 435–9, Aug. 2004.

[124] H. J. A. Crooijmans, M. Gloor, O. Bieri, and K. Scheffler, "Influence of MT effects on T2 quantification with 3D balanced steady-state free precession imaging.," *Magn. Reson. Med.*, vol. 65, no. 1, pp. 195–201, Jan. 2011.

[125] H. J. A. Crooijmans, K. Scheffler, and O. Bieri, "Finite RF pulse correction on DESPOT2.," *Magn. Reson. Med.*, vol. 65, no. 3, pp. 858–62, Mar. 2011.

[126] B. Aubert-Broche, C. Grova, G. B. Pike, and D. L. Collins, "Clustering of atlas-defined cortical regions based on relaxation times and proton density.," *Neuroimage*, vol. 47, no. 2, pp. 523–32, Aug. 2009.

[127] G. P. Liney, A. J. Knowles, D. J. Manton, L. W. Turnbull, S. J. Blackband, and A. Horsman, "Comparison of conventional single echo and multi-echo sequences with a fast spin-echo sequence for quantitative T2 mapping: application to the prostate.," *J. Magn. Reson. Imaging*, vol. 6, no. 4, pp. 603–7, 1996.

[128] S. C. L. Deoni, "Transverse relaxation time (T2) mapping in the brain with off-resonance correction using phase-cycled steady-state free precession imaging.," *J. Magn. Reson. Imaging*, vol. 30, no. 2, pp. 411–7, Aug. 2009.

[129] T. C. Wood, S. J. Wastling, and G. J. Barker, "Removing SSFP Banding Artifacts from DESPOT2 Images Using the Geometric Solution," in *Proc Intl Soc Magn Reson Med*,

2015, vol. 23, p. 1680.

[130] Y. Zur, S. Stokar, and P. Bendel, “An analysis of fast imaging sequences with steady-state transverse magnetization refocusing.,” *Magn. Reson. Med.*, vol. 6, no. 2, pp. 175–93, Feb. 1988.

[131] Y. Zur, M. L. Wood, and L. J. Neuringer, “Motion-insensitive, steady-state free precession imaging.,” *Magn. Reson. Med.*, vol. 16, no. 3, pp. 444–59, Dec. 1990.

[132] K.-J. Jung, “Synthesis methods of multiple phase-cycled SSFP images to reduce the band artifact and noise more reliably.,” *Magn. Reson. Imaging*, vol. 28, no. 1, pp. 103–18, Jan. 2010.

[133] M. L. Lauzon and R. Frayne, “Analytical characterization of RF phase-cycled balanced steady-state free precession,” *Concepts Magn. Reson. Part A*, vol. 34A, no. 3, pp. 133–143, May 2009.

[134] R. Dharmakumar and G. A. Wright, “Understanding steady-state free precession: A geometric perspective,” *Concepts Magn. Reson. Part A*, vol. 26, no. 1, pp. 1–10, 2005.

[135] O. Bieri and K. Scheffler, “On the origin of apparent low tissue signals in balanced SSFP.,” *Magn. Reson. Med.*, vol. 56, no. 5, pp. 1067–74, Nov. 2006.

[136] O. Bieri and K. Scheffler, “SSFP signal with finite RF pulses.,” *Magn. Reson. Med.*, vol. 62, no. 5, pp. 1232–41, Nov. 2009.

[137] J. Zhang, S. H. Kolind, C. Laule, and A. L. Mackay, “How Does Magnetization Transfer Influence mcDESPOT Results ?,” *Magn. Reson. Med.*, vol. 74, no. 5, pp. 1327–1335, 2014.

[138] R. M. Lebel and A. H. Wilman, “Transverse relaxometry with reduced echo train lengths via stimulated echo compensation,” *Magn. Reson. Med.*, vol. 64, no. 5, pp. 1340–1346, 2010.

[139] A. Petrovic, E. Scheurer, and R. Stollberger, “Closed-form solution for T2 mapping with nonideal refocusing of slice selective CPMG sequences,” *Magn. Reson. Med.*, vol. 73, pp. 818–827, 2015.

[140] G. E. Gold, E. Han, J. Stainsby, G. Wright, J. Brittain, and C. Beaulieu, "Musculoskeletal MRI at 3.0 T : Relaxation Times and Image Contrast," *Am. J. Neuroradiol.*, vol. 183, no. November, pp. 1479–1486, 2004.

[141] N. Ben-Eliezer, D. K. Sodickson, and K. T. Block, "Rapid and accurate T2 mapping from multi-spin-echo data using bloch-simulation-based reconstruction," *Magn. Reson. Med.*, vol. 73, pp. 809–817, 2015.

[142] A. MacKay, K. Whittall, J. Adler, D. Li, D. Paty, and D. Graeb, "In vivo visualization of myelin water in brain by magnetic resonance," *Magn. Reson. Med.*, vol. 31, no. 6, pp. 673–677, 1994.

[143] G. J. Stanisz, E. E. Odrobina, J. Pun, M. Escaravage, S. J. Graham, M. J. Bronskill, and R. M. Henkelman, "T1, T2 relaxation and magnetization transfer in tissue at 3T.," *Magn. Reson. Med.*, vol. 54, no. 3, pp. 507–12, Sep. 2005.

[144] K. C. . McPhee and A. H. Wilman, "Comparison of Indirect and Stimulated Echo Compensated T2 Relaxometry Techniques : Extended Phase Graph vs Shinnar Le Roux Based Modelling," in *International Society of Magnetic Resonance in Medicine*, 2015, vol. 23, p. 1688.

[145] N. K. Focke, G. Helms, S. Kaspar, C. Diederich, V. T??th, P. Dechent, A. Mohr, and W. Paulus, "Multi-site voxel-based morphometry - Not quite there yet," *Neuroimage*, vol. 56, no. 3, pp. 1164–1170, 2011.

[146] K. J. Chang and H. Jara, "Application of quantitative T1, T2, and proton density to diagnosis," *Appl. Radiol.*, vol. 34, no. 1 SUPPL., pp. 34–42, 2005.

[147] G. Bartzokis, J. L. Cummings, C. H. Markham, P. Z. Marmarelis, L. J. Treciokas, T. A. Tishler, S. R. Marder, and J. Mintz, "MRI evaluation of brain iron in earlier- and later-onset Parkinson's disease and normal subjects," *Magn. Reson. Imaging*, vol. 17, no. 2, pp. 213–222, 1999.

[148] G. Bartzokis, D. Sultzer, J. Cummings, L. E. Holt, D. B. Hance, V. W. Henderson, and J. Mintz, "In vivo evaluation of brain iron in Alzheimer disease using magnetic resonance imaging," *Arch. Gen. Psychiatry*, vol. 57, no. 1, pp. 47–53, 2000.

[149] J. D. Jutras, K. Wachowicz, and N. De Zanche, “Analytical corrections of banding artifacts in driven equilibrium single pulse observation of T2 (DESPOT2),” *Magn. Reson. Med.*, vol. 0, 2015.

[150] N. Stikov, M. Boudreau, I. R. Levesque, C. L. Tardif, J. K. Barral, and G. B. Pike, “On the accuracy of T1 mapping: Searching for common ground,” *Magn. Reson. Med.*, vol. 73, no. 2, pp. 514–522, 2015.

[151] S. Chavez and G. J. Stanisz, “A novel method for simultaneous 3D B1 and T1 mapping: the method of slopes (MoS).,” *NMR Biomed.*, vol. 25, no. 9, pp. 1043–55, Sep. 2012.

[152] J.-D. Jutras, K. Wachowicz, G. Gilbert, and N. De Zanche, “SNR Efficiency of Combined Bipolar Gradient Echoes: Comparison of 3D FLASH, MPRAGE, and Multi-Parameter Mapping with VFA-FLASH and MP2RAGE,” *Magn. Reson. Med.*, vol. In Press, 2016.

[153] M. Boudreau, C. Dardif, N. Stikov, and G. B. Pike, “A Comparison of B1 Mapping Methods for T1 Mapping at 3T,” in *Iternational Society of Magnetic Resonance in Medicine*, 2014, vol. 22, p. 3207.

[154] J. Wang, W. Mao, M. Qiu, M. B. Smith, and R. T. Constable, “Factors influencing flip angle mapping in MRI: RF pulse shape, slice-select gradients, off-resonance excitation, and B0 inhomogeneities.,” *Magn. Reson. Med.*, vol. 56, no. 2, pp. 463–8, Aug. 2006.

[155] S. A. Hurley, V. L. Yarnykh, K. M. Johnson, A. S. Field, A. L. Alexander, and A. A. Samsonov, “Simultaneous variable flip angle-actual flip angle imaging method for improved accuracy and precision of three-dimensional T1 and B1 measurements.,” *Magn. Reson. Med.*, vol. 68, no. 1, pp. 54–64, Jul. 2012.

[156] P. J. Wright, O. E. Mougin, J. J. Totman, A. M. Peters, M. J. Brookes, R. Coxon, P. E. Morris, M. Clemence, S. T. Francis, R. W. Bowtell, and P. A. Gowland, “Water proton T1 measurements in brain tissue at 7, 3, and 1.5 T using IR-EPI, IR-TSE, and MPRAGE: results and optimization.,” *MAGMA*, vol. 21, no. 1–2, pp. 121–30, Mar. 2008.

[157] D. C. Zhu and R. D. Penn, “Full-brain T1 mapping through inversion recovery fast spin echo imaging with time-efficient slice ordering.,” *Magn. Reson. Med.*, vol. 54, no. 3, pp. 725–31, Sep. 2005.

[158] R. D. Newbould, S. T. Skare, M. T. Alley, G. E. Gold, and R. Bammer, "Three-dimensional T1, T2 and proton density mapping with inversion recovery balanced SSFP.," *Magn. Reson. Imaging*, vol. 28, no. 9, pp. 1374–82, Nov. 2010.

[159] H. Lu, L. M. Nagae-Poetscher, X. Golay, D. Lin, M. Pomper, and P. C. M. van Zijl, "Routine clinical brain MRI sequences for use at 3.0 Tesla.," *J. Magn. Reson. Imaging*, vol. 22, no. 1, pp. 13–22, Jul. 2005.

[160] J. Wang, M. Qiu, H. Kim, and R. T. Constable, "T1 measurements incorporating flip angle calibration and correction in vivo.," *J. Magn. Reson.*, vol. 182, no. 2, pp. 283–292, 2006.

[161] B. Mädler, T. Harris, and A. L. Mackay, "3D-Relaxometry - Quantitative T1 and T2 Brain Mapping at 3T," in *International Society of Magnetic Resonance in Medicine*, 2006, vol. 14, p. 958.

[162] T. Ethofer, I. Mader, U. Seeger, G. Helms, M. Erb, W. Grodd, A. Ludolph, and U. Klose, "Comparison of longitudinal metabolite relaxation times in different regions of the human brain at 1.5 and 3 Tesla.," *Magn. Reson. Med.*, vol. 50, no. 6, pp. 1296–301, Dec. 2003.

[163] Y. Jiang, D. Ma, N. Seiberlich, V. Gulani, and M. A. Griswold, "MR fingerprinting using fast imaging with steady state precession (FISP) with spiral readout," *Magn. Reson. Med.*, vol. 0, pp. 1–11, 2014.

[164] D. Ma, E. Y. Pierre, Y. Jiang, M. D. Schluchter, K. Setsompop, V. Gulani, and M. A. Griswold, "Music-based magnetic resonance fingerprinting to improve patient comfort during MRI examinations," *Magn. Reson. Med.*, vol. 0, no. January, 2015.

[165] K. Hattori, Y. Ikemoto, W. Takao, S. Ohno, T. Harimoto, S. Kanazawa, M. Oita, K. Shibuya, M. Kuroda, and H. Kato, "Development of MRI phantom equivalent to human tissues for 3.0-T MRI.," *Med. Phys.*, vol. 40, no. 3, p. 32303, 2013.

[166] J. K. Barral, E. Gudmundson, N. Stikov, M. Etezadi-Amoli, P. Stoica, and D. G. Nishimura, "A robust methodology for in vivo T1 mapping," *Magn. Reson. Med.*, vol. 64, no. 4, pp. 1057–1067, 2010.

[167] S. M. Smith, "Fast robust automated brain extraction," *Hum. Brain Mapp.*, vol. 17, no. 3,

pp. 143–155, 2002.

[168] V. Keereman, Y. Fierens, T. Broux, Y. De Deene, M. Lonneux, and S. Vandenberghe, "MRI-based attenuation correction for PET/MRI using ultrashort echo time sequences.," *J. Nucl. Med.*, vol. 51, no. 5, pp. 812–8, May 2010.

[169] C. Catana, A. van der Kouwe, T. Benner, C. J. Michel, M. Hamm, M. Fenchel, B. Fischl, B. Rosen, M. Schmand, and a G. Sorensen, "Toward implementing an MRI-based PET attenuation-correction method for neurologic studies on the MR-PET brain prototype.," *J. Nucl. Med.*, vol. 51, no. 9, pp. 1431–8, Sep. 2010.

[170] B. K. Navalpakkam, H. Braun, T. Kuwert, and H. H. Quick, "Magnetic resonance-based attenuation correction for PET/MR hybrid imaging using continuous valued attenuation maps.," *Invest. Radiol.*, vol. 48, no. 5, pp. 323–32, May 2013.

[171] A. Johansson, M. Karlsson, and T. Nyholm, "CT substitute derived from MRI sequences with ultrashort echo time," *Med. Phys.*, vol. 38, no. 5, p. 2708, 2011.

[172] G. Delso, K. Zeimpekis, M. Carl, F. Wiesinger, M. Hüllner, and P. Veit-haibach, "Cluster-based segmentation of dual-echo ultra-short echo time images for PET / MR bone localization," pp. 1–13, 2014.

[173] S.-H. Hsu, Y. Cao, K. Huang, M. Feng, and J. M. Balter, "Investigation of a method for generating synthetic CT models from MRI scans of the head and neck for radiation therapy.," *Phys. Med. Biol.*, vol. 58, no. 23, pp. 8419–35, Dec. 2013.

[174] F. Wiesinger, L. I. Sacolick, A. Menini, S. S. Kaushik, S. Ahn, P. Veit-Haibach, G. Delso, and D. D. Shanbhag, "Zero TE MR bone imaging in the head," *Magn. Reson. Med.*, vol. 114, no. October 2014, pp. 107–114, 2015.

[175] F. Springer, G. Steidle, P. Martirosian, C. D. Claussen, and F. Schick, "Effects of in-pulse transverse relaxation in 3D ultrashort echo time sequences: analytical derivation, comparison to numerical simulation and experimental application at 3T.," *J. Magn. Reson.*, vol. 206, no. 1, pp. 88–96, Sep. 2010.

[176] R. Cusack and N. Papadakis, "New robust 3-D phase unwrapping algorithms: application to magnetic field mapping and undistorting echoplanar images.," *Neuroimage*, vol. 16, no.

3 Pt 1, pp. 754–764, 2002.

[177] A. P. Aitken, D. Giese, C. Tsoumpas, P. Schleyer, S. Kozerke, C. Prieto, and T. Schaeffter, "Improved UTE-based attenuation correction for cranial PET-MR using dynamic magnetic field monitoring.," *Med. Phys.*, vol. 41, no. 1, p. 12302, Jan. 2014.

[178] D. M. Grodzki, P. M. Jakob, and B. Heismann, "Ultrashort echo time imaging using pointwise encoding time reduction with radial acquisition (PETRA).," *Magn. Reson. Med.*, vol. 67, no. 2, pp. 510–8, Feb. 2012.

[179] M. Kapanen and M. Tenhunen, "T1/T2*-weighted MRI provides clinically relevant pseudo-CT density data for the pelvic bones in MRI-only based radiotherapy treatment planning.," *Acta Oncol.*, vol. 52, no. 3, pp. 612–8, Apr. 2013.

[180] A. Torrado-Carvajal, J. L. Herraiz, J. A. Hernandez-Tamames, R. San Jose-Estepar, Y. Eryaman, Y. Rozenholc, E. Adalsteinsson, L. L. Wald, and N. Malpica, "Multi-atlas and label fusion approach for patient-specific MRI based skull estimation," *Magn. Reson. Med.*, vol. 1807, no. May 2015, pp. 1797–1807, 2015.

[181] S. Renisch, T. Blaffert, J. Tang, and Z. Hu, "Validation of model-based pelvis bone segmentation from MR images for PET/MR attenuation correction," *SPIE Proc.*, vol. 8314, no. 4, pp. 1–11, Feb. 2012.

[182] V. Keereman, P. Mollet, Y. Berker, V. Schulz, and S. Vandenberghe, "Challenges and current methods for attenuation correction in PET/MR.," *MAGMA*, vol. 26, no. 1, pp. 81–98, Feb. 2013.

[183] G. Wagenknecht, H. J. Kaiser, F. M. Mottaghy, and H. Herzog, "MRI for attenuation correction in PET: Methods and challenges," *Magn. Reson. Mater. Physics, Biol. Med.*, vol. 26, no. 1, pp. 99–113, 2013.

[184] S. Suzuki, O. Sakai, and H. Jara, "Combined volumetric T1, T2 and secular-T2 quantitative MRI of the brain: age-related global changes (preliminary results)," *Magn. Reson. Imaging*, vol. 24, no. 7, pp. 877–887, 2006.

[185] C.-H. Chang and J. Ji, "Compressed sensing MRI with multichannel data using multicore processors.," *Magn. Reson. Med.*, vol. 64, no. 4, pp. 1135–9, Oct. 2010.

[186] M. F. Callaghan, O. Josephs, M. Herbst, M. Zaitsev, N. Todd, and N. Weiskopf, "An evaluation of prospective motion correction (PMC) for high resolution quantitative MRI," *Front. Neurosci.*, vol. 9, no. March, pp. 1–9, 2015.

[187] V. S. Khoo and D. L. Joon, "New developments in MRI for target volume delineation in radiotherapy," *British Journal of Radiology*, vol. 79, no. Spec No 1. pp. S2–S15, 2006.

[188] C. La Fougère, B. Suchorska, P. Bartenstein, F. W. Kreth, and J. C. Tonn, "Molecular imaging of gliomas with PET: Opportunities and limitations," *Neuro. Oncol.*, vol. 13, no. 8, pp. 806–819, 2011.

[189] V. Gulani, P. Schmitt, M. A. Griswold, A. G. Webb, and P. M. Jakob, "Towards a Single-Sequence Neurologic Magnetic," *Invest. Radiol.*, vol. 39, no. 12, pp. 767–774, 2004.